A comprehensive study of detached-eddy simulation

vorgelegt von

Charles Mockett
M.Eng

Von der Fakultät V – Verkehrs- und Maschinensysteme
der Technischen Universität Berlin
zur Erlangung des akademischen Grades
Doktor der Ingenieurwissenschaften (Dr.-Ing.)
genehmigte Dissertation

Promotionsausschuss:

Vorsitzender:	Prof. Dr.-Ing. Wolfgang Nitsche
Berichter:	Prof. Dr.-Ing. Frank Thiele
	Prof. Mikhael Strelets

Tag der wissenschaftliche Aussprache: 17.04.2009

Berlin 2009
D 83

ISBN (online) 978 3 7983 2159 5
ISBN (print) 978 3 7983 2160 1

∞ Gedruckt auf säurefreiem alterungsbeständigem Papier

Druck/ Printing: docupoint GmbH Magdeburg
Maxim-Gorki-Straße 10, 39108 Magdeburg

Vertrieb/ Publisher: Universitätsverlag der TU Berlin
Universitätsbibliothek
Fasanenstr. 88 (im VOLKSWAGEN-Haus), D-10623 Berlin
Tel.: (030)314-76131; Fax.: (030)314-76133
E-Mail: publikationen@ub.tu-berlin.de
http://www.univerlag.tu-berlin.de/

To Silke and Frederick

Abstract

Detached-eddy simulation (DES) is a prominent example of a new family of methods that seek to bridge the gap existing in terms of computational cost and predictive accuracy between Reynolds-averaged Navier–Stokes (RANS) and large-eddy simulation (LES) approaches for turbulent flows. As such, DES targets computational resources expected to become widespread in the near future, and is expected to be particularly valuable for scenarios in which RANS is known to be unreliable (e.g. strongly-separated flow) or in which resolution of unsteady turbulent motion is required (e.g. computational aeroacoustics).

In this work a comprehensive study of DES has been carried out. In the literature review, a detailed introduction of the method and its various derivative versions is offered together with a summary of the relevant turbulent flow physics. The presentation and discussion of results draws upon a wide selection of test cases, ranging between canonical and complex configurations and with a comprehensive variety of turbulent flow phenomena. The topics covered include elementary implementation issues and the verification and calibration of model features, the fundamental interaction of the model with the numerical scheme, the detailed comparison of DES results with wind tunnel experiments, the dependency of DES on the underlying RANS model in different scenarios, the sensitivity of DES to the choice of numerical time step, the importance of long simulation times for reliable statistics, the perspectives for a dynamic determination of the model parameter, the performance of a recent extension of the DES formulation when applied as a wall-modelled LES and a proposed extension to this that relaxes the stringent requirements on the wall-normal grid spacing. A concise summary of the principle findings is provided in the conclusion, which includes links to the relevant sub-sections for easy reference.

Zusammenfassung

Die *Detached-Eddy-Simulation* (DES) ist ein typischer Vertreter einer neuen Familie von Methoden, welche in Hinblick auf die Vorhersagegenauigkeit und den numerischen Aufwand eine Brücke zwischen Lösungsverfahren auf Basis Reynolds-gemittelter Navier–Stokes-Gleichungen (*RANS*) und Grobstruktursimulationen (*LES*) für die Berechung turbulenter Strömungen bilden. Die DES ist daher so ausgelegt, dass sich ihr Ressourcenbedarf durch die typischerweise in naher Zukunft weitverbreitet zur Verfügung stehenen Rechenkapazitäten decken lässt. Besonders geeignet ist ihre Anwendung dabei in Szenarien, in denen RANS-Modelle bekannterweise unzuverlässig sind, wie z.B. stark abgelösten Strömungen, oder wo die Auflösung instationärer turbulenter Strukturen erforderlich ist, etwa bei aeroakustischen Anwendungen.

Im Rahmen dieser Arbeit wurden umfassende Studien zur DES durchgeführt. So wird im Überblick zum aktuellen Stand der Forschung zunächst die Methode in ihren verschiedenen Versionen detailliert vorgestellt und eine Zusammenfassung der relevanten strömungsphysikalischen Phänomenen gegeben. Die anschließende Diskussion der Ergebnisse erstreckt sich über eine breite Auswahl von Testfällen, von vereinfachten bis hin zu komplexen Konfigurationen, um so unterschiedlichste Turbulenzphänomenen zu erfassen. Dabei umfassen die Untersuchungen verschiedene Themenbereiche, wie elementare implementierungstechnische Fragen, die Verifikation und Kalibrierung von Modellkomponenten, die grundlegende Wechselwirkung zwischen Modell und numerischem Schema, detaillierte Vergleiche von DES-Ergebnissen mit Windkanaldaten, die Modellabhängigkeit der DES in verschiedenen Situationen, der Einfluss des Zeitschrittes auf die DES, die Wichtigkeit von langen Simulationszeiten, um verläßliche statistische Größen zu gewinnen, die Perspektiven einer dynamische Bestimmung des Modellparameters, die Bewertung einer kürzlich entwickelten Erweiterung der DES–Formulierung als Wandmodellierung für eine LES, und eine vorgeschlagene Erweiterung, um die strikten Anforderungen an die wandnormale Gitterauflösung zu lockern. Am Abschluss wird eine kompakte Zusammenfassung der prinzipiellen Erkentnisse gegeben, wobei Verweise auf die relevanten Abschnitte ein Nachschlagen erleichtern sollen.

Thanks and acknowledgements

I would like to express my profound graditude to the following people, without whose help this work would not have been possible, or at least not nearly so enjoyable:

First and foremost to Prof. Frank Thiele, who has provided a fantastic working environment and research facilities, the freedom to follow my own initiative and continual support and guidance.

To Prof. Mikhael Strelets for his valuable and detailed review of the manuscript as examiner for the PhD defence. Likewise, to Prof. Wolfgang Nitsche for his role as chairman of the examining committee.

To the following, who have directly assisted in many of the investigations and in some cases reviewed sections of the manuscript: Dr. Ulf Bunge, Angelo Carnarius, Thilo Knacke, Dr. Rodolphe Perrin, Thorsten Reimann and Dr. Jianping Yan.

To Prof. Mikhael Shur and Prof. Mikhael Strelets, and more recently Dr. Philippe Spalart for the invigorating discussions and open exchange of ideas, which I have valued tremendously over the years.

To my current and former colleagues at the Institute of Fluid Mechanics and Engineering Acoustics (ISTA), for their companionship, continual assistance and many fruitful discussions, as well as for the continual stream of interesting reading matter.

To Martin Franke, Lars Oergel and Norbert Schönwald for their invaluable IT support (and, indeed, patience).

For helping with the "necessary evils" of the administrative world: Gabrielle Gründig-Hänszke, Lilly Lindemann and Edelgard Schröder.

For the generous provision of data and pictures, and the permission to reproduce them: Cambridge University Press, Dr. Sergio Hoyas, Prof. Tee Tai Lim, Prof. Christoffer Norberg, Dr. Philippe Spalart, Dr. Katrina Swalwell and Dr. Jianping Yan.

To the following members of the CFD turbulence modelling community for their very important input in the form of many memorable and lively discussions and informal coaching: Jonas Ask, Dr. Bertrand Aupoix, Dr. Sofiane Benhamadouche, Dr. Marianna Braza, Prof. Lars Davidson, Dr. Sébastien Deck, Prof. Tom Gatski, Dr. Werner Haase, Prof. Charles Hirsch, Dr. Yannick Hoarau, Dr. Suad Jakirlic, Dr. Tobias Knopp, Dr. Johan Kok, Dr. Robin Langtry, Prof. Dominique Laurence, Prof.

Michael Leschziner, Dr. Ivan Mary, Dr. Florian Menter, Prof. Christoffer Norberg, Prof. Shia-Hui Peng, Dr. Alistair Revell, Prof. Thomas Rung, Dr. Dieter Schwamborn, Dr. Lionel Temmerman, Dr. Dominic von Terzi, Dr. Fabrizio Tessicini, Dr. Harmen van der Ven, Dr. Stefan Wallin, Dr. Keith Weinman, Dr. Don Wu.

Finally, on the home front I am deeply grateful to my family and friends, both in England and in Berlin, for the tireless support and patience, and for politely putting up with increasingly abstract responses to the question "So how is work going?".

* * *

This work was undertaken in the framework of the European FLOMANIA[1] and DESider[2] projects, both of which were excellently coordinated by Dr. Werner Haase. Many of the more time consuming computations were conducted on the IBM pSeries 690 at the *Zuse-Institut Berlin* (ZIB) and the *Norddeutschen Verbund für Hoch- und Höchstleistungsrechnen* (HLRN)[3], with valuable technical support provided by Dr. Wolfgang Baumann. This substantial support is gratefully acknowledged.

[1] FLOMANIA (Flow Physics Modelling – An Integrated Approach) was funded by the European Community represented by the CEC, Research Directorate General, in the 5th Framework Program, under Contract No. G4RD-CT2001-00613. See `http://cfd.mace.manchester.ac.uk/flomania/index.html` and Haase et al., 2006 [55] for more details.

[2] DESider (Detached-Eddy Simulation for Industrial Aerodynamics) was funded by the European Community represented by the CEC, Research Directorate General, in the 6th Framework Program, under Contract No. AST3-CT-2003-502842. See `http://cfd.mace.manchester.ac.uk/desider/index.html` and Haase et al., 2009 [56] for more details.

[3] `http://www.hlrn.de`

Contents

List of symbols and abbreviations

Upper-case Roman

A	coefficient of Smagorinsky-form of DES implementation
B	intercept constant of log law of the wall
C	constant from Pope's model spectrum
C_D	coefficient of drag, integrated over entire span
C_{DES}	DES model constant
C_d	coefficient of drag, integrated over single spanwise section
C_L	coefficient of lift, integrated over entire span
C_l	coefficient of lift, integrated over single spanwise section
C_l	IDDES model-specific constant for f_l
$C_{\ell 0}$	large scale constant from Pope's model spectrum
C_p	pressure coefficient
C_{pb}	base pressure coefficient on the rear surface of a bluff body
C_S	Smagorinsky constant
C_t	IDDES model-specific constant for f_t
C_w	near-wall constant for IDDES Δ function
C_η	dissipative scale constant from Pope's model spectrum
C_μ	turbulent viscosity constant in $k-\varepsilon$ model
D	cylinder diameter
D	diffusion term of transport model
D'	wake width of bluff body
E	log law parameter $E = e^{\kappa B}$
$E(\kappa)$	energy spectrum function
L_{DDES}	DDES length scale
$\tilde{L}_{\text{DDES}}$	modified DDES length scale from IDDES
L_{DES}	DES length scale
L_{IDDES}	IDDES length scale (combining DDES and WMLES functions)
L_{LES}	LES length scale
L_{RANS}	RANS length scale
L_{WMLES}	length scale of hybrid WMLES model
M	Mach number
Re	Reynolds number
Re_{crit}	critical Reynolds number
P	production term of transport equation
S_{ij}	strain rate tensor
S_ϕ	source term of ϕ
S^*	rate of strain invariant
St	Strouhal number
St^*	Roshko's universal Strouhal number for bluff bodies
Tu	free stream turbulence intensity
$\overline{U}_i$	time or ensemble averaged velocity vector

$\overline{U}^+$	normalised mean velocity (magnitude) in wall units
$\overline{U}_\delta$	mean velocity at channel centreline
$\overline{U}_\tau$	friction velocity
$\langle U_i \rangle$	phase-averaged velocity vector
$\widehat{U_i}$	filtered (resolved) velocity vector
U_i	filtered or averaged velocity vector (in hybrid RANS-LES)

Lower-case Roman

c	airfoil chord length
d_w	wall-normal distance
f	frequency
f_{amp}	solution-dependent magnitude function for $f_{restore}$
f_d	DDES boundary layer shield function
$\tilde{f}_d$	DDES RANS-LES blending function for IDDES
f_{dt}	DDES modelled log-law region shield function for IDDES
f_{hill}	grid-dependent shape function for $f_{restore}$
f_l	blending function for viscous sublayer from f_{amp}
$f_{\ell 0}$	large scale function from Pope's model spectrum
$f_{restore}$	IDDES RANS length scale boosting function
f_{step}	IDDES hybrid weighting function of RANS-LES blending
f_t	blending function for modelled log-law region from f_{amp}
f_η	dissipative scale function from Pope's model spectrum
h	grid spacing
h_{max}	maximum grid cell edge length
h_{wn}	grid cell edge length in wall-normal direction
k	turbulent kinetic energy
k	base pressure parameter
ℓ	length scale
ℓ_0	length scale of the largest eddies
n	normal component of x_i
$\tilde{p}$	pressure
p	modified pressure
p_0	large scale constant from Pope's model spectrum
r_d	modelled turbulent boundary layer sensor from DDES
r_{dl}	IDDES viscous sublayer sensor from f_l
r_{dt}	IDDES modelled log-law region sensor from f_t
t	time
u	x-component of velocity
u_i	velocity vector
$\tilde{u}_i$	periodic fluctuation of velocity vector
u_i'	fluctuation of velocity vector
u_i''	incoherent fluctuation of velocity vector
$\overline{u_i' u_j'}$	Reynolds stress tensor

$\overline{\tilde{u}_i\tilde{u}_j}$	coherent part of Reynolds stress tensor
$\overline{u_i'' u_j''}$	incoherent part of Reynolds stress tensor
$\langle u_i'' u_j'' \rangle$	phase-averaged turbulent stresses
$\widehat{u_i' u_j'}$	sub-grid stress tensor
u_{mean}	convective velocity averaged over outflow plane
$\lvert u_s \rvert$	velocity magnitude of free streamline at separation
u_∞	free stream x-component of velocity
$\lvert u_\infty \rvert$	free stream magnitude of velocity
u_η	Kolmogorov velocity scale
v	y-component of velocity
w	z-component of velocity
x_i	position
y^+	normalised wall distance in wall units
y^+_{hyb}	y^+ from hybrid-adaptive wall boundary condition

Upper-case Greek

Γ_ϕ	diffusivity coefficient of ϕ
Δ	LES filter width
Δt	time step size
Δx	grid cell spacing in x-direction
Δ_f	fixed filter width
Ψ	function to prevent wall-term activation in LES-mode
$\mathbf{\Psi}$	body forces
Ω_{ij}	rate of rotation tensor
Ω^*	rate of rotation invariant

Lower-case Greek

α	angle of attack
α	IDDES near-wall grid function from f_{step}
β	dissipative scale constant from Pope's model spectrum
δ	channel half-height
δ_{ij}	Kronecker delta
ϵ	dissipation term in a transport equation
ε	rate of dissipation of k
η	Kolmogorov length scale
θ	effective viscosity to wall-normal distance parameter of hybrid-adaptive wall boundary condition
κ	von Kármán constant
κ	wavenumber
λ_2	vortex core criterion
μ	dynamic viscosity

ν	kinematic viscosity
ν_t	turbulent/eddy (kinematic) viscosity
$\tilde{\nu}$	SA model eddy viscosity
ρ	density
σ	hybrid blending function for convection scheme
τ	period of a harmonic oscillation
τ_{ij}	stress tensor
τ_w	wall shear stress
τ_η	Kolmogorov time scale
ϕ	generic conserved intensive flow quantity
ϕ_{ij}	pressure – rate of strain redistribution tensor
φ	phase angle
φ	blending function for hybrid-adaptive wall boundary condition
ω	turbulent frequency

Superscripts

$+$	quantity normalised in frictional wall units (w.r.t. $\overline{U_\tau}$)

Subscripts

c	quantity based on airfoil chord length
ref	reference value of a quantity
sgs	sub-grid scale quantity
w	value at a solid boundary (wall)
0	largest turbulent scales
∞	free stream value at infinite distance from configuration

Symbols

$\overline{x}$	ensemble averaged x
$\langle x \rangle$	phase averaged x
$\widehat{x}$	filtered x
$\lvert x \rvert$	magnitude of a vector x_i
x'	fluctuation of x
$\tilde{x}$	coherent, quasi-periodic fluctuation of x
x''	incoherent, random fluctuation of x

Abbreviations

2C	two-component
3C	three-component
CEASM	compact explicit algebraic Reynolds stress model
CFD	computational fluid dynamics
DDES	delayed DES
DES	detached-eddy simulation
DES97	the original DES formulation
DNS	direct numerical simulation
ELAN	the CFD solver: "Elliptic Analysis of the Navier–Stokes equations"
FD	finite difference
FE	finite element
FV	finite volume
GIS	grid-induced separation
IDDES	improved DDES
L	laminar vortex shedding regime
LES	large-eddy simulation
LL	Lien–Leschziner $k-\varepsilon$ model
LLM	log-layer mismatch
LLR	linear local realisable $k-\omega$ model
MSD	modelled stress depletion
PIV	particle image velocimetry
RANS	Reynolds-averaged Navier–Stokes
RMS	root mean square
SA	Spalart–Allmaras model
SAE	Spalart–Allmaras model with Edwards correction
SALSA	strain-adaptive linear Spalart–Allmaras model
SAS	scale-adaptive simulation
SGS	sub-grid scale model
SST	shear stress transport model
TrBL	transition-in-boundary-layer vortex shedding regime
TRPIV	time-resolved PIV
TrSL	transition-in-shear-layer vortex shedding regime
TrW	transition-in-wake vortex shedding regime
URANS	unsteady RANS
VLES	very-large-eddy simulation
WCX	Wilcox $k-\omega$ model
WMLES	wall modelled LES
X-LES	extra-large-eddy simulation

Part I

State of the art and literature review

1 Introduction

1.1 Background

Fluid flow is an important phenomenon in many aspects of the natural sciences and engineering. From aerodynamics to meteorology, chemical processing to medical applications, fluid dynamics plays a central role. Following the pioneering theoretical and experimental work of the last centuries, the application of computer simulation has in recent times established itself as a tool to further understanding and to aid the solution of practical problems. With the rapid increase in computing power and the improvement of simulation algorithms, the use of computational fluid dynamics (CFD) for practical applications is clearly set for continued growth. Despite this optimistic outlook, significant barriers to accuracy and efficiency remain to be overcome before CFD can be considered a truly everyday tool.

Turbulent flows have long presented a considerable obstacle to the accuracy, applicability and popularity of CFD in industrial application. Although direct numerical simulation (DNS) allows the resolution of the complete range of turbulent scales, the computational cost renders this approach unfeasible for many decades to come. At the other end of the spectrum, the Reynolds-averaged Navier–Stokes (RANS) equations significantly reduce the computational cost whilst introducing uncertainties due to modelling approximations. Large-eddy simulation (LES) lies conceptually between the extremes of pure turbulence simulation (DNS) and pure turbulence modelling (RANS), whereby only the largest energy-containing turbulent motions are resolved, with the influence of the smallest unresolved scales provided by a model. Although offering a reduced computational cost compared to DNS, LES still proves too expensive for most practical applications. This expense is particularly high in attached turbulent boundary layers, as the turbulence scales are very small compared to the geometry in question. It is therefore widely acknowledged that a gap exists between RANS and LES, and recent activity in the development of hybrid RANS-LES methods is aimed at addressing this. One such method, which perhaps shows the greatest promise for widespread practical application, is detached-eddy simulation (DES).

1.2 Objectives

The global objective to which this work contributes has been outlined in the previous section: The problem presented by turbulent flow prediction, which strongly limits the reliability and applicability of CFD in engineering. The study focuses on DES, which seeks to blend the level of direct turbulence resolution and modelling empiricism to an optimum level targeted at the computing capability expected in the near

future. As such, DES and hybrid RANS-LES methods in general attempt to provide a bridge between the current industrial workhorse of RANS models and pure LES methods that will not become affordable until the mid-term to distant future. The work forms part of wider efforts to enhance the reliability and applicability of DES.

Specific objectives of the thesis work are formulated as follows:

- To review available DES methods and to establish their relationship to alternative hybrid RANS-LES approaches.
- To implement the selected methods in the in-house CFD solver "ELAN" and to validate these implementations using carefully selected test cases and procedures.
- To document the experience gained in this implementation and validation process, which should provide a useful reference to readers wishing to implement DES methods themselves.
- To assess the level of predictive accuracy that can be achieved using DES in a range of situations representative of diverse target applications.
- To identify any problems encountered and to investigate potential remedies.
- To document remaining open issues and suggest corresponding future work based on these findings.

Acknowledging that the suitability of various turbulence prediction methods depends on the flow phenomena concerned, considerable value is placed on the consideration of a wide range of test cases, which exhibit contrasting and complimentary flow physics. It is with this aim in mind that the adjective "comprehensive" is used in the title. Such an approach is intended to provide the greatest possible degree of generality of the conclusions drawn. The thesis also targets completeness in the sense that all phenomenological arguments are founded on concepts described in the literature review, rather than relying too strongly on external references.

Finally, the ultimate goal of the methods examined is considered to be their application to engineering problems. This principle implicitly defines the criteria for success or failure in the interpretation of results. This furthermore serves to eliminate any modifications from consideration that would require excessive levels of user input or that are fundamentally limited to simple geometries.

1.3 Outline of the thesis

An overview of the structure of the thesis will be given to assist orientation. The thesis is organised into three parts plus a collection of appendices. Part I contains the introduction and literature review. The goal of the literature review is to summarise

all physical and numerical background information to be drawn upon in the later discussions. As such, the literature review is organised into two chapters. Chapter 2 provides physical descriptions of the relevant turbulent flow phenomena, whereas chapter 3 describes existing numerical methods for the simulation and modelling of turbulent flow, with a particular emphasis on the DES approach.

Part II describes the methodology of the investigations, beginning in chapter 4 with a concise description of the ELAN CFD solver applied. In chapter 5, details concerning the DES implementation are given and in chapter 6 the selection of test cases is presented. Each case is described in detail, from the characteristics of the underlying flow phenomena to the numerical details and post processing techniques.

The results are presented and discussed concurrently in Part III, which consists of a multi-faceted collection of investigations. These are roughly grouped into two chapters: In chapter 7, investigations targeted at the validation of key implementation features are collated, which provide a foundation for the demonstration and analysis of chapter 8. Each of the investigations is presented in a self-contained manner, with conclusions drawn for each. These conclusions are collated concisely in chapter 9, with explicit references to the more detailed discussions in preceding chapters. A particularly important outcome of this work is the collection of directions identified for further study, which are also collated in chapter 9.

To enhance the readability, all derivations above a certain level of complexity are placed in the appendices. These also contain a collection of topics that can be considered non-essential background information, which some readers may however find useful.

1.4 Conventions

Certain nomenclature conventions have been adopted throughout the document, which are summarised here. Where feasible, tensor notation with the Einstein summation convention will be used in equations. When used, vectors are identified with bold type. A capital C with a subscript will be reserved for quantities that are truly constant, e.g. C_μ, whereas a lower-case f with subscript will be applied for varying parameters or functions, e.g. f_{C_μ}.

2 Physical background

The phenomenon of fluid turbulence introduces one of the greatest challenges facing CFD. A range of methods are available to incorporate turbulence effects in fluid flow simulations, each with their respective strengths and weaknesses. Before these are reviewed in Chapter 3, a summary of the characteristics of turbulent flow relevant to these methods will be given, which naturally does not constitute an exhaustive treatment. For this, the interested reader is referred to the extensive available literature (e.g. [169], [61], [116]). Furthermore, an attempt will be made to convey an understanding of turbulent phenomena on a physical level, restricting the presentation of mathematical relationships to those necessary for discussion and analysis in the following chapters.

Bradshaw's definition of turbulence [14] makes an ideal introduction to this section, giving a preview of many key aspects:

> "Turbulence is a three dimensional time dependent motion in which vortex stretching causes velocity fluctuations to spread to all wavelengths between a minimum determined by viscous forces and a maximum determined by the boundary conditions. It is the usual state of fluid motion except at low Reynolds numbers."

The important role that turbulence plays in science, engineering and nature (outlined in Chapter 1) is highlighted by the recognition that turbulent flow is the rule and laminar flow the exception. The quotation also identifies turbulent motion to be three-dimensional and unsteady in nature. The fluctuations in the velocity field are apparent in the form of overlapping eddies over a wide range of scales, a state of affairs brought about by the phenomenon of vortex stretching. Analysis of the vorticity equation (obtained by applying the curl operator to the Navier–Stokes equations) reveals that the intensity of a line vortex increases when it is stretched. This vortex stretching term is inactive in the two-dimensional form of the equations, hence the statement that turbulence is three-dimensional. The sheer and obvious complexity of turbulence has long fascinated and baffled scientists, not just through its nature, but also the fact that such a random state can arise from the deterministic Navier–Stokes equations. The apparent futility of the struggle to describe, explain and understand turbulence motivated the following lament by Horace Lamb [79]:

> "I am an old man now, and when I die and go to heaven there are two matters on which I hope for enlightenment. One is quantum electrodynamics, and the other is the turbulent motion of fluids. And about the former I am rather optimistic."

2.1 Laminar to turbulent transition

Nonetheless, much progress has been made in finding "laws" or expressions of recurring patterns of behaviour. The pioneering work on analysing and predicting the occurrence of a laminar or turbulent flow state was carried out by Osborne Reynolds in the late 19th century [119]. Reynolds observed the flow of fluids through glass pipes, using injected dye for visualisation. Initially the thread of dye flowed smoothly, however after a certain distance the thread was seen to develop regular waves followed by a transition to fully-turbulent flow, which rapidly mixed the dye with the surrounding fluid. An everyday example of this transition from laminar to turbulent flow is the behaviour of a buoyant plume of cigarette smoke. Figure 2.1 shows a cigarette placed in a low-turbulence wind tunnel that provides a smooth cross flow [113]. The initially laminar smoke plume develops regular vortex rings, which then degrade into a disordered turbulent state.

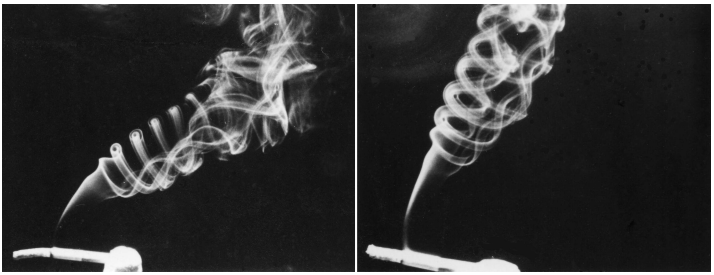

Figure 2.1: Laminar to turbulent transition illustrated with an everyday example [113] (reproduced with permission).

A central parameter in the study of turbulent flows bears Reynolds' name, originating from the pipe flow study outlined above [119]. The Reynolds number is the ratio of inertial forces to viscous forces acting on the fluid and can be expressed as

$$\mathrm{Re} = \frac{u_{ref}\,\ell_{ref}}{\nu}\,, \tag{2.1}$$

where u_{ref} and ℓ_{ref} are reference values of velocity and length particular to the flow in question and $\nu = \mu/\rho$ is the kinematic viscosity. Laminar flow occurs at low values and turbulent flow at high values of Re.

The transition to turbulence can occur via a variety of different mechanisms, and is highly sensitive to disturbances such as free stream fluctuations or geometric imperfections. Because of this at most a range of typical values for the critical Reynolds number can be given. In practical applications, predicting the precise location of boundary layer transition is both highly important and exceedingly challenging,

with many different methods currently under development. Transition prediction is generally considered a separate discipline to the modelling of turbulence itself, and is therefore not considered in this work.

2.2 The turbulent energy cascade

A principal concept in the understanding of fluid turbulence is the energy cascade. As identified in the introductory paragraphs of this chapter, turbulence consists of overlapping three-dimensional eddies of different scales. The majority of the kinetic energy is contained in the largest eddies, the length scale ℓ_0 of which is of the order of magnitude of the geometry or flow feature in question (e.g. bluff body wake, boundary layer thickness). These large eddies draw their energy from the velocity gradients in the mean flow, and are anisotropic and strongly affected by the mean flow topology. A cascade process then ensues driven by vortex stretching, in which energy is continually passed to successively smaller scales. The energy of the smallest eddies is then dissipated to heat by the action of molecular viscosity. This fundamental concept has been lyrically expressed by Lewis Richardson [123] as follows:

> "Big whorls have little whorls,
> Which feed on their velocity;
> And little whorls have lesser whorls,
> And so on to viscosity."

2.2.1 Kolmogorov's hypotheses

More specific details of the turbulent cascade emerge from Kolmogorov's theory [77], which is expressed as three hypotheses. These provide important information such as the size of the smallest scales and the characteristics of the turbulence across the length scales. The first of the hypotheses describes the nature of the small-scale motions.

Kolmogorov's hypothesis of local isotropy

> At sufficiently high Reynolds number, the small-scale turbulent motions ($\ell \ll \ell_0$) are statistically isotropic.

The directional information of the anisotropic large scales is therefore lost along the turbulent cascade, resulting in locally-isotropic small scales. An important outcome of this is that the small motions have a universal character, which implies that these may be modelled more simply than the large scales.

Kolmogorov's first similarity hypothesis:

> In every turbulent flow at sufficiently high Reynolds number, the statistics of the small-scale motions have a universal form that is uniquely determined by ν and ε.

The variables upon which this universal form depends arise from considerations of the dominant physical processes. The small-scale motions are considered to operate like a conveyer belt, transferring the energy received from the larger scales to be dissipated by the viscosity. This rate of dissipation, ε, is therefore one of the determining parameters together with ν. The range of scales at which this process occurs is referred to as the *universal equilibrium range*.

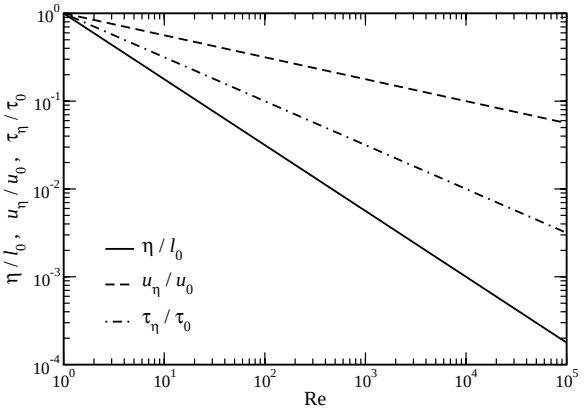

Figure 2.2: Ratios of smallest to largest turbulent scales as functions of Re.

The very smallest eddies are characterised by the Kolmogorov length, velocity and time scales given by

$$\eta \equiv (\nu^3/\varepsilon)^{1/4}\,, \tag{2.2}$$

$$u_\eta \equiv (\varepsilon\,\nu)^{1/4}\,, \tag{2.3}$$

$$\tau_\eta \equiv (\nu/\varepsilon)^{1/2}\,, \tag{2.4}$$

respectively. An important feature that justifies the premise that the Kolmogorov scales correspond to the smallest turbulent motions is the Reynolds number based on these scales, $u_\eta \eta/\nu$, which has a value of unity.

It can furthermore be observed that the smallest scales become smaller (compared to the largest scales, ℓ_0) as the Reynolds number of the flow increases. The ratios of the Kolmogorov scales to the largest scales as a function of Reynolds number are given in Eqs.(2.5 – 2.7) and depicted graphically in Fig. 2.2.

$$\eta/\ell_0 \propto \mathrm{Re}^{-3/4}\,, \tag{2.5}$$

$$u_\eta/u_0 \propto \mathrm{Re}^{-1/4}\,, \tag{2.6}$$

$$\tau_\eta/\tau_0 \propto \mathrm{Re}^{-1/2}\,. \tag{2.7}$$

There exists therefore at high Reynolds number an intermediate range of scales that are large enough not to be affected by viscosity ($\ell \gg \eta$) yet small compared to the energy-containing large scales and not affected by the boundary conditions of the flow ($\ell \ll \ell_0$). As a consequence of this and of the first similarity hypothesis:

Kolomogorov's second similarity hypothesis:

> In every turbulent flow at sufficiently high Reynolds number, the statistics of the motions of scale ℓ in the range $\ell_0 \gg \ell \gg \eta$ have a universal form that is uniquely determined by ε, independent of ν.

The universal equilibrium range is therefore subdivided into two subranges, the *dissipation range*, where ℓ approaches η and viscous effects dominate, and the larger *inertial subrange* where viscous effects are negligible. The scale range of the largest eddies is referred to as the *energy-containing range*. Pope [116] suggests that the boundary between the dissipation and inertial subranges is located at 60η. The energy-containing range is suggested to occupy $\frac{1}{6}\ell_0 < \ell < 6\ell_0$, such that the boundary between the energy-containing and universal equilibrium ranges is located at $\frac{1}{6}\ell_0$. A schematic of the energy flow and regions of the turbulence cascade is given in Fig. 2.3

2.3 The turbulence energy spectrum

To examine the distribution of energy over different scales, the energy spectrum function of wavenumber $E(\kappa)$ is useful (the wavenumber of a particular length scale is given by $\kappa = 2\pi/\ell$). As a consequence of the second Kolmogorov hypothesis, it is found that $E(\kappa) \propto \kappa^{-5/3}$ in the inertial subrange [116]. For isotropic turbulence, the energy spectrum function has a universal form, depending only on the Reynolds number of the flow.

Pope [116] proposed a model spectrum, which returns $E(\kappa)$ for a given length scale of the large eddies, $\ell_0 = k^{3/2}/\varepsilon$ and value of ε. The expression for the model spectrum is

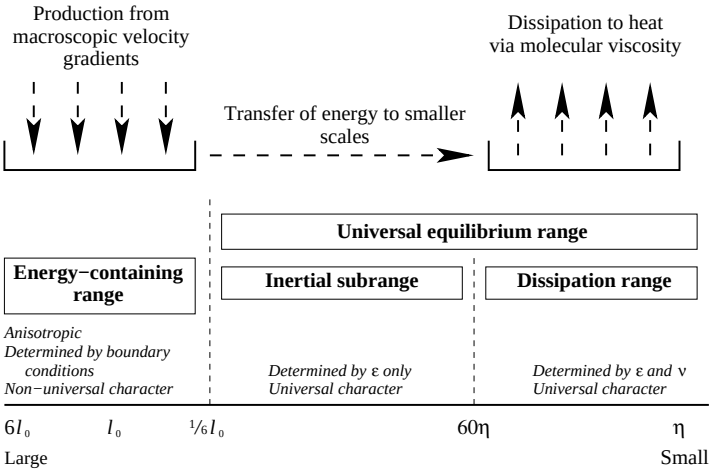

Figure 2.3: Schematic diagram of the energy flow and regions of the turbulent energy cascade.

$$E(\kappa) = C\,\varepsilon^{2/3}\,\kappa^{-5/3}\,f_{\ell_0}(\kappa\ell_0)\,f_\eta(\kappa\eta)\,,$$

$$f_{\ell_0}(\kappa\ell_0) = \left(\frac{\kappa\ell_0}{\sqrt{(\kappa\ell_0)^2 + C_{\ell_0}}}\right)^{5/3+p_0}, \qquad f_\eta(\kappa\eta) = e^{-\beta\{[(\kappa\eta)^4 + C_\eta^4]^{1/4} - C_\eta\}}\,, \quad (2.8)$$

where the constant values are $C = 1.5$, $C_{\ell_0} = 6.78$, $p_0 = 2$, $\beta = 5.2$ and $C_\eta = 0.4$. The Reynolds number based on the large scales is defined as $\mathrm{Re}_{\ell_0} = k^{1/2}\ell_0/\nu$, and examples of the model spectrum for various values of Re_{ℓ_0} and $\ell_0 = \varepsilon = 1$ are shown in Fig. 2.4. The increasing separation of large and small scales with increasing Reynolds number can be clearly seen, as can the slope of exponent $-5/3$ for the inertial subrange. The physical interpretation of the low wavenumber region (scales larger than the energy-containing range) is of a merging of large vortices, in contrast to the stretching and break up of smaller vortices in the energy cascade at higher wavenumber [169].

The various ranges of the turbulent cascade are annotated on the model spectra of Fig. 2.5 for two Reynolds numbers. The values of the Kolmogorov length scale η and the borders between the different regions are taken from the definitions in Section 2.2.1. The inertial subrange is seen to exist only at the higher Reynolds number, being eliminated by an overlap of the energy-containing range and dissipation range at lower Reynolds number.

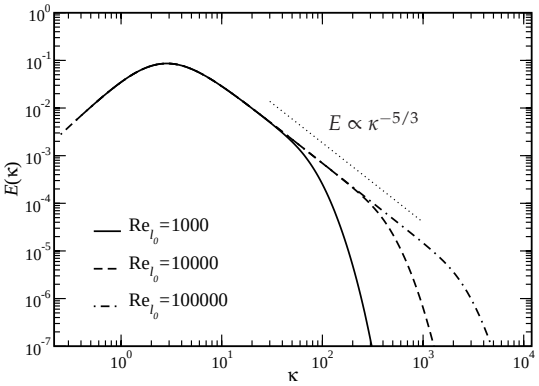

Figure 2.4: Model energy spectra $E(\kappa)$ [116] for varying turbulence Reynolds number Re_{ℓ_0}. Values of $\ell_0 = 1$ and $\varepsilon = 1$ are assumed.

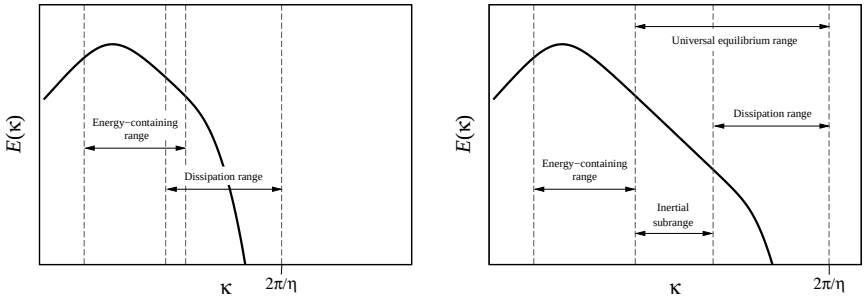

Figure 2.5: Model energy spectra $E(\kappa)$ [116] annotated with the regions of the turbulence energy cascade. Values of $\ell_0 = 1$ and $\varepsilon = 1$ are assumed.

2.3.1 Important length scales

The length scale of the largest eddies, ℓ_0, and the Kolmogorov length scale, η, have been introduced in the above sections. Some further length scales are of importance to later material, which shall be introduced briefly. For a more detailed account of the derivations and physical interpretations of these, the reader is referred to the textbook of Pope [116].

Two important length scales are derived from the streamwise and lateral autocorrelation functions $f(r,t)$ and $g(r,t)$, the former of which in isotropic turbulence completely determines the two-point correlation $R_{ij}(\boldsymbol{r},t)$. The first of these is the longitudinal integral scale

$$L_{11}(t) \equiv \int_0^\infty f(r,t)dr \,, \tag{2.9}$$

which is simply the area under the curve of $f(r,t)$ and is characteristic of the larger eddies.

The longitudinal and lateral Taylor microscales are somewhat more difficult to define intuitively. They are geometrically obtained from the curvature of the longitudinal and transverse autocorrelation functions at $r = 0$, describing the intersection of an osculating parabola with the axis $f = 0$ or $g = 0$. The longitudinal and lateral Taylor microscales are defined as

$$\lambda_f = \sqrt{\frac{2u_{rms}^2}{\overline{\left(\frac{\partial u_1}{\partial x_1}\right)^2}}} \quad \text{and} \quad \lambda_g = \left[-\frac{1}{2}g''(0,t)\right]^{-1/2} . \tag{2.10}$$

It can be shown that in isotropic turbulence $\lambda_g = \lambda_f/\sqrt{2}$.

The length scale characterising the largest eddies can be defined in terms of k and ε as

$$L \equiv \frac{k^{3/2}}{\varepsilon} \,, \tag{2.11}$$

and some relationships between the various length scales can be determined analytically as

$$\frac{\lambda_g}{L} = \sqrt{10}\mathrm{Re}_L^{-1/2} \,, \tag{2.12}$$

$$\lambda_g = \sqrt{10}\eta^{2/3}L^{1/3} \,. \tag{2.13}$$

At high Reynolds number therefore, λ_g lies between η and L. The Taylor microscale is often used to characterise the Reynolds number of isotropic turbulence:

$$\mathrm{Re}_\lambda \equiv \frac{u_{rms}\lambda_g}{\nu} \quad \text{and} \quad \mathrm{Re}_\lambda = \left(\frac{20}{3}\mathrm{Re}_L\right)^{1/2} . \tag{2.14}$$

2.4 Wall-bounded turbulence

The cascade process and properties of the range of scales in turbulent flow introduced above have profound consequences as far as the treatment of turbulence in CFD is concerned. However, analysis has so far been limited to the simplest conceivable occurrence of turbulence, that of statistically isotropic (and hence homogeneous) turbulence. Although describing important aspects (isotropy is the state to which turbulent flows return in the absence of external forcing), the effects of solid boundaries must be included in a complete discussion. It has been mentioned in Section 2.2 that the larger, energy-containing scales are strongly affected by the flow topology and geometry. For the majority of engineering applications, the proximity of solid boundaries (referred to as walls) is the most important mechanism by which anisotropy occurs in turbulence. The properties of wall-bounded turbulent flows (relevant to both internal flows such as pipes and external flows such as airfoil boundary layers) will be summarised here.

The principal effect of wall proximity on turbulence is a damping of the fluid fluctuations in the direction normal to the wall. The energy of these fluctuations is redistributed to the directions tangential to the wall, which are hence amplified. As such, turbulence far away from the wall is relatively isotropic, and becomes increasingly anisotropic nearer to the wall. Indeed an alternative description is that the turbulence is strongly three-dimensional away from the wall, and becomes increasingly two-dimensional nearer to the wall. The fluid in direct contact with the wall exhibits zero relative velocity to the boundary (the "no-slip" condition, $u_w = v_w = w_w = 0$), and the damping effect on the wall-normal turbulent fluctuations naturally increases with proximity to the wall. As a consequence, the turbulent motions nearest to the wall are eliminated entirely, and molecular viscosity becomes the dominant energy dissipation mechanism. Correspondingly, turbulent boundary layers are characterised by distinct zones arranged tangentially to the wall within which different physical phenomena predominate.

There are three key canonical wall-bounded flows, namely that along an un-inclined flat plate and the flow through planar channels and circular pipes. The flat plate boundary layer is characterised by zero pressure gradient and a continually thickening boundary layer in the streamwise (x) direction. The domain in the spanwise (z) direction is considered to be homogeneous, so that the mean streamwise velocity profile in the wall-normal (y) direction $\overline{U}(y)$ is a function of the streamwise location only. The early boundary layer is laminar, whereas at some downstream position a transition region to turbulence occurs. As outlined in Sect. 2.1, the transition position is characterised by the Reynolds number. The local Reynolds number for a flat plate is defined as

$$\mathrm{Re}_x = \frac{\overline{U}_\infty x}{\nu} , \tag{2.15}$$

where $\overline{U}_\infty$ is the mean uniform on-flow velocity and x is the distance downstream of the beginning of the plate. The critical Reynolds number is quoted by Massey [87] as lying in the range $3 \times 10^5 < \mathrm{Re}_x < 5 \times 10^5$, whereas Pope [116] gives a value of $\mathrm{Re}_x \approx 10^6$. The precise value varies strongly from case to case, depending for example on such parameters as free-stream turbulence or surface roughness. More detail on boundary layer transition is given by Schlichting [143].

By contrast, the internal wall-bounded flows (pipes and channels) require a negative pressure gradient in the streamwise direction to overcome the wall shear stresses caused by the boundary layer. As is the case for the flat plate, the boundary layer begins in a laminar state followed (at a sufficiently high Reynolds number) by transition to turbulence. The boundary layer at each wall grows continually until meeting the boundary layer edge from the opposing wall at the central line of a pipe or plane of a channel. Following this, the velocity profile remains fixed, and is hence referred to as *fully-developed*. In the fully-developed state, the channel or pipe velocity profiles $\overline{U}(y)$ are hence independent of the streamwise direction in addition to the spanwise or radial directions.

2.4.1 Universality of boundary-layer profiles

The outermost regions of the turbulent boundary layers of a flat plate and fully-developed channel can be expected to differ, as the former approaches a laminar region of uniform velocity whereas the latter approaches the edge of an opposing turbulent boundary layer. Apart from this distinction however, it emerges that the boundary layer profiles of zero-pressure gradient flat plates and fully-developed channels exhibit a universal behaviour described by the "law of the wall"[1]

The basis of the law of the wall is the the renormalisation of flow and geometric quantities in terms of the wall shear stress, τ_w. Such scaled quantities are referred to as "wall friction units" and denoted by the superscript $^+$. The mean wall friction velocity is defined as

$$\overline{U}_\tau = \sqrt{\frac{\tau_w}{\rho}}\,, \tag{2.16}$$

and is used to normalise the mean streamwise velocity and wall-normal distance as follows:

$$y^+ = \frac{\overline{U}_\tau d_w}{\nu}\,, \qquad \overline{U}^+ = \frac{\overline{U}}{\overline{U}_\tau}\,. \tag{2.17}$$

A wall friction Reynolds number, Re_τ, can be formulated as

[1] The law of the wall is a much-debated concept, and many researchers question the existence of a true universal character (see e.g. Bradshaw & Huang [16] for a review of this issue). Nonetheless, the law of the wall can be said to apply at least approximately, and forms the cornerstone of many modelling approaches.

$$\mathrm{Re}_\tau = \frac{\overline{U}_\tau \, \delta}{\nu} \,, \tag{2.18}$$

where δ represents the boundary layer thickness (corresponding to the channel half height in fully-developed flow).

As mentioned in the introductory passages, a series of regions exist across the boundary layer, each characterised by different physical phenomena. A description of these zones and their approximate extents in terms of y^+ and y/δ is given by Pope [116], which is summarised below.

Inner layer ($y/\delta < 0.1$): The mean velocity profile is determined by $\overline{U}_\tau$ and y^+, independent of $\overline{U}_\delta$ and δ.

Viscous wall region ($y^+ < 50$): The effect of molecular viscosity is significant.

Viscous sublayer ($y^+ < 5$): The Reynolds shear stress is negligible in comparison to the viscous shear stress. The velocity profile is linear, given by

$$\overline{U}^+ = y^+ \,. \tag{2.19}$$

Outer layer ($y^+ > 50$): The effect of molecular viscosity on the mean velocity profile is negligible.

Overlap region ($y^+ > 50$, $y/\delta < 0.1$): The region where the inner and outer layers overlap, which only occurs at high Reynolds number.

Log-law region ($y^+ > 30$, $y/\delta < 0.3$): The "log-law" applies:

$$\overline{U}^+ = \frac{1}{\kappa} \ln y^+ + B \,. \tag{2.20}$$

The constant κ, known as the von Kármán constant, describes the exponent of the profile and B its intercept. The values of κ and B are obtained through curve-fitting to experimental or DNS data, so some scatter is apparent. Widely-accepted values are $B = 5.2$ and $\kappa = 0.41$.

Buffer layer ($5 < y^+ < 30$): The transitional region between the viscous sublayer and the log-law region.

To illustrate the relationship of these zones to the mean velocity profile, Fig. 2.6 shows the profile $\overline{U}^+(y^+)$ obtained at $\mathrm{Re}_\tau = 2000$ from direct numerical simulation by Hoyas and Jiménez [63, 67][2], upon which the zones are depicted.

[2] Data used with permission.

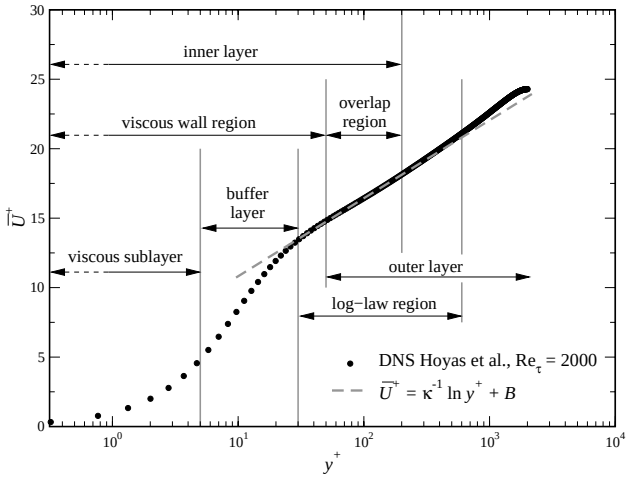

Figure 2.6: Mean velocity profile for a fully-developed turbulent channel flow at $Re_\tau = 2003$ computed using DNS by Hoyas and Jiménez [63, 67] compared to the log-law profile of Eq. 2.20. The physical zones are plotted as given by Pope [116].

2.4.2 Empirical correlations for boundary layer flows

For reasons that will become apparent in Chapter 3, direct numerical simulation is considered the most reliable source of benchmark data for turbulent channel flow, but is limited to low Reynolds numbers due to computational expense. To provide engineers with information on the higher Reynolds numbers of practical relevance, experimental measurements are therefore indispensable. A number of mathematical expressions have been proposed that correlate principal characteristics of the flow with known input parameters. These have been calibrated to experimental measurements and are hence only as accurate as the data upon which they are based. Such correlations are employed in this study to give an indication of the accuracy of simulations above the DNS Reynolds numbers and hence represent distillations of experimental data.

Reichardt [118] proposed a correlation describing the inner layer velocity profile in wall units. Reichardt's correlation is given by

$$\overline{U}^+ = \frac{1}{\kappa} \ln\left(1 + \kappa y^+\right) + 7.8 \left(1 - e^{-y^+/11} - \frac{y^+}{11} e^{-y^+/3}\right) , \tag{2.21}$$

which is plotted in comparison to the DNS profile of Hoyas and Jiménez in Fig. 2.7. It can be seen that the Reichardt correlation, although describing the viscous sublayer and buffer layer well, predicts a log-law region with an excessive intercept value B.

Reichardt also formulated a wake term for the outer layer, which is not employed here.

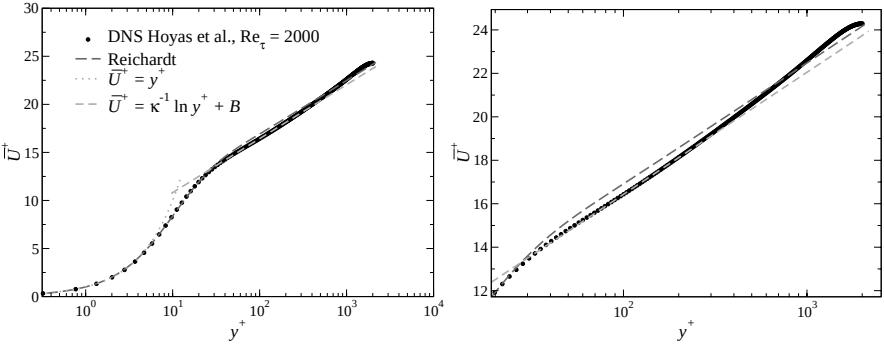

Figure 2.7: Comparison of the normalised mean velocity profiles between the DNS of Hoyas and Jiménez [63, 67] and the Reichardt correlation of Eq. 2.21. The right hand figure shows a zoom of the log law region.

Although Re_τ is the dependent parameter for the self-similarity, a more accessible quantity is a Reynolds number based on the mean bulk velocity $\overline{U}_b$, where

$$\overline{U}_b = \frac{1}{2\delta} \int_0^{2\delta} \overline{U}\, dy \,. \tag{2.22}$$

The bulk Reynolds number is hence given by

$$\mathrm{Re}_b = \frac{\overline{U}_b\, 2\delta}{\nu} \,. \tag{2.23}$$

A relationship between Re_τ and the bulk Reynolds number, Re_b has been suggested for channel flows by Pope [116] as

$$\mathrm{Re}_\tau \approx 0.09\, \mathrm{Re}_b^{0.88} \,. \tag{2.24}$$

An approximate relationship between the mean centreline velocity (at $y = \delta$) and $\overline{U}_\tau$ is also given by Pope:

$$\frac{\overline{U}_\delta}{\overline{U}_\tau} \approx 5 \log_{10} \mathrm{Re}_b \,. \tag{2.25}$$

Further useful correlations based on the bulk Reynolds number have been formulated for channel flow by Dean [34]. These are based on an extensive review of the experimental data available at the time (1978) and claim validity within the range $6 \times 10^3 \leq \mathrm{Re}_b \leq 6 \times 10^5$. The skin friction coefficient is correlated to Re_b by

$$C_f \approx 0.073\ \mathrm{Re}_b^{-1/4}\ , \tag{2.26}$$

where C_f is defined as follows:

$$C_f = \frac{\tau_w}{\frac{1}{2}\,\rho\,\overline{U}_b^2}\ . \tag{2.27}$$

The ratio between the centreline and bulk velocities is furthermore proposed by Dean to follow

$$\frac{\overline{U}_\delta}{\overline{U}_b} \approx 1.28\ \mathrm{Re}_b^{-0.0116}\ . \tag{2.28}$$

The agreement of Dean's correlation for C_f with more recent DNS data is demonstrated in Fig. 2.8 to be largely satisfactory. The C_f values returned by Dean's correlation consistently exceed those from the DNS however.

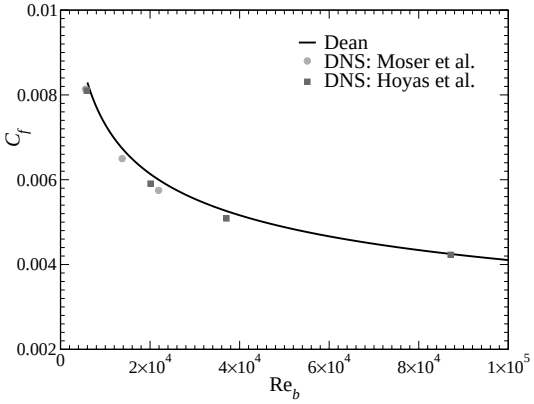

Figure 2.8: Comparison of Dean's correlation for $C_f(\mathrm{Re}_b)$ [34], Eq. 2.26, with more recent DNS data of Moser et al. [100] (at $\mathrm{Re}_\tau = 180,\ 395,\ 590$) and Hoyas et al. [63] (at $\mathrm{Re}_\tau = 180,\ 550,\ 950,\ 2000$).

It is essential to close the description of the law of the wall and the empirical correlations with a remark as to their validity. The law of the wall is only valid for boundary layers in which a weak streamwise pressure gradient is present, allowing the neglection of history effects and the reduction to a simple one-dimensional system. In practice however, strong distortions of the boundary layer profile can be caused by phenomena such as adverse pressure gradients (particularly arising across shock waves), surface curvature, separation and re-attachment and three-dimensional skewing ef-

fects (occurring for example on swept wings). The law of the wall and by extension any modelling approaches reliant upon it would prove to be highly inaccurate in such situations.

2.5 Bluff body flows

An important class of flows, particularly relevant to many of the test cases studied in this work and to detached-eddy simulation in general, are bluff body flows. The term "bluff" is essentially intuitive in nature, referring more to flow characteristics than it does to geometric features. As a result, it is hard to define precisely what is meant by a bluff body, although it is perhaps helpful to consider that a streamlined body constitutes its opposite.

For flows at all but very low Reynolds numbers, bluff bodies are characterised by strong flow separation and generally unsteady wakes. Furthermore, bluff body flows exhibit a negligible contribution of the skin friction drag in comparison to the pressure drag. For flows around streamlined bodies however, the skin friction drag plays an important role. Examples of bluff body flows in industrial applications include buildings, undersea oil pipelines, heavy goods vehicles and wings or rotor blades in deep stall.

Due to the opportunities that these offer for simplified two-dimensional analysis, prismatic bluff bodies have long been the focus of much study – none more so than circular cylinders. As remarked by Roshko [129], the wake structure of different bluff bodies is similar in nature. The circular cylinder is therefore an important canonical flow, many of the characteristics of which can be translated to other bluff bodies.

A brief overview of the characteristics of bluff body flows relevant to this work will be presented. The emphasis is therefore on the behaviour near to the critical Reynolds number (introduced in Section 2.5.2) as well as on a selection of influencing parameters such as blockage, aspect ratio and free stream turbulence.

2.5.1 Vortex shedding

Over a wide range of Reynolds numbers (detailed in the case of a cylinder in Section 2.5.2) the wake behind many bluff bodies is characterised by the periodic and asymmetric shedding of large scale vortices. This phenomenon is more prevalent for high aspect ratio or prismatic bluff bodies, but by no means limited to these. An experimental visualisation of the vortex shedding behind a circular cylinder is shown in Fig. 2.9. It can be seen that both the wake width and the size of the shed vortices are of the order of the cylinder diameter. This phenomenon was first analysed theoretically by von Kármán in 1912 [176], and is as a result known as the von Kármán vortex street.

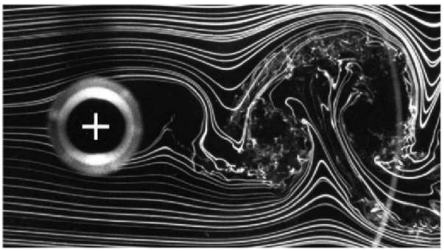

Figure 2.9: Smoke-wire visualisation of the vortex shedding behind a circular cylinder at Re = 8000 [103] (reproduced with permission).

The alternating shedding of vortices from the upper and lower surfaces of the bluff body gives rise to a strongly fluctuating lift force. Before von Kármán's analysis, the frequency of this fluctuation had been studied by Strouhal [165] and was found to depend on the free stream velocity and cylinder diameter[3]. The non-dimensional frequency, or Strouhal number, is defined as

$$\mathrm{St} = \frac{fD}{|u_\infty|} , \tag{2.29}$$

where f is the dominant frequency, D is the cylinder diameter and $|u_\infty|$ is the free stream velocity magnitude. For bluff bodies other than the circular cylinder, D is to be substituted by the frontal height of the bluff body. In particular, for an inclined flat plate or airfoil, $c \sin \alpha$ is to be used (with c the chord length and α the angle of incidence).

A further step forward in the analysis of bluff body wake flow was achieved by Roshko [129], who demonstrated that the centreline pressure coefficient on the rear surface of a bluff body (known as the "base pressure", C_{pb}) arises due to the vortex formation. When the region of this formation is shifted further downstream (for example through the use of a splitter plate), an increase of the base pressure and corresponding decrease of the drag is observed. This is furthermore accompanied by a reduction in the shedding frequency. One outcome of Roshko's analysis was the derivation of a "universal Strouhal number" St^* for bluff bodies, based upon the velocity magnitude of the free streamline at boundary layer separation, $|u_s|$ and the wake width D':

$$\mathrm{St}^* = \frac{fD'}{|u_s|} . \tag{2.30}$$

As $|u_s|$ is a difficult quantity to establish, a formulation employing the base pres-

[3] In fact, it emerged that the value of St is not constant but dependent on parameters such as the Reynolds number. The Strouhal number remains however a useful non-dimensionalised frequency.

sure parameter $k = \sqrt{1 - C_{pb}}$ is more convenient. This relates to the conventional Strouhal number as follows:

$$\mathrm{St}^* = \frac{\mathrm{St}}{k}\frac{D'}{D} \,. \tag{2.31}$$

Roshko established a value of $\mathrm{St}^* \approx 0.16$, which was demonstrated to hold for a range of bluff body geometries and over a wide range of Re.

This analysis was further extended by Abernathy [1] for sharp-edged flat plates over a wide range of angles of incidence. It was observed experimentally that the wake width could be expressed as $D' = 1.41c \sin\alpha$, giving

$$\mathrm{St}^* = \frac{f\ 1.41\ c\ \sin\alpha}{k\ |u_\infty|} \,. \tag{2.32}$$

The value $\mathrm{St}^* \approx 0.15$ was found to hold for $0.35^\circ \leq \alpha \leq 90^\circ$.

Another outcome of Roshko's work was some more insight into the concept of "bluffness", namely:

- For two bodies with the same frontal area, the bluffer diverges the flow more strongly creating a larger wake and experiencing a higher drag.
- Bluffer cylinders have a lower shedding frequency, which is inversely proportional to the wake width[4].

2.5.2 Circular cylinder wake flow regimes

The wake flow behind a circular cylinder shows a high sensitivity to the Reynolds number, passing through a number of distinct regimes as the Reynolds number is varied. An excellent introduction and review of this behaviour is given by Zdravkovich [189], a summary of which is presented here. At very low Reynolds numbers the flow remains attached around the entire cylinder ("creeping" flow), separating to a steady attached recirculation region at slightly higher Re. As Re is increased further the von Kármán instability gives rise to the alternating vortex shedding described in the previous section. The formation of the vortex street is a laminar phenomenon up to $\mathrm{Re} \approx 200$. The entire laminar flow regime is denoted with the abbreviation L by Zdravkovich.

As Re is increased further, transition to turbulence takes place – at first in the far wake (denoted TrW), then moving forward to the free shear layers (TrSL) and finally reaching the cylinder boundary layers (TrBL). The behaviour of the Strouhal number and mean drag coefficient over a wide range of Re was reported by Schewe [142] and is reproduced in Fig. 2.10. The rapid drop in C_D and increase in St at $\mathrm{Re} \approx 3 \times 10^5$ marks

[4] With reference to the work of Fage & Johansen [41].

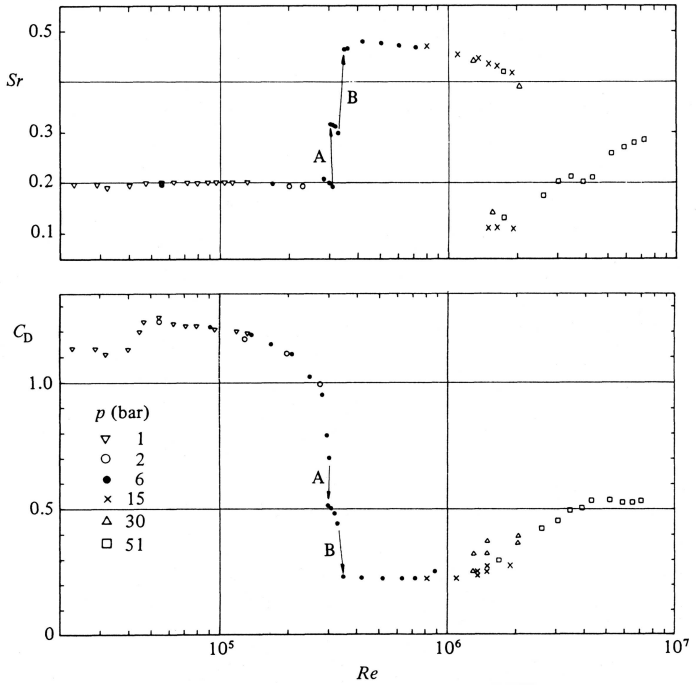

Figure 2.10: Variation of Strouhal number (above) and mean drag coefficient, C_D, (below) of a circular cylinder with Reynolds number. From Schewe [142] (reproduced with permission).

the onset of turbulence in the attached boundary layers. This causes a dramatic rearward shift of the separation point and a corresponding narrowing of the wake. This phenomenon is referred to as the "drag crisis" and the Reynolds number at which it occurs the *critical* Reynolds number, Re_{crit}. The TrSL regimes at $\mathrm{Re} < \mathrm{Re}_{crit}$ are correspondingly referred to as *subcritical*.

The TrSL regime begins with the formation of instability waves in the shear layer, which were identified and analysed by Bloor [11]. At higher Re, these form small-scale eddies with a size of the order of the shear layer thickness. At still higher Re, occasional bursts of incoherent turbulence are observed in the shear layer. The transition waves and turbulent bursts are considered analogous to the Tollmien–Schlichting waves and turbulent spots [143] observed in boundary layer transition.

In contrast to the Strouhal number increase, the drop in drag coefficient begins grad-

ually from Re $\approx 1 \times 10^5$ as the TrBL regime is entered. This gradual decrease is caused by sporadic occurrences of boundary layer turbulence, varying from one vortex shedding cycle to the next. Humphreys [64] furthermore observed the formation of a cellular pattern of the separation position in the spanwise direction, which was stable in time. This was shown to be caused by alternating laminar and turbulent separation along the span, with a cell size of roughly $1.4D$ to $1.7D$. The steep region of the drag crisis is characterised by two discontinuous jumps, labelled A and B in Fig. 2.10. The first of these represents the establishment of a single laminar separation bubble on one side of the cylinder, giving rise to an asymmetric flow condition discovered by Bearman [7]. The second jump is caused by the formation of a bubble on the opposite side of the cylinder and the re-establishment of symmetry.

Abbreviation:	Description:	Re range:
L1	Creeping flow	$0 <$ Re $<$ (4-5)
L2	Steady separation regime	(4-5) $<$ Re $<$ (30-48)
L3	Periodic laminar regime	(30-48) $<$ Re $<$ (180-200)
TrW	Transition-in-wake regime	(180-200) $<$ Re $<$ (350-400)
TrSL1	Transition waves in shear layers	(350-400) $<$ Re $<$ (1k-2k)
TrSL2	Transition eddies in shear layers	(1k-2k) $<$ Re $<$ (20k-40k)
TrSL3	Burst to turbulence	(20k-40k) $<$ Re $<$ (100k-200k)
TrBL0	Precritical regime	(100k-200k) $<$ Re $<$ (300k-340k)
TrBL1	one-bubble regime	(300k-340k) $<$ Re $<$ (380k-400k)
TrBL2	two-bubble regime	(380k-400k) $<$ Re $<$ (500k-1M)
TrBL3	supercritical regime	(500k-1M) $<$ Re $<$ (3.4M-6M)
TrBL4	post-critical regime	Re $>$ (3.5M-6M)

Table 2.1: Overview of vortex shedding regimes for circular cylinders [189].

The vortex shedding regimes can be broken down into sub-regimes describing the development of the vortex shedding behaviour. A summary of the shedding regimes is given together with their abbreviations and Reynolds number range according to Zdravkovich [189] in Tab. 2.1. Much of the complexity of this behaviour arises due to the wide range of positions for the flow separation on the smooth cylinder surface, and is hence not necessarily typical for all bluff bodies. A contrasting example is that of a normal flat plate, where a constant C_D was reported by Abernathy [1][5] across the range $6000 <$ Re < 600000.

Particularly around the critical Reynolds number, the flow exhibits a very strong

[5] With reference to experiments by Flachsbart [45]

sensitivity to a number of influencing parameters. A selection of these relevant to this work will be summarised in the following.

Influence of free stream turbulence

The flow around circular cylinders has been shown to exhibit a strong sensitivity to the turbulence properties of the oncoming free stream flow. This is a central issue concerning the comparison of wind tunnel experimental data both with industrial applications (usually involving high levels of free stream turbulence) and with simulations (typically with a steady laminar on-flow). A review and discussion of this issue for bluff bodies in general has been published by Bearman & Morel [8], and a later set of detailed experiments for cylinder flow was conducted by Norberg [102].

The interactions of free stream turbulence with the flow around bluff bodies involve three principal mechanisms: enhanced mixing and entrainment by the wake, distortion of the oncoming turbulence itself by the bluff body and accelerated transition to turbulence. Of these, the latter is of the greatest relevance to this work. For subcritical cylinder flows, the position of transition in the free shear layer can be shifted upstream by the presence of free stream turbulence. To fully characterise the free stream turbulence (assumed to be isotropic far upstream of the bluff body), information on both the turbulence intensity and the integral length scale is required. The integral length scale must be comparable with the characteristic scales of the flow, such as the cylinder diameter and shear layer thickness, in order to have an effect.

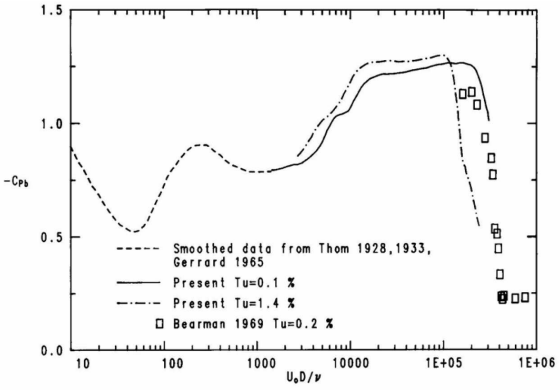

Figure 2.11: Variation of the mean base pressure coefficient, C_{pb}, with Reynolds number for various values of free stream turbulence intensity, Tu [102] (reproduced with permission).

Figure 2.11 shows the effect of different levels of free stream turbulence intensity Tu [6] (obtained using upstream turbulence-generating grids) on the base pressure coefficient over the range $10 < \mathrm{Re} < 10^6$ [102]. A clear reduction of the critical Reynolds number by more than 100000 is seen as Tu is increased from $Tu = 0.1\%$ to $Tu = 1.4\%$. A mild increase in the drag coefficient (i.e. reduction of C_{pb}) is furthermore seen in the subcritical regime.

Influence of blockage coefficient

Wind tunnel blockage is caused by the constraining effects of the test section walls on the object tested and can be an important influence parameter for bluff body flows. The blockage coefficient is defined as the ratio of the bluff body frontal height (e.g. cylinder diameter) to the test section height. The effect of this parameter on the flow around a circular cylinder was studied by Richter et al. [124], whose results for the mean drag coefficient variation with Reynolds number are reproduced in Fig. 2.12.

Increased blockage coefficient is seen to lead to a reduction of the critical Reynolds number as well as an increase in the drag coefficient at subcritical Re, qualitatively the same effect as that of free stream turbulence discussed above. The increase of subcritical drag coefficient is however much stronger than is the case for free stream turbulence. The effect on the critical Reynolds number can be explained by the acceleration of the shear layer flow leading to earlier transition to turbulence.

A further effect of wind tunnel blockage is an increase in the shedding frequency. An interesting observation of Richter et al. [124] is that the universal Strouhal number of Roshko, Eq. (2.31), remains valid despite the effects of confinement.

Influence of aspect ratio

The effect of aspect ratio was studied experimentally by Szepessy & Bearman [168] using end plates with varying spanwise separation for aspect ratio values between 0.25 and 12 and across the Reynolds number range 8000 to 140000. The greatest sensitivity to aspect ratio was seen for the root-mean-square of the lift fluctuation, which increased strongly for decreasing aspect ratio. This was explained by the observed accompanying increase in spanwise correlation of the vortex shedding. Additionally, a reduction of Re_{crit} was measured for low aspect ratio cases. A convergence of the measured quantities was seen for aspect ratio values in excess of around five for high subcritical Reynolds numbers.

This study also has important implications for the three-dimensionality of the flow. Low frequency modulation of the force fluctuations is commonly observed for bluff bodies around the high subcritical Reynolds number range (e.g. [64, 167]). This behaviour is characterised by a temporary reduction of the vortex shedding strength,

[6] $Tu = \sqrt{\frac{2}{3}k} \,/\, |\overline{U}|$

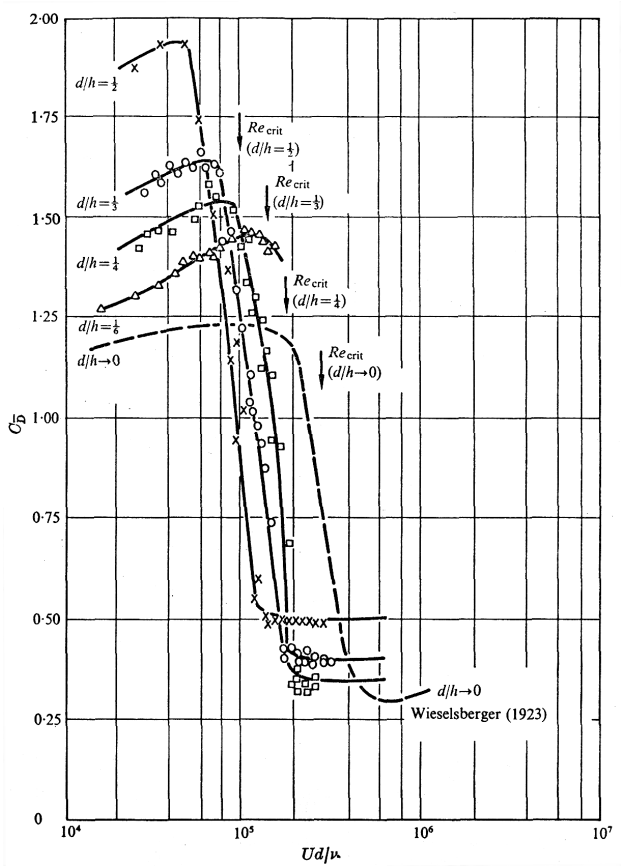

Figure 2.12: Effect of blockage coefficient on the mean drag coefficient of a circular cylinder around the critical Reynolds number range. From Richter et al. [124] (reproduced with permission).

which occurs fairly randomly approximately every 10 to 20 vortex shedding cycles. The occurrence of these "weak shedding cycles" was observed by Szepessy & Bearman [168] to be strongly reduced as the end plates were moved closer together, giving rise to the interpretation that these are associated with sudden three-dimensionality of the wake.

3 Simulation and modelling of fluid turbulence

3.1 Numerical simulation of fluid flow

The Navier–Stokes equations provide the fundamental description of fluid motion, and are based solely on the assumption that the fluid can be considered as a continuum of differentiable variables. The derivation and characteristics of the governing equations of fluid motion are summarised in Appendix A. Since all of the presented applications concern incompressible flows of Newtonian fluids, the incompressible Navier–Stokes equations are considered, resulting in considerable simplification of their formulation and implementation. In conservation form, the continuity and momentum equations are

$$\frac{\partial u_i}{\partial x_i} = 0 \quad \text{and} \tag{3.1}$$

$$\frac{Du_i}{Dt} = -\frac{1}{\rho}\frac{\partial p}{\partial x_i} + \frac{\partial}{\partial x_j}(2\nu S_{ij}) \,, \tag{3.2}$$

respectively. u_i is the velocity vector, ρ is the density, p is the modified pressure (see Section A.2), ν is the kinematic viscosity and S_{ij} is the strain rate tensor.

The analytical solution of the Navier–Stokes equations is only possible for a very confined number of flows with very simple boundary conditions, or with the inclusion of further assumptions and approximations. When analytical solution is not possible, the most appropriate method is to obtain approximate solutions using numerical procedures. In order to do this, a *discretisation method* is required, which approximates the differential equations as a system of algebraic equations that can be solved computationally. CFD therefore works on the basis of the discretised Navier–Stokes equations, coupled with a range of algorithms to achieve iterative solutions. Three principal discretisation methods are commonly used: finite differences, finite volumes and finite elements. Of these, the most widespread in industrial CFD is the finite volume method, which also forms the basis of the ELAN CFD solver [184] used in these investigations.

The starting point of the finite volume discretisation method is the integral form of the governing equations. The fluid domain is divided completely into a finite number of tessellating control volumes (i.e. the numerical grid described in the following paragraphs), with the conservation equations applied to each of these. Once approximations are applied for the integral of the flow variables over the control volume, the interpolated values at the control volume faces and the integration over these, an algebraic equation for each control volume is obtained. These equations are ex-

pressed in terms of the values of the fluid variables at the control volume centre and those of the neighbouring control volumes. The reasons for the popularity of the finite volume method are probably the inherent conservation of the scheme together with the intuitive nature of the quantities to be approximated. The particulars of the finite volume scheme employed in the ELAN solver used in this work are outlined in Chapter 4. For a detailed review of finite volume discretisation methods, the reader is referred to the textbook of Ferziger and Perić [44].

The discretised system of equations must be solved iteratively on a spatial domain consisting of discrete points corresponding to the fluid region of the problem under investigation. The design of this computational grid is very important, having a strong impact on the accuracy and stability of the solution. Regions with strong gradients in the flow variables such as boundary layers or shear layers must be resolved using a sufficient number of points, where the number required depends on the order of accuracy of the method (higher-order methods requiring less points). Furthermore, certain constraints may exist on the shape of grid cells, with sharp internal angles (sheared cells) or high aspect ratios causing instabilities or errors in the numerical solution. As a result of these factors, grid generation for complex geometries can be a very time consuming process and is considered a specialism in itself.

The main classification of meshes in CFD concerns the manner in which individual points are related to their neighbours to form grid volumes. In a *structured* grid, every non-boundary point has a constant number of neighbours, which are found by the code using a system of index directions. As such, structured grids consist of rectangles in two dimensions or hexahedra in three dimensions. To be able to capture complex geometries, multiple regions or blocks can be combined, each of which must contain a constant number of points in each index direction. Structured codes benefit from simplified implementation and higher numerical efficiency, as the neighbours of each point are implicitly known and the solution matrix has a regular diagonal structure. Furthermore, in regions of parallel flow (e.g. boundary layers) structured grids can be aligned with the flow direction resulting in higher accuracy of the solution. Hexahedral cells can also be generated with very high aspect ratios, efficiently allowing fine resolution of the strong wall-normal gradients found in boundary layers. However, the constraints on the grid design can lead to great difficulty in meshing complex geometries. Furthermore, necessary local refinement in one flow region often causes refinement in other less important regions, which is wasteful of computational resources. Very high aspect ratio cells can also give rise to numerical convergence problems. An example of a structured grid around an airfoil is shown in Fig. 3.1(a).

The principal alternative methodology is *unstructured* grid generation. Instead of indices to allocate the neighbours of each grid cell, the neighbours are explicitly listed in connectivity tables. This has the advantage of allowing arbitrary cell shapes, such as tetrahedra, prisms and other polyhedra, which in turn allow strong local refine-

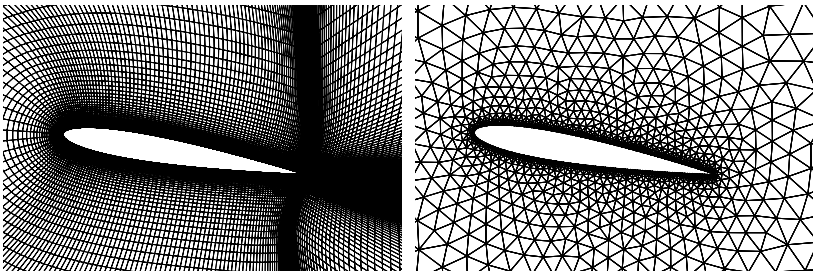

(a) structured (b) unstructured

Figure 3.1: Examples of structured and unstructured grids around a NACA0012 airfoil (n.b. the structured grid is intended for viscous computation with resolution of the boundary layers, whereas the unstructured grid is intended for inviscid computation).

ment where necessary and coarsening of the grid where acceptable. Unstructured grids for complex geometries can be rapidly generated using automatic algorithms, vastly reducing the work load in grid generation, which is the key reason why unstructured codes are favoured in industrial CFD. However, the storage of connectivity data and a sparse solution matrix brings an associated computational overhead, and irregular cell shapes cause a reduction in accuracy for parallel flows such as boundary layers. As such, a common trade off is to use a hybrid methodology of hexahedral or prismatic cells in boundary layer regions, and tetrahedra outside of this. An example of an unstructured grid is shown in Fig. 3.1(b) [1].

Naturally, the necessary computing resources (RAM and CPU time) are directly linked to the number of points in the numerical grid. For large problems, a solution can be obtained in parallel by a number of CPUs in a supercomputer or cluster. The principal method of parallel computing used in CFD is domain decomposition, whereby the grid is divided up and distributed among the computing units. An exchange of data between the boundary cells on neighbouring CPUs is necessary as the solution progresses, which causes a parallelisation overhead and a demand on the networking speed between CPUs. Nonetheless, a lot can be achieved on relatively low cost clusters of networked PCs, which has contributed to an increased accessibility of CFD.

3.2 Overview of computational approaches to turbulent flow

A wide variety of methods exist to represent turbulence and its effects in a simulation, each with characteristic advantages and drawbacks in terms of computational cost and simulation quality. In principle, it is possible to simulate turbulent flows

[1] Courtesy of the German Aerospace Center (Deutsches Zentrum für Luft- und Raumfahrt).

with perfect accuracy, however for practical applications this would require computing power not expected to exist for many decades to come. Reducing the computational burden to manageable levels necessitates the introduction of simplifications and modelling assumptions concerning the turbulence behaviour. These represent sources of uncertainty and strong differences can therefore arise between alternative models. As such, the selection of the appropriate method and model presents a considerable demand on the knowledge and experience of the user. Before these issues are clarified in more detail in the remaining sections of this chapter, an overview of the principal simulation and modelling methodologies will be given.

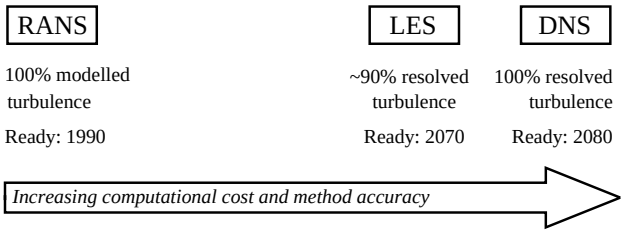

Figure 3.2: Diagram of the relative computational cost, method accuracy and forecast "readiness" date [153] for the principal turbulence treatment methods.

The principal classes of turbulence method can be arranged, somewhat simplistically, along a conceptual axis of increasing computational cost and predictive accuracy. Figure 3.2 provides such a qualitative representation, together with a description of the underlying methodology. The axis also represents one of decreasing empiricism, from Reynolds-averaged Navier–Stokes (RANS) methods (Sect. 3.4) in which the entire range of turbulent motions are described by mathematical models through to direct numerical simulation (DNS, Sect. 3.3), in which all turbulent motions are directly resolved in space and time with no empirical modelling. Recalling from Chapter. 2 that turbulence is inherently three-dimensional and unsteady in nature, it is easily recognised that DNS is correspondingly a four-dimensional simulation problem. By contrast, for statistically steady turbulent flows RANS allows a steady-state description of the mean flow field. Furthermore, for geometrically two-dimensional problems (such as the flow around an airfoil profile), a two-dimensional spatial domain can be employed in a RANS computation resulting in a dramatic reduction of computational expense compared to DNS.

Large-eddy simulation (LES, Sect. 3.5) consists of simulating the energy-containing scales of turbulent motion, whilst the relatively isotropic and universal scales are modelled. Although therefore lying conceptually between RANS and DNS, its placement very close to DNS in Fig. 3.2 is not accidental; certainly in the vicinity of solid boundaries the "large eddies" are indeed very small as described in Sect. 2.4.

Furthermore, the method naturally inherits the requirement of three space dimensions and one in time from DNS. Hence, the numerical cost and scaling of this with Reynolds number verges upon that of DNS [153].

To relate this overview of computational expense to the realities of engineering application, the "readiness date" of each method as estimated by Spalart [153] are quoted[2]. The message is clear: there is no escaping the introduction of modelling empiricism for complex high Reynolds number applications for the foreseeable future. This fact has motivated a tremendous effort in the development and validation of more accurate and computationally efficient RANS models (e.g. the European FLOMANIA project [55]). An observation of particular relevance to this work is that of a considerable gap in the spectrum of turbulence methods for the "near future" between RANS and LES. This is the motivation for an increasing amount of work on the development of hybrid RANS-LES methods for many conceivable target applications, as outlined in Sect. 3.6.

3.3 Direct numerical simulation (DNS)

In DNS, the entire range of turbulent scales is resolved directly in space and in time. Consideration of some of the properties of turbulent flows outlined in Chapter 2 helps to explain why DNS is an inherently expensive technique. Firstly, turbulence is three-dimensional in space and unsteady in time, which makes DNS a four-dimensional problem. Secondly, the shrinking of the Kolmogorov scales relative to the largest turbulent scales with Reynolds number (i.e. increasing scale separation described in Section 2.2.1) means that the numerical cost of DNS grows strongly for higher Reynolds numbers. For isotropic turbulence, a minimum domain size of eight times the integral length scale and a maximum spatial resolution of $\Delta x \approx 2.1\eta$ are quoted by Pope [116][3]. As the motion of the smallest eddies must also be temporally resolved, the numerical time step size must be balanced to the spatial resolution. An appropriate guideline is that a fluid particle may only traverse a fraction of a grid cell per time step, as embodied in the Courant–Friedrichs–Lewy (CFL) criterion [31].

These considerations allow a derivation of the numerical cost of DNS for isotropic turbulence. For this, the required number of grid points and time steps is the dominating factor, which has been derived by Pope [116] to be proportional to $160\mathrm{Re}_{\ell_0}^3$ or $0.55\mathrm{Re}_\lambda^6$. For non-isotropic flows, this scaling is seen to be even more severe. Pope furthermore demonstrates that typically well over 99% of the modes lie within the dissipative range, a fact that emphasises the attractiveness of the large-eddy simulation concept to be described in Section 3.5. As was given in Fig. 3.2, Spalart esti-

[2] This forecast is based on the first "grand challenge" (i.e. non-routine) application of each method to a complete transport aircraft or car, and assumes a fivefold increase in computational power every five years. The description LES in Fig. 3.2 corresponds to Spalart's designation "QDNS" (quasi-DNS), Sect. 3.5.2.

[3] A multiple of the Kolmogorov scale is quoted because this in fact underestimates the dissipative scale size, Fig. 2.5.

mates the date of the first DNS "grand challenge" application to a complete aircraft at 2080 [153].

Particular attention is paid to numerical schemes for DNS, with accurate, low-dissipative methods considered essential. In regard to the numerical cost, efficient schemes with massive parallelisation capabilities are furthermore of great importance. Spectral or pseudo-spectral methods are hence favoured for applications in which homogeneous directions exist. As a result, DNS is usually applied to flows involving simple geometries.

Provided that sufficient resolution, an adequate numerical scheme and appropriate boundary conditions are used, DNS contains no empiricism and can be considered accurate. As such, despite the numerical cost, DNS proves immensely useful for fundamental turbulence research, providing access to statistical quantities all but impossible to obtain experimentally. DNS is also highly important as a source of numerical databases for the validation and calibration of more economical methods.

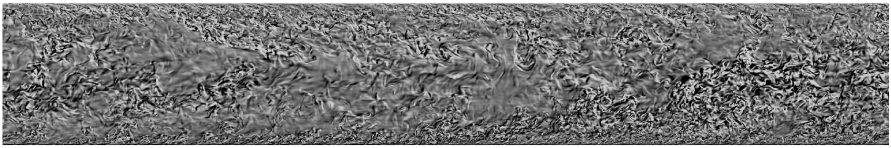

Figure 3.3: Instantaneous vorticity contours at a slice normal to the spanwise direction through the $\mathrm{Re}_\tau = 2000$ channel DNS computation of Hoyas & Jiménez [63, 67] (reproduced with permission). Flow is from left to right and only half of the streamwise domain is shown.

A recent "grand challenge" DNS study is the fully-developed turbulent channel flow computation at $\mathrm{Re}_\tau = 2000$ of Hoyas & Jiménez [63, 67]. The computation of this unprecedentedly high Reynolds number was carried out using a grid of 18 billion ($\times 10^9$) cells and 2048 CPU cores of the Mare Nostrum at Barcelona Supercomputing Centre. The resolution in the wall-normal direction was adjusted to $\Delta y \approx 1.5\eta$. The instantaneous snapshot from this simulation shown in Fig. 3.3 gives a remarkable impression of both the fine resolution of the DNS as well as the complexity of turbulent flow in general.

3.4 Statistical modelling of turbulence (RANS)

The opposite end of the conceptual scale to DNS involves the statistical description of turbulence by mathematical models. Based on the Reynolds-averaged Navier–Stokes (RANS) equations (Sect. 3.4.1), these models assume a steady mean flow field

with no turbulent motion being resolved directly. Correspondingly, steady-state solutions can be sought and highly anisotropic grids can be used with large tangential spacing near solid boundaries. Furthermore, there is no requirement to compute in three spatial dimensions for two-dimensional applications such as airfoil cross-sections. As a result, the computational costs are several orders of magnitude lower than DNS, and RANS methods have already found widespread industrial application. However, the approximations and modelling assumptions give rise to fundamental conceptual flaws in the simpler model categories and high levels of uncertainty in all cases. As such, the simpler models must be carefully calibrated, resulting in applicability for only a limited range of physical phenomena. The promise of a universal model offered by the most complex class of approaches has yet to be demonstrated, and these are beset with the additional disadvantages of implementation complexity, computational cost and lack of numerical robustness. These issues will be discussed at greater detail in the following.

3.4.1 Reynolds-averaged Navier–Stokes equations

The basis of all statistical turbulence models is given by the Reynolds-averaged Navier–Stokes (RANS) equations. These are derived via the technique of *Reynolds decomposition* [120], whereby ensemble averaging is applied to the turbulent flow field quantities, $\phi(x_i, t)$. For an ergodic process where the ensemble averaged signal at each spatial point does not vary with time, ensemble averaging is equivalent to time averaging. For spatially homogeneous fields, ensemble averaging is equivalent to spatial averaging at each moment in time. For the purposes of this introduction ensemble averaging will be considered equivalent to time averaging. Reynolds decomposition hence splits the unsteady turbulent field $\phi(x_i, t)$ into a mean and fluctuating part, $\overline{\phi}(x_i)$ and $\phi'(x_i, t)$ respectively:

$$\phi(x_i, t) = \overline{\phi}(x_i) + \phi'(x_i, t). \tag{3.3}$$

In this sense, Reynolds decomposition can therefore be interpreted as an assumption that a turbulent flow has a statistically steady state, and that all fluctuations away from this are due to turbulence[4]. This concept is depicted in Fig. 3.4 for an example velocity component signal at a single location in space.

Applying the Reynolds decomposition to the governing flow equations gives rise to the Reynolds-averaged Navier–Stokes (RANS) equations. The Reynolds-averaged continuity and momentum equations for incompressible Newtonian flow are:

[4]This is not always a safe assumption, as many flows also exhibit unsteadiness that is non-turbulent in origin. This issue is discussed in Appendix F, together with a triple decomposition method applicable to some such situations.

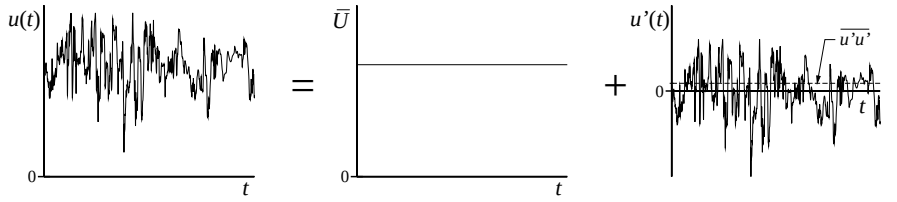

Figure 3.4: Concept of Reynolds averaging illustrated for a velocity component time signal at a single spatial location, $u(t)$.

$$\frac{\partial \overline{U}_i}{\partial x_i} = 0 \tag{3.4}$$

$$\frac{D\overline{U}_i}{Dt} = -\frac{1}{\rho}\frac{\partial \overline{p}}{\partial x_i} + \frac{1}{\rho}\frac{\partial \overline{\tau}_{ij}}{\partial x_j} - \frac{\partial \overline{u_i' u_j'}}{\partial x_j}\,, \tag{3.5}$$

where the time-averaged viscous stress tensor is

$$\overline{\tau}_{ij} = \mu\left(\frac{\partial \overline{U}_i}{\partial x_j} + \frac{\partial \overline{U}_j}{\partial x_i}\right) = 2\mu\overline{S}_{ij}\,. \tag{3.6}$$

These are identical in form to the original equations, except that the time-averaged quantities $\overline{\phi}$ have replaced the instantaneous quantities ϕ, and the additional tensor $\rho\overline{u_i' u_j'}$ has emerged. This is the *Reynolds stress tensor*, which describes the influence of the turbulent fluctuations on the mean flow field. Unfortunately this represents an additional unknown in the equation system, leading to a closure problem. Closure intrinsically requires the introduction of approximations – it is impossible to derive a closed set of exact equations. RANS models are hence tasked with providing prescriptions for the Reynolds stress tensor in terms of known quantities such as the mean flow field or geometric parameters.

3.4.2 The Boussinesq eddy viscosity hypothesis and Reynolds stress models

An important method of approximating the Reynolds stress tensor is based on the hypothesis that the effects of turbulence are analogous to an increased viscosity. This is intuitively justifiable when effects such as energy dissipation and increased mass transport normal to mean flow streamlines are considered. The Boussinesq relationship [13] between the deviatoric Reynolds stresses[5] and the mean flow strain embod-

[5]The deviatoric Reynolds stress tensor is obtained by subtracting the isotropic stress tensor, i.e. $-\rho\overline{u_i' u_j'} + \frac{2}{3}\rho k\delta_{ij}$.

ies this hypothesis and is formulated as

$$-\rho\overline{u_i'u_j'} + \frac{2}{3}\rho\delta_{ij}k = \mu_t\left(\frac{\partial\overline{U}_i}{\partial x_j} + \frac{\partial\overline{U}_j}{\partial x_i}\right) = 2\mu_t\overline{S}_{ij}\ . \tag{3.7}$$

Here, $\mu_t = \rho\nu_t$ is known as the *eddy viscosity* or *turbulent viscosity*. Note that a mathematical analogy is established between the Boussinesq relation and the Newtonian stress–rate-of-strain relation (A.5). This is appropriate as mean flow strain is the primary mechanism by which turbulence is produced and sustained.

The class of models that provide a scalar value of the eddy viscosity to close the RANS equations are hence referred to as *linear eddy viscosity models* (LEVM). An alternative to this is the direct prescription of each component of the Reynolds stress tensor, a technique known as *Reynolds stress modelling* (RSM) or *second moment closure*. The Reynolds stress transport equations can be derived by combining the Navier–Stokes and RANS equations, although this doesn't circumvent the closure problem; on the contrary, an additional six transport equations must be solved for the Reynolds stresses, which introduce a further twenty-two unknowns into the equation system [133].

Analysis of the Reynolds stress transport equations for simplified flow conditions such as simple shear and homogeneous compression can be used to assess the validity of the Boussinesq hypothesis and the LEVM family. A list of fundamental inadequacies of the LEVM framework is given by Leschziner & Drikakis [80]. For example, no resolution of normal stress anisotropy is possible; the rigid linkage of stresses with strain does not account for stress transport by convection or diffusion; stresses are strongly over-estimated at high strain rates; the response to curvature strain, normal straining and rotation is incorrect.

3.4.3 Modelling hierarchy

A wide range of RANS modelling categories therefore exist, with different levels of physical approximation and mathematical complexity, between full differential Reynolds stress models (DRSM) and LEVM. In an attempt to summarise this model landscape as effectively as possible, a modelling hierarchy is drawn up in Fig. 3.5. A series of physical approximations and mathematical model reductions lead to a number of steps on the path from DRSM to LEVM. All of these model types are capable of resolving anisotropy of the Reynolds stresses, and the explicit algebraic Reynolds stress model (EARSM) is a particularly popular formulation. Models of this variety represent a compromise between the generality, complexity and expense of DRSM on the one hand, and the physical inadequacy, simplicity and robustness of LEVM on the other hand. The EARSM framework was first introduced by Pope [115], and a prominent example is the model of Wallin & Johansson [178].

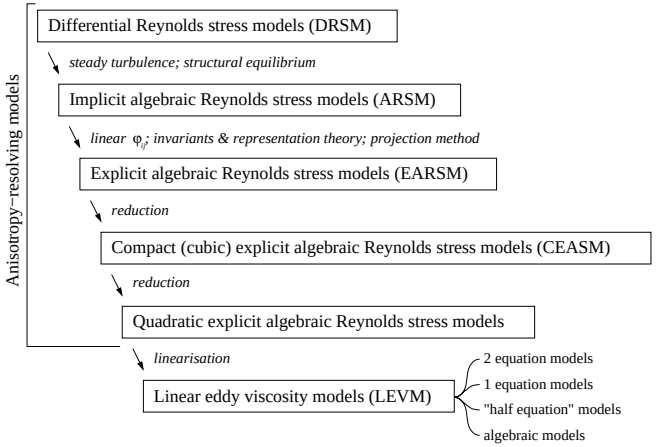

Figure 3.5: Hierarchy of RANS models in order of decreasing modelling complexity (top to bottom). Adapted from an unpublished figure by U. Bunge and from Rung, 2000 [132].

At least theoretically, the model hierarchy represents a trend of increasing generality, physical accuracy, numerical cost and complexity, as well as one of decreasing numerical robustness in the direction LEVM $\rightarrow$ DRSM. In practice, however, this is not so simple – it is often reported that a well-formulated LEVM can provide more accurate predictions of certain key turbulent flow phenomena than full DRSM [55, 80].

Within the LEVM family itself, many different methods are used to determine the eddy viscosity. Dimensional analysis reveals that two characteristic scales are required to formulate the eddy viscosity, a fact leading to the common two-equation modelling framework. Transport equations for two characteristic scales are solved, such as k and ε (Jones & Launder [71]), k and ω (Wilcox [181, 182]), k and ℓ (Rotta [130]) or k and $\sqrt{k}\ell$ (Menter et al. [91]). Applying the assumption of local equilibrium (a balance of turbulent production and dissipation) to two-equation models allows the derivation of one-equation models [131, 42, 89], although not all such models have been derived in this way. The more recent one-equation models involve a transport equation for the eddy viscosity and the model of Spalart & Allmaras [157] is a well-known example. This model, like many one-equation models, requires the prescription of a length scale in the form of the wall-normal distance. This effectively restricts the model's validity to attached boundary layer flows. Other one-equation models, such as those of Menter [89] and Fares & Schröder[42] do not suffer from this limitation, which is achieved by applying the Bradshaw hypothesis [15] that the turbulent shear stress scales with the turbulent kinetic energy.

The simplest form of LEVM are known as *algebraic* or *zero-equation* eddy viscosity models, because they specify the eddy viscosity purely from local information without consideration of transport and history effects. Algebraic models are based on the mixing length theory of Prandtl [117] and von Kármán [175]

$$\nu_t = \ell_m \left| \frac{d\overline{U}}{dy} \right| , \qquad \ell_m = \kappa d_w , \tag{3.8}$$

which is applicable to the log-law region (Section 2.4). To describe the viscous wall region and boundary layer edge, the van Driest damping function [173] and Klebanoff intermittency function [73] are often used, respectively. Algebraic models such as those of Cebeci & Smith [25] or Baldwin & Lomax [6] have previously found extensive application in thin boundary layers typical in external aerodynamic applications. Owing to increasing computing power however, these are seldom still in use.

One interesting intermediate between algebraic and one-equation models are the so-called *half-equation models*, of which that of Johnson & King [70] is exemplary. This model uses an algebraic expression for the wall-normal distribution of eddy viscosity (based on the Cebeci–Smith model), which is scaled using an ordinary differential equation to describe the streamwise transport of the maximum turbulence energy. The Johnson–King model has been reported to give excellent results for the prediction of adverse pressure gradient flows and separating boundary layers, as well as the effect of separation on the mean field [80, 88], in some cases even out-performing $k - \omega$ models.

3.4.4 Wall boundary conditions

Conventionally, two types of wall boundary condition are available for the solution of the RANS model equations. These exhibit very different requirements on the wall normal distance of the first grid point and any violation of these leads to a drastic degeneration in the solution quality[6]. This places a very high level of importance on the design of the numerical grid, and contributes to the excessive human resources typically spent on this task. Furthermore, these criteria depend strongly on the local flow quantities, which means that prior knowledge of the solution is required for correct grid design. In practice this often means that an iterative process is required, causing further grid generation expenditure.

In order to address these problems, a more general unified boundary condition that can deliver robust and reliable solutions on arbitrary grids is highly desirable. Such a generic boundary condition has been proposed by Rung et al. [135], the formulation of which is presented in detail in Appendix C. Similar and functionally equivalent boundary conditions have also been proposed by Esch et al. [40] and Knopp [74].

[6] For example, an under-prediction of the skin friction coefficient of up to a factor of five has been reported for airfoil flows when inappropriate wall treatment is applied [145].

3.4.5 Unsteady RANS

Many important flows exist for which strong unsteadiness of a non-turbulent origin is apparent, which can be broadly classed in two categories:

- Externally-enforced unsteadiness, such as the imposition of a moving geometry or time-variant boundary condition.

- Unsteadiness of a non-turbulent nature inherent to the flow and arising from hydrodynamic instabilities, e.g. the vortex shedding behind a bluff body, shock oscillation.

In such cases the application of time-averaging for the Reynolds decomposition (and subsequent steady-state solution of the mean flow) is inappropriate and can lead to a significant source of error. Instead, an ensemble averaging over a suitable finite time period is required, such that the non-turbulent unsteadiness is resolved in the mean flow and the turbulent fluctuations are described by the RANS model. Such a simulation is most often referred to as unsteady RANS (URANS) although the acronym TRANS for "transient RANS" is sometimes used. For bluff body flows involving unsteadiness of the second type identified above, URANS results of an impressive degree of accuracy have been reported together with a severe degradation of results for steady-state simulations, e.g. by Durbin [38] and Shur et al. [147].

URANS is however not without its difficulties, which can be significant. The central concept of resolving motions larger than the simulation time step and modelling those smaller than this requires a significant spectral gap between the non-turbulent unsteadiness and the largest turbulent time scales. Such a large scale separation is seldom present, in which case the conceptual foundation of URANS becomes murky and ill-defined. A strong and undesirable sensitivity to the choice of RANS model is unfortunately a well-established feature of URANS (see e.g. test cases reported in the FLOMANIA project [55]). A troublesome sensitivity to the spanwise domain extent has furthermore been reported for two-dimensional bluff bodies resolved three-dimensionally by Shur et al. [146]. URANS simulations are furthermore saddled with a higher computational expense than steady-state RANS, with Durbin for example claiming a factor of two orders of magnitude in his study of separated flows [38]. The precise increase in numerical expense depends of course strongly on the flow in question and is naturally less than that of large-eddy simulation.

3.5 Partial resolution of turbulence (LES)

The final family of turbulence methods from the overview of Fig. 3.2 is large-eddy simulation (LES). This is dealt with last, because of the intermediate conceptual space that this occupies between RANS and DNS, as has been summarised in Section 3.2. As was outlined, LES inherits the requirement of three-dimensional spatial resolution and unsteady simulation from DNS. The reduction in numerical expense com-

pared to DNS is achieved by the introduction of a measure of empiricism.

The conceptual basis of large-eddy simulation is the spectral separation of larger turbulent motions from the smaller scales, whereby the former are resolved directly and the latter approximated by some manner of model. Recalling the description of the turbulence energy spectrum arising from the Kolmogorov hypotheses from Section 2.2.1, the smaller scales can be considered statistically isotropic. It therefore follows that a tenable representation of the small scale motions can be achieved with a relatively simple model in comparison to a full RANS closure. The scale separation is formalised by a filtering operation, which can be considered similar to a localised averaging over a region within the filter width, Δ. Application of such a filter operator to the flow field variables results in the following decomposition:

$$\phi(x_i, t) = \widehat{\phi}(x_i, t) + \phi'(x_i, t) \,, \tag{3.9}$$

where $\widehat{\phi}$ is the large-scale filtered or resolved field at each position and time and ϕ' is the small-scale fluctuation away from the filtered value, which is not resolved. A schematic illustration of this process is given in Fig. 3.6.

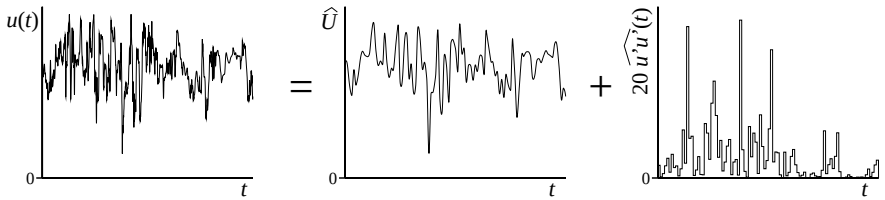

Figure 3.6: Conceptual sketch of filtering applied to a fully-resolved velocity signal u.

The filter operator can be explicitly applied, whereby operators such as the Gaussian, top-hat or cut-off filters[7] are used with a specified filter width Δ. The filter width must be at least as large as the local grid spacing, h, and is either uniform throughout the domain or applied as a constant multiple of h. Alternatively, it is recognised that the discretisation scheme in itself acts as a filter function, since scales smaller than h cannot be resolved. This is known as *grid filtering* or *implicit filtering*. Explicit filtering has the advantage that a known filter function is specified, allowing a controllable separation of the resolved and unresolved scales and the derivation of models for the unresolved scales in a mathematically rigorous manner. However, the usual specification of $\Delta > h$ can be considered wasteful in terms of the grid resolution, since turbulence is not resolved right down to the smallest structures possible. Some explicit filter types can furthermore give rise to implementation difficulties and additional computational cost. Implicit filtering is by contrast considered more

[7] For example, a detailed study of explicit filtering is presented in the PhD thesis of S. Benhamadouche [9].

pragmatic in the sense that it involves no additional implementation and the grid resolution is fully-exploited. However, the exact filter behaviour is not known and varies depending on the numerical discretisation scheme. It is furthermore the case that the smallest resolved eddies are represented with decreasing accuracy as their size approaches the grid spacing (dependent on the order of accuracy of the numerical scheme).

When the filtering decomposition of (3.9) is applied to the Navier–Stokes equations, the resulting filtered equations for the large-scale motion are of the same form as the Reynolds-averaged Navier–Stokes equations (3.4, 3.5), despite the fundamental difference in the averaging applied. Due to the prevalence of implicit filtering in early LES work, the unknown term describing the action of the unresolved scales on the resolved scales is widely referred to as the *sub-grid stress tensor* and is denoted $-\rho\widehat{u_i' u_j'}$.

3.5.1 Modelling of the unresolved turbulence

Some means of approximating the sub-grid stress tensor is therefore required, for which two principal classes of approach exist. In the class known as *implicit LES* (ILES), a numerical scheme with an appropriate quality and quantity of numerical dissipation is considered to provide the dissipative action of the unresolved scales. ILES has emerged predominantly from the atmospheric and meteorological research community, where the effects of solid boundaries are not of great importance. ILES typically encounters problems when applied to wall-bounded flows, although some considerable progress has been achieved recently (e.g. Hickel & Adams [60]). Another potential problem with ILES is that the magnitude of the sub-grid stresses remains unknown, which can present a disadvantage in applications where knowledge of the total Reynolds stresses is of importance. Implicit LES is not considered further in this work, and reference is made to the book of Grinstein et al. [53] for further details.

The contrasting approach to implicit LES, sometimes referred to as *classical LES* involves the explicit introduction of a mathematical model to describe the sub-grid turbulence. This family of methods has largely been developed within the framework of aeronautics research, for which the correct representation of near-wall flows is of central importance. A brief description of some important sub-grid scale models will now be given.

The Smagorinsky model

The first, simplest and still perhaps the most widely-applied sub-grid scale model is that of Smagorinsky [150]. The first application of the Smagorinsky model (together with a simple wall function) to the three-dimensional simulation of turbulence was published by Deardorff in 1970 [35] for the case of fully-developed channel flow. The model is an eddy viscosity model, employing the Boussinesq hypothesis (Sec-

tion 3.4.2) to relate the sub-grid scale stresses to the local flow strain. The model is a simple explicit algebraic expression, which was derived heuristically by Smagorinsky[8] as

$$\nu_{sgs} = (C_S \Delta)^2 S^* \,, \tag{3.10}$$

where

$$S^* = \sqrt{2 S_{ij} S_{ij}} \,. \tag{3.11}$$

Under the assumption that the cut-off wave number lies within the inertial subrange, Lilly [82] derived a value of $C_S = 0.1825$ for isotropic turbulence[9]. Deardorff [35] found a much lower value to be appropriate in his pioneering channel flow investigation, which has been widely corroborated by other researchers quoting values of $0.08 < C_S < 0.11$ for shear-driven flows.

A number of deficiencies are inherent to the Smagorinsky model, which can be summarised as follows:

- The Smagorinsky parameter C_S is clearly not a constant, as shown by the strong difference in values appropriate for homogeneous and sheared flows. The specification of a global value is inappropriate for realistic flows with mixed turbulence phenomena.
- The positive and uniform value of C_S causes the generation of eddy viscosity in sheared laminar flow, and the model is hence incapable of predicting transition to turbulence.
- For the same reason, the model contribution does not vanish in the limit of a fully-resolved DNS.
- The effect of wall proximity in the viscous sublayer (Section 2.4) is not correctly reproduced by the model, requiring the addition of damping terms such as the van Driest formulation [173].
- The model is purely dissipative, i.e. the sub-grid scales always extract energy from the resolved scales. Although this cascade principle (Section 2.2) is true in the Reynolds-averaged sense, the reverse process of *backscatter* from small to large scales can occur locally within the resolved field. The Smagorinsky model cannot predict backscatter.

Dynamic sub-grid scale models

These fundamental problems with the Smagorinsky closure listed above form the motivation for the dynamic sub-grid scale procedure of Germano et al. [51]. In this

[8] It is however possible to derive the Smagorinsky model by many other means [144].
[9] This value cited by B. Aupoix in [3].

method, the appropriate value of C_S is computed dynamically and locally in space and time using a test filter larger than the LES filter width Δ (a test filter width of 2Δ was found by Germano et al. to be optimal). In this manner, the stress-strain relationship is evaluated within the "test window" of the smallest resolved scales of motion and C_S is computed at each time step as a function of position from the information already contained in the resolved velocity field. This procedure is explicit and algebraic in nature, hence a minimal additional computational cost is involved per iteration.

The original Germano formulation demonstrated much improved performance and generality, addressing all of the problems experienced with the Smagorinsky model:

- The dynamically-determined value of C_S was shown to be capable of producing high-quality results for both homogeneous and shear-driven flows.
- $C_S = 0$ is returned in laminar regions allowing the simulation of transition to turbulence.
- $C_S = 0$ is likewise returned in the limit of full DNS resolution.
- The correct wall-normal distribution of eddy viscosity is returned in the viscous sublayer without resorting to damping functions.
- Locally negative values of C_S are produced, allowing a reproduction of backscatter effects.

However, when applied to each grid point individually, excessive regions of negative C_S can be predicted, which lead to computational instabilities. For this reason, Germano et al. suggested averaging of the C_S values in homogeneous flow directions, thereby rendering the dynamic model inapplicable to complex geometries. Lilly [83] proposed a modified technique for determining C_S based on a least-squares method, which although reducing the problem, still requires some degree of averaging for stability.

Firm theoretical foundations for the dynamic procedure were provided by the work of Ghosal et al. [52], from which a dynamic method free from the constraints of averaging was introduced. A *k*-equation based dynamic model was proposed, which is however associated with a high numerical cost due to the need to solve a complex integral equation for the localised parameters. A dynamic one-equation subgrid-scale (DOESGS) model was later proposed by Davidson [32], based on a transport equation for the subgrid-scale kinetic energy, k_{sgs}. By including the dynamically-determined parameters in the *k*-equation source terms rather than directly into the impulse equations, a greater degree of numerical stability is achieved: the oscillations of the dynamic parameters are smoothed naturally by the convection and diffusion terms of the transport equation. Despite the higher numerical effort per iteration required by the solution of the transport equation, the DOESGS model in fact exhibits a lower numerical cost than the dynamic Smagorinsky model [151, 144]. This

is because less iterations are required per time step owing to the greater numerical stability.

Yoshizawa k equation model

As mentioned in the preceding section, a family of transport equation based subgrid-scale models exist. A prominent example is that of Yoshizawa [188]. The motivation of the model was a desire to eliminate the assumption, inherent to the Smagorinsky model, that a balance between subgrid energy production and destruction exists. A transport equation for the subgrid-scale turbulent kinetic energy, k_{sgs} was formulated, which reduces to the Smagorinsky model under the local-equilibrium assumption:

$$\frac{Dk_{sgs}}{Dt} = \frac{\partial}{\partial x_j}\left[\left(\nu + \frac{\nu_{sgs}}{\sigma_{sgs}}\right)\frac{\partial k_{sgs}}{\partial x_j}\right] + P_{k_{sgs}} - C_\varepsilon \frac{k_{sgs}^{3/2}}{\Delta} \tag{3.12}$$

$$\nu_{sgs} = C_k\, \Delta\, k_{sgs}^{1/2}\,, \tag{3.13}$$

with

$$P_{k_{sgs}} = \nu_{sgs}\, S^{*2}\,. \tag{3.14}$$

Only approximate values for the model constants were provided by Yoshizawa [188], hence those published by Fureby [48] are given:

$$\sigma_{sgs} = 1.0 \quad C_\varepsilon = 1.05\,, \quad C_k = 0.07\,. \tag{3.15}$$

Such models include transport and history effects of the subgrid quantities, however there is no dynamic character: the model constants are fixed. This model has been described due to its relevance in some DES formulations and to discussions in Sects. 3.7.6 & 8.3.

3.5.2 Requirements on the numerical scheme and resolution

First and foremost, it is worth repeating the statement made in Section 3.2 that LES requires a three-dimensional spatial domain as well as temporal resolution, a property inherited from DNS and owing to the fundamental dimensionality of turbulence (Chapter 2).

Whereas in ILES use is made of the numerical scheme's inherent dissipative character to act as a subgrid-scale model, in the derivation of classical LES models the assumption is made that no dissipation is presented by the numerical scheme. The requirement of negligible numerical dissipation therefore constitutes one of the principal demands placed by classical LES on the numerics. The widely propagated doctrine of ensuring the kinetic energy conservation of the numerical scheme [10, 43, 86] is indeed centred upon this issue. Although such requirements are also placed on

DNS numerics, in contrast to both RANS and DNS the solution is not smooth at the grid level in LES.

In the general situation that the local structure of the turbulence is not known in advance, it should be ensured that an isotropic grid resolution is employed. Assuming isotropic large eddies, the resolution capability will be dictated by the coarsest grid direction, meaning that strong grid anisotropy can be wasteful in LES. Only in very specific cases can anisotropic grids be recommended, for example in the near wall region when the predominant flow direction is known in advance. Because of the streak-like structures of the large-eddies here (see e.g. [49]), a coarser grid resolution in the streamwise direction relative to the spanwise direction is routinely applied in LES of canonical wall-bounded flows [128]. The distribution of the grid resolution should furthermore be as smooth as possible. Sudden jumps in the grid resolution can be very detrimental, particularly when oriented normal to the mean streamwise direction (an issue investigated in detail by Vanella et al. [174]). When judiciously applied tangentially to the flow direction, discontinuities in the grid resolution can however prove both benign and beneficial [9, 144].

Concerning the necessary grid resolution for LES, it can be generally said that a minimum resolution up to a cut-off wave number in the inertial subrange is required. This arises from Kolmogorov's hypotheses (Sect. 2.2.1) and the general philosophy of resolving the large, geometry-specific eddies and modelling only the more isotropic and universal small eddies. Indeed, the derivation of many SGS models is founded upon this assumption. The scales corresponding to the onset of the inertial subrange depend however on the length scale of the largest eddies (recall Pope's estimate [116] of $\frac{1}{6}\ell_0$, cited in Sect. 2.2) and hence on the local nature of the turbulence. Indeed, the extent of the inertial subrange depends on the Reynolds number, vanishing entirely at lower Re (Fig. 2.5). This presents LES of low Reynolds number flows with conceptual difficulties[10]. Even at higher Re, the dependence on the local length scale renders a-priori grid design difficult[11], and leads to the reliance on rules of thumb for particular situations. These can be principally divided into guidelines for boundary layer flows and "detached" flows.

LES of boundary layer flows is dominated by the need to resolve the streak structures existing around the buffer layer. The grid dimensioning is scaled in wall friction units (Sect. 2.4.1), although quite some scatter is observed in published resolution recommendations (a review of which is given by Sagaut [138]). The appropriate resolution will undoubtedly vary depending on the accuracy of the numerical scheme and subgrid-scale model [128]. Commonly-cited values are however $\Delta x^+_{max} \approx 40$

[10] A further situation where the inertial subrange vanishes is the near-wall damping effect on turbulence. In contrast to the Reynolds number reduction effect however, this is because of a shrinking of the large scales ℓ_0 instead of a growth of the Kolmogorov scales η. For this reason, fully-resolved LES hence approaches DNS levels of resolution near the wall.

[11] One notable approach however involves the extraction of length scale estimates from a precursor RANS simulation, which are employed to define the required LES grid resolution [2].

and $\Delta z^+_{max} \approx 20$ in the streamwise and spanwise directions respectively. The wall-normal grid spacing should be condensed towards the wall giving rise to $\Delta y^+_{max} \approx 1$ at the wall and $\Delta y^+_{max} \approx \max(\Delta x \ ; \ \Delta z)$ near the boundary layer edge. For this a geometric stretching is often used, with a stretching ratio $k \leq 1.15$ often cited as a guideline (e.g. [148]).

The domain size for LES of boundary layer flows is determined by the need to capture the important large scales of the energy-containing range (estimated at $6\ell_0$ by Pope, Sect. 2.2). For channel flow, Moser et al. [100] report that a tangential domain size of $L_x = 2\pi\delta$ and $L_z = \pi\delta$ is sufficient to provide a near complete decay in the two-point correlations over the half-lengths in each direction. A further study to identify the "minimal flow unit" for DNS of channel flow by Jiménez & Moin [68] found this to scale in wall units, with a minimum $L^+_x \approx 250$ to 350 and $L^+_z \approx 100$ cited. Combining the domain size and resolution guidelines allows the grid scaling of LES for wall-bounded flows to be derived. Assuming the ability to vary Δx and Δz optimally across the boundary layer, Chapman [26] determined the required number of grid points to scale as $N_{xyz} \propto \mathrm{Re}^{1.8}$. For structured solvers however, such "nested" optimised grids are not possible, and Reynolds [121] gives a more expensive $N_{xyz} \propto \mathrm{Re}^{2.2}$. This dominance of the fine near-wall structures on the computational cost of LES for wall-bounded flows motivated Spalart [159, 153] to refer to such simulations as quasi-DNS or QDNS. Because the size of the largest eddies grows linearly with wall distance, whereas the Kolmogorov length scale grows more slowly (proportional to $d_w^{1/4}$ [116]), the wall region penalty is *relatively* more severe for LES than it is for DNS.

The resolution requirement for detached turbulent flows in the absence of the length scale reducing effect of wall proximity is less severe. The requirement to resolve the energy-containing range sufficiently gives rise to a fixed number of grid points irrespective of Re_{ℓ_0}. Assuming Pope's estimate of the extent of the energy containing range, this results in a minimum box size of 36^3 grid points, and Spalart [154] quotes a more pragmatic minimum of 32^3 cells. As mentioned, the difficulty of the dependency on ℓ_0 leads to a lack of clear a-priori LES refinement criteria for detached flows. As such, a range of diagnostic methods to assess the sufficiency of grid resolution for an existing LES solution field exist. One approach is to compute the turbulence energy spectra and inspect the existence of a $\kappa^{-5/3}$ exponent at the highest resolved wave numbers as an indicator of resolution up to the inertial subrange. This is however an arduous process when applied throughout the turbulent region, and is furthermore strictly invalid for anisotropic flows. Another set of methods is based upon the expectation that a minimum ratio of resolved to modelled turbulent kinetic energy should result from a sufficiently-resolved LES, with the value 80% suggested by Pope [116]. Upon this basis, the diagnostic index LES_IQ (for "LES index of quality") was proposed by Çelik et al. [24]. In still another approach, Šarić et al. [177] conducted an LES grid resolution estimate based on a multiple of the Kolmogorov length scale, obtaining its distribution from a precursor Reynolds stress model com-

putation[12].

In addition to spatial resolution, a sufficiently fine time step is required to capture the motion of the resolved turbulent structures properly. This issue was investigated by Choi & Moin [27] for DNS of turbulent channel flow at $Re_\tau = 180$ using a fully-implicit method. For very large time steps, the flow relaminarised due to the time filtering effect on the resolved turbulent fluctuations. In contrast, convergence of the solution was obtained for the two finest time step sizes tested. In between these extremes, an over-prediction of streamwise Reynolds stresses and under-prediction of the spanwise and normal components was seen, qualitatively mimicking the effect of insufficient spatial resolution and/or excessive numerical dissipation. The concept of a CFL criterion has been introduced in Sect. 3.3 as a means of checking the balance of spatial with temporal resolution. Indeed, the converged fine steps reported by Choi & Moin were for values of CFL $= 0.5$ and 1. The criterion of CFL ≤ 1 also corresponds to the advice given by Spalart [154] for LES.

3.6 Hybrid RANS-LES

The level of interest in hybrid RANS-LES approaches has increased dramatically in recent years. This is believed to be motivated by the following factors:

- Dissatisfaction with the RANS modelling paradigm (as described in Sections 3.2 and 3.4): Despite many years of intense effort, the accuracy of RANS methods leaves much to be desired. Sources of uncertainty are significant and a "universal model" remains elusive. This is particularly true for flows featuring separation.
- Excessive expense of fully-resolved pure LES methods (Section 3.5): Although more accurate than RANS models, the computational cost of pure LES remains prohibitive at high Reynolds numbers, particularly for wall-bounded flows.
- The significant gap between the computing demands of pure RANS and LES (Fig. 3.2): Commonly-available computing power is expected to occupy this region in the near future.
- The growth of interest in unsteady flow prediction: For example in aeroacoustic and flight mechanical applications, and for greater accuracy in aerodynamic design near the limits of performance envelopes where separation and unsteadiness are characteristic. URANS approaches reveal a number of key weaknesses in this respect (Section 3.4.5).

As a result, there has been an explosion of new methods reported in the literature. The common and distinguishing features between these are often difficult to discern,

[12] In this last case however, it would appear as if the factor of η applied to determine the LES resolution should depend on the Reynolds number. Such approaches to identify the inertial subrange based on the Kolmogorov scales hence appear less suitable than equivalents based on the large eddy length scales.

as are hypothetical or proven advantages or suitability to different applications. A valiant attempt to combat this problem by summarising and grouping the methods into a taxonomy has been published by Fröhlich & von Terzi [47]. Their approach has been to define and class methods based on key aspects of their formulation, and the resulting taxonomy is fairly complex. Nonetheless the work serves as an excellent overview of the diversity of approaches pursued, to which the reader is referred. Another highly competent and comprehensive review can be found in Sagaut et al. [139], which furthermore offers a formulation-oriented nomenclature system of its own. A detailed review of hybrid RANS-LES approaches other than DES is considered outside of the scope of this work, however an original perspective on taxonomy will be described and employed.

In the proposed taxonomy, it is acknowledged that several different perspectives exist as to the *goals* of hybrid RANS-LES. This aspect has not been considered in as much depth as the formulation issues by Fröhlich & von Terzi [47], however it offers a much simpler means to categorise hybrid RANS-LES methods by ignoring formulation issues entirely. Four such "hybrid RANS-LES ambitions" are hence identified as:

1. Very large-eddy simulation (VLES): Allowing coarser grids for LES *within the LES region* by enabling a filter width at scales larger than the inertial subrange.

2. Embedded LES: An arbitrary, user-defined LES region of interest within an encompassing RANS domain.

3. Wall-modelled LES (WMLES): RANS applied to the near-wall region of an LES computation to reduce tangential grid resolution requirements (with the RANS/LES interface *inside* the boundary layer).

4. Regional RANS/LES activity dependent on flow physics: Division of the RANS and LES domains on the basis of local flow characteristics, e.g. attachment or separation, respectively.

Because there isn't a single method that lays claim to all of these ambitions or target applications, their consideration is particularly important. Unfortunately these are seldom explictly declared by the method authors, which appears to contribute significantly to widespread misunderstanding. Attempts to apply various hybrid methods to fundamentally inappropriate target applications is an all too common occurrence in the literature. The terminology of the hybrid RANS-LES ambitions is hence proposed to assist clarity of discussion within this work and, it is hoped, within the research community. It must of course be acknowledged that nomenclature is arbitrary and subjective in nature, and different meanings for these terms are widespread (e.g. some interpretations of URANS as VLES, or limitation of the definition hybrid RANS-LES to a much more specific class of approaches than the umbrella term used here). This taxonomy approach is furthermore proposed as a good framework for the formulation of best practice guidance for industrial application of hybrid RANS-LES methods.

3.6.1 Nomenclature for filtering and averaging

In Section 3.4 the nomenclature $\overline{U}_i$ was introduced to refer to the averaged velocity vector in pure RANS approaches, whereas in pure LES $\widehat{U}_i$ is the filtered velocity vector (Sect. 3.5). However, for many hybrid RANS-LES methods, these concepts are used interchangeably in the same solution field (which doesn't "know" whether it is averaged or filtered). The upper case symbol U_i will hence be used to refer to the velocity vector in hybrid RANS-LES, which can be considered to be either averaged or filtered depending on the activity of the RANS or LES mode respectively. In cases where a distinction is necessary, the subscript *sgs* will be applied to refer to sub-grid scale quantities. Concerning DES, as will become clear, the same variable is used for the eddy viscosity in both RANS and LES operation. The notation ν_t will hence be used universally.

3.7 Detached-eddy simulation

Detached-eddy simulation is the particular hybrid RANS-LES method forming the subject of this work, which has since its introduction in 1997 [159] enjoyed widespread acceptance in the industrial CFD community. In this section a detailed account of the development history of DES will be given, beginning with a discussion of the central philosophy of the method in Sect. 3.7.1. The original formulation will then be introduced in Sect. 3.7.2, before a summary of its principal limitations is given in Sect. 3.7.3. The extensive and largely successful work undertaken to rectify these problems will then be described in Sects. 3.7.4, 3.7.5 & 3.7.6.

The driving forces behind the development of DES are the research groups of P. Spalart (Boeing Aircraft Company, USA) and M. Shur, M. Strelets and A. Travin (St. Petersburg Technical University and New Technologies and Services, Russia), and the publications of these authors are considered the authoritative sources of information on DES. In addition, considerable testing and validation work has been carried out in collaborative European research programs, notably the EU-funded FLOMANIA [55] and DESider [56] projects from which the majority of this work has originated. The interested reader is also referred to the recent review article of Spalart [156] for an overview of prominent application examples and a discussion of the DES state of the art.

3.7.1 Philosophy of the method: "The 'D' in DES"

To begin this discussion on the conceptual foundation of DES, the definition provided by Travin et al. [171] will be cited:

> "A Detached-Eddy Simulation is a three-dimensional unsteady numerical solution using a single turbulence model, which functions as a subgrid-scale model in regions where the grid density is fine enough for a large-eddy simulation, and as a Reynolds-averaged model in regions where it is not."

The first specification of a three-dimensional and unsteady solution relate to the properties inherited from LES, described in Sect. 3.5. As a result, any two-dimensional or steady-state solution of the DES equations is a misnomer as well as a conceptual error. The following item, that DES involves a single turbulence model, relates to what is often referred to as the "non-zonal" nature of DES (together with the single solution field aspect). However, as commented in the review of Fröhlich & von Terzi [47], the terms zonal and non-zonal are of limited use in categorising hybrid RANS-LES methods, not least because of inconsistent use in the literature. Finally, a fundamental coupling of the RANS and LES activity to the local grid resolution is expressed in the definition. As will be discussed in Sections 3.7.2 & 3.7.3, this aspect is central to the formulation of DES as well as to some of its early shortcomings.

The above definition precisely outlines key attributes of the DES formulation whilst avoiding unnecessary rigidity and formalism[13]. However, it doesn't address the ambitions or uses of the method directly. The four hybrid RANS-LES ambitions introduced in Section 3.6 will now be revisited in an effort to elucidate the targeted application range of DES as well as to demarcate it from other hybrid RANS-LES strategies. The terminology of "natural" and "extended" uses of DES outlined by Spalart [155] will be drawn upon.

Natural uses, or "the 'D' in DES": Natural uses of DES involve the RANS treatment of attached turbulent boundary layers *in their entirety*, whilst LES is applied to regions of massively separated flow (only detached eddies are simulated). Natural uses of DES hence correspond to the fourth hybrid RANS-LES ambition, whereby the flow-physical criterion dictating the RANS or LES operation is the attached or separated status of the local flow. As a consequence, any incursion of the RANS–LES interface inside turbulent boundary layers is a violation of this requirement. Expressed differently, any DES method must be capable of modelling an entire boundary layer with RANS[14] [155].

Extended uses: Extended uses of DES correspond to the third hybrid RANS-LES ambition, namely wall-modelled LES (WMLES). The adjective extended is applied for two reasons: Firstly, WMLES was not the ambition envisaged in the original publication of the method [159], which carefully expresses the the motivation of the formulation in terms of natural DES usage. Secondly, the first tests of DES-based WMLES for channel flow [101] revealed a fundamental inaccuracy of such simulations (to be described in more detail in Sect. 3.7.3).

The rationale motivating the intended natural use of DES can be explained when some fundamental properties of pure RANS and LES approaches are considered

[13] Note, for example, that the precise formulation of the RANS–LES switching mechanism is left open and that the method is not limited to a particular RANS model.

[14] This requirement hence eliminates DES formulations based on simple algebraic mixing length models unless they include additional terms for the viscous sublayer and outer layer. It furthermore differentiates DES from many WMLES methods proposed.

with respect to attached and separated flow. As described in Sect. 3.4, RANS models can be well-tuned to handle simple boundary layer flows at minimal computational cost, however exhibit significant deficiencies in massively-separated flows (even when computed in unsteady mode, i.e. URANS, Sect. 3.4.5). LES by contrast inherently delivers more accurate predictions due to the limitation of modelling empiricism to the smallest turbulent scales (Sect. 3.5). However, as described in Sect. 3.5.2, the numerical cost for wall-bounded flows is enormous and increases strongly with Reynolds number. For detached flows far from the influence of walls, however, the cost of LES is manageable and Reynolds number independent[15]. These motivational factors underlying DES are summarised diagrammatically in Fig. 3.7.

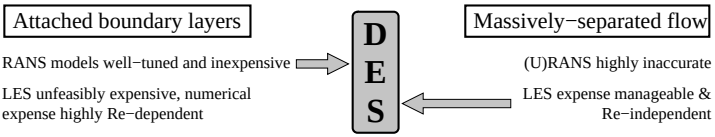

Figure 3.7: Diagrammatical summary of the motivation of DES.

Having been of use in describing what DES *is*, it is informative to draw upon the hybrid RANS-LES ambitions of Sect. 3.6 to discuss what DES *is not*. Firstly, DES is not a method for VLES: There is no ingredient in DES targeted at allowing a coarser grid in the LES-mode region than would be acceptable for the Smagorinsky model. As a result, the usual requirements for LES spatial and temporal resolution outlined in Sect. 3.5.2 must be adhered to in the region where LES-mode operation is desired in DES.

Secondly, DES is not an embedded LES: Although it is in principle possible to control the local RANS or LES functionality via the grid design, an arbitrary placement of these regions will not give the desired behaviour. Such arbitrary zone placement requires considerably more elaborate methods than DES, particularly concerning the formulation of interface conditions. In particular, where a RANS domain is convected into an LES domain, physically-viable resolved turbulent fluctuations must be explicitly injected into the solution. This is closely related to the grey area problem to be described in Sect. 3.7.3.

The original DES concept sketch from the presentation of the 1997 paper is shown in Fig. 3.8, which illustrates well the envisioned application area of DES. The extensive surface area covered by thin boundary layers is typical of external aerodynamic applications. These can be reliably treated using RANS, and would incur unman-

[15] In the statement "Reynolds number independent", the Reynolds number based on the largest eddy length scale ℓ_0 is considered. Of course, situations could be envisaged where ℓ_0 itself depends on the configuration Reynolds number (e.g. decrease of the wake width behind a cylinder at supercritical Re, Sect. 2.5.2.

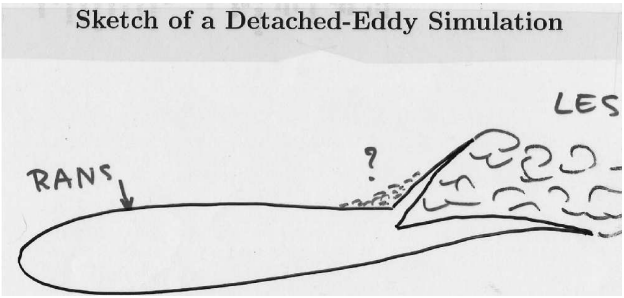

Figure 3.8: Original concept sketch of DES from the presentation of the 1997 paper [159]. Courtesy P. Spalart.

ageable numerical expense with LES or even WMLES. The separated region of large-scale turbulence behind the spoiler contrastingly represents an ideal application region for LES for the reasons already outlined. The onset of this region is furthermore clearly-defined by sharp geometric features, which raises the question of the predictive quality of DES in cases with more sensitive flow separation. In such cases, the separation point will be dictated by the RANS model, which as identified in Sect. 3.4 is a distinct disadvantage. It is clear therefore that a hybrid RANS-LES method aiming to improve separation point prediction relative to RANS must involve some LES element in the upstream boundary layer and hence the higher associated costs. Natural DES in contrast only aims to improve the flow prediction following separation.

The shallow area of separation and re-attachment labelled with a question mark in Fig. 3.8 reflects some of the conceptual problems with DES already identified at the outset. These will be outlined in Sect. 3.7.3, following the description of the original DES formulation in the next section.

3.7.2 The original DES formulation: DES97

The motivation and intended application area of DES (described in the previous section) was well identified and discussed in the original proposal of 1997 [159], together with the first method formulation. Accompanying the publication of the first major revision [158] (DDES, Sect. 3.7.4), the authors proposed the title of DES97 for the original formulation, which is hence adopted in this work. Because of the emphasis on dividing the RANS and LES operation between attached and separated flow, respectively, RANS models that incorporate the wall-normal distance, d_w, as a length scale were first considered a natural choice for the DES97 formulation. The Spalart–Allmaras (SA) model [157], the equations of which are listed in Appendix B, was hence chosen. The DES length scale was introduced to replace d_w in all terms of the SA model equations:

$$L_{\mathrm{DES97}} = \min\left(d_w\ ;\ L_{\mathrm{LES}}\right)\ ,\quad L_{\mathrm{LES}} = C_{\mathrm{DES}}\,\Delta\ ,\quad \Delta = \max\left(\Delta_i\ ;\ \Delta_j\ ;\ \Delta_k\right)\ . \tag{3.16}$$

The wall-normal distance occurs in the destruction term of the $\tilde{\nu}$ transport equation, which is proportional to $1/d_w^2$. Near to the wall, where $d_w < L_{\mathrm{LES}}$, the DES length scale is equal to the RANS model length scale, and the model formulation is identical to the SA RANS model. Far from the wall, where $L_{\mathrm{LES}} < d_w$, the length scale L_{LES} is employed, which consists of a measure of the local grid cell size, Δ, multiplied by a model constant C_{DES}. Δ corresponds to the LES filter width, and is formulated as the maximum cell length in each index direction[16]. This formulation is proposed assuming that no knowledge of the local turbulent structure is available in advance, such that the smallest resolvable isotropic eddies would scale with the coarsest grid cell dimension.

It was shown that under assumed conditions of local turbulent equilibrium, i.e. equality of the production and destruction terms in the model transport equations, a proportionality of eddy viscosity to the strain rate and square of the filter width analogous to the Smagorinsky model, Eq. (3.10), is returned (see e.g. Appendix D). This provides evidence that the subgrid-scale modelling in the LES-mode operation of DES is viable, and furthermore that C_{DES} can be considered an analogue to the Smagorinsky constant. The value $C_{\mathrm{DES}} = 0.65$ was first calibrated for SA-based DES on the basis of decaying, isotropic turbulence (DIT) by Shur et al., 1999 [148] alongside the publication of the first three-dimensional DES results.

The formulation hence successfully relates near wall regions to RANS modelling and finer grid regions far from the wall to LES as desired. However, no consideration of the boundary layer thickness is included, such that a danger of LES-mode activity inside attached boundary layers is present. The original formulation however relied on the expectation that RANS grids for external aerodynamic applications typically involve grid spacings tangential to the wall much larger than the boundary layer thickness.

Generalisation to other RANS models

The connection between the DES methodology and models with a length scale based on the wall-normal distance was originally believed to be fundamental [159]. However, later publications demonstrated the applicability of the DES methodology to RANS models in general. The model's specific turbulence length scale was employed in place of d_w in the DES length scale definition as:

$$L_{\mathrm{DES97}} = \min\left(L_{\mathrm{RANS}}\ ;\ L_{\mathrm{LES}}\right)\ . \tag{3.17}$$

The first demonstrations of DES with alternative RANS models were published by

[16] This formulation hence assumes hexahedral structured grids and an equivalent must be formulated for unstructured grid applications with arbitrary cell geometries.

Travin et al. [172] and Strelets [163], who presented a formulation based on the Menter SST model [90]. The value of C_{DES} was found to vary relative to the SA model value, and specific values were calibrated against DIT for each of the $k-\varepsilon$ and $k-\omega$ branches of the SST model. The generalisation of the DES methodology to other RANS models was an important step: As commented in Sect. 3.7.1, DES can be expected to be "at the mercy" of the underlying RANS model in cases with sensitive flow separation. Furthermore, the non-generality of RANS models has led to the establishment of preferred models for different applications in the framework of industrial best practice [23, 55].

The generalised methodology for the DES modification is in fact less clear cut than the length scale substitution in SA model, where d_w is only present in a single term of the transport equation. For models such as SST however, the length scale is incorporated explicitly or implicitly in a number of terms in both transport equations. Indeed, Strelets [163] acknowledged this freedom of choice concerning the term selected for substitution of L_{DES}. The decision taken to substitute only the length scale in the k equation destruction term was motivated as follows: Firstly, the modification should be as simple as possible as long as the basic requirement of a derivable Smagorinsky-like form is met. Secondly, such a substitution provides the greatest degree of similarity with the established SA-DES. The substitution of the DES length scale in alternative terms was subsequently investigated by Bush & Mani [22] and Yan et al. [186] and incorporated in the DES-like approach "X-LES" of Kok et al. [76]. These formulations will be described in Sect. 3.7.6 and this issue will be returned to in the analysis summarised in Sect. 8.3.

Early results obtained with DES97 were highly encouraging, with considerable advantages relative to URANS methods demonstrated for flows featuring massive separation [55, 94, 148, 163, 171].

3.7.3 Problems with the original formulation

A number of shortcomings have however been identified with DES97, some of which were anticipated from the outset [159] and some of which emerged upon further scrutiny. Many of these have been successfully addressed in later revisions and some remain open issues, apparently fundamental to the methodology itself. These will be introduced in the following sub-sections before the respective enhancements are described in Section 3.7.4.

Erroneous activation of near-wall damping terms in LES mode

Certain RANS models (including the SA model) contain additional damping terms to ensure correct near-wall behaviour, such as in the viscous sublayer. When applied in DES, the activity of the LES length scale can under certain circumstances conspire to cause a spurious damping of the subgrid eddy viscosity to near zero levels. Such damping terms are often sensitised to quantities such as the near-wall distance

and eddy viscosity levels, becoming active only when low levels of both are present. In LES-mode regions with very fine grids however, the small value of Δ together with low levels of subgrid-scale eddy viscosity activate these damping terms. This effect also destroys the analogy to the Smagorinsky model, as the effective Smagorinsky parameter value (a model-specific expression built up of damping terms, model constants and C_{DES}) ceases to be constant. Although discovered earlier, this error mechanism was first published in 2006 [158]. In the same paper, a methodology to derive an antidote function that restores the desired Smagorinsky model behaviour was presented. This remedy is described in Sect. 3.7.4.

Incursion of LES mode inside the boundary layer

As described in Sect. 3.7.1, the DES97 formulation is based on the assumption that the tangential grid spacing near the wall exceeds the boundary layer thickness by a good margin. Only then will the interface where $d_w = C_{\mathrm{DES}}\,\Delta$ be located outside of the boundary layer as required. The problems to be expected when this condition is violated were indeed anticipated in the original publication, however it was assumed that grids fine enough to cause them would be unfeasibly expensive for the foreseeable future.

However, it did not take long before an occurrence of this problem was reported (by Menter & Kunz [92]) for the case of a highly-loaded airfoil with a small separation region near the trailing edge. The separation point predicted by DES97 was found to move further upstream than the location found by RANS (using the same model). As a result, the authors named the phenomenon "grid-induced separation" (GIS), due to the central role played by the grid resolution. The mechanism was identified as an encroachment of the RANS-LES interface inside the boundary layer, giving rise to reduced levels of eddy viscosity on the LES-mode side. However, whilst proving too fine for the correct functioning of DES97, the grid spacing was at the same time not fine enough to resolve turbulent structures above the interface in the sense of a WMLES.

In a later analysis of the problem by Spalart et al. [158], the problem caused by such ambiguous grids was entitled "modelled stress depletion" (MSD), reflecting the effect of reducing the RANS Reynolds stresses. MSD can of course give rise to reduced skin friction prediction without the GIS phenomenon arising.

MSD and GIS probably represent the most serious deficiency of the DES97 method as far as industrial applicability is concerned. Such an over-sensitivity to the grid resolution results in impractical grid design constraints as guaranteeing a sufficiently coarse tangential resolution can in many cases be impossible, particularly for structured grid methodologies[17]. Furthermore, the result that a refinement of the grid can

[17] The example of a planar channel with a backward-facing step can be considered: A streamwise refinement approaching the step would give rise to the same streamwise refinement along the opposite flat wall.

in fact deteriorate the results is both paradoxical and undesirable.

A number of proposals to combat this problem have been made, most notably by Menter & Kunz in the same paper [92] and by Spalart et al. [158]. These will be introduced in Sect. 3.7.4.

The grey area problem

The grey area problem was identified in the original DES publication [159] and refers to a region of undefined modelling existing between the RANS mode and fully-developed LES zones. The severity of the grey area problem is furthermore highly case-specific. The grey area can be described by considering a turbulent boundary layer which at some point separates from a solid surface to become a free shear layer. It is assumed for the sake of simplicity that the grid resolution is sufficient for a well-resolved LES immediately following separation (which is unlikely to be the case in practice). As established, the attached boundary layer should be handled entirely by RANS mode with all turbulence modelled and none resolved. The problem arises when considering the region immediately following separation where LES should be carried out, in which the majority of the turbulent kinetic energy should be resolved. However, this resolved turbulence is not convected from the upstream RANS solution. Hence, when the DES switches to LES mode in such cases, the initial lack of resolved turbulence results in something that is neither RANS nor LES, due to insufficient modelled and resolved turbulence respectively. Instead, as far as the resolved field is concerned, a kind of pseudo laminar-turbulent transition must occur resulting in fully-developed resolved turbulence further downstream. This problem is fundamental to all hybrid RANS-LES methods and the focus of much study. In the case of DES and similar hybrid methods however, the problem is exacerbated by the transport of eddy viscosity from the RANS boundary layer into the LES-mode region. Similarly, the grid cannot in general be expected to be sufficiently fine for such thin shear layer LES resolution. Both effects further delay the development of resolved structures.

It is clear that the extent and severity of the grey area problem is highly dependent on the flow in question and the strength of the shear layer instability. Indeed for massively-separated flows (e.g. bluff body wakes), the impact of recirculating resolved turbulence upon the early shear layer provides an amplification mechanism to the development of resolved turbulence, resulting in a negligible grey area. This feedback mechanism is weaker or non-existent for cases of more shallow flow separation, in which case a significant grey area problem can be expected. This is the reason why DES is considered particularly suitable for massively separated flows. However, taking the example of wing or airfoil aerodynamics, it is precisely the weakest occurrences of separation in the early stall onset that are of greatest relevance to predicting the off-design performance. For cases with an extensive grey area therefore, the net deficit in turbulent shear layer mixing (resolved or modelled) can be expected to re-

sult in delayed flow reattachment and exaggerated recirculating regions.

It should be noted that in some publications the term grey area is applied to the RANS/LES interface in a WMLES setting and the associated problem of log-layer mismatch to be described in the next subsection. Although this is clearly related in some ways, the term grey area is applied solely to the RANS/LES interface occurring between attached and separated flow in this work.

The grey area problem remains an open issue in DES, effectively limiting its recommended application range. A remedy but not a cure could emerge from considerations of alternative length scale substitutions, as will be described in Sect. 8.3. It must be acknowledged however that a full resolution of the grey area problem would require the explicit addition of realistic turbulent fluctuations at the onset of the LES-mode region, which is expected to be a highly complex task.

Log-layer mismatch in WMLES scenarios

Recalling that WMLES is considered an extended and not a natural use of DES, such simulations are nonetheless a highly attractive prospect. Detailed tests of the performance of DES97 for fully-developed turbulent channel flow at a range of Reynolds numbers were performed by Nikitin et al. [101]. These test were considered successful in certain key respects: The resolved turbulence in the LES-mode channel core was sustained and high Reynolds numbers could be simulated with wall-tangential grid spacing unlimited in wall units. However, a consistent pathology was identified in the form of a kink in the velocity profiles between the RANS and LES log-layers, which has since become known as *log-layer mismatch* (LLM) [170]. This gave rise to an unacceptable under-prediction of the skin friction coefficient of the order of 15%.

LLM is in fact a very common feature of hybrid RANS-LES methods targeting WMLES applications, having been reported for a wide range of simpler formulations (e.g. by Baggett [5], Hamba [57] and Piomelli et al. [114]). Opinions vary on both the cause of the phenomenon and its remedy (see e.g. Hanjalić et al. [58]), however the super buffer-layer that emerges between the RANS and LES log-layers is consistently associated with oversized streak structures known as super streaks.

The LLM problem has been addressed in a recent major extension to the DES concept, to be described in Sect. 3.7.5.

3.7.4 Enhanced versions of DES

Many of the problems outlined above have been tackled in subsequent enhanced DES versions. The DES improvements aimed at natural DES applications (Sect. 3.7.1) will be described in this section, whereas an improvement enabling extended WMLES usage is treated in the following Section 3.7.5.

Correction of RANS model damping term behaviour

A correction function to resolve the problem of unwanted activity of the RANS model damping terms in LES mode was published for the SA-model by Spalart et al. [158]. As this function is model-specific, a general methodology for analysing the need for such a function in different RANS models and, where needed, the derivation thereof was described. The correction function, Ψ, functions as an antidote to restore the Smagorinsky model behaviour for all values of eddy viscosity. The correction function is incorporated in the LES length scale

$$L_{\mathrm{LES}} = C_{\mathrm{DES}} \Psi \Delta \,, \tag{3.18}$$

and for models where no such function is required (e.g. the 1988 Wilcox $k-\omega$ model [181]), $\Psi = 1$ can be set.

The published function, including numerical limiters, for the Spalart–Allmaras model with trip terms activated is

$$\Psi^2_{\mathrm{SA}} = \min \left\{ 10^2 \,;\; \frac{1 - \frac{C_{b1}}{C_{w1}\kappa^2 f_w^*} \left[f_{t2} + (1 - f_{t2})\, f_{v2} \right]}{f_{v1} \max\left(10^{-10} \,;\; 1 - f_{t2}\right)} \right\} \,, \tag{3.19}$$

where f_w^* is the asymptotic value of the function f_w for high eddy viscosity values. The methodology for deriving these functions is described in more detail in Appendix D, where the derivations for the RANS models considered in this work are also reported.

The Ψ function methodology was shown by its authors to be an effective remedy of the damping function problem, whilst leaving the behaviour of these functions unaltered in RANS mode.

Protection of RANS mode operation in boundary layers

To resolve the problem of MSD caused by encroachment of LES-mode activity inside the boundary layer, a fairly significant modification of the original DES97 formulation was found to be necessary. Instead of depending purely on the grid (and turbulence length scale in the case of the generalised formulation), some aspect of solution dependence must be incorporated into the DES length scale definition. Only with a suitable sensor for the presence of a turbulent boundary layer can it be ensured that this is modelled using pure RANS.

The first such proposed shield function, known as a GIS-shield, was proposed by Menter & Kunz together with their diagnosis of the GIS problem [92]. This was a model-specific fix for DES based on the SST model, which exploited the SST model's F_2 function to sense the presence of an attached turbulent boundary layer. Inside this region, LES-mode operation of the DES was disabled.

An analogous and more generally-applicable function was later proposed by Spalart

et al. [158], for which the boundary layer sensor, r_d, the shield function, f_d and the corresponding modification to the DES length scale are

$$r_d = \frac{\nu_t + \nu}{\kappa^2 d_w^2 \ \max\left(\sqrt{\frac{\partial U_i}{\partial x_j}\frac{\partial U_i}{\partial x_j}}\,;10^{-10}\right)}\,, \tag{3.20}$$

$$f_d = 1 - \tanh\left[(8r_d)^3\right]\,, \tag{3.21}$$

$$L_{\mathrm{DDES}} = L_{\mathrm{RANS}} - f_d\ \max\left(0\,;\ L_{\mathrm{RANS}} - L_{\mathrm{LES}}\right)\,. \tag{3.22}$$

The sensor function r_d is based strongly on the function r from the Spalart–Allmaras model, Eq. (B.5), however slightly modified so as to be applicable to any eddy viscosity model. The hyperbolic tangent blending function in f_d was tuned such that the earliest onset of LES mode occurs just outside the boundary layer whilst avoiding an excessively strong shield function. The function assumes the value $f_d = 0$ inside a turbulent boundary layer, blending smoothly to $f_d = 1$ at the boundary layer edge. Incorporated into the DES length scale definition as it is, the shield function delays the switch to LES mode until outside the turbulent boundary layer. For this reason, the method was named delayed DES (DDES).

DDES has been shown to successfully shield attached boundary layers irrespective of the grid resolution, and hence represents a significant robustness enhancement. The method has hence been proposed to replace DES97 entirely. The solution dependency however does give rise to a new peculiarity, namely the possibility of a dual solution. In the presence of resolved turbulence near the wall, the shield function recedes back inside the boundary layer. This enables WMLES-type simulations to produce sustained resolved turbulence, however the LLM problem remains [170]. For cases such as a periodic channel, the solution dependency boils down to a dependency on initial conditions: For simulations begun from a smooth initial solution field, the shield function grows from each wall and meets in the middle, returning a valid RANS solution. However, if the solution is initialised with turbulent fluctuations, the shield function activity remains near to the wall and the nominal WMLES situation emerges. In an asymmetric test, with one side initialised with fluctuations, the other with a smooth RANS profile, the LES side was shown to prevail, engulfing the entire channel core [149].

3.7.5 Incorporation of WMLES functionality

The LLM imperfection identified for DES by Nikitin et al. [101] and described in Sect. 3.7.3 has been tackled in the most recent DES development work. The motivation for this extended capability is first and foremost the promise that WMLES offers in a wide range of applications, particularly internal flows with thick boundary layers. The necessity of proper WMLES prediction is however also a result of the dual-solution nature of DDES. To illustrate this, the example of a separating-re

attaching flow such as a backward-facing step is considered. Even if a natural DES is targeted, the impact of resolved turbulence on the boundary layer at the reattachment point gives rise to some unavoidable WMLES content in the simulation. A WMLES situation will arise even with boundary layer shielding such as DDES applied, as described in the above section. The fact that WMLES regions can occur in natural DES simulations therefore underscores the importance of such capability.

The outcome of this effort is the "improved DDES" (IDDES) formulation, first published by Travin et al. [170], which was followed by a more detailed discussion (and nomenclature revision for enhanced clarity) by Shur et al. [149]. IDDES consists of a novel hybrid RANS-LES formulation for pure WMLES application, which is incorporated into the DDES concept. As such, the WMLES model will first of all be described in the next subsection, followed by the complete combined model.

The hybrid model for WMLES

The hybrid RANS-LES model for WMLES has been formulated to eliminate LLM, whilst maintaining a formulation compatible with the general DES approach. As such, the method is in principle applicable to any RANS model and non-zonal in nature. Furthermore, unlike many existing hybrid RANS-LES methods for WMLES (see e.g. [47, 58]), it is in no way constrained to channel flows or flows with a homogeneous direction and requires no specific user input (such as interface placement or input from DNS data).

The principal ingredients of the method can be summarised as a near-wall modification of the LES filter, Δ, and a more sudden transition between the RANS and LES length scales than given by DES97 or DDES. The method is based on a number of sensors of different boundary layer regions and blending functions that have been formulated through a combination of theoretical considerations and empirical tuning.

The motivation for a modification to the grid filter definition is the observation that strongly different values of the Smagorinsky constant are required for homogeneous and sheared turbulent flows (Sect. 3.5.1). An alternative to local variation of the Smagorinsky constant applied in dynamic LES was proposed for IDDES, based on the observation that the Smagorinsky constant always appears as a product with Δ in the model equation. The model parameter C_{DES} is therefore held constant and the value of Δ is reduced near to the wall from the standard "maximum" formulation, as given by Eq. (3.23).

$$\Delta = \min\left[\max\left(C_w d_w; C_w h_{max}; h_{wn}\right); h_{max}\right], \tag{3.23}$$

where C_w is an empirical constant with the value 0.15, h_{max} is the maximum of the grid spacing in all three directions (i.e. the standard DES formulation of Δ), and h_{wn} is the grid spacing in the wall-normal direction. This formulation gives rise to three distinct zones: far from the wall, where $\Delta = h_{max}$, very near to the wall, where

$\Delta = C_w h_{max}$ and a linear blending in between. The blending is given by $\Delta = C_w d_w$ for grids with a stretching ratio less than $1 + C_w = 1.15$ in the wall-normal direction, and is steeper than this for stronger stretching ratios. Adoption of this Δ definition was shown to enable fully-resolved LES of channel flow using the Smagorinsky constant value obtained by calibration against DIT [170, 149], whereas the cubic root of the cell volume and $\Delta = h_{max}$ variants give very poor results.

The blending between RANS and LES length scales is governed by the hybrid length scale L_{WMLES}, the basic weighting function of which is f_{step}. This is constructed such that in the near wall region $f_{step} = 1$ and $L_{\mathrm{WMLES}} = L_{\mathrm{RANS}}$; away from the wall $f_{step} = 0$ and $L_{\mathrm{WMLES}} = L_{\mathrm{LES}}$. This function is dependent on the grid construction only, more precisely upon the ratio of the wall-normal distance and the maximum cell length d_w/h_{max}. The formulation of f_{step} is given in Eq. (3.24).

$$f_{step} = \min\left(2e^{-9\alpha^2}; 1\right) \tag{3.24}$$

$$\alpha = 0.25 - \frac{d_w}{h_{max}} \tag{3.25}$$

It can be seen by inspection that the begin of the switch between RANS and LES length scales occurs when $\alpha = (\ln 0.5/-9)^{1/2} = \pm 0.2775$, i.e. when $d_w = 0.53\, h_{max}$. The shape of f_{step} is shown in Fig. 3.9, from which the sharp switch at $d_w/h_{max} = 0.5275$ and rapid drop to zero at around $d_w/h_{max} \approx 1$ can be seen.

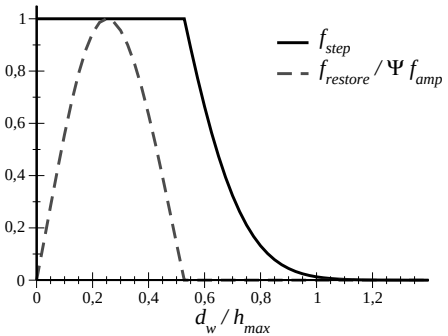

Figure 3.9: The grid dependent RANS-LES blending function f_{step} and the grid dependent part of $f_{restore}$ (i.e. $\max\left[(f_{hill} - 1), 0\right]$) as functions of the wall normal distance ratio with maximum cell spacing, d_w/h_{max}.

The second component function of L_{WMLES} is intended to counteract the undesirable reduction of the RANS modelled stresses near to the interface caused by interac-

tion with the LES region of reduced eddy viscosity. The RANS length scale is therefore multiplied by a positive "boosting" function $f_{restore}$, which itself consists of both grid dependent and solution dependent components, f_{hill} and f_{amp} respectively. The complete constitution of $f_{restore}$ is given in Eqs. (3.26–3.32).

$$f_{restore} = \max\left[(f_{hill} - 1)\,; 0\right] \Psi f_{amp} \tag{3.26}$$

$$f_{hill} = \begin{cases} 2e^{-11.09\alpha^2} & \text{if } \alpha \geq 0, \\ 2e^{-9\alpha^2} & \text{if } \alpha < 0. \end{cases} \tag{3.27}$$

$$f_{amp} = 1 - \max\left(f_t; f_l\right) \tag{3.28}$$

$$f_t = \tanh\left[\left(C_t^2 r_{dt}\right)^3\right] \tag{3.29}$$

$$f_l = \tanh\left[\left(C_l^2 r_{dl}\right)^{10}\right] \tag{3.30}$$

$$r_{dt} = \frac{\nu_t}{\kappa^2 d_w^2 \ \max\left(\sqrt{\dfrac{\partial U_i}{\partial x_j}\ \dfrac{\partial U_i}{\partial x_j}}\,; 10^{-10}\right)} \tag{3.31}$$

$$r_{dl} = \frac{\nu}{\kappa^2 d_w^2 \ \max\left(\sqrt{\dfrac{\partial U_i}{\partial x_j}\ \dfrac{\partial U_i}{\partial x_j}}\,; 10^{-10}\right)} \tag{3.32}$$

The grid dependent part, f_{hill}, is a function of the ratio d_w/h_{max} in a similar manner to f_{step}, indeed identically when $f_{step} < 1$. f_{hill} provides the shape function of $f_{restore}$, whereas the (locally varying) amplitude of $f_{restore}$ depends on the solution field, and is given by f_{amp}. This component is built of sensor functions for the viscous sublayer and for the modelled log law region, r_{dl} and r_{dt} respectively, which are analogous to the sensor function for the complete modelled turbulent boundary layer r_d from DDES (Eq. 3.20). Indeed, by comparing Eqs. (3.31) and (3.32) with Eq. (3.20), it can be seen that $r_d = r_{dt} + r_{dl}$. The parameters C_l and C_t are model-specific constants, which must be tuned such that f_{amp} is virtually zero when either f_t or f_l are close to unity. The values quoted by the authors [170, 149] are $C_l = 3.55$ and $C_t = 1.63$ for the Spalart–Allmaras model, and $C_l = 5.0$ and $C_t = 1.87$ for the Menter SST model. The grid-dependent part of $f_{restore}$ is shown in Fig. 3.9, where it can be seen that $f_{restore}$ is only active in the RANS simulation region, i.e. where $f_{step} = 1$.

The functions f_{step} and $f_{restore}$ are combined to give the WMLES length scale, Eq. (3.33), which is substituted into the background RANS model according to standard DES practice (Sect. 3.7.2).

$$L_{\text{WMLES}} = f_{step}\left(1 + f_{restore}\right) L_{\text{RANS}} + \left(1 - f_{step}\right) L_{\text{LES}} \tag{3.33}$$

The behaviour of the solution-dependent parameters and blending functions is pre-

sented together with a validation of the IDDES implementation for fully-developed channel cases in Part III.

Combination of WMLES and DDES functionality: IDDES

The combination of the hybrid model presented above with DDES is intended to allow "mixed mode" computations, for which the model must be capable of selecting the appropriate DDES or WMLES functionality for different flow regions. As such, the combined method can be considered as an extension to DDES allowing a wider range of flow types to be computed successfully, but with full backwards compatibility.

The authors of IDDES did not find a way of combining the original DDES length scale definition, Eq. (3.22), with the WMLES length scale, Eq. (3.33), and presented the reformulated $\tilde{L}_{\mathrm{DDES}}$ given in Eq. (3.34) [149]. This was demonstrated to be equivalent to the original.

$$\tilde{L}_{\mathrm{DDES}} = \tilde{f}_d L_{\mathrm{RANS}} + \left(1 - \tilde{f}_d\right) L_{\mathrm{LES}} \tag{3.34}$$

$$\tilde{f}_d = \max\left[\left(1 - f_{dt}\right); f_{step}\right] \tag{3.35}$$

$$f_{dt} = 1 - \tanh\left[\left(8 r_{dt}\right)^3\right] \tag{3.36}$$

The modified DDES length scale formulation can be combined with the WMLES length scale to give the IDDES length scale of Eq. (3.37).

$$L_{\mathrm{IDDES}} = \tilde{f}_d \left(1 + f_{restore}\right) L_{\mathrm{RANS}} + \left(1 - \tilde{f}_d\right) L_{\mathrm{LES}} \tag{3.37}$$

In regions of resolved turbulence, $r_{dt} \ll 1$ and $f_{dt} \approx 1$. This is the same behaviour shown by the DDES shield function, described in Sect. 3.7.4. Hence, $\tilde{f}_d = f_{step}$ and $L_{\mathrm{IDDES}} = L_{\mathrm{WMLES}}$. In the absence of resolved turbulence, $f_{restore} = 0$ and consequently $L_{\mathrm{IDDES}} = \tilde{L}_{\mathrm{DDES}}$. A demonstration of the behaviour of the IDDES length scale for a mixed-mode computation is presented in Part III, where a separating-reattaching internal flow is computed with a steady-state RANS inflow condition.

3.7.6 Other modifications to the DES formulation

A number of further modified DES formulations have been proposed by various authors, of which two shall be briefly described.

The Breuer et al. modification [18] and "EDDES" of Riou et al. [125, 126]

A direct comparison of SA-DES97 with Smagorinsky LES was conducted for the massively-separated flow over an inclined flat plate by Breuer et al. [18]. The DES was seen to exhibit very high levels of eddy viscosity in the separated shear layer

in comparison to the Smagorinsky model, which caused a delay in the development of resolved turbulent structures. This was attributed to two factors: Firstly, the definition of $\Delta = \sqrt[3]{\Delta_i\,\Delta_j\,\Delta_k}$ in the LES compared to $\Delta = \max(\Delta_i;\Delta_j;\Delta_k)$ for DES resulted in a much larger value of Δ for DES in the highly-stretched shear layer cells. Secondly, the f_{v1}, f_{v2} and f_w damping terms were observed to deviate from the asymptotic values expected far from the wall. A modification was hence proposed, whereby

$$\begin{aligned} \Delta &= \sqrt[3]{\Delta_i\,\Delta_j\,\Delta_k} \\ f_{v1} &= 1 \\ f_{v2} &= 0 \\ f_w &= 1 \end{aligned} \tag{3.38}$$

was set in the zone of LES-mode operation (i.e. when $C_{\mathrm{DES}}\Delta < d_w$). Indeed, the eddy viscosity levels and flow field in the early shear layer were seen to adopt the LES behaviour and the mean velocity and Reynolds stress profiles became more similar to those of the LES.

The same modification was later proposed by Riou et al. [125, 126], apparently independently, although in conjunction with DDES and similarly applied to the LES-mode region only. The method was baptised "extended DDES" (EDDES) and the same improvement in early shear layer resolved turbulence was reported.

These modifications are clearly intended to tackle the grey area issue, which is achieved with a certain degree of success. The extent to which these modifications to the damping functions can be generalised to DES based on different RANS models and indeed the necessity of this remains to be seen however. Furthermore, it is not entirely certain how the modification of the damping terms interacts with, overlaps with or indeed replaces the Ψ function[18]. It is also unclear why the value $f_w = 1$ is specified, and it indeed appears unjustified: As emerges from the analysis leading to the derivation of the Ψ function (see [158], Sect. 3.7.4 and Appendix D), the asymptotic (i.e. high ν_t) value $f_w^* = 0.424$ is derived for the LES-mode operation of SA-DES. Setting $f_w = 1$ in the LES mode region hence corresponds to lowering the effective Smagorinsky constant value. Furthermore, in normal RANS operation $f_w = 1$ occurs within the log law region of a boundary layer only, with the function reducing near the boundary layer edge finally tending to $f_w = 0$ in free shear flow far from the wall. In addition to the reduced effective C_S therefore, the application of these modifications exclusively to the LES-mode region hence gives rise to a discontinuity

[18] If the SA-model trip terms are not active (i.e. $f_{t1} = f_{t2} = 0$), the modification of Eq. (3.38) indeed causes a constant behaviour of the coefficient A of the Smagorinsky form of the model (presented in Appendix D).

of the solution field at the interface. This could be perceived as contradictory to the "non-zonal" philosophy of DES.

Alternative substitution of the DES length scale by Bush & Mani [22] and in the "X-LES" method of Kok et al. [76]

Two alternative hybrid RANS-LES methods have been proposed by Bush & Mani (2001) [22] and Kok et al. (2004) [76], which are closely related to DES in a number of ways. The first method was not given a name by its authors, and is hence referred to by their initials BM. The second method was called "extra-large-eddy simulation" and the corresponding acronym X-LES will be applied. These methods are both based on two-equation RANS models and both involve substitution of an analogy to the DES97 length scale in the dissipation term of the k-equation, ϵ_k, as follows:

$$\epsilon_{k,\,\mathrm{BM}} = \frac{k^{3/2}}{L_{\mathrm{BM}}} \tag{3.39}$$

$$L_{\mathrm{BM}} = \min\left(L_{\mathrm{RANS}}\,;\; C_{\mathrm{BM}}\Delta\right) \tag{3.40}$$

$$\epsilon_{k,\,\text{X-LES}} = \beta_k \frac{k^{3/2}}{L_{\text{X-LES}}} \tag{3.41}$$

$$L_{\text{X-LES}} = \min\left(\sqrt{k}/\omega\,;\; C_{\text{X-LES}}\Delta\right)\,. \tag{3.42}$$

The Bush & Mani hybrid length scale is clearly identical to the DES97 length scale, and hence $C_{\mathrm{BM}} = C_{\mathrm{DES}}$. The value for this constant was quoted as $C_{\mathrm{BM}} = 0.1$, although no detailed calibration study was carried out. In the case of X-LES, the hybrid length scale differs only due to a formulation issue: The parameter $\beta_k = 0.09$ of the TNT $k-\omega$ RANS model [75] upon which the method is based is not included in the RANS length scale definition given by Kok et al. [76], rather as a coefficient of the destruction term. This is however not a fundamental difference, as $C_{\text{X-LES}} = \beta_k C_{\mathrm{DES}}$. The authors calibrated $C_{\text{X-LES}} = 0.06$ against DIT, which hence corresponds to $C_{\mathrm{DES}} = 0.667$.

A common feature of both formulations, and a point where they differ from standard DES, concerns an additional substitution of the hybrid length scale in the expression for the eddy viscosity:

$$\nu_{t,\,\mathrm{BM}} = C_\mu L_{\mathrm{BM}}\sqrt{k} \tag{3.43}$$

$$\nu_{t,\,\text{X-LES}} = L_{\mathrm{BM}}\sqrt{k}\,. \tag{3.44}$$

It is readily shown that such a dual substitution gives rise to a subgrid-scale model of identical form to the k equation model of Yoshizawa [188] (See Eq. (3.12) in Section

3.5.1). In LES mode therefore, the auxiliary equation (for ε or ω) of the background RANS model is hence decoupled from the solution field. In both papers the possibility to obtain an identifiable SGS model in LES mode, not just under the assumption of local equilibrium[19], is touted as a particular advantage. Although perhaps elegant, it is however open to debate to what extent this represents an advantage: It cannot be stated that the SGS version of standard DES formulations is a priori worse than any "identifiable" SGS model[20].

This additional length scale substitution is not considered a sufficient criterion to differentiate these methods from DES: The precise formulation is left open in the method definition given by Travin et al. [171] (Sect. 3.7.1) and both methods appear to target the fourth hybrid RANS-LES ambition (for X-LES this is explicitly stated, whereas the Bush & Mani method is less clearly defined). Both methods however each include further features that serve to differentiate them from each other, as well as representing further differences to the standard DES formulation.

Beginning with the Bush & Mani formulation, a further additional feature concerns the filter width Δ. This extends the standard DES filter definition of Eq. (3.9) with additional terms based on the time step size, Δt:

$$\Delta_{\mathrm{BM}} = \max\left(\Delta_i\ ;\ \Delta_j\ ;\ \Delta_k\ ;\ |U|\,\Delta t\ ;\ \sqrt{k}\,\Delta t\right)\ . \tag{3.45}$$

This formulation is very interesting, as it seeks to include an indicator of the temporal filter width in the LES mode filter definition. The first Δt term is based on the local resolved velocity magnitude, whereas the second employs a velocity scale based on the subgrid turbulence. As such, a kind of CFL criterion is incorporated implicitly in the model, affecting both the filter width (and hence the level of sub-grid model activity) and the RANS/LES switching. The method will hence seek to counter the effects of time filtering, to be expected where an excessive time step is applied. These effects are not taken into account by standard DES formulations, which are based solely on the spatial filter size and assume that the user has selected an appropriate time step. The performance and behaviour of this feature has however not been demonstrated by the method's authors.

The final distinguishing feature of X-LES also concerns the filter definition. The authors here give preference to a fixed filter width defined by the user from case to case. Although this is termed explicit filtering, the application of an explicitly-defined filter kernel to the resolved field (Sect. 3.5) is not meant, rather a fixed value of Δ. This is motivated by a desire to seek grid-convergent solutions in the sense of separating the numerical and modelling problems. By keeping the Δ value fixed and refining the grid spacing, h, the numerical error should be diminished in such an approach. This was pursued in the investigation of Weinman et al. [179], however concrete

[19] Recall from Sect. 3.7.2 that the Smagorinsky model can be derived from the DES formulation under the assumption of a balance between production and destruction terms.

[20] As was pointed out by Prof. Strelets in his review of this manuscript.

conclusions were hard to construe. The practical advantages of this procedure are furthermore unclear, and it can be expected that a higher numerical cost results compared to DES with $\Delta = h$.

Part II

Methodology

4 Numerical flow solver

4.1 Introduction

The flow solver used in this investigation is the ISTA in-house solver "ELAN" (Elliptic Analysis of the Navier–Stokes equations), the foundation of which was laid by Leiping Xue in the framework of his PhD thesis [184]. Upon this basis a number of important extensions were implemented as reported in subsequent theses:

- The validation of a range of LES models and statistical averaging capabilities by Schmidt (2000) [144]
- Non-linear RANS models by Lübcke (2001) [84]
- Combustion models, multi-grid acceleration methods and DES simulations for aero-acoustic studies by Yan (2003) [185]
- Exploration of the grid deformation, turbulence modelling and DES capabilities for flow control by Schatz (2003) [141]
- Fluid–structure coupling, grid deformation and the implementation and validation of DES methods by Bunge (2004) [19]

Alongside these theses specific to the ELAN solver, general descriptions and analyses of related second order, finite-volume methods can be found in the literature. As examples the textbooks of Ferziger and Perić [44] and Patankar [106], the lecture course notes (in German) of Rung et al. [137] and the PhD thesis of Jasak [65] are cited.

Within the scope of this work, no fundamental modifications to the numerical methods or architecture of ELAN have been undertaken. Correspondingly, a summary level of detail will be given here with reference to precise descriptions elsewhere. Furthermore, the purpose of this chapter is to describe the numerical schemes employed in the investigation, not to give a complete account of all ELAN features. In particular, the incompressible mode of ELAN has been applied in all the test cases considered. The new or modified versions of DES implemented during the course of these studies are described in more detail in Chapter 5.

4.2 Discretisation

Discretisation transforms the underlying partial differential equations into a set of algebraic equations. The discretisation of the solution domain has been introduced in Section 3.1 together with an overview of the finite volume methodology. The

principal characteristics of the ELAN solver in this respect can be summarised as follows:

- Multi-block structured grids are used.
- Cell-centred discretisation: the variables are stored at the centre of each grid cell, as opposed to the vertices.
- The transport equations are formulated in a curvilinear coordinate system aligned with the grid, allowing body-fitted grids for complex geometries.
- Temporal discretisation is achieved with a specified time step, which is uniform throughout the domain.

All of the transport equations to be solved, including those of the turbulence models, can be expressed in a generic form consisting of a temporal derivative, a convection term (these can be combined to form the substantial derivative, Eq. A.1), a diffusion term and a source term. In Cartesian coordinates the generic transport equation is

$$\underbrace{\frac{\partial \rho\phi}{\partial t}}_{\text{temporal derivative}} + \underbrace{\frac{\partial \rho u_j \phi}{\partial x_j}}_{\text{convection term}} - \underbrace{\frac{\partial}{\partial x_j}\left(\Gamma_\phi \frac{\partial \phi}{\partial x_j}\right)}_{\text{diffusion term}} = \underbrace{S_\phi(\phi)}_{\text{source term}} , \tag{4.1}$$

where ϕ is the generic transported variable and Γ_ϕ and S_ϕ are the diffusivity coefficient[1] and source term of the variable, respectively. Each of these terms require specific discretisation methods, and those implemented in ELAN and applied in this work are described in the following.

4.2.1 Diffusion term

As can be seen from Eq. 4.1 the first derivative of ϕ on each of the cell faces is required to approximate the diffusive flux. These are modelled with a second order central approximation, whereby the diffusion normal to the face is treated implicitly and the cross diffusion explicitly.

4.2.2 Convection term

To determine the convective flux over the cell faces, the value of ϕ must be interpolated onto the cell faces with reference to the neighbouring cell centres. A number of interpolation schemes are available, the choice of which has a strong impact on the quality and robustness of the solution.

Central differencing scheme (CDS)

In CDS a simple linear interpolation of ϕ is applied drawing on the neighbouring cell centres. This scheme is of second order accuracy both on uniform and non-uniform

[1] Here ρ is considered to be incorporated into Γ_ϕ.

meshes [44] and exhibits very low numerical dissipation. However for convection-dominated flows on coarse meshes where the cell Péclet number[2] is large, CDS suffers from spurious oscillations [106].

For LES, where negligible numerical dissipation is required together with very fine grid resolutions to resolve the turbulent scales, CDS convection schemes are frequently used. The problems of unboundedness arise typically for RANS simulations where coarse grids are applied to modelled turbulence at high Reynolds numbers.

Upwind differencing scheme (UDS)

In such convection-dominated flows described above, it can intuitively be expected that the flow variables at the cell face are more strongly influenced by the upstream cell centre than by that lying downstream: this is the principle underlying upwind schemes. In the most simple of these, ϕ at the cell face is set equal to the value at the upstream cell centre. This has the advantage that boundedness of the solution is guaranteed, so the kind of spurious oscillations that CDS exhibits are not a feature of UDS. However, this stability comes at the expense of accuracy; UDS shows only a first order error reduction and is characterised by high levels of numerical diffusion. The numerical diffusion is furthermore magnified when the local flow direction is oblique to the grid orientation, which can be guaranteed to occur in all but the most simple of applications.

Total variation diminishing scheme (TVD)

Attempts to find a convection scheme that is both bounded and accurate have resulted in a number of more complex schemes than the basic UDS and CDS. Higher-order convection schemes are based upon interpolation using polynomials of higher order, for which the number of local extrema increase in proportion to the polynomial order. Higher-order convection schemes hence suffer from unboundedness, and techniques of limitation have been developed as a remedy. For example, the flux-limiting procedure of Boris & Book [12] creates differencing schemes that are higher than first-order accurate but without spurious oscillations. A methodology for oscillation-free flux-limited schemes is given by the notion of total variation diminution (TVD) introduced by Harten [59]. The TVD methodology can in principle be applied to many higher-order convection schemes.

In ELAN, the higher-order convection schemes are implemented using deferred correction of the basic UDS scheme, with a user parameter that specifies the precise scheme. All of these are however subjected to a TVD limiter, hence TVD is the most appropriate nomenclature for the family of higher-order schemes implemented in ELAN. These are of maximum third order accuracy, which is however reduced when the TVD limiter is activated. The TVD scheme is reported by Schatz [141]

[2] The cell Péclet number is a measure of the relative importance of convection to diffusion across a grid cell, $\mathrm{Pe} = u\Delta x/\Gamma_\phi$ (considering the x-direction).

and Bunge [19] to give the highest quality results for RANS simulations with ELAN. More details concerning the precise formulation are given by Xue [184] and Schatz [140].

Flux blending

An alternative attempt to trade off between accuracy and boundedness of the scheme has been proposed by Perić [107]. In this technique, known as flux blending, a linear blending between UDS and CDS is carried out in a ratio specified by the user. For each specific simulation, the user can therefore decide on the required amount of numerical diffusion to guarantee stability. Flux blending is applied uniformally throughout the solution domain. A localised variation of the flux blending parameter has been specifically developed for DES by Travin et al. [172], which is described in Section 5.4. For the ELAN implementation of the hybrid scheme however, the blending is between TVD and CDS rather than UDS and CDS.

4.2.3 Time discretisation

Second order backward differencing in time is applied, whereby values of ϕ at each new time step $(t+1)$ are determined from the values at the previous two time steps (t and $t-1$) according to

$$\left.\frac{\partial \phi}{\partial t}\right|_{t+1} = \frac{1}{2\,\Delta t}\left(3\phi^{(t+1)} - 4\phi^{(t)} + \phi^{(t-1)}\right) . \tag{4.2}$$

Because the temporal discretisation is implicit, a stable solution is guaranteed independent of the time step size. This is therefore adjusted such that a satisfactory temporal resolution of transient flow phenomena is achieved.

Source term

The source term is linearised and decomposed into a constant part and a component that is linearly dependent on ϕ. To preserve the diagonal dominance of the equation system for implicit solution, the constant of proportionality of ϕ should always be negative. In the case of a positive sign, the source term is handled explicitly. This procedure is particularly important for the turbulent transport equations, which exhibit strong dominance of the source term. Further comments on source term treatment are given by Patankar [106].

4.3 Pressure–velocity coupling

The discretised form of the incompressible Navier–Stokes equations exhibit linear dependence of velocity on pressure and vice-versa. This inter-equation coupling requires special treatment. A segregated approach is used, whereby the equations are solved sequentially rather than simultaneously. The procedure is based on the SIMPLE algorithm [72] with which the pressure is iterated to convergence using a pres-

sure correction. This method ensures mass conservation as the pressure equation is derived from the continuity equation. A generalised Rhie and Chow interpolation is used to avoid an odd-even decoupling of pressure and velocity with the collocated storage scheme applied [105].

Only the gradient of the pressure affects an incompressible flow; the absolute value is of no significance. In order to set the absolute value therefore, the pressure is fixed to a user-specified value (the choice of which is immaterial) at a single point in the solution field. This point should be located in a uniform, undisturbed flow region; near to the inflow boundary is usually a good choice for external aerodynamic problems.

4.4 Boundary conditions

Because the underlying flow equations are elliptic in character, all borders of the computational domain must be treated with appropriate boundary conditions corresponding to the flow case at hand.

Treatment of pressure

For all the boundary condition types considered, the pressure is treated in the same manner: a linear extrapolation onto the boundary condition plane is conducted and a zero-gradient boundary condition is applied to the pressure correction equation.

In the following, the treatment of the momentum and turbulence model equations at various boundary condition types will be described.

Inflow

At the inflow far field boundary the values of ϕ for the momentum and turbulence model equations to be solved must be specified. The specification of the individual components of u_i allows the variation of the global angle of attack or sideslip in external aerodynamic calculations. The correct specification of turbulence model parameters at the inflow boundary is for some applications far from trivial and can have a strong effect on the results. This matter has been examined and discussed in depth by Spalart & Rumsey [160] for the particular difficulties arising for external aerodynamic investigations. A uniform inflow boundary can be specified in ELAN with a single set of values, or alternatively a non-uniform profile can be read from an input file.

Outflow

At the far field exit planes of the flow domain a convective outflow profile is applied, which allows resolved turbulent structures to be transported out of the domain undisturbed [152]. The boundary condition is formulated as:

$$\frac{\partial \phi}{\partial t} + u_{mean} \frac{\partial \phi}{\partial n} = 0 \,, \tag{4.3}$$

where u_{mean} is the average convective velocity over the outflow plane and n is the component of x_i normal to the outflow plane. The derivative in the normal direction is determined to second order accuracy on the basis of the gradient in the cell centre adjacent to the outflow plane. The time derivative is also determined to second order accuracy as described in Section 4.2.3. In this way the value of ϕ can be determined at the exit plane.

Solid walls

The no-slip condition is effectively applied to the velocity components at solid walls[3], i.e. $u = v = w = 0$. This is however not carried out directly, rather by specifying the wall shear stress as an area force on the wall cell face [184]. For the turbulent quantities the hybrid-adaptive boundary condition as described in Section 3.4.4 and Appendix C, [135] and [145] is applied. This boundary condition seamlessly combines the standard low-Re and high-Re formulations allowing a flexible positioning of the first wall-normal grid vertex.

Symmetry

A symmetric boundary condition can also be applied, which treats each of the component boundary faces as a symmetry plane. This enforces flow tangential to the boundary face, resulting in zero flow across the plane. This boundary condition can hence be considered as equivalent to a frictionless (Euler) wall.

Periodicity

Periodicity can also be applied to a pair of parallel boundary planes of the same size and with the same point distribution; the flow conditions at each cell face are set equal to those at the corresponding face on the paired boundary plane. Unlike the symmetry plane, no restriction on through-flow or normal gradient is apparent. However the enforcement of periodicity between parallel planes in the flow can cause the amplification of harmonic modes and the attenuation of disharmonic modes that may occur. Depending on the flow in question, a suitable separation of the periodic planes (and sufficient resolution between these) must be ensured.

For a two-dimensional laminar, RANS or URANS simulation both symmetry and periodic boundaries can be applied to the domain extents in the homogeneous spanwise direction. If however a three-dimensional turbulence-resolving simulation is conducted, the symmetric condition would artifically damp the spanwise fluctuations of vortices near the boundary. The periodic boundary condition must therefore be applied in such cases.

[3] The components of velocity relative to the wall are referred to here.

4.5 Solution of the linear equation system

The discretisation methods described in the above sections lead to the construction of a linear equation system to solve for the unknown flow quantities in each grid block in an iterative manner. To this end, a three-dimensional extension by Xue [184] of the nominally two-dimensional strongly implicit procedure (SIP) of Stone [162] is used. The SIP solver is an incomplete lower–upper decomposition method specifically designed for algebraic equations that are discretisations of partial differential equations. The solver requires an ordered multi-diagonal solution matrix and is hence limited to structured grids. The linearised equation systems for each transport variable are solved sequentially to convergence using the SIP solver. The non-linear coupling of the equations is handled by a re-computation of the coefficient matrix following convergence of the SIP solver on all equations. The SIP solver iterations can hence be considered as inner iterations, and the computation of the coefficients as outer iterations.

5 Implementation of detached-eddy simulation

Having summarised the numerical background of the ELAN solver in Chapter 4, a more detailed description of the DES implementations will be given. The validation and calibration of some of these basic features will be presented in Chapter 7.

5.1 Preceding work

As is the case for the ELAN flow solver, initial implementations of DES were inherited from predecessors. The majority of the earlier implementation work was carried out by U. Bunge as reported in his PhD thesis [19], chiefly within the framework of the FLOMANIA project [55]. This included DES97 implementations based on the SALSA, LLR and CEASM models (Section 5.2) and the hybrid convection scheme of Travin et al. [172] (Section 5.4). These were tested on the stalled NACA0012 test case as well as on a range of oscillating bluff bodies. Early applications of DES to the study of flow control devices were reported by Schatz [141] and to aero-acoustic source simulation by Yan [185].

5.2 RANS models applied

The RANS models to which DES has been implemented are summarised in Tab. 5.1, together with the shorthand abbreviation with which they are referred to in this work. The archival literature references are also given in the table. The equations, functions and constants of each model are listed in Appendix B. The Lien–Leschziner $k-\varepsilon$ model is not applied for DES directly. It is included however as it serves as the background model for the CEASM.

5.3 Overview of implemented versions

A summary of the implemented DES versions is given in Tab. 5.2, in which the substituted length scale and the available DES versions (DES97, DDES or IDDES) are listed. The DES switch is implemented within the routine for each model, and the specification of the DES97, DDES or IDDES length scale is currently done by manual alteration of the source code.

Some of the results presented in Part III pre-date the implementation of the DDES shield or the Ψ functions for low-Reynolds number term correction. It will therefore always be stated whether the DES97, DDES or IDDES implementation has been applied. The Ψ function is here considered to be a component of DDES and IDDES, so

Model name	Transport variable(s)	Abbreviation	References
Spalart–Allmaras model with Edwards modification	$\tilde{\nu}$	SAE	Edwards et al. (1996) [39]
Strain-adaptive linear Spalart–Allmaras model	$\tilde{\nu}$	SALSA	Rung et al. (2003) [134]
Wilcox $k-\omega$ model	k, ω	WCX	Wilcox (1988) [181]
Local linear realisable $k-\omega$ model	k, ω	LLR	Rung et al. (1996) [136]
Lien–Leschziner $k-\varepsilon$ model	k, ε	LL	Lien et al. (1993) [81]
Compact explicit algebraic stress model	k, ε	CEASM	Lübcke et al. (2002) [85]

Table 5.1: Summary of RANS models applied for DES.

Model	L_{RANS}	DES97	DDES	IDDES
SAE	d_w	•	•	•
SALSA	d_w	•	•	
WCX	$\frac{k^{\frac{1}{2}}}{C_\mu \omega}$	•	•	
LLR	$\frac{k^{\frac{1}{2}}}{f_{\beta_k}\omega}$	•	•	
LL	$\frac{k^{\frac{3}{2}}}{\varepsilon}$			
CEASM	$\frac{k^{\frac{3}{2}}}{\varepsilon}$	•	•	•

Table 5.2: Overview of implemented DES versions.

these designations imply that the Ψ function is active (if required) unless explicitly stated otherwise.

5.4 Hybrid numerical convection scheme

As discussed in Section 4.2.2, CDS is often an acceptable choice for pure LES applications due to the fine grids required to resolve the turbulent scales. For RANS however, the unboundedness of CDS for high cell Péclet numbers results in spurious oscillations on the typically coarser grids and more stable upwind-biased schemes are practicable. These however prove to be too dissipative for LES.

It is clear therefore that DES (and indeed hybrid RANS-LES methods in general) place conflicting demands on the convection scheme. To address this problem, Travin et al. [172] proposed a form of locally-adaptive flux blending known as the hybrid convection scheme. Similarly to standard flux blending (Section 4.2.2), a weighting parameter $0 \leq \sigma \leq 1$ between upwind-based and central-based convection is applied to determine the the cell face values ϕ_f:

$$\phi_f = (1-\sigma)\,\phi_{f,\text{CDS}} \;+\; \sigma\,\phi_{f,\text{TVD}}\,. \tag{5.1}$$

In the ELAN implementation, blending is carried out between the TVD ($\sigma = 1$) and CDS ($\sigma = 0$) schemes, whereas the authors of the hybrid scheme blend between a third/fifth order upwind and fourth order central scheme. The local value of σ depends on Δ, ν_t, S^*, Ω^* and the convective time scale of the simulation $\tau = \ell_{ref}/u_{ref}$ and its formulation is given in Eq. (5.2)[1].

[1]Some typographical errors for the formulation of l_{turb} and C_{H3} were present in the original publica-

$$\sigma = \sigma_{max} \tanh\left(A^{C_{H1}}\right) , \qquad A = C_{H2} \max\left(\frac{C_{\mathrm{DES}}\,\Delta}{l_{turb}\,g} - 0.5\,;\,0\right) ,$$

$$l_{turb} = \sqrt{\frac{\nu_t + \nu}{C_\mu^{3/2} K}} , \qquad K = \max\left(\sqrt{\frac{S^{*2} + \Omega^{*2}}{2}}\,;\,\frac{0.1}{\tau}\right) ,$$

$$g = \tanh B^4 , \qquad B = \frac{C_{H3}\,\Omega^* \max\left(S^*\,;\,\Omega^*\right)}{\max\left(\frac{S^{*2} + \Omega^{*2}}{2}\,;\,10^{-20}\right)} ,$$

$$\sigma_{max} = 1 , \qquad C_{H1} = 3 , \qquad C_{H2} = 1 , \qquad C_{H3} = 2 . \tag{5.2}$$

This empirically-formulated blending function applies CDS to fine grid regions with resolved turbulent content (sensed as higher vorticity and lower strain), and UDS to coarser grid regions or regions of irrotational flow. This has been demonstrated in a comprehensive parameter study of the scheme conducted by Bunge [19]. As such, CDS is only applied to regions where LES is possible and desirable, with TVD used elsewhere. The importance of applying CDS for LES is demonstrated in Section 7.1 and the correct functionality of the hybrid convection scheme is demonstrated for DES computations in Section 7.2 (also reported by Mockett et al. [97]). In a further confirmation of the scheme's functionality, near-identical spectra were obtained using the hybrid scheme in comparison to CDS for calculations of decaying isotropic turbulence (DIT) [19, 21].

5.5 Model-specific implementation details

5.5.1 Calibration of the DES model parameter C_{DES}

The parameter C_{DES} has been calibrated for each model using DIT. The method is described in Sect. 6.1 and some example calibration spectra are given with an accompanying analysis in Section 7.3. The calibrated and implemented values of C_{DES} are listed in Tab. 5.3 for each model.

	SAE	SALSA	WCX	LLR	CEASM
C_{DES}	0.65	0.60	0.70	0.75	0.65

Table 5.3: Calibrated values of the C_{DES} parameter for each model. (In the case of WCX-DES the value for the standard length scale substitution in the destruction term of the k equation is given.)

tion [164], and the correct formulation is presented here.

5.5.2 Ψ functions

The problem of the unwanted activation of RANS-model low-Reynolds number terms in LES mode has been described in Chapter 3 together with the remedy proposed by Spalart et al. [158] in the form of the Ψ correction function. The necessity of such a function depends on the specific formulation of the RANS model in question. For those applied in this study, such an analysis has been carried out and is detailed in Appendix D. The analysis and derivation is based upon the sub-grid scale form of the model and its comparison to the Smagorinsky model, for which a coefficient A is derived. If A is constant, no correction term is necessary and $\Psi = 1$ can be applied. If however A is not constant, a function Ψ must be sought to correct this. The coefficients A and correction functions Ψ derived for each considered model are listed in Tab. 5.4.

For the LLR and CEASM models, the complexity of the expression A is such that the derivation of a corresponding Ψ remains elusive. The implications of this are analysed in Sect. 7.4, and a demonstration of the functionality of the derived corrections is given.

5.5.3 Alternative DES length scale substitutions

Some alternative means of substituting the DES length scale, L_{DES}, in different expressions of the background RANS model have been investigated. For this, three alternative formulations of WCX-DES are implemented, which are referred to as DES1, DES2 and DES3 depending on the terms in which L_{DES} is substituted (described in Section 8.3 and by Yan et al. [186]). As part of the investigation, the values of C_{DES} were calibrated for each variant using DIT and the implemented values are summarised in Tab. 5.5.

5.5.4 Specific features of the CEASM-DES implementation

The DES implementation for the CEASM model exhibits some particular features that warrant further description. The first of these concerns the choice of RANS model length scales to be substituted by L_{DES}, and the second is a model-specific shield formulation for the prevention of grid-induced separation (GIS – Section 3.7.3). Details of this formulation have also been published by Bunge et al. [21].

The formulation of the LL $k-\varepsilon$ model [81], the background model used in the CEASM, is given in Appendix B. The LL $k-\varepsilon$ model is based on the idea of two-layer models [127] and as such includes the wall normal distance d_w in addition to the RANS model length scale given in Tab. 5.2. The wall normal distance appears in the damping terms f_μ and $\tilde{C}_{\varepsilon 1}$ and is hence not substituted by L_{DES} in order to avoid the erroneous activation of these terms in the LES-mode region.

The availability of the wall-normal distance in the model furthermore allows the formulation of a GIS-shield following the methodology introduced by Menter &

Model	A	Ψ^2
SA	$\frac{C_{b1}\, f_{v1}}{C_{w1}\, f_w}\, \frac{\tilde{S}}{S^*}$	$\min\left[10^2\,;\, \frac{1}{f_{v1}} - \frac{f_{v2}\, C_{b1}}{f_w^*\, f_{v1}\, \kappa^2\, C_{w1}}\right]$
SAE	$\frac{C_{b1}\, f_{v1}}{C_{w1}\, f_w}\, \frac{\tilde{S}}{S^*}$	$\min\left\{10^2\,;\, \left[\frac{\max(f_{v1}\,;\,10^{-10})}{\max(\chi\,;\,10^{-10})} + f_{v1}^2\right]^{-1}\right\}$
SALSA	$\frac{f_{C_{b1}}\, f_{v1}}{f_{C_{w1}}\, f_w}\, \frac{\tilde{S}}{S^*}$	$\min\left\{10^2\,;\, \left[\frac{\max(f_{v1}\,;\,10^{-10})}{\max(\chi\,;\,10^{-10})} + f_{v1}^2\right]^{-1}\right\}$
WCX	$\left(\frac{C_{\omega 2}}{C_{\omega 1}}\right)^{3/2}$	1
LLR	$\left[\frac{f_1}{f_{C_\mu}^{3/2}\, f_{\beta_\omega}}\left(f_{C_1} - \frac{f_{C_\mu}\, S^*}{\omega}\right)\right]^{2/3}$	—
LL	$\left(\frac{\tilde{C}_{\varepsilon 2}\, f_\mu\, C_\mu}{\tilde{C}_{\varepsilon 1}}\right)^{3/2}$	$\min\left\{10^2\,;\, \left[\frac{C_{\varepsilon 2}\, \tilde{C}_{\varepsilon 1}}{\max(f_\mu\,;\,10^{-10})\, \tilde{C}_{\varepsilon 2}\, C_{\varepsilon 1}}\right]^{3/2}\right\}$
CEASM	$\left(\frac{\tilde{C}_{\varepsilon 2}\, f_\mu\, f_{C_\mu}}{\tilde{C}_{\varepsilon 1}}\right)^{3/2}$	1

Table 5.4: Overview of coefficients of the Smagorinsky form, A, and the implemented low-Reynolds number correction functions, Ψ.

	DES1	DES2	DES3
Calibrated C_{DES}	0.70	0.95	0.90

Table 5.5: Calibrated values of C_{DES} for the alternative length scale substitution formulations of WCX-DES (Section 8.3, [186]).

Kunz [92]. The GIS-shield employs exclusively variables and functions already present in the background RANS model and is formulated as follows:

$$\epsilon_k = k^{3/2} \max\left\{ \frac{1}{L_{\text{RANS}}} \; ; \; \frac{1}{C_{\text{DES}}\Delta}\left[1 - \tanh\left(A_{L-\nu}^2\right)\right] \right\}$$

$$A_{L-\nu} = \max\left(2\frac{k^{3/2}}{d_w\,\varepsilon}; \frac{\nu\, k}{d_w^2\,\varepsilon} \right) . \tag{5.3}$$

This shield function is validated in Section 7.5 for a simple flat plate boundary layer flow. The development of the function was shortly followed by the publication of the generally-applicable DDES method with an equivalent functionality ([158], described in Section 3.7.4). As a result, the CEASM-DDES formulation has since superceded that of Eq. (5.3) in the ELAN implementation.

5.5.5 IDDES implementation

The IDDES method [170, 149], described in Section 3.7.5, has been implemented on the basis of the SAE and CEASM methods as indicated in Tab. 5.2.

The modified formulation of the filter width Δ, Eq. (3.23), requires the wall-normal grid spacing h_{wn} and hence information at every grid cell as to which grid index direction is the closest to being normal to the nearest wall. To avoid case-specific and tedious user input a sensor has been implemented that compares the wall normal distance of each cell vertex. In this manner, the wall-normal index direction is determined as that for which the vertices exhibit the greatest difference in wall-normal distance.

Additionally, the IDDES blending function $f_{restore}$ contains two model-specific parameters C_l and C_t. These must ideally be tuned for each model such that f_{amp} is close to zero when either f_l or f_t are close to one. These parameters affect the model performance only in the limit of a pure RANS solution, where $f_{restore} \neq 0$ would distort the RANS model behaviour. As such, for the purposes of initial testing the values published by Travin et al. [170, 149] for the Spalart–Allmaras and Menter SST models have been employed for the SAE and CEASM models respectively. For the former case, it is not expected that the published values will be too incorrect as the models are highly similar. In the latter case however it is doubtful that the published

values would be appropriate. Therefore, to consider the implementation complete and to ensure that the model performs correctly in the full RANS limit, C_l and C_d must be specifically tuned for the SAE and CEASM model implementations.

6 Description of test cases

In this final chapter of the methodology, the test cases employed in the investigations of Part III will be described. Collating the test case descriptions in a dedicated chapter is considered preferential to a grouping of descriptions together with the results, as the investigations are structured thematically and results from some cases are employed in multiple sections.

For each test case, an overview of the flow-physical features will be given, together with a description of the benchmark data and relevant references. The important numerical parameters, grids and setup issues will also be reported, together with an overview of any special post-processing techniques. Where relevant, any known limitations on the comparability of the benchmark data with simulations will also be reported. Finally, a list of publications where the results from each test case can be found will be given.

6.1 Decay of isotropic turbulence

Decaying isotropic turbulence (DIT) represents mathematically the simplest conceivable realisation of turbulent flow, and is therefore a fundamental test case for new turbulence modelling or simulation techniques. In DES, a RANS model is modified to provide LES functionality and this test case is central to the assessment of the LES capability of the implementation. The motivation of this case can be summarised as follows:

- DIT represents a basic and readily-verifiable test, at minimal computational cost, of the capability of the model/solver combination to *resolve* turbulent structures and to predict the energy cascade.
- The formulation of DES includes the empirical parameter C_{DES} that must be calibrated. DIT offers a basis for this.
- The level of numerical dissipation within a given solver can be established. In cases where this is excessive, steps must be taken to reduce it (Sect. 3.5.2).

Demonstration of these basic LES capabilities and calibration of new model constants are considered an essential prerequisite to the implementation of a hybrid RANS-LES method. Although analytical methods may exist to derive the values of subgrid-scale model parameters (e.g. the expressions for C_{DES} as a function of C_S and other RANS model parameters derived in Appendix D and discussed in Sect. 8.2), these can in some cases be self-contradictory (as discussed in Sect. 8.3 and [186]). Furthermore, such derivations do not take numerical dissipation into account.

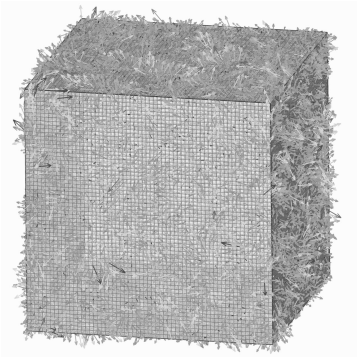

Figure 6.1: Visualisation of the decaying isotropic turbulence test case (velocity vectors are shown on the surface of the 3D, periodic grid). The data is taken from the DNS of Jiménez et al. [69] re-sampled to 64^3 control volumes.

In addition to the primary goals of demonstrating LES capability and calibrating parameters, a variety of secondary uses can be exploited. These include the demonstration of the functionality of model features (e.g. the derived Ψ functions, Sect. 7.4) and a measure of the dissipation of the numerical scheme using a "no-model" test (Sect. 7.1).

Despite, or perhaps owing to its simplicity, real isotropic turbulence is seldom found in nature or practical applications. It is also a very difficult flow state to approximate in a wind tunnel. Nonetheless, its usefulness as a computationally-inexpensive and canonical turbulent flow for the purposes stated above is not diminished. Investigations based on this test case have been published in Bunge et al., 2003 [20], Bunge et al., 2007 [21], Haase et al., 2006 [55], Haase et al., 2009 [56], Michel et al., 2007 [93], Mockett & Thiele, 2007 [99], Mockett et al., 2008 [96] and Yan et al., 2005 [186].

Flow description

The isotropy of the flow means that statistical quantities are invariant to coordinate system rotations, and as a consequence the statistical field is also homogeneous (invariant to a shift in the coordinate system). This flow is hence often referred to as decaying isotropic homogeneous turbulence, although the adjective "homogeneous" is redundant. The isotropy also eliminates the existence of any mean flow shear, the mechanism by which turbulence is produced[1]. As a result of the lack of energy input combined with the dissipative action of the turbulent cascade (Section 2.2), the energy level decays with time.

[1]The production term of the turbulence kinetic energy equation is $P_k = -\overline{u_i u_j}\frac{\partial \overline{U_i}}{\partial x_j}$.

Benchmark data

A range of alternative benchmark data is available for DIT, with various advantages and disadvantages. The experiment by Comte-Bellot & Corrsin [30], referred to as CBC in this work, was conducted at a Reynolds number too low for an inertial subrange to exist in the energy spectra (Sect. 2.3). Experiments also have the general disadvantage that the three-dimensional, unsteady velocity field cannot be measured. As a result, the initialisation velocity field for the simulation must be generated using an inverse Fourier transform of the upstream energy spectra. Although exhibiting the correct spectral distribution, such a velocity field does not contain physically valid spatial correlations. This disadvantage is alleviated by using DNS data as a benchmark, such as that of Wray [183, 69]. The CBC data was employed in earlier DIT investigations with the Wray DNS data adopted for later studies. No significant difference was observed in the basic spectral analysis that would lead to a change in the calibrated values of C_{DES}.

Energy spectra are available for the CBC experiment at stations corresponding to the non-dimensional times of 0, 0.87 and 2.0. Spectra for the DNS data are available at many different time steps, however those at the non-dimensional times of 0.19938, 1.79940 and 3.03694 were chosen for comparison, as these correspond closest to values rounded to the nearest 0.1 units.

Grids and numerical setup

The simulation of DIT is conducted in a cubic computational domain with three pairs of periodic boundary conditions in each spatial direction, to reflect the homogeneity of the flow. In experiments, the turbulence is generated at an upstream station by a grid, and the measurement reference frame moves with the mean convective velocity downstream to capture the decay of the turbulence. A coordinate transformation from space to time is conducted for the simulations, such that the computational box is considered to be transported with the mean velocity. The experimentally spatial decay of turbulence is therefore tracked temporally in the simulation; the initial solution field is set with a suitable instance of isotropic turbulence, the decay of which is then solved in an unsteady manner.

The grids employed were all equidistant and cubic, with external dimensions of 2π and varying grid resolutions of 16^3, 32^3 and 64^3 cells. The lowest and highest resolved wavenumbers[2] corresponding respectively to the largest and smallest resolved scales are therefore 1 and $N_x/2$. The time step was 0.01 non-dimensional units in each case, which was found to deliver CFL $\ll 1$ throughout the domain and at all time steps. For all DES simulations, pure LES mode of the model was enforced by setting $L_{\mathrm{DES}} = L_{\mathrm{LES}}$ and the central difference convection scheme (Sect. 4.2.2) was applied unless stated otherwise.

[2] $\kappa = 2\pi/x$, Sect. 2.3.

Field initialisation

The velocity field for the solution initialisation was obtained from the benchmark data, either by inverse Fourier transform of the CBC experimental spectra or by truncation of the DNS field to the desired grid resolution in the case of the Wray data[3]. For the inverse Fourier transform, a tool written by St. Petersburg Technical University (SPTU) [148] was provided in the framework of the FLOMANIA and DESider projects. To obtain the remaining solution quantities (pressure and turbulence model parameters), a steady-state computation of "frozen turbulence" was carried out by holding the velocity field fixed. In this manner, the initial subgrid eddy viscosity is obtained by the model to be calibrated and this step must therefore be repeated for every model variation. In earlier work [20, 19], the initial eddy viscosity was obtained using the explicit Smagorinsky model. This however has the disadvantage that the calibration result depends on the value of C_S chosen, which is undesirable. Following convergence of the frozen turbulence calculation, a restart file is produced that can be used to initialise the unsteady decay computation.

Post processing

The complete velocity field was output at selected time steps corresponding to the non-dimensional times of 0.87 and 2.0 in the case of the CBC-based computations, and 0.2, 1.8 and 3.0 for the Wray DNS-based computations. Turbulence energy spectra as a function of wavenumber, $E(\kappa)$, were computed from these using the SPTU three-dimensional Fourier transform tool mentioned above.

6.2 Fully developed turbulent channel flow

The fully-developed turbulent channel flow is a very useful canonical test case for wall-bounded flows. The test case is employed in Part III for the examination and validation of WMLES using the IDDES method. Such results from this test case have been published in Mockett & Thiele, 2007 [99], Mockett et al., 2008 [96] and Haase et al., 2009 [56].

Geometry and flow conditions

The physical background of fully-developed turbulent channel flow has been summarised in Section 2.4. The fully-developed flow between two parallel flat plates of infinite extent in the streamwise (x) and spanwise (z) directions is considered. The channel half-height in the perpendicular (y) direction is denoted δ, by which all spatial coordinates are normalised. The coordinate origin is placed at the lower wall in

[3] It has since been noted that this simple truncation gives rise to an aliasing effect, whereby spurious energy is superimposed on the highest resolved wavenumbers. In very recent work, this has been countered by employing a suitable filtering operation, however all DIT based on the Wray benchmark data presented in this work is affected by aliasing. Thankfully, this was not seen to modify any of the conclusions and it was not considered necessary to repeat the computations.

the normal direction, such that the upper wall is at $y = 2\delta$. In the streamwise direction the origin is at the entry of the numerical domain.

The flow is driven by a streamwise pressure gradient dp/dx, which is balanced by the wall shear stress, τ_w. Consideration of this force balance gives the following relationship:

$$\frac{dp}{dx} = \frac{\tau_w}{\delta} \,. \tag{6.1}$$

The test case is defined such that $\tau_w = 1$ and $\delta = 1$, as a consequence of which the pressure gradient $dp/dx = 1$ is applied. The density is specified as $\rho = 1$, as a result of which the wall-friction velocity (Section 2.4) is $\overline{U}_\tau = 1$. The desired skin friction Reynolds number, Re_τ, is hence applied by setting the molecular viscosity to $\nu = 1/\mathrm{Re}_\tau$.

Benchmark data

For lower Reynolds number cases, DNS data is considered preferential to experimental measurements as the latter include many sources of uncertainty (e.g. the influence of side walls and limited aspect ratio, intrusive measurement techniques and the difficulty of obtaining well-resolved data very near to the wall). The DNS database of Moser, Kim & Mansour, 1999 [100] is employed for $\mathrm{Re}_\tau = 395$ and $\mathrm{Re}_\tau = 590$, and the more recent DNS of Hoyas & Jiménez, 2006 [63] is used for $\mathrm{Re}_\tau = 2000$. For higher Reynolds numbers for which no DNS data are available, the empirically-tuned correlations described in Section 2.4.2 are used.

Grids and numerical setup

The computational domain size specified for the mandatory grid in the DESider project channel flow test case [56] has been used[4], which extends to $L_x = 6.4\delta$ and $L_z = 3.2\delta$, respectively. This slightly exceeds the typical values used for fully-resolved LES quoted in Section 3.5.

Two families of grids have been applied, as depicted in Fig. 6.2; one set of wall-refined grids with a stretched point distribution applied to the wall-normal cells, and an equidistant, cubic grid. For the wall-refined grids the tangential point distributions of the DESider project grid have been used with 64 equidistant cells in both directions. This results in a resolution of $\Delta x = 0.1\delta$ and $\Delta z = 0.05\delta$, the streamwise-elongated cells conforming to standard LES practice in cases where the mean flow direction is known (Section 3.5). The wall-normal resolution has been adjusted to deliver $\Delta y^+ \approx 1$ at the wall for each Reynolds number with low stretching ratios between $1.137 \leq k \leq 1.150$. The cubic grid by contrast has a resolution of $\Delta x = \Delta y = \Delta z = 0.05\delta$, whereby the halving of the streamwise grid cell size with respect to the wall-refined grids has been introduced to represent more general sit-

[4]The channel flow test case within DESider was coordinated by L. Davidson of Chalmers University.

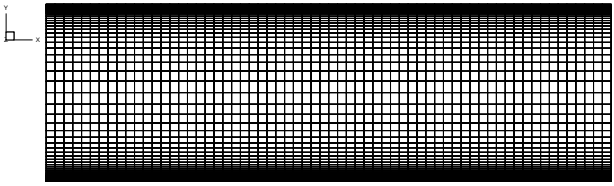

(a) WR-4000

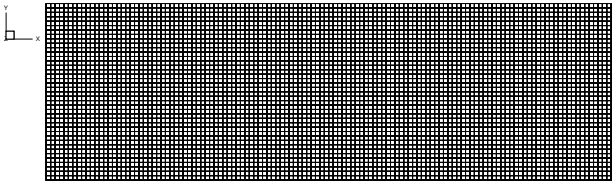

(b) C-4000

Figure 6.2: Cross-section through the x/y plane of a wall-refined (WR) and cubic (C) grid.

uations in which the mean flow direction is not known at the grid generation stage. The grid properties together with the computational case names are summarised in Tab. 6.1.

The values of the grid cell sizes in wall units are determined from the distance between neighbouring cell vertices. Because a cell-centred solver is used, the distance of the first cell centre to the wall is in fact half of the $\Delta y^+|_{y=0}$ value quoted in Tab. 6.1. It is unclear however, whether the requirement of $\Delta y^+|_{y=0} \leq 0.5$ should be applied to the nearest cell centre to the wall in such solvers. To investigate this, a refined version of the WR-18000 grid has been generated that conforms to this requirement and no effect on the results was observed.

Periodic boundary conditions are applied in the streamwise and spanwise directions, with no-slip walls (as described in Section 4.4) at the channel plates. The cubic grid is intended to investigate the applicability of the hybrid-adaptive wall boundary condition ([135, 145] and Appendix C) in combination with WMLES simulations. The driving pressure gradient is applied in the form of a corresponding pressure difference between the periodic boundaries in the streamwise direction. A constant pressure difference is superimposed on the pressure fluctuations arising from the resolved turbulence of the simulation.

For the numerical convection scheme, pure CDS (Section 4.2.2) was applied in all cases. The time step size was specified with the goal of delivering CFL < 1 through-

Case:	Re_τ:	N_x:	N_y:	N_z:	N_{xyz}:	Δx^+:	Δz^+:	$\Delta y^+\|_{y=0}$:	$\Delta y^+\|_{y=\delta}$:	k:
WR-395	395	64	50	64	204800	39.5	19.75	2.25	50	1.138
WR-4000	4000	64	80	64	327680	400	200	2.25	524	1.150
WR-18000	18000	64	108	64	442368	1800	900	2.25	2193	1.139
C-590	590	128	40	64	327680	29.5	29.5	29.5	29.5	1.000
C-4000	4000	128	40	64	327680	200	200	200	200	1.000
C-18000	18000	128	40	64	327680	900	900	900	900	1.000
C-100000	100000	128	40	64	327680	5000	5000	5000	5000	1.000

Table 6.1: Summary of channel flow test cases and corresponding grid properties.

out the domain[5]. The time step required was estimated based on the centreline velocity and the streamwise grid spacing including a safety factor. The approximate expressions of Pope [116], Eqs. (2.24) and (2.25), were used to obtain a value for the expected mean centreline velocity at each Re_τ. Following the establishment of a fully-developed flow state, the CFL number was inspected to ensure that the targets had been met, and in some cases adjusted accordingly.

Field initialisation

The specification of the initial field is of central importance in LES and WMLES computations of channel flow. If a smooth mean flow profile is used without any spatial fluctuations, a quasi-laminar profile arises in the case of LES [144] or a RANS solution results from the IDDES method [170, 149]. The superposition of simple white noise has been demonstrated by many investigators to be inadequate (e.g. by Schmidt, 2000 [145]), as the fluctuations decay too rapidly.

The approach used to initialise the channel flow simulations in this work (in the absence of a suitable restart field from a previous simulation) involves a combination of the mean velocity profile from a two-dimensional precursor RANS simulation with fluctuations derived from isotropic turbulence. The isotropic turbulence data was obtained from the 64^3 truncated field of the Wray DNS simulation [183], which was used to initialise the DIT simulations (described in Section 6.1). By mapping the homogeneous turbulence from its equidistant Cartesian grid to the wall-refined channel grids, a qualitative similarity to the real flow is achieved with stretched vortices near the wall and near-spherical vortices in the core flow. This method proved satisfactory as a source of sustainable velocity fluctuations.

Post processing

Following the field initialisation or a simulation restart with a modified setup, the temporal development of $\overline{U}_\tau$ and the bulk velocity, $\overline{U}_b$, were monitored throughout each computation. Statistical analysis was only conducted following the establishment of a fully-developed flow state with the initial transient behaviour eliminated.

The entire field was output at regular time intervals, which could be selected for post processing following examination of the temporal evolution described above. Reynolds averaging (Section 3.4.1) with respect to time and both homogeneous directions was carried out using a purpose-written Fortran tool[6]. In addition, the instantaneous WMLES blending functions of the IDDES calculations were output at an arbitrary wall-normal location to analyse the functionality of the models.

[5] The CFL number is discussed in Section 8.6.
[6] Based on that written by A. Carnarius, TU-Berlin.

Limitations on comparability with benchmark data

No limitations on the comparability with the DNS benchmark data are anticipated, as the benchmark DNS computations all exhibit sufficient spatial resolution and statistical convergence. The DNS computations are similarly carried out using a periodic domain in the streamwise and spanwise direction meaning that no geometric uncertainties arise. The Reichardt correlation [118], applied for the higher Reynolds numbers and described in Section 2.4, does however include some uncertainty. The parameters of the expression were calibrated based on what must by now be considered as outdated experimental data. The Reichardt correlation can therefore only be interpreted as a guideline for approximate comparison. The same reservation applies to the empirical correlations of Dean [34] and Pope [116]; as mentioned in Section 2.4, these can only be considered as accurate as the experimental data upon which they are based and considerable scatter is apparent.

6.3 NACA0012 airfoil in deep stall

The first three-dimensional test of the DES method was conducted on the flow around a symmetric NACA0012 airfoil profile at very high angles of attack [148]. Due to the apparently promising improvement in the results and relatively low numerical cost, this test case subsequently became the focus of cross-validation efforts for the implementation of DES in many CFD solvers. A good example of such use was the European FLOMANIA project [55], in which the first DES implementations in ELAN were also compared [19, 94]. The time-averaged lift and drag coefficients were obtained in experiments published by Hoerner [62]. No unsteady information is available experimentally at such high angles of attack, and important details such as the aspect ratio of the airfoil in the experiment are unknown.

However, from the evidence of subsequent studies in the DESider project [56] (which were based on the initial investigation of Guenot [54]), it appeared as if the absolute agreement with experimental force values was due to a "cancellation of errors" effect arising from an insufficient spanwise simulation domain. This effect is described in detail in Part III.

Despite this lack of comparability with experiment, the results obtained from this test case allow some important insight into the basic LES/RANS activity of DES solutions (Sect. 8.1.2) and a comparison of different DES length scale substitutions (Sect. 8.3).

The symmetric NACA0012 airfoil exhibits a 12% thickness-to-chord ratio, and has been studied here at the high angle of attack $\alpha = 60°$. A depiction of the geometry and coordinate system (with origin at the profile nose) is shown in Fig. 6.3. The incompressible flow around the profile is of Reynolds number $\mathrm{Re}_c = |U|_\infty c/\nu = 1 \times 10^5$. All quantities reported are normalised by the chord length, c, and the free stream velocity magnitude $|U|_\infty$.

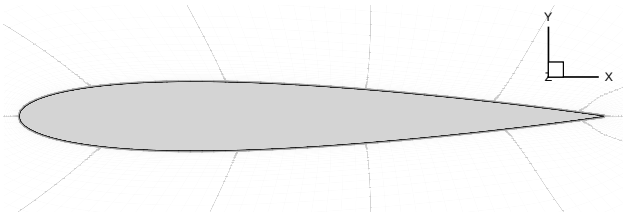

Figure 6.3: Schematic of geometry and coordinate system for NACA0012 test case.

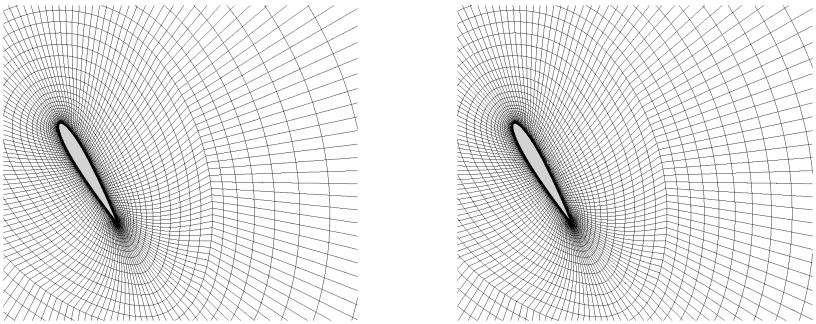

(a) Coarse (b) Medium, fine

Figure 6.4: Near field views of numerical grids used for the NACA0012 test case (slices normal to the spanwise, z, direction). The medium and fine grids differ only in the spanwise resolution.

The numerical grids used were provided by M. Shur and M. Strelets of St. Petersburg Technical University (SPTU) to the partners of the FLOMANIA project. Three refinement levels were computed, with 201600, 268800 and 324800 control volumes on the coarse, medium and fine grids respectively. All grids were of the same O-topology, and exhibit a uniform distribution of approximately cubic cells in the near wake "focus region" [154]. Detailed information on the grids is given in Tab. 6.3, and a visual comparison is depicted in Fig. 6.4.

The far field domain boundary is circular, and situated at a distance of $L_r/2$ from the airfoil. Depending on the angle of attack, an appropriate segment of arc length around 60° is allocated as an inflow boundary condition, and the remainder of the far field boundary is designated outflow. The surface of the airfoil is treated as a no-slip wall boundary, and the grid resolution is sufficient for full resolution to $y^+ = 1$ everywhere. The boundary conditions in the spanwise direction are periodic. For all

Grid	N_r	N_θ	N_z	N_{tot}	L_r	L_z	Δ_z
Coarse	60	140	24	201600	$30c$	$1c$	$0.0417c$
Medium	80	140	24	268800	$30c$	$1c$	$0.0417c$
Fine	80	140	29	324800	$30c$	$1c$	$0.0345c$

Table 6.2: Details of the SPTU grids for the NACA0012 test case. N_r, N_θ and N_z respectively denote the cell numbers in the radial, circumferential and spanwise directions, and the L values are the total numerical domain size in these directions (i.e. distance from boundary to boundary, not from geometry to boundary).

computations, the numerical time step size was set to $0.025c/|U_\infty|$.

6.4 NACA0021 airfoil in deep stall

Following the initial studies on the NACA0012 airfoil detailed above, a search was conducted for a set of experimental data that included unsteady quantities. No such data was found, however a detailed experimental campaign by Swalwell et al. [167, 166] was found for the thicker NACA0021 profile at a slightly higher Reynolds number of $\mathrm{Re}_c = 2.7 \times 10^5$. This data was collected as part of an investigation of wind turbine blade stall, and involves long time series of force component data obtained from arrays of surface pressure sensors scanned at a high sampling rate. It was therefore decided to adopt this test case instead of the NACA0012 for the extensive computations conducted in the European DESider project [56]. Results for this test case have been published in Braza et al. [56], Bunge et al., 2007 [21], Michel et al. [93], Mockett & Thiele, 2007 [97], Mockett et al., 2008 [96], Swalwell [166] and Weinman et al. [179] (although in the last publication a different set of grids was employed).

Apart from the profile thickness and Reynolds number, essentially the same investigation was carried out as for the NACA0012 profile, so only information that differs from the NACA0012 case will be given here. In contrast to the FLOMANIA investigation, only the deep stall attitude of $\alpha = 60^\circ$ was studied. The geometry and coordinate system of the NACA0021 profile is shown in Fig. 6.5.

The computational grid was again prepared by the St. Petersburg group of Profs. Shur and Strelets, and was based on the same O-topology construction as for the NACA0012. Results from a grid with a spanwise domain extent of $1c$ are reported here. Following the findings of Guenot [54] that a spanwise domain extent of $1c$ was insufficient for the NACA0012 test case at $\alpha = 45^\circ$, no comparison with experimental data is presented[7]. Details of the grid computed with the ELAN solver are given in Tab. 6.4. A two-dimensional view of the grid is given in Fig. 6.6.

[7] A grid with an extended spanwise domain of $3.24c$ was also computed within the DESider project [**?**].

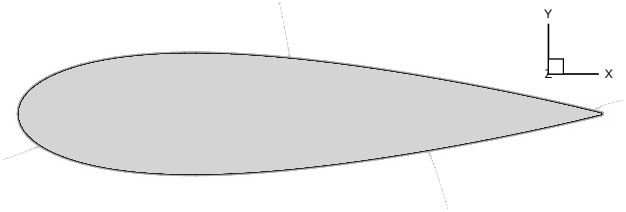

Figure 6.5: Schematic of geometry and coordinate system for NACA0021 test case.

Grid	N_r	N_θ	N_z	N_{tot}	L_r	L_z	Δ_z
NTS	100	140	34	476000	$30c$	$1c$	$0.0294c$

Table 6.3: Details of the NTS grid for the NACA0021 test case. The quantities have the same meaning as those in Tab. 6.3.

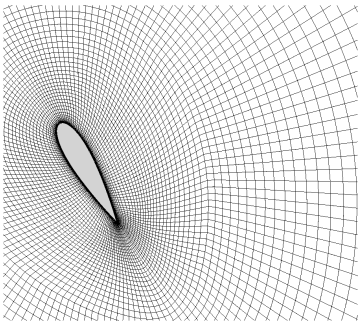

Figure 6.6: Near field views of the numerical grid used for the NACA0021 test case (slice normal to the spanwise, z, direction).

6.5 Circular cylinder in a square channel

As described in Section 2.5, circular cylinders have long served as canonical test cases for bluff body aerodynamics. The highly unsteady, massively separated turbulent wake that occurs at high Reynolds numbers represents a significant challenge to CFD methods. The particular case computed in this study has been selected for two principal reasons. Firstly, very detailed unsteady experimental data are available, which have been obtained using state of the art non-intrusive techniques. Secondly, the relatively confined experimental domain can be directly reproduced in the simulation, thereby eliminating some of the typical sources of uncertainty in CFD–experimental

comparison. Indeed, the provision of a useful database for the validation of numerical methods was one of the key aims of the experiment, and the test case has been employed as such during the European FLOMANIA [55] and DESider [56] projects.

The test case is therefore employed for the validation of DES working at its "design condition", namely massively separated bluff body flows, as is presented in Section 8.5. An investigation of time step sensitivity, Section 8.6, is also based on this case. Published results include a validation of the numerical method by Mockett et al. [97, 98] as well as in the framework of a joint numerical and experimental study of the flow physics by Perrin et al. [110, 112]. Other publications employing these results less centrally in an overview role include Michel et al., 2007 [93], Mockett & Thiele, 2007 [97], Mockett et al., 2008 [96], as well as the recent review paper of Spalart [156].

Geometry and flow conditions

A visual impression of the cylinder and channel geometry can be obtained from Fig. 6.7, in which the axis system for the test case is also depicted. The cylinder is enclosed within the square channel, which it traverses symmetrically at the channel mid height. As a result of the confining channel, the cylinder aspect ratio (span / diameter) is fairly low at 4.7 and the blockage coefficient (cylinder diameter / channel height) is relatively high at 0.208. This arrangement is in stark contrast with the majority of experimental cylinder investigations, in which a simulation of "infinite conditions" is targeted using a low blockage coefficient, a high aspect ratio and often elaborate end-plates at the cylinder fixture to the wind tunnel side walls. The anticipated effects of these geometric constraints are described in the literature review, Section 2.5.2.

The channel is $22D$ long and situated in an open-jet wind tunnel. The channel inflow is located $7D$ upstream of the cylinder, and measurements have confirmed that the velocity of the open jet is uniform across the channel inlet with a turbulence intensity of $Tu = 1.5\%$ [108]. The coordinate system has its origin at the centre of the cylinder at the mid span position.
The Reynolds number of 140000 is realised with respect to the inlet velocity $u_\infty = 15\text{m/s}$, cylinder diameter of $D = 0.14\text{m}$ and kinematic viscosity of $\nu = 1.5 \times 10^{-5}$ m^2/s. Through experimental observation of the drag coefficient variation with Re [108], the flow has been seen to exhibit behaviour corresponding to the precritical regime, TrBL0, at the beginning of the drag crisis (described in Section 2.5.2). This occurs at a lower Re than that quoted in the literature, which is due to the effects of the inflow turbulence intensity and the channel blockage (as described in Section 2.5.2).

Experimental data

The principal experiments of this cylinder flow were conducted at the Institut de Mécanique des Fluides de Toulouse (IMFT) [108, 109, 110, 111] with some accompa-

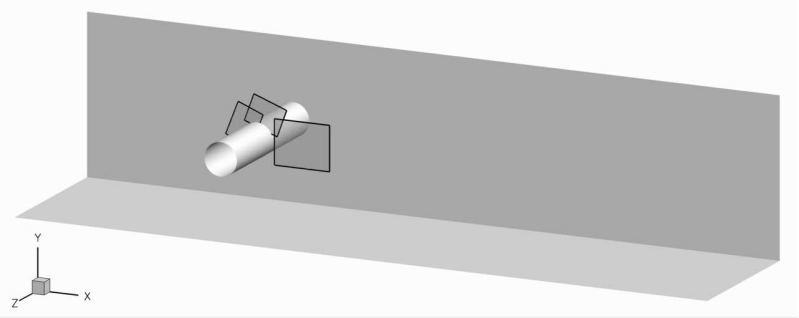

Figure 6.7: Geometry of the cylinder flow domain including representation of the PIV measurement planes.

nying earlier studies carried out at the Institut de Recherche de l'Ecole Navale de Brest (IRENav) [37] on an equivalent configuration in a water tunnel. The following data were acquired:

- Unsteady pressure measurements at a number of locations around the circumference of the cylinder at the mid-span plane.
- Two-component (2C) particle image velocimetry (PIV) measurements at the planes shown in Fig. 6.7, providing uncorrelated snapshots of the u and v velocity field.
- Three-component (3C) stereoscopic PIV at the same measurement planes providing uncorrelated snapshots of u, v and w.
- 3C time-resolved PIV (TRPIV) providing the u, v and w fields with a high sampling rate of 1kHz (giving a maximum resolved frequency of $\mathrm{St} = fD/2u_\infty = 4.67$ observing the Nyquist condition [104]).
- Time-resolved single point laser Doppler anemometry (LDA) measurements with a high sampling rate at discrete points within the PIV planes (from the IRENav investigation).

An excellent agreement between the TRPIV and LDV spectra as well as between the TRPIV and low-frequency PIV fields was demonstrated [110], which suggests a high degree of fidelity of the measurements. For a more detailed report of the experimental apparatus, the quoted references should be consulted.

Grid and numerical setup

The entire experimental domain, including the cylinder and all four walls of the surrounding channel have been directly reproduced in the numerical domain, shown in

Fig. 6.8. No-slip boundary conditions have been applied on all walls, and the hybrid adaptive wall boundary condition described in Section 3.4.4 has been exploited to save grid points by using a large value of y^+ on the less important channel boundary layers whilst fully-resolving the cylinder boundary layer with $y^+_{max} \leq 1$.

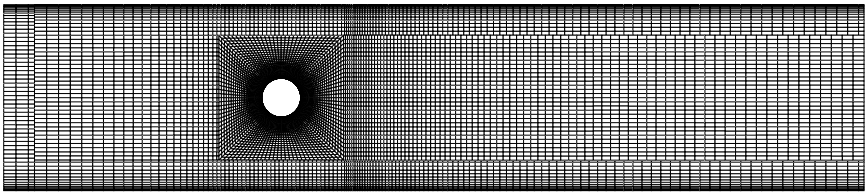

(a) Complete domain, every second point omitted.

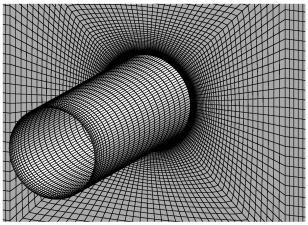

(b) Zoom of cylinder region, every second point omitted.

Figure 6.8: Flow domain and numerical grid for the cylinder in a square channel.

The resulting grid consists of some 5 million volumes, with a high circumferential resolution of 240 uniformly spaced cells applied to the cylinder and 96 in the spanwise direction. The spanwise spacing is uniform along the central portion of the cylinder and compressed towards each wall within a region of one diameter from each end. The spacing of the uniform section has been matched to that of the other grid directions in the focus region of the near wake to give roughly cubic cells here in accordance with DES grid guidelines [154]. The grid was generated by J. Yan during his occupation as a research assistant at ISTA, and was made available to the DESider consortium [56] for comparative computation within the project.

The inflow plane, situated at the same location as the channel entrance in the experiment, is assumed to be far enough upstream of the cylinder for unsteadiness effects to be negligible. As such, a steady uniform velocity profile is applied here. It was found that placing the inflow boundary condition directly at the channel entrance caused convergence problems. The solution adopted was to add a short inflow section of five cells upstream of the channel entrance, to the sides of which a symmetry

boundary condition was applied in the y and z directions.

The time step size used for the validation test case is 3×10^{-4}s, which corresponds to roughly $0.03D/u_\infty$ or a Strouhal sampling frequency of $\mathrm{St} = D/(2\,\Delta t\,u_\infty) = 15.6$ (observing the Nyquist condition [104]). A variation of the time step size was also studied with the additional value of $\Delta t = 5 \times 10^{-4}$s computed. The majority of the simulations were run using 32 CPUs on the IBM pSeries 690 supercomputer at the HLRN (see Acknowledgements). Each time step was found to achieve satisfactory numerical convergence of at least two orders of magnitude in the residua after roughly 12 inner iterations. Following the establishment of a fully-developed flow state, a minimum physical time of 4.2s or $450D/u_\infty$ was computed for statistical analysis in each case.

Data capturing and post processing

Much of the post-processing necessary for the comparison with the experiments was conducted by R. Perrin, during his post-doctoral research work at ISTA. Because he was also responsible for the collection and analysis of the experimental data at IMFT, it can be said that exactly the same post-processing methods were applied to both data sets, thereby enhancing the directness of the comparison.

The circumferential distribution of mean and RMS pressure coefficient has been obtained for both the simulation and the experiment. The mean experimental drag coefficient was estimated by integration of the mean pressure on the cylinder at the mid-span position, assuming homogeneity of the flow on a significant spanwise portion and neglecting the contribution of the viscous forces. In the simulation, the drag has been calculated both as in the experiment as well as over the entire cylinder including pressure and friction components[8]. An evaluation of the experimental assumptions on the basis of the numerical simulations is therefore possible.

For the PIV data, global averaging has been carried out using about 3000 instantaneous fields. These can be considered uncorrelated in time due to the low sampling rate, and uncertainties have been determined to the order of 2% [110]. Concerning the simulation, global averaging has been performed on the entire domain during the calculation, giving access to information about the homogeneity of the flow in the spanwise direction and wall effects. As is reported in Sect. 8.5, the mean flow field can be considered uniform in the spanwise direction within a region greater than $1D$ from each side wall. To further improve the statistical convergence, additional averaging of the computational field was conducted in the spanwise direction within the homogeneous region.

[8] The sectional drag coefficient is denoted C_d, whereas the drag coefficient integrated over the entire span is denoted C_D.

For the analysis of unsteady flow features, the computed flow field has been stored every time step on a 2D slice located at the mid-span position $z = 0$ corresponding to the PIV and TRPIV measurements. Point velocity spectra have been computed from the time-resolved experimental and numerical data using Welch's averaged periodogram method [180].

The nearly periodic nature of the vortex shedding in the wake enables the use of phase averaging to characterise the unsteady mean motion and the turbulence quantities. This method allows the classical decomposition of the flow into a mean part, a quasi-periodic fluctuation and a random fluctuation, which can be written as $u_i = \overline{U_i} + \tilde{u}_i + u_i''$ [122]. The phase-averaged motion is then defined as $\langle U_i \rangle = \overline{U_i} + \tilde{u}_i$. A more detailed description of phase averaging is given in Appendix F. An earlier technique employed to obtain the phase angle φ required to conduct the phase averaging involved the use of the surface pressure on the cylinder upstream of the separation point as a trigger signal. Due to the large spatial separation between the trigger signal point and the wake field, this however gave rise to a residual periodic component in the random fluctuations (known as "phase jitter"). A much more precise separation of the periodic and random fluctuations was achieved when the phase angle was defined using the coefficients from a proper orthogonal decomposition (POD) of the velocity field to be averaged, as described in detail by Perrin et al. [110]. This phase averaging technique was applied to both the numerical (for the $\Delta t = 3 \times 10^{-}4$s case only) and experimental velocity fields, with roughly 170 fields averaged for each phase angle in the case of the experiment, and 90 for the simulation. From the simulation a two-dimensional slice through the entire domain at $z = 0$ was output every time step for the purposes of phase averaging and unsteady analysis. The simulation therefore doesn't suffer from the limited spatial coverage of the PIV windows used in the experiments.

Limitations on the comparability between CFD and experiment

The inlet turbulence intensity of $Tu = 1.5\%$ measured in the experiment unfortunately represents a serious limitation on the comparability with simulation[9]. The cylinder flow at such precritical Reynolds number has been demonstrated to be highly sensitive to free stream turbulence (FST), as is outlined in Sect. 2.5.2, with strong effects seen at such levels. Furthermore, a measurement of the length scale is not available, which is necessary for a full description of the FST.

Including FST effects, even with knowledge of the length scale, presents both RANS and LES simulations with difficulties: In a pure RANS, the problem of a non-physical decay between the inlet and cylinder gives rise to difficulties in the specification of suitable inlet values of the turbulence parameters [160]. Having overcome this, the effect of the FST on the sensitive transition processes would require a well-calibrated and dedicated model for transition and lies outside the scope of RANS models. For

[9] Attention was drawn to this important fact by C. Norberg.

LES, the problem is partly one of the specification of physically-realistic resolved inlet turbulence, and partly one of numerical expense (the inlet fluctuations must be resolved well all the way to the cylinder). In any case, for the DES computation with steady-state inlet conditions used here, it cannot be expected that the FST effect is accounted for correctly.

6.6 Separating-reattaching flow over a bump in a rectangular duct

This test case was conceived within the DESider project [56] with the intention of providing a particularly challenging combination of flow phenomena:

- Turbulent boundary layer separation from a smoothly curved surface, making the prediction of the separation location very sensitive to modelling errors.
- A shallow separation, as opposed to the "massive separation" of the bluff body flows, for which the grey area problem concerning the transition from modelled to resolved turbulence (Sect. 3.7.3) can be expected to be particularly influential.
- Flow reattachment, the position of which should prove highly sensitive to the level of predicted turbulent shear stress in the separated shear layer (and hence the grey area issue).
- The reattachment and recovery region, in which resolved turbulence impinges upon the wall boundary layer. This would require WMLES capability of the hybrid RANS-LES model, which is not one of the target applications of natural DES (Sect. 3.6).
- A high Reynolds number, such that pure LES computations would be unfeasibly expensive.
- A low aspect ratio allowing the computation of the complete domain including side walls, hence eliminating problems associated with the experimental approximation of infinite spanwise conditions.

As such, the test case intentionally casts DES outside of its intended application range, thereby demonstrating weaknesses in various areas and allowing the effect of improvements to be assessed. Within this work, the case is employed to investigate the model dependency of DES (Sect. 8.4.2) and to assess the predictive accuracy of DDES and IDDES in comparison with experimental data (Sect. 8.7). To avoid repetition, the figures concerning this test case are presented separately in Appendix G, to which both aforementioned sections refer **CHECK THIS!**. Results from the bump test case have been published in Haase et al. [56], Mockett et al. [96] and Mockett & Thiele [99].

Geometry and flow conditions

The duct is rectangular, of height $H = 0.28\,\mathrm{m}$ and width $W = 0.5\,\mathrm{m}$ and constricted to half its height by a bump mounted on the lower wall. The geometry of the bump was designed by Y. Egorov and F. Menter of Ansys Inc. employing precursor RANS and URANS computations using their CFX solver, with the goal of achieving the desired flow phenomena outlined above. An early indication of the high sensitivity of the flow was given by the strong model dependency of the RANS solutions in these preliminary calculations [4]. A hyperbolic tangent geometry was decided upon for the downstream bump curvature, given by

$$h = H_b \left[\tanh\left(\tan(\alpha) \frac{L_b - x}{H_b} \right)^{\beta} \right]^{1/\beta}, \tag{6.2}$$

where $H_b = 0.138\,\mathrm{m}$ is the bump height, $L_b = 0$ is the position of the end of the bump, $\alpha = 35^\circ$ is the slope angle of bump and $\beta = 5$ is a shape contour exponent. The upstream, contracting portion of the bump is a straight ramp with smoothed intersections to the channel floor and the bump plateau. The bump geometry included in the computational domain is shown together with the coordinate directions in Fig. 6.9. The coordinate origin is located at the downstream end of the bump in the spanwise symmetry plane.

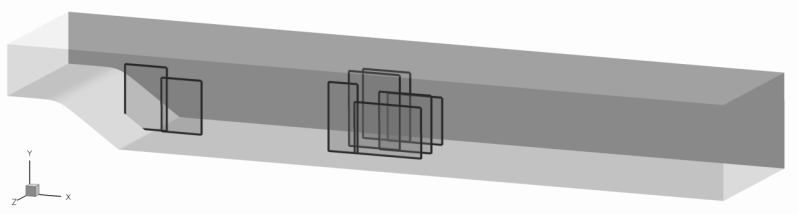

Figure 6.9: Geometry of the bump flow domain including representation of the PIV measurement planes.

The fluid employed was water of density $\rho = 997\,\mathrm{kg/m^3}$ and a dynamic viscosity of $\mu = 0.89 \times 10^{-3}\,\mathrm{Pa\,s}$. The Reynolds number based on the bump height and the bulk velocity above the bump is $\mathrm{Re}_b = 1.044 \times 10^6$.

Experimental data

The experimental data for this test case was collected during a measurement campaign at ONERA in the course of the DESider project. The THALES water tunnel at ONERA Toulouse was employed, into which the bump model was mounted. The data acquisition consisted of:

- 90 pressure tappings arranged in three parallel lines (along the x-direction) at $z = -0.170\,\text{m}$, $z = -0.085\,\text{m}$ and $z = 0.0\,\text{m}$.
- Unsteady pressure tappings at four locations along the bump and downstream wall.
- Laser Doppler velocimetry (LDV) measurements across the entire plane intended to represent the entry plane in the computations, $x = -0.367\,\text{m}$.
- LDV measurements along the symmetry plane, $z = 0$.
- PIV measurements at various planes normal to the spanwise direction, depicted in Fig. 6.9. These were located in the region of the separation and downstream of the reattachment point. The downstream planes were at three spanwise locations, $z = -0.125\,\text{m}$, $z = 0.0\,\text{m}$ and $z = 0.125\,\text{m}$.

The PIV measurement planes at $z = \pm 0.125\,\text{m}$ were intended to allow an assessment of the spanwise homogeneity and symmetry of the flow.

More details on the experimental setup, data acquisition and post processing are given by Aupoix et al. [4].

Grid and numerical setup

The computational grid was generated by Ansys Inc. and set as a mandatory mesh for the DESider participants. The grid consists of around 3.9×10^6 volumes, with 220, 120 and 150 cells in the streamwise, vertical and spanwise directions, respectively. The boundary layers are refined appropriately for low-Re boundary conditions (Sect. 3.4.4) and a relatively fine and isotropic grid spacing is evident throughout the channel around the separated region. The streamwise grid spacing is coarsened gradually after around two bump heights downstream of the bump foot in order to limit the computational expense. A collection of visualisations of the grid are shown in Fig. 6.10.

The inlet and outlet of the computational domain were located at $x = -0.367\,\text{m}$ and $x = 2.0\,\text{m}$, respectively. To specify the flow at the inlet, a precursor computation including the upstream convergent ramp portion of the bump was conducted by Ansys Inc., using a DRSM. The goal of this was to provide common inlet profiles for all partners as well as to match the experimental inlet data as closely as possible. Very good agreement between the Ansys inlet data and the LDV measurements was achieved, except for the spurious vortical structures apparent in the experiment, which are discussed later. Some visualisations of the Ansys inlet plane are given in Fig. 6.11, showing the relatively thin boundary layers (i.e. the flow is far from fully-developed) as well as the secondary flow predicted by the DRSM. A weak secondary flow is apparent in the inflow channel core, whereas the corner vortex structures inside the boundary layers are strong by comparison. The bulk velocity in the stream-

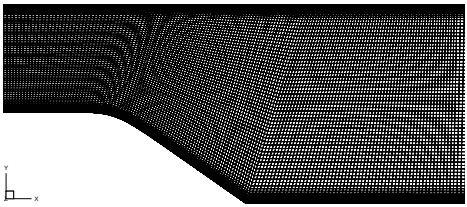

(a) z slice in vicinity of bump

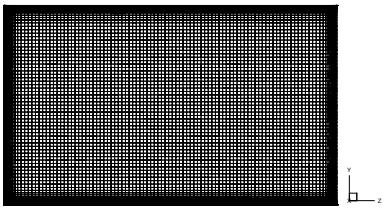

(b) x slice downstream of bump

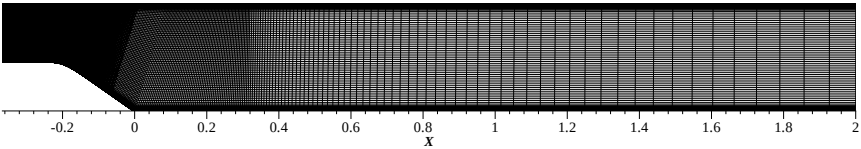

(c) z slice through entire flow domain

Figure 6.10: Depictions of the grid at various slices through the domain.

wise plane, upon which the Reynolds number is based, is $U_b = 6.751\,\mathrm{m/s}$.

All computations employed the hybrid convection scheme (Sect. 5.4, [172]), and a time step of either $\Delta t = 8 \times 10^{-4}\,\mathrm{s}$ or $\Delta t = 5 \times 10^{-4}\,\mathrm{s}$ was used. The computations were conducted in parallel on 16 CPUs of the HLRN's IBM p690 series supercomputer. DES computations were initialised either from precursor RANS simulations or from existing DES solutions. An initial transient period was simulated before commencing the statistical analysis. Quantities are not non-dimensionalised for this case, unless explicitly stated.

Data capturing and post processing

The entire flow field was Reynolds averaged, allowing the examination of the mean field and resolved as well as modelled Reynolds stress data throughout the domain. The time-averaged pressure distribution was obtained at the walls together with pressure time traces at the locations of the experimental unsteady transducers.

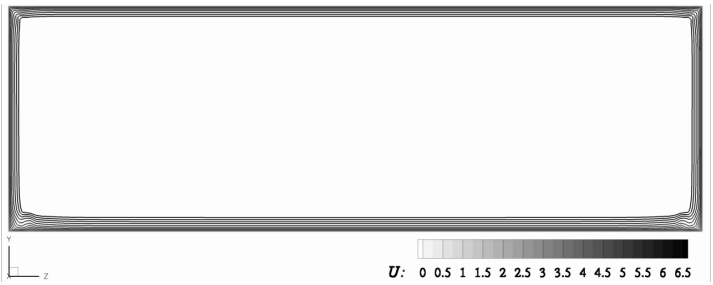

(a) Contours of U

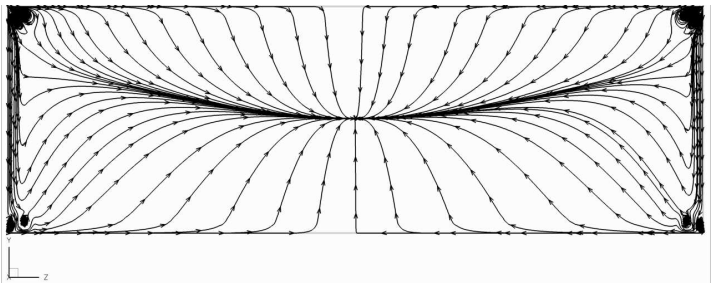

(b) Cross-flow streamlines

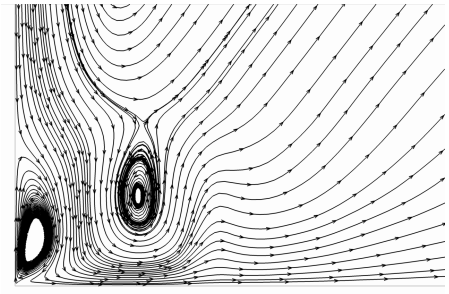

(c) Cross-flow streamlines, zoom in corner region

Figure 6.11: Visualisations of the flow imposed at the domain inlet. Cross-flow streamlines are integrated using the tangential V and W components only.

To compute the pressure coefficient, the same reference velocity of $U_{ref} = 4\,\mathrm{m/s}$ used in the experiment was applied. The pressure reference point was chosen at $x_{ref} = 0.01\,\mathrm{m}$ at the z position currently considered.

Limitations on the comparability between CFD and experiment

The limitations of the comparability between CFD and experiment are based on two principal sources of uncertainty concerning the experimental data [4]:

- The LDV and PIV measurements at the same locations show some degree of disagreement in the separated region. This is relatively minor for the $\overline{U}$ component, but unfortunately significant for the vertical $\overline{V}$ component. The Reynolds stresses also show relatively strong disagreement, whereby the turbulence levels of the PIV are lower than those given by LDV, particularly in regions of high turbulence levels. The published account of the experiments places a greater level of trust in the LDV measurements, stating that this technique will be pursued in future campaigns [4].

- Spurious localised velocity defects coinciding with increased turbulence levels are evident in the LDV inflow plane measurements. These are believed to represent streamwise vortical disturbances and occur near the side wall boundary layer edges, outside of the upper and lower boundary layers. Their origin is not fully understood, although it may be that they are propagated from upstream technical installations. The vortices do not appear in the precursor RSM calculation of Ansys, which apart from this otherwise give very good agreement with the experimental inlet plane.

As a result, only the LDV profiles are plotted in the comparison with CFD, as these are considered more reliable. It is unclear to what extent the neglected streamwise vortices in the inflow plane will affect the computational results.

Part III

Validation, demonstration and analysis

7 Validation of the implementation

In this chapter, results will be presented and discussed that serve to demonstrate key functionality and correct implementation of certain features of the DES components of ELAN. The results are based primarily on simple test cases before more complex flows are considered in Chapter 8.

7.1 Influence of the numerical convection scheme

The basic numerical convection schemes were described in Section 4.2.2, where it was noted that the choice of scheme has a strong impact on the accuracy and robustness of the solution. The LES-mode operation of DES corresponds to a classical or explicit LES (see Section 3.5), for which SGS models are derived under the assumption that the dissipative behaviour of the fine, unresolved scales is prescribed in its entirety by the model. It is therefore essential to establish the validity of this assumption for the underlying numerical implementation in order to demonstrate the fundamental LES capability of the solver and to establish the most suitable numerical parameters.

One method of investigating this issue is based on the simulation of decaying, isotropic turbulence (DIT). The physics of the turbulent cascade and the energy spectrum have been introduced in Sections 2.2 and 2.3 respectively, and background information concerning the simulation of DIT can be obtained together with implementation details from Section 6.1. In the usual computation of DIT, the performance of subgrid models can be investigated for a particular Reynolds number, for which it is assumed that the following components constitute the total level of dissipation ε_{tot}:

$$\varepsilon_{tot} = \varepsilon_{\mathrm{SGS}} + \varepsilon_{\nu} + \varepsilon_{num} \ , \tag{7.1}$$

where $\varepsilon_{\mathrm{SGS}}$, ε_{ν} and ε_{num} represent the SGS model, molecular and numerical contributions to the dissipation, respectively. In order to isolate ε_{num}, the SGS model is deactivated and the molecular viscosity is set to zero. The criterion to assess whether $\varepsilon_{num} = 0$ is obtained from theoretical considerations of the energy cascade process of inviscid turbulence. In the absence of dissipation and in the presence of a spectral truncation at high wavenumber (i.e. a finite grid resolution), the flow can obtain a state of absolute statistical equilibrium with an equipartition of energy over wavevectors. The energy spectrum then has the form $E(\kappa) \propto \kappa^2$ (see e.g. Kraichnan, 1967 [78]). For flow initialised with an arbitrary spectral energy distribution, the κ^2 behaviour begins at the highest wavenumbers, progressing to lower wavenumbers and feeding on their energy content. This behaviour has been clearly demonstrated in a DNS study by Cichowlas et al., 2005 [29], where an inertial range exhibiting $E(\kappa) \propto \kappa^{-5/3}$ exists at low wavenumbers with the $E(\kappa) \propto \kappa^2$ at high wavenumbers

serving as a form of virtual viscous dissipation. Such use of this theoretical result for a test of the energy conservation of a numerical scheme was proposed by Benhamadouche & Laurence, 2002 [10].

DIT has been computed on the basis of the Wray benchmark DNS data starting from an initial velocity field that reproduces the turbulent $E \propto \kappa^{-5/3}$ distribution of the inertial subrange at the highest resolved wavenumbers. The numerical grid of 64^3 control volumes was used, upon which the initial field was truncated from the 512^3 DNS data[1]. Fig. 7.1 shows the turbulent energy spectra arising at various time steps for "no-model" inviscid simulations using the CDS, UDS and TVD schemes.

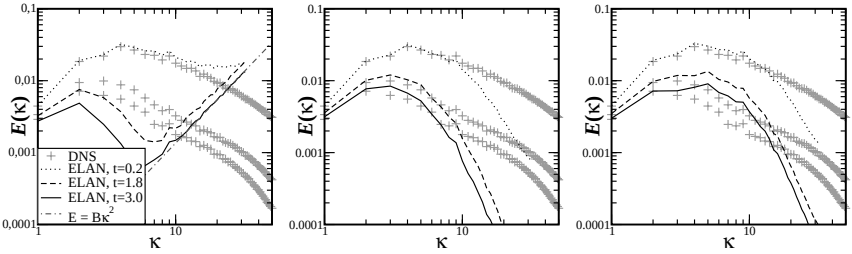

(a) CDS (b) UDS (c) TVD

Figure 7.1: Energy spectra for "no-model" solutions of DIT with different convection schemes, $\nu = 0$, 64^3 grid, Wray DNS benchmark data [183].

It can be seen for CDS that the high wavenumbers indeed begin to turn upwards with time to approach the κ^2 gradient, and that this behaviour spreads to successively lower wavenumbers. It therefore appears as if the numerical dissipation of the CDS convection scheme is negligible, at least for the orthogonal and equidistant grid used here. On the basis of this evidence, an indication is given of the numerical suitability of the ELAN solver for LES when CDS is applied. It must be acknowledged that this test alone falls short of a full demonstration of kinetic energy conservation of the numerics, for which further tests such as temporal energy conservation for inviscid Taylor–Green vortices would be of value [10, 86].

The spectra returned by UDS and TVD show the opposite behaviour – the high wavenumber motion is damped very strongly by UDS and slightly less so by TVD, with energy levels much lower than the benchmark data returned. Even though no SGS model was active in these simulations, it can be seen that ε_{num} is greater than the ε_{SGS} that an appropriate model would provide. The UDS and TVD convection

[1] The problem of aliasing in the initial velocity field, outlined in Sect. 6.1 is of no consequence here.

schemes must therefore not be employed in conjunction with LES.

For an impression of the adverse impact of dissipative upwind-biased schemes on the LES of more complex flows, reference is made to the study of channel flow by Breuer [17]. A higher-order upwind scheme caused a strong deterioration of the solution quality in an analogous manner to a strongly excessive value of the Smagorinsky parameter. Second order CDS in contrast produced good agreement with benchmark DNS.

Finally, some consideration will be made of cases where weak numerical dissipation is present, such that the high wavenumber spectral exponent falls short of the $E(\kappa) \propto \kappa^2$ but still exceeds $\kappa^{-5/3}$. A good candidate for such behaviour would for example be flux blending with a small percentage of UDS (Sect. 4.2.2). In such cases, a reduced model dissipation could in principle be added to match the benchmark spectral behaviour. Such balancing of numerical and model dissipation could indeed prove of use in solver architectures where a weak residual numerical dissipation cannot be eliminated. The expectation is that such a setup would perform well in detached flow regions, however problems would be expected in the near wall region in a pure LES context: The wall damping effect (Sect. 2.4) reduces the turbulent dissipation to zero and the spurious presence of ε_{num} in addition to ε_ν becomes critical. In the context of DES or WMLES however, the balancing of numerical and model dissipation could indeed prove to be a viable and pragmatic approach.

7.2 Functionality of the hybrid convection scheme

The hybrid scheme of Travin et al. [172] has been implemented in order to resolve the conflicting demands placed by the RANS and LES modes on the numerical convection scheme. The importance of this in particular for the LES mode region has been demonstrated in Section. 7.1. The motivation of the scheme and its formulation are described in Section 5.4. The functionality of the hybrid convection scheme for DES of massively-separated flows is demonstrated using the cylinder and NACA0021 cases.

Figure 7.2 shows the contours of the hybrid scheme's σ function, which blends between TVD ($\sigma = 1$) and CDS convection ($\sigma = 0$), for the cylinder and NACA0021 cases, described respectively in Sects. 6.5 and 6.4[2]. For both cases the σ function tracks the unsteady wake regions of resolved turbulence very closely (visible in the contours of vorticity magnitude on the left-hand side), ensuring a dominance of low-dissipative CDS convection there. In the irrotational flow outside of the wake and further from the cylinder, the more stable TVD is ensured. The hybrid scheme is therefore seen to fulfil its intended role perfectly for this kind of flow simulation.

[2]The same slice and snapshot as used in Figures 8.2 and 8.3 have been employed, allowing a direct comparison with the RANS/LES functionality plotted there.

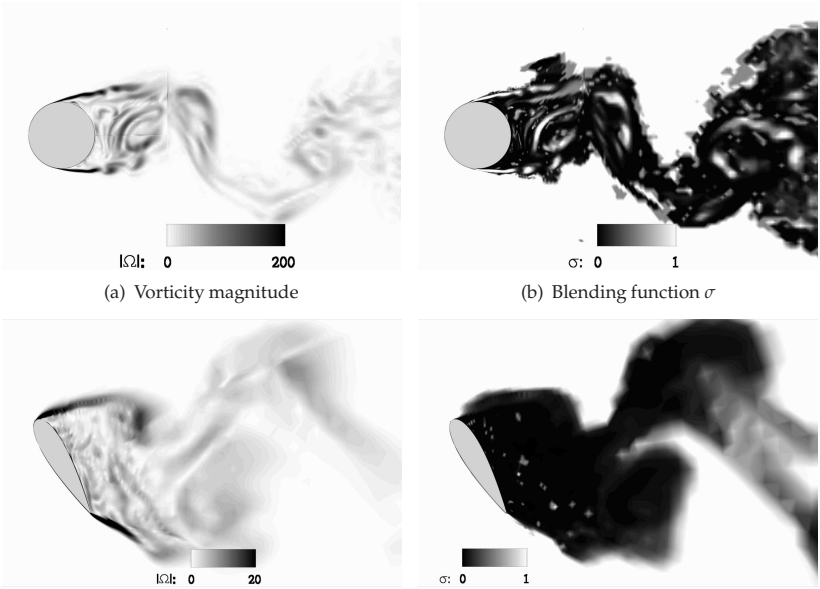

(a) Vorticity magnitude

(b) Blending function σ

(c) Vorticity magnitude

(d) Blending function σ

Figure 7.2: Hybrid scheme functionality for the cylinder case (CEASM-DES, $\Delta t = 0.03D/u_\infty$, above) and NACA0021 case (SALSA-DES97, NTS-1c grid, below) for a slice at the spanwise mid-section.

7.3 Calibration of the C_{DES} parameter

Although it is possible to derive analytical relationships that provide values of C_{DES} in relation to the Smagorinsky constant and other parameters of the underlying RANS model, an empirical calibration is considered essential for a number of reasons. Firstly, the model expressions do not take the level of numerical dissipation of the flow solver into account. Secondly, as has been demonstrated by Yan et al. [186], such derivations can be conceptually dubious and even deliver contradictory values. These issues are discussed in more detail in Sect. 6.1.

The C_{DES} values for all implemented DES variants have been calibrated using DIT, a test case described in Sect. 6.1. The first calibration of C_{DES} using DIT was reported by Shur et al. [148]. The earlier calibration work of the ELAN DES implementations was similarly based on the benchmark experimental data of Comte-Bellot and Corrsin [30] and the general method was reported by Bunge et al. [20]. Later on, within the framework of the DESider project, the technique was revised somewhat

and utilises the DNS benchmark data of Wray [183] for comparison. Comparative calculations have however not demonstrated a strong enough dependency on the method used to justify a modification of the earlier calibrated parameter values. Details and discussion of the calibration of C_{DES} can be found in [19, 20, 21, 55, 56, 163, 172, 186].

Due to the considerable previous reporting of the calibration, an exhaustive presentation of the DIT spectra for all models will not be given. Instead, spectra for the SALSA-DES implementation alone will be presented and discussed and reference is made to Tab. 5.3, where the calibrated values of C_{DES} for all models have been summarised. Figure 7.3 compares various spectra for the SALSA-DES implementation with the Ψ function active: For a range of C_{DES} on the 32^3 and 64^3 grids, and a cross-plot of spectra at the calibrated value $C_{\mathrm{DES}} = 0.60$ on the 16^3, 32^3 and 64^3 grids. In accordance with the findings of Sect. 7.1, pure central differencing has been applied for the convection scheme.

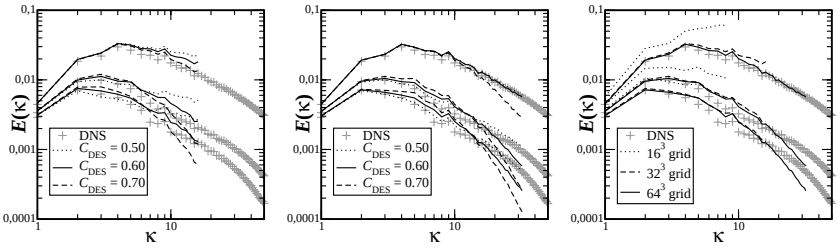

(a) Variation of C_{DES}, 32^3 grid (b) Variation of C_{DES}, 64^3 grid (c) Variation of grid resolution, $C_{\mathrm{DES}} = 0.60$

Figure 7.3: Example energy spectra for C_{DES} calibration computations, showing the effects of varying C_{DES} and grid resolution. SALSA-DES model with Ψ function active compared to Wray DNS benchmark data [183] at $t = 0.2$, $t = 1.8$ and $t = 3.0$ (in order of decreasing energy). All computations with pure CDS convection scheme.

The effect of varying C_{DES} is seen to be relatively strong, with a noticeable influence on the strength of the damping at high wavenumbers. In line with expectation, the damping is stronger for higher values of C_{DES}. Interestingly, stronger damping of the higher wave numbers gives rise to an over-prediction of the energy in the lower wavenumber range, with an intersection of the spectra at approximately $\kappa_{max}/2$ (corresponding to approximately the resolution 4Δ). Furthermore, the influence of varying C_{DES} appears to be stronger on the coarser grid. This is in accordance with the general properties of LES: Modelling empiricism is confined to the smallest scales and finer resolution therefore results a reduction of the relative influence of the model. Finally, it is worth noting that such a clear influence of the model can only

be achieved with a low-dissipative numerical scheme. In the DESider project [56][3], results submitted for solvers with strong levels of numerical dissipation exhibited a negligible influence of C_{DES} or equivalent model parameters.

Were the results for the 64^3 grid to be considered in isolation, a value of $C_{DES} = 0.50$ would clearly emerge as the most appropriate choice: The agreement with the DNS benchmark spectra is excellent at all time samples. Cross-reference to the 32^3 grid results however reveal a poor performance for this value, with an insufficient level of damping apparent. The spectra for $C_{DES} = 0.60$ in contrast perform better on the 32^3 grid, but are mildly too dissipative on the 64^3 grid. A significant grid dependency on the chosen value is hence observed, with higher C_{DES} required on coarser grids. The final decision in favour of $C_{DES} = 0.60$ was motivated by the consideration that 32^3 is likely to be more representative of the level of resolution affordable in more complex practical applications. The comparison of the DIT spectra from three different grid resolutions furthermore enables an assessment of the resolution requirements for LES discussed in Sect. 3.5.2. There, minimum cube sizes of the order of 36^3 volumes were identified based on the estimates of Pope [116], and the estimate 32^3 of Spalart [154] was cited. These results appear to corroborate these estimates: The spectra at a resolution of 32^3 are reasonable whereas 16^3 points are clearly insufficient[4].

As identified, a priority is given to the results at 32^3 resolution when choosing the calibrated value of C_{DES} for pragmatic reasons. A further ambiguity can arise between the time snapshots (e.g. on the 32^3 grid, $C_{DES} = 0.7$ gives the best agreement at $t = 0.2$ whereas this is excessively dissipative at later snapshots). It is believed that emphasis should be placed on the later time steps when deciding the calibrated value.

The discussion of the DIT results for the calibration of C_{DES} will be continued in Sect. 8.2, where the variation of C_{DES} between models will be analysed and the scope for a dynamic determination of C_{DES} will be discussed.

7.4 Validation of the Ψ functions

The problem of undesired activation of the damping functions of some RANS models in LES mode has been described in Section 3.7.4. An analysis based on the methodology described by Spalart et al. [158] is presented in Appendix D for the models considered and the implemented correction functions, Ψ, are summarised in Section 5.5.2. Here, the functionality of the Ψ functions will be demonstrated. Furthermore, for the models for which no Ψ function could be derived (LLR and CEASM),

[3] In particular, see Chap. IV, Sect. 5 therein.

[4] This observed grid dependency has since been found to result primarily from the spurious aliasing effect, mentioned in Sect. 6.1, which is stronger for coarser grids. Later studies employing filtered initial velocity fields to eliminate the aliasing effect (not shown) exhibit a much weaker (yet still apparent) sensitivity of the calibrated C_{DES} value upon the grid resolution.

an empirical assessment is conducted.

To demonstrate the Ψ functionality, the DIT test case (described in Section 6.1) is employed using the Wray benchmark DNS data [183]. As the damping nature of the SGS-mode coefficient term A emerges only for low values of ν_t/ν (which can be interpreted as proportional to the "sub-grid scale Reynolds number"[5]), a fine grid resolution is required for the effect to emerge. The tests have therefore been conducted using the 64^3 grid.

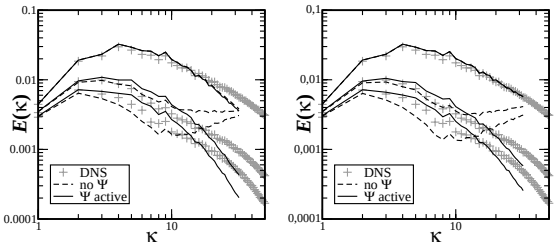

(a) SAE-DES (b) SALSA-DES

Figure 7.4: DIT spectra demonstrating the functionality of the derived Ψ functions for SAE-DES and SALSA-DES compared to Wray [183] benchmark data at $t = 0.2$, $t = 1.8$ and $t = 3.0$ (in order of decreasing energy), calibrated values of C_{DES}, 64^3 grid.

Figure 7.4 shows the spectra resulting from SAE-DES and SALSA-DES simulations of DIT with and without the derived Ψ function active. In both cases it can be seen that the high wavenumber energy is strongly over-predicted in the absence of the Ψ function, which is due to the strong damping of sub-grid eddy viscosity. Comparison with the "no-model" simulations using the CDS convection scheme (Fig. 7.1 in Sect. 7.1) reveals a similar qualitative nature – in both cases a positive gradient emerges at high wavenumbers. However, the fact that this gradient is lower than the exponent 2 suggests that the eddy viscosity is not entirely absent. Confirming this, Fig. 7.5 shows contour plots of the ν_t/ν levels active for the SAE-DES computation with and without the Ψ function active.

A further effect to note from Fig. 7.4 is that the strength of the eddy viscosity damping appears to increase as the time step increases and the turbulence decays. This is because, as mentioned, the damping strength of the A coefficient increases as ν_t/ν decreases. As the turbulence Reynolds number decays with time, so does the sub-grid scale Reynolds number (for a constant grid spacing) and with it the level of ν_t/ν.

[5]The turbulence Reynolds number [116] $\mathrm{Re}_L = \frac{\sqrt{k}L}{\nu} = \frac{k^2}{\varepsilon\nu}$. As $\nu_t = \frac{C_\mu k^2}{\varepsilon}$, $\mathrm{Re}_L = \frac{\nu_t}{C_\mu \nu} \propto \frac{\nu_t}{\nu}$. The term "sub-grid scale Reynolds number" is used as here $\nu_t = \nu_{sgs}$.

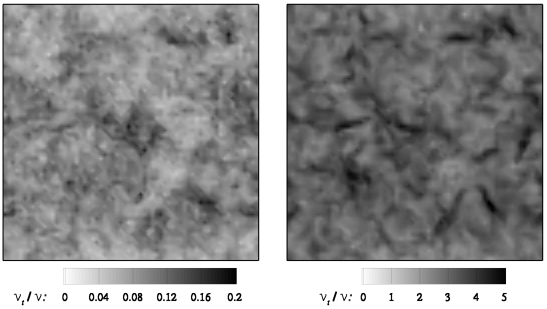

(a) SAE-DES, no Ψ (b) SAE-DES, Ψ active

Figure 7.5: Plots of the eddy viscosity ratio ν_t / ν at slices through the DIT domain for SAE-DES computation with and without the Ψ function, $t = 3.0$, $C_{\mathrm{DES}} = 0.60$, 64^3 grid. Note that the contours are scaled differently.

The failure mechanism of DES based on models without the necessary Ψ function is therefore in accordance with expectation. More importantly, the correct functionality of the Ψ functions derived for SAE-DES and SALSA-DES has been demonstrated; in both cases a sensible spectral energy distribution is restored. The strength of the deviation caused by the spurious damping is observed to be very strong, underlining the importance of the Ψ function analysis and derivation.

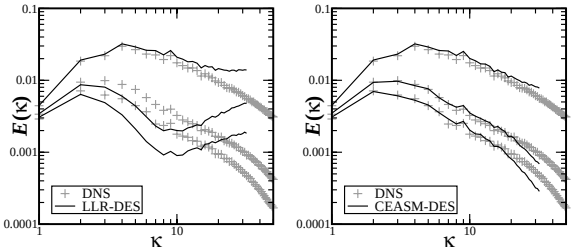

(a) LLR-DES (b) CEASM-DES

Figure 7.6: DIT spectra for the DES variants for which a Ψ function could not be derived, compared to Wray [183] benchmark data at $t = 0.2$, $t = 1.8$ and $t = 3.0$ (in order of decreasing energy), calibrated values of C_{DES}, 64^3 grid.

Attention will finally be turned to the models for which a Ψ function was seen to be

necessary but could not be derived, namely the LLR and CEASM models (details can be found in Appendix D). The spectra returned by LLR-DES indeed demonstrate, at least qualitatively, the typical failure mechanism observed for the SAE and SALSA variants. The fact that the eddy viscosity damping is already present at $t = 0.2$ furthermore suggests that the threshold level of ν_t/ν is higher for the LLR model. The behaviour at $t = 1.8$ and $t = 3$ differs from that of the SAE and SALSA models however; the strength of the damping appears to be *lower* at $t = 3$ compared to $t = 1.8$. An explanation for this may be the complex dependencies upon the velocity field gradients remarked upon in Appendix D (the relevant LLR model expressions are given in Eq. (B.20)). Until this problem is resolved, the computation of DES on the basis of the LLR model cannot be advised. For the LLR-DES results presented in this work (which pre-dated this analysis), an assessment of the sub-grid Reynolds number is suggested; if ν_t/ν is sufficiently high throughout the LES-mode region, it can be assumed that the damping problem has not occurred.

Contrasting results have been obtained for the CEASM model, with sensible spectra returned despite the lack of an implemented Ψ function. Precisely why this is the case is not understood, however the implication is that the CEASM-DES formulation is valid – at least for the range of ν_t/ν that emerge in the 64^3 DIT test. Were the damping problem to have occurred for the CEASM model, the Ψ function derived for the background LL $k-\varepsilon$ model could have been tested as a potential remedy. In light of these favourable results however, Ψ_{LL} has not been implemented for the CEASM-DES.

7.5 Validation of boundary layer shield function for CEASM-DES

To validate the functionality of the model-specific GIS-shield function derived for CEASM-DES [21], Eq. (5.3), the canonical test case of a boundary layer developing along an un-inclined flat plate will be employed. Because of its simplicity and the lack of benchmark data required, a dedicated description of the test case was not included in Chap. 6. A flat plate of unit length has been meshed in two dimensions with a uniform grid in the streamwise direction (except for some compression towards the leading edge) and stretched grid in the wall-normal direction. The streamwise spacing over the uniform portion was set to $\Delta x = 4 \times 10^{-3}$, targeting the occurrence of MSD (Sect. 3.7.3) as $\Delta x \ll \delta$. The wall-normal grid was adjusted to $y^+_{max} < 1$ at the first cell centre. A short section with a symmetry boundary condition was placed upstream of the leading edge of the plate, and a block profile of constant velocity was applied at the inflow. Outflow boundary conditions were set at the upper and downstream domain limits. The Reynolds number was set such that $\mathrm{Re}_{max} = 1 \times 10^6$.

A steady RANS computation was conducted, which serves as the benchmark: When the shield functions as intended, an identical velocity profile should be returned by the shielded DES. The computations with the DES97 and shielded DES model acti-

vated were conducted steady-state and were only resolved in two dimensions. For the purposes of this simple validation of the shield function, this is acceptable as no resolution of LES content is sought.

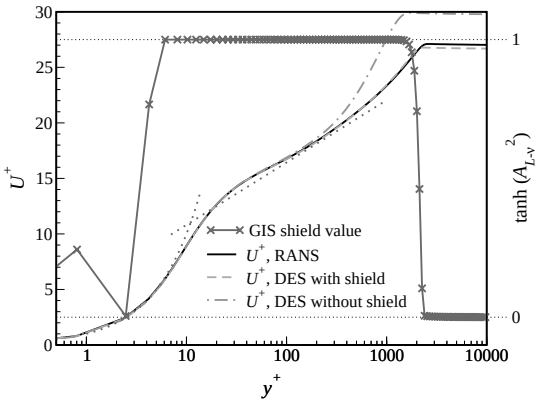

Figure 7.7: Velocity profiles and shield function behaviour at a location near the end of the plate, demonstrating the effectiveness of the model-specific GIS-shield formulation for CEASM-DES.

The normalised velocity profiles (in skin friction units, Sect. 2.4.1) from a location towards the downstream end of the plate are shown in Fig. 7.7. These are superimposed with the value of the boundary layer shield function, $\tanh\left(A_{L-v}^2\right)$ from Eq. (5.3). The occurrence of MSD in the unshielded DES97 computation can be clearly seen in the form of a strong increase in the exponent of the velocity profile above $y^+ \approx 200$. The effect of this is an under-estimation of the boundary layer thickness of 27% relative to the RANS, and an 18% under-prediction of the wall shear stress. The magnitude of these effects of course depend on the location along the plate and the grid resolution.

The computation including the shield function however matches the RANS profile very well. The agreement is however not absolutely perfect, with some minor discrepancy apparent in the skin friction[6]. The activity of the shield function is superimposed over the velocity profiles in Fig. 7.7. This is seen to correctly detect the turbulent log law region (Sect. 2.4.1) of the boundary layer, equalling unity between $y^+ \approx 6$ and the boundary layer edge around $y^+ \approx 2000$. The fact that the shield

[6]This is concluded from the level of U^+ outside of the boundary layer. Because of the unconfined flow domain, the velocity magnitude outside the boundary layer should be constant irrespective of differences in the boundary layer thickness. Changes in U^+ outside the boundary layer hence arise from differences in τ_w.

function drops very near to the wall is due to its dependence on k and the turbulence damping effect of the wall in the viscous sublayer. This is however not considered a deficiency of the formulation. The remaining minor discrepancy could probably be eliminated with some tuning of the hyperbolic tangent blending function. Since the publication of the generalised DDES method [158] (Sect. 3.7.4) however, the motivation for this is slight.

8 Demonstration and Analysis

In Chapter 7, the implementation of key DES features was validated and the properties of the numerical convection schemes were examined. This lays the groundwork for the presentation of a comprehensive range of studies in this chapter. Some of these seek to establish a deeper understanding of the DES method whereas others target the derivation of best practice advice for its application in an industrial context. A particular emphasis is placed on the assessment of the predictive accuracy of DES in a comparison with experimental data at an unprecedented level of detail.

The individual sections are dedicated to a particular topic, and in some cases draw upon multiple test cases. Likewise, results from certain cases are called upon to support the discussion on multiple topics. Reference is hence made to Chapter 6, where the detailed test case descriptions are collated. An attempt has been made to order the sections in this chapter such that the latter sections build upon the former. Due to the inherent inter-dependencies however, this has not proved possible in all cases.

8.1 RANS and LES activity in DES

To investigate the spatial distribution of the RANS and LES modes from DES, reference will be made to three bluff body test cases, the NACA0012 and NACA0021 stalled airfoils and the circular cylinder. These are introduced in Sections 6.3, 6.4 and 6.5 respectively. The influence of grid refinement is investigated using LLR-DES97 results from the NACA0012 coarse and fine grids. Results for SALSA-DES97 and LLR-DES97 are compared for the NACA0021 case with the NTS-1c grid, and the CEASM-DES with the GIS-shield described in Section 5.5.4 has been applied to the cylinder case using a time step of $\Delta t = 0.03D/u_\infty$. A qualitative impression of the simulated flow fields will be given in Section 8.1.1 before the RANS/LES functionality is analysed and discussed in Section 8.1.2.

8.1.1 Instantaneous snapshot of the flow field

A visual impression of the flow physics and the structures resolved by the DES can be obtained from Fig. 8.1, which shows instantaneous snapshots of the vortex cores for the cylinder and NACA0021 cases[1]. The vortex cores are portrayed using a negative value of the λ_2 criterion proposed by Jeong & Hussain [66]. For the cylinder, clearly-defined horseshoe vortices are evident at the cylinder/wall junctions, as are the breakup of the shear layer and the organisation of the chaotic turbulent eddies

[1] The NACA0021 and NACA0012 cases do not differ qualitatively, hence only one of these is presented here.

into a coherent vortex street pattern. The same phenomena can be observed for the NACA0021 case, with exception of the horseshoe vortices due to the spanwise periodicity. Both cases are hence typical examples of bluff-body flows with massive separation.

The existence of such fine-grained resolved turbulence provides evidence of the desired LES-mode functionality in the separated wake region. Although the resolved eddies are of a similar scale in the near wake region of both geometries, it is clear that these coarsen rather rapidly downstream in the case of the NACA0021. This can be explained when the grids are compared (Fig. 6.6 for the NACA0021 and Fig. 6.8 for the cylinder); the NACA0021 grid exhibits a much more rapid expansion of the cell size than the cylinder grid, for which a relatively constant cell size is maintained downstream.

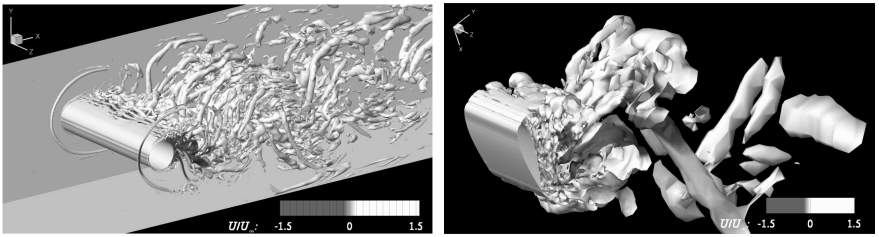

(a) (b)

Figure 8.1: Instantaneous vortex core structures portrayed using isosurfaces of the λ_2 criterion [66] shaded by streamwise velocity. (a) cylinder case, CEASM-DES, $\Delta t = 0.03D/u_\infty$; (b) NACA0021 case, SALSA-DES97, NTS-1c grid.

8.1.2 Distribution of the RANS and LES zones

Two-dimensional snapshots of the vorticity magnitude at a slice through the wake region[2] and the functionality of the DES are compared in Fig. 8.2 for the cylinder case. Using the ratio of the RANS to LES length scales $L_{\text{RANS}}/L_{\text{LES}}$ as an indicator, the regions in which the alternative modes of the DES are in operation are shown. In this representation a value less or greater than unity corresponds to the RANS and LES modes respectively and the interface value of $L_{\text{RANS}}/L_{\text{LES}} = 1$ is highlighted by dashed contour lines.

The model can be seen to operate in LES-mode throughout the finely-resolved turbulent wake and in the outer irrotational flow region, and as RANS in the separated shear layers and outer edges of the turbulent wake. The majority of the attached

[2] This figure (and the slice shown for the SALSA-DES97 NACA0021 in Fig. 8.3) depict the same snapshot as the examination of the σ blending function in Fig. 7.2, allowing a cross-comparison.

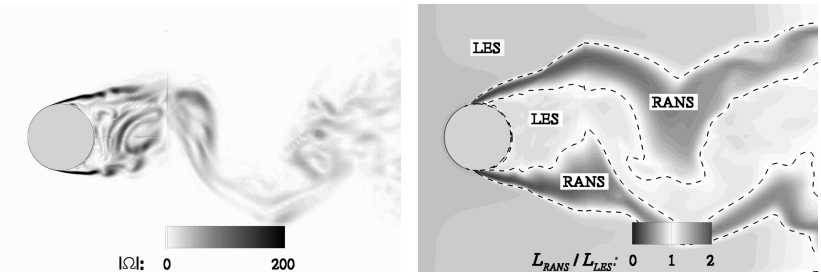

(a) Vorticity magnitude (b) LES-mode region

Figure 8.2: Analysis of the DES functionality for the cylinder case (CEASM-DES, $\Delta t = 0.03D/u_\infty$) for a slice at the spanwise mid-section.

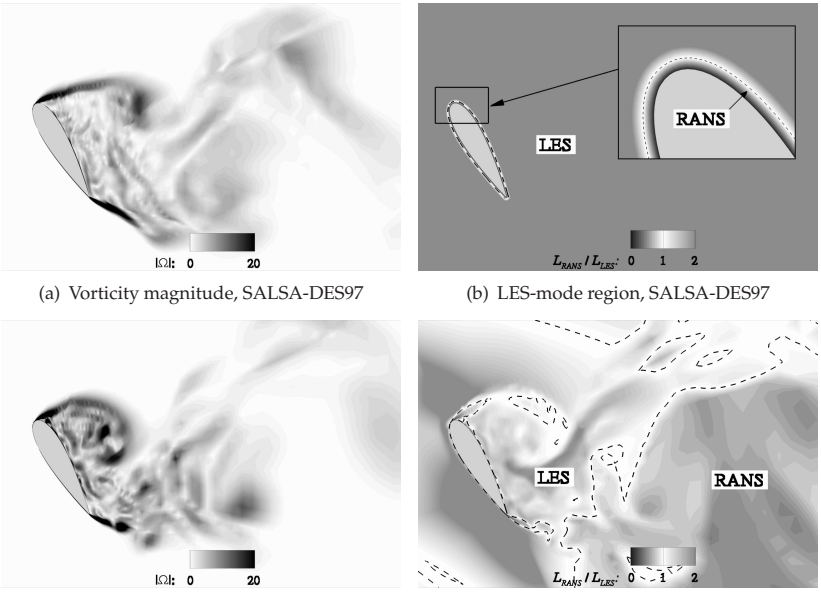

(a) Vorticity magnitude, SALSA-DES97 (b) LES-mode region, SALSA-DES97

(c) Vorticity magnitude, LLR-DES97 (d) LES-mode region, LLR-DES97

Figure 8.3: Comparison of DES functionality for the one-equation SALSA-DES97 (above) and two-equation LLR-DES97 (below) computations of the NACA0021 case at the spanwise mid-section.

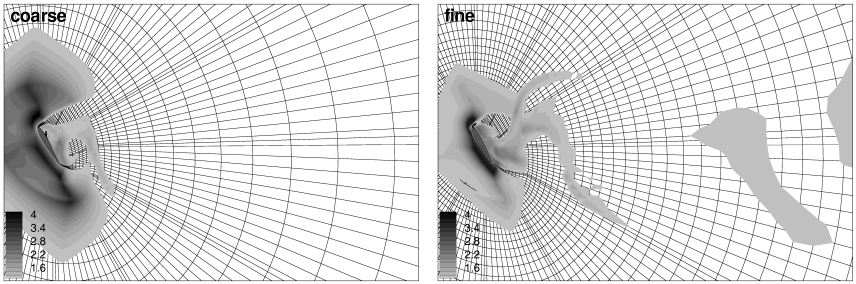

(a) Coarse grid (b) Fine grid

Figure 8.4: Extent of the instantaneous LES-mode region as a function of grid resolution. The quantity $L_{\mathrm{RANS}}/L_{\mathrm{LES}}$ is shown for values exceeding unity such that the shaded regions portray the LES-mode operation. LLR-DES97 computations of the NACA0012 case.

cylinder boundary layer is also handled with LES-mode, which at first inspection appears incorrect. This is however an outcome of the laminar boundary layer prior to separation, which is discussed in Sect. 8.5.1. Such an unsteady interface is typical of DES based on two-equation models, where the RANS length scale is derived locally from the model parameters (see Tab. 5.2). This behaviour can be interpreted as a rough measure of the grid's capability to resolve the turbulent scales present at each point, reverting to URANS modelling when this is insufficient[3]. When the DES definition proposed by Travin et al. [171] (cited in Sect. 3.7.2) is recalled, this switch-back to RANS mode in the separated regions with coarser grids is clearly in accordance with the underlying concept of DES.

Examination of the values of $L_{\mathrm{RANS}}/L_{\mathrm{LES}}$ in the region of the interface reveals a further aspect of the switch between RANS and LES modes, namely that this is a continuous transition without any discontinuities in the solution field. There is therefore no strong difference in the model behaviour just either side of the interface for values of $L_{\mathrm{RANS}}/L_{\mathrm{LES}} \approx 1$, even though a formal transition between two contrasting modelling frameworks has occurred.

Unlike the cylinder case, the NACA0021 airfoil has been computed using a range of turbulence models. This case can therefore be used to demonstrate the difference in RANS/LES switching behaviour for one-equation and two-equation models. As demonstrated for the cylinder, the local definition of the RANS length scale causes a

[3]Caution is however advised: Although denoted L_{RANS}, the length scale constructed from the local turbulence variables is not necessarily equivalent to the RANS length scale. This is because the LES activity serves to damp k to k_{sgs}. L_{RANS} is hence often closer to a length scale of the subgrid-scale modelled turbulence.

switching between RANS and LES modes also in regions of separated flow for two-equation models. This behaviour is also seen for the LLR-DES97 solutions of the NACA0021 case in Figs. 8.3 (c) and (d). For the one-equation SALSA-DES97 solutions (Figs. 8.3 (a) and (b)) however the picture is very different; RANS-mode operation is confined to a thin region encompassing the attached boundary layers. This is because of the length scale definition $L_{\mathrm{RANS}} = d_w$, and the RANS/LES switching behaviour is hence purely grid-dependent.

Upon initial consideration it is tempting to interpret more into this difference than it perhaps deserves. Indeed the DES switch is activated to LES mode everywhere far from the wall, and it can be shown that under the local-equilibrium assumption this LES mode is equivalent to the Smagorinsky model (Appendix D). However, the only modification compared to the RANS model is that the dissipation term (Eq. B.2) becomes proportional to $1/\Delta^2$ instead of $1/d_w^2$. In cases where a large grid cell occurs far from the wall, the RANS and LES modes therefore become essentially equivalent. The length scale definition of d_w used in the majority of one-equation models is in any case only valid for attached boundary layers and for this reason one-equation models are strictly only applicable to attached flows (Sect. 3.4.3, [80, 157]). The demonstrated behaviour of switching back to RANS mode in separated regions of coarser grids is therefore inherent to DES regardless of the chosen background model.

Nonetheless, two-equation models offer a minor advantage that the formal division of RANS/LES operation can be easily inspected. It can even be considered advisable to check to what extent the focus region [154] targeted for LES mode activity is actually computed as such. This can be used as a simple and approximate thumb-rule to check whether the grid resolution is sufficiently fine[4], a remark that will be clarified by the discussion to follow.

The effect of the grid resolution on the RANS/LES mode regions is portrayed in Fig. 8.4 for the NACA0012 case. Although the difference in grid resolution is not very strong (and indeed the "fine" grid could be considered relatively coarse by modern standards), the impact on the RANS/LES switching can be clearly discerned. The fine grid sustains regions of LES mode operation much further downstream than the coarse grid, for which no LES mode is apparent further than around $1.5c$ downstream of the airfoil.

[4]It was however suggested by Prof. Strelets in his review of this work that visualisation of the fraction of time spent locally in RANS or LES mode may be more useful than snapshots of the length scale ratio in this respect.

8.2 Variation of C_{DES} between models and the scope for a "dynamic DES"

The calibration of C_{DES} using DIT has been demonstrated in Section 7.3 and the implemented calibrated values are listed for each model in Table 5.3. These show a certain degree of model-specific variation within the range $0.60 \leq C_{\mathrm{DES}} \leq 0.75$. In order to derive the Ψ correction function for each model, analysis of the LES-mode behaviour using the methods described in Appendix D was applied. Here it will be investigated whether such analysis can provide an explanation for the variation in C_{DES} witnessed. In so doing, the possibility of analytically deriving an appropriate value of C_{DES} for each model (naturally under the assumption of negligible numerical dissipation, Sect. 7.1) will be assessed. Finally, a discussion will be given on the scope for developing a "dynamic DES" method based on the derived relationships.

An expression linking C_{DES} to the Smagorinsky model parameter C_S can be derived for each model. The first step is a comparison of the Smagorinsky model (Eq. (3.10)) with the generalised form of DES models in LES-mode (derived in Appendix D):

$$\nu_t = (C_S\,\Delta)^2\,S^* = A(\Psi\,C_{\mathrm{DES}}\,\Delta)^2 S^*\,. \tag{8.1}$$

By incorporating the definition of Ψ (Eq. (D.3)), the desired expression for the equivalent Smagorinsky parameter value can be obtained for each model as

$$C_S = \sqrt{A^*}\,C_{\mathrm{DES}}\,. \tag{8.2}$$

If the values of C_{DES} calibrated by DIT have been obtained in a consistent manner and if the assumption of local equilibrium underlining the derivation is valid, then similar values of C_S should be returned by each model. The values of C_S corresponding to the calibrated C_{DES} are given together with the asymptotic coefficient A^* (for high values of ν_t/ν) in Table 8.1[5].

	SA	SAE	SALSA	WCX	CEASM (LL)
A^*	$\frac{C_{b1}}{C_{w1}f_w^*}$	$\frac{C_{b1}}{C_{w1}f_w^*}$	$\frac{f^*_{C_{b1}}}{f^*_{C_{w1}}f_w^*}$	$\left(\frac{C_{\omega 2}}{C_{\omega 1}}\right)^{3/2}$	$\left(\frac{C_\mu\,C_{\varepsilon 2}}{C_{\varepsilon 1}}\right)^{3/2}$
A^* value	0.0986	0.0893	0.0993	0.0496	0.0416
Calibrated C_{DES}	0.65	0.65	0.60	0.70	0.65
C_S	0.2041	0.1942	0.1891	0.1559	0.1325

Table 8.1: Values of C_S equivalent to the calibrated C_{DES} parameter for each model, using Eq. (8.2).

[5] The table does not include the LLR model for which A^* cannot be derived and uses the expression for the background LL $k-\varepsilon$ model for the CEASM (which is only valid for constant $C_\mu = 0.09$).

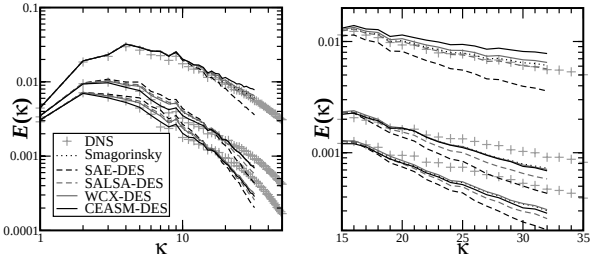

(a) Spectral comparison

(b) Zoom of high κ region (linear κ scale)

Figure 8.5: Cross plot of DIT spectra for all DES variants compared to Wray [183] benchmark data at $t = 0.2$, $t = 1.8$ and $t = 3.0$ (in order of decreasing energy), calibrated values of C_{DES}, 64^3 grid.

The values of C_S in fact exhibit a fairly high degree of scatter, especially when recalling from Section 3.5 that $C_S \approx 0.2$ is typical for DIT calibration whereas $C_S \approx 0.1$ is used for wall-bounded flows. For the SA-based models the values are very close to the $C_S \approx 0.2$, however those for the WCX and CEASM models are rather low. Cross plotting the DIT spectra for all models reveals that the trend in equivalent C_S corresponds precisely to the moderate differences in dissipation of the high wavenumber spectra (Fig. 8.5). Spectra for the Smagorinsky model with the analytical value $C_S = 0.1825$ (Sect. 3.5.1, [82, 3]) are also included. Particularly at $t = 0.2$, the models are ranked CEASM → WCX → Smagorinsky → SALSA → SAE correlating perfectly with the equivalent C_S trend in Tab. 8.1. This trend is maintained in the later spectra for all models with the exception of CEASM, which appears to become increasingly dissipative (relative to the other models) as the solution progresses. It is supposed that this irregular behaviour is due to the lack of a derivable Ψ function for this model and the observed variable behaviour of A_{LL} (Section 7.4, Appendix D).

This apparent correlation between the scatter of equivalent C_S values and the high wavenumber behaviour of the spectra raises the possibility of determining $C_{\mathrm{DES}}(C_S)$ for a fixed target value of C_S. If the underlying assumptions in the analysis are correct, then identical spectra should be returned. The C_{DES} values corresponding to $C_S = 0.1825$ are listed in Tab. 8.2, and the resulting spectra on the 32^3 and 64^3 grids are plotted in Fig. 8.6.

At the first time instant, $t = 0.2$, the spectra are indeed very similar on both grids (indeed more so than the calibrated values) and the same grid-dependent nature reported in Sect. 7.3 is apparent. However, at later instants the spectra diverge strongly: Those from the SA-model family remain similar and show a reasonable behaviour, whereas the WCX and especially the CEASM spectra are excessively dissipative on

	SA	SAE	SALSA	WCX	CEASM (LL)
C_{DES} for $C_S = 0.1825$	0.581	0.611	0.579	0.819	0.895

Table 8.2: Values of C_{DES} equivalent to the analytical value $C_S = 0.1825$ for each model, using Eq. (8.2).

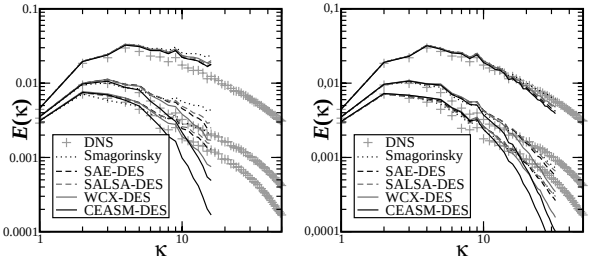

(a) 32^3 (b) 64^3

Figure 8.6: Cross plot of DIT spectra for all DES variants compared to Wray [183] benchmark data at $t = 0.2$, $t = 1.8$ and $t = 3.0$ (in order of decreasing energy), C_{DES} values corresponding to $C_S = 0.1825$.

both grids. This suggests that the analytical relationship between C_{DES} and C_S can be considered valid for the one-equation models tested, whereas effects unaccounted for in the simple equilibrium analysis appear to play an important role in the two-equation models. One possible explanation for this behaviour concerns the method of length scale substitution applied in the two-equation models (Sects. 3.7.2 & 8.3). As L_{DES} is only substituted in the destruction term of the k equation the variable k is limited directly, whereas the second equation variable (ε or ω) is limited only implicitly through its dependency on k. The mixture of an LES-limited k and a "natural" value of the second equation variable in the eddy viscosity expression may be the cause of this behaviour. Were the results for the CEASM-DES to be considered in isolation, one might also conjecture that the Ψ problem identified with this model (Appendix D) were to blame. However, the similar behaviour seen for the WCX-DES contradicts this.

The implications of this are that a derivation of C_{DES} as a function of C_S can indeed provide sensible values for some models (on the basis of this evidence, apparently the SA family of models). However, caution is advised when considering new models for DES: Such analytically derived values should at most be used as a starting value for an empirical calibration based on DIT and a test should always be conducted.

Dynamic DES?

A further implication of the demonstrated link between C_{DES} and C_S, at least for the SAE and SALSA models, concerns the possibility to extend the SGS modelling capability of DES. In principle, enhancements developed originally for the Smagorinsky model could be applied to the LES mode of DES. In particular, the dynamic determination of C_S pioneered by Germano et al. [51] and described in Sect. 3.5.1 could offer considerable advantages.

As outlined in that section, the Smagorinsky parameter demonstrates strong case-dependency and a range of disadvantages of a constant C_S for LES have been listed. Dynamic determination of C_S, or dynamic one-equation models incorporating analogous features have been shown to offer a wide range of advantages in LES, not least improved generality through the elimination of the dependency on case-specific calibration. Under first consideration therefore, the motivation for investigating such a dynamic DES is strong.

It can however also be argued that such dynamic parameter determination is of less interest in the context of DES. For example, Smagorinsky LES solutions are strongly sensitive to the value of C_S for the near-wall flow only. For flow further from the wall (including the log law region), the solution is only weakly dependent on C_S [17, 159]. In both natural DES as well as WMLES applications, the near-wall RANS treatment is expected to result in a low general dependency on C_{DES}[6]. Furthermore, the advantages of dynamic LES concerning transition prediction and the deactivation of the subgrid-scale model in the limit of full DNS resolution are of limited relevance in the expected application scope of DES.

Nonetheless, dynamic DES is considered worth pursuing for a number of reasons, and some initial DIT experimentation with the Germano/Lilly dynamic model [51, 83] (Sect. 3.5.1) has enforced this view. It was demonstrated in Sect. 7.3 that the calibrated value of C_{DES} depends on the grid resolution (compare e.g. the spectra for $C_{\mathrm{DES}} = 0.50$ on the 32^3 and 64^3 grids in Fig. 7.3). It is conceivable that an appropriate dynamic modification of C_{DES} could reduce such sensitivity, and DIT computations were conducted to investigate this. Figure 8.7 compares spectra from the Smagorinsky model using $C_S = 0.1825$ with those returned by the dynamic model for a variation of grid resolution. The Smagorinsky model exhibits a strong grid dependency, with an insufficient level of dissipation apparent on the 32^3 grid and very poor spectra at 16^3 (which is clearly under-resolved). The dynamic determination of C_S however significantly improves the situation: The spectra at 32^3 overlap almost perfectly with those at 64^3, and even the under-resolved 16^3 spectra are improved.

[6] Some evidence supporting this is given in Sect. 8.4.1. In a comparison of models with strongly differing values of "effective C_S" for massively separated flow, the solutions were identical to within the statistical error despite significant differences in the eddy viscosity levels in the wake. Furthermore, in an attempt (not shown) to reduce the residual LLM in channel flow IDDES, a lower value of C_{DES} was computed. The influence on the mean flow was again negligible.

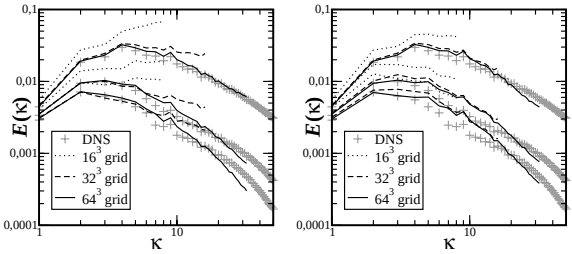

(a) Smagorinsky model, $C_S = 0.1825$

(b) Dynamic model [51, 83]

Figure 8.7: DIT spectra for LES with the Smagorinsky model (constant $C_S = 0.1825$) and the dynamic model of Germano/Lilly ([51, 83]) compared to Wray [183] benchmark data at $t = 0.2$, $t = 1.8$ and $t = 3.0$ (in order of decreasing energy).

This indicates therefore, that dynamic models offer the potential to improve LES on coarser grids and to resolve the grid-dependent nature of the model parameter.

A further possible benefit of a dynamic DES concerns its usefulness in the context of IDDES. Recall from Sect. 3.7.5 that an empirically-tuned grid-dependent near wall damping of the filter width, Δ, was introduced to address the discrepancy between suitable values of C_{DES} for DIT calibration and fully-resolved LES of wall-bounded flows. The generality of such a grid-dependent formulation remains to be demonstrated however. It could indeed emerge, that a truly dynamic C_{DES} reproduces the desired behaviour with increased generality.

It appears therefore that the prospect of concrete advantages to be expected from a dynamic DES are uncertain, however worth well worth pursuing. Future investigations in this direction must aim to demonstrate measurable advantages of the formulation. If these prove to be marginal at best, then these benefits must be weighed against the increased complexity of the formulation. Concerning the formulation, the simplest variant would be to employ the usual dynamic determination of C_S according to Germano [51] or Lilly [83], and the simple expression of Eq. (8.2) to translate this to the corresponding C_{DES}. For the reasons of numerical stability and generality outlined in Sect. 3.5.1 however, an approach along the lines of Davidson's dynamic one-equation SGS model would be considered preferable. This may be easily formulated on the basis of a double substitution of the DES length scale (Sects. 3.7.6 & 8.3), as such formulations give rise to a k equation SGS model.

8.3 Alternative length scale substitutions in DES

As described in Sect. 3.7.2, the DES methodology was generalised by Travin et al. [171] and Strelets [163] to be applicable to RANS models in general. Whereas the substitution of the length scale d_w affected only the destruction term of the transport equation in the original SA model based DES, for other RANS models length scales can be identified in a range of terms. This gives rise to a degree of freedom as to the length scale(s) to be substituted by L_{DES}. Alternative formulations employing an additional substitution in the eddy viscosity expression of two-equation models have been explored by Bush & Mani [22] and Kok et al. [76], which are described in Sect. 3.7.6. However a comparative study to assess the impact of these alternative formulations and to identify practical advantages were not presented by those authors. A thorough investigation of this issue was published by Yan, Mockett & Thiele [186] the principal findings of which will be summarised here. The interested reader is referred to the original publication for more detail.

Formulations

The 1988 Wilcox $k-\omega$ model [181] chosen as the object of the study, because it is a well-known and representative model with a simple formulation. Furthermore, no complications arise concerning spurious behaviour of damping terms in LES mode (as demonstrated in Appendix D). The model formulation is listed in Appendix B.2.1.

Three alternative DES formulations are derived, which entail the substitution of the DES length scale, Eq. (3.16), in different combinations of the model terms. The dissipation term of the k equation, given in Eq. (B.12), and the eddy viscosity expression, Eq. (B.14), are reformulated as follows:

$$\epsilon_k = C_\mu k\omega = \frac{k^{3/2}}{L_k}\,, \tag{8.3}$$

$$\nu_t = \frac{k}{\omega} = C_\mu L_\nu \sqrt{k}\,, \tag{8.4}$$

$$L_k = L_\nu = \frac{\sqrt{k}}{C_\mu \omega}\,. \tag{8.5}$$

The RANS turbulence length scale is the same in both expressions and the notation L_k and L_ν is employed merely to aid description in the following. The three DES formulations are labelled DES1, DES2 and DES3, and the corresponding substitutions of the DES length scale are summarised in Tab. 8.3. DES1 hence corresponds to the standard DES practice, DES2 to the dual substitution applied by Bush & Mani [22] and Kok et al. [76], and DES3 is the remaining formulation that completes the possible combinations of length scale substitutions.

	L_k	L_ν
DES1	L_{DES}	L_ν
DES2	L_{DES}	L_{DES}
DES3	L_k	L_{DES}

Table 8.3: Summary of the substitutions of the length scale in the k equation destruction term, L_k, and in the eddy viscosity expression, L_ν, by the DES length scale L_{DES}.

The alternative formulations in SGS mode

As described in Sect. 3.7.2, the minimum requirement upon the length scale substitution to give a valid DES formulation is that a form corresponding to the Smagorinsky model, Eq. (3.10), can be derived in LES mode [163]. Such an analysis is therefore conducted to assess the alternative formulations, which also addresses possible derivations of C_{DES} in relation to other model parameters. Beginning with DES1, reference is made to Appendix D, where the local equilibrium assumption applied to both model equations is shown to give rise to the following Smagorinsky-like form:

$$\nu_t = \left(\frac{C_{\omega 2}}{C_{\omega 1}}\right)^{3/2} \left(C_{\mathrm{DES}}\Delta\right)^2 S^* \,. \tag{8.6}$$

In the spirit of the analysis of Sect. 8.2, a dependency of C_{DES} on a given value of C_S can be derived. For the analytical value of $C_S = 0.1825$, the corresponding $C_{\mathrm{DES}} = 0.82$ is obtained.

For DES2, it emerges that a k equation SGS model of identical form to that of Yoshizawa [188] is obtained:

$$\frac{Dk}{Dt} = \frac{\partial}{\partial x_j}\left[\left(\nu + \frac{\nu_t}{\sigma_k}\right)\frac{\partial k}{\partial x_j}\right] + \nu_t S^{*2} - \frac{k^{3/2}}{C_{\mathrm{DES}}\Delta} \tag{8.7}$$

$$\nu_t = C_\mu C_{\mathrm{DES}}\Delta\sqrt{k} \tag{8.8}$$

The dual substitution of L_{DES} in fact leads to a decoupling of the ω equation from the solution. As noted in Sect. 3.5.1, when the assumption of a balance between the production and destruction terms is applied to the k equation SGS model, the Smagorinsky model is indeed returned:

$$\nu_t = C_\mu^{3/2} \left(C_{\mathrm{DES}}\Delta\right)^2 S^* \,. \tag{8.9}$$

Again, an expression for C_{DES} as a function of C_S can be derived, which delivers $C_{\mathrm{DES}} = 1.11$ for $C_S = 0.1825$. However, by comparing the Yoshizawa model with the k equation SGS model inherent to DES2, a plethora of additional expressions for C_{DES} can be derived. For example:

	DES1	DES2	DES3
C_{DES}	0.70	0.95	0.90

Table 8.4: Calibrated values of C_{DES} for the three alternative length scale substitutions.

$$C_{\mathrm{DES}} = \frac{C_k}{C_\mu} = 0.78 \tag{8.10}$$

$$C_{\mathrm{DES}} = \frac{1}{C_\varepsilon} = 0.95 \tag{8.11}$$

$$C_{\mathrm{DES}} = \sqrt{\frac{C_k}{C_\mu C_\epsilon}} = 0.86\ . \tag{8.12}$$

Although all these values are of approximately the correct order of magnitude, the spread is large enough to give rise to significant discrepancies in a DIT test. The inherent contradiction arising from such analytical C_{DES} derivations further emphasises the importance of empirical calibration calculations, a recurring theme throughout this work.

Finally, for the DES3 formulation, no derivation of a Smagorinsky form of the SGS model is possible, although both k and ω are indirectly limited through the limitation of ν_t in their production terms. As such, DES3 cannot strictly count as a valid DES formulation.

DIT calibration of C_{DES} for the alternative formulations

The DIT test case (described in Sect. 6.1) employing the experimental benchmark data of Comte-Bellot & Corrsin [30] was applied to ascertain appropriate values of C_{DES} for the DES1, DES2 and DES3 formulations. The use of DIT for such calibration has been discussed in Sect. 7.3. The resulting values are given in Tab. 8.4.

The calibrated values exhibit a relatively strong variation, which indeed exceeds the greatest difference between background RANS models (compare for example with the values listed in Tab. 5.3). The DES2 and DES3 exhibit much higher values of C_{DES}, which appears to represent a lower "inherent dissipativity" of the formulation, a concept to be returned to in the discussion subsection to follow.

Comparison for massively-separated flow

To compare the three DES formulations for a more complex and practically-relevant flow, the NACA0012 test case (Sect. 6.3) was computed using the coarse grid and the

	DES1	DES2	DES3
$\overline{C_L}$	0.978	0.990	1.038
$\overline{C_D}$	1.635	1.664	1.740
St	0.176	0.173	0.182

Table 8.5: Time-averaged lift and drag coefficient and vortex shedding Strouhal number for the NACA0012 case simulated using each length scale substitution.

calibrated values of C_{DES} for each variant (Tab. 8.4). Following an elimination of initial transient behaviour, over 1000 non-dimensional time units ($c/|U|_\infty$) were computed for each case for statistical analysis, corresponding to over 200 vortex shedding periods. Although this is a very long simulated time, an appreciable statistical error can still be expected in the mean values. This arises from the highly stochastic nature of the flow and the occurrence of strong low-frequency modulation, and is described in detail for the similar NACA0021 case in Sect. 8.4.1.

Force spectra, plots of the mean surface pressure coefficient and statistical wake flow quantities were compared, with a high degree of similarity observed between the formulations. To give an indication of this, the time-averaged force coefficients with the vortex shedding Strouhal number are given in Tab. 8.5. These results are not sufficiently different to reveal a systematic discrepancy outside of the expected statistical convergence error.

Results reported for a coaxial jet

Despite the negligible effect that the length scale substitution method has exhibited for the massively separated flow around the NACA0012 profile, more recent applications of the DES1 and DES2 formulations to a coaxial jet flow have revealed a very interesting difference. These computations, carried out by Yan et al. [187] and funded by the European project CoJeN[7], have also been reported by Michel et al. [93], Mockett & Thiele [99] and Mockett et al. [96]. The goal of the investigation was to develop a simulation methodology for the development of strategies to reduce jet engine noise. Such modifications include chevrons introduced to the engine nacelle lip, and inclusion of the geometry was hence considered important. As such, DES would appear to represent a well-suited method combining RANS of the nozzle geometry with LES of the resolved turbulent fluctuations. However, the weakness of the shear layer instability and lack of convective transport of turbulent disturbances through recirculation cause exacerbation of the grey area problem discussed in Sect. 3.7.3.

The DES1 and DES2 variants were compared for a short-cowl generic coaxial jet geometry. The core stream is heated and flows at M $= 0.90$, whereas the bypass stream

[7] Computation of Coaxial Jet Noise, Contract No. AST3-CT-2003-502790.

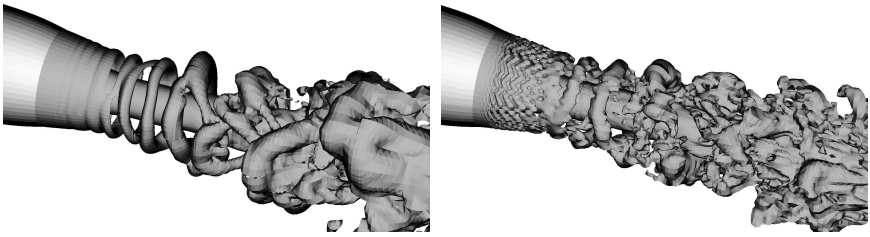

(a) DES1 (b) DES2

Figure 8.8: Density isosurfaces showing resolved structures in the jet shear layer using the DES1 and DES2 length scale substitution variants of WCX-DES. Courtesy of J. Yan.

is at ambient temperature and M = 0.86, flowing into static surrounding air. The configuration was computed using a grid of 3.8×10^6 cells on the Bavarian HLRB supercomputer. Density isosurfaces are used to visualise the resolved turbulent structures in Fig. 8.8. The two variants are seen to exhibit strong differences in the levels of resolved turbulence in the early shear layer, with much finer structures obtained using DES2. This represents a significant advantage for the aeroacoustic application in question, where the resolved turbulent structures are the dominant sound source. The accelerated development of resolved turbulence corresponds to a reduction of the grey area extent. The mechanism believed to be responsible for this improvement will explained in the following discussion.

Discussion

The initial investigations of the alternative length scale substitutions, incorporating the DIT and NACA0012 test cases and published by Yan et al., 2005 [186], analysed the SGS form of the variants and indicated an equivalence once the strong differences in C_{DES} have been balanced through calibration. That the results are indiscernible for such a massively-separated (and LES-mode-dominated) flow is indeed reassuring, however the later investigation of jet flow (Yan et al., 2007 [187]) indicates that this is not the whole story. The DES2 form appears to significantly reduce the impact and extent of the grey area, an important and promising result that warrants some further discussion.

A convincing explanatory mechanism is proposed, the key to which was indeed identified in the original paper when discussing the strongly different values of C_{DES} that arise. In the above subsection, these were vaguely linked to the concept of inherent dissipativity of the formulation, without elaboration as to the meaning of this. The inherent dissipativity regards the strength or rapidity with which RANS levels of eddy viscosity are damped to SGS levels once the LES length scale is active in the model equations. That both of the variants with a direct length scale substitution

in the eddy viscosity expression exhibit a lower inherent dissipativity (based on the higher C_{DES} values) can be analysed by considering the model terms in question. The limitation of the eddy viscosity due to the LES length scale results in a reduction of the production and diffusion terms in the transport equations, whereas the standard length scale substitution only increases the destruction term. The k equation production and destruction terms sit physically at opposite ends of the turbulent cascade, being responsible for the generation of turbulence from mean-flow shear and its dissipation into heat via molecular viscosity, respectively (Sect. 2.2). These phenomena involve entirely different physical scales and a time lag is furthermore apparent between production and destruction. Considering the situation of a switch from RANS to LES mode along a streamline, the response of the model in terms of damping ν_t will be rapid when the production term is limited (the modelled turbulence is cut off at its source) and more delayed when only the destruction term is increased.

Such consideration of the respective strong and weak effects of the production and destruction terms serves to explain both the differences in the C_{DES} values[8] as well as the shortened grey area observed for the jet flow. The encouraging results concerning the grey area reduction should be investigated in more detail on the basis of a suitable and more simple test case[9].

8.4 Sensitivity of DES to the RANS model used

Since the generalisation of the DES formulation from its SA-specific origin to a generally-applicable methodology ([163], Section 3.7.2), the question of the model sensitivity of DES has been of high practical importance. Is this similar to the URANS situation, where a very strong model sensitivity is observed (see e.g. [94], [55] and [146]), or is this alleviated by the introduction of the LES ingredient? It can be expected that the model sensitivity would depend upon the flow in question, in particular upon the extent to which the RANS region influences the global flow. With the variety of DES implementations and test cases to hand, these issues can be explored in a comprehensive manner. Two test cases with contrasting flow physics are chosen: the geometry-induced massive separation of the NACA0021 airfoil in deep stall (Section 8.4.1) and the bump test case, for which a weaker separation from a smooth curved surface occurs (Section 8.4.2). In both cases results are compared between DES variants based on different RANS models, with identical grids and numerical setup. No comparison with experiments will be made – this is done in Sections 8.5 and 8.7.

[8] That the DES2 and DES3 values are so much higher than that of DES1 corroborates the interpretation that the production term has a stronger influence than the destruction term. Furthermore, the fact that DES2 has the highest value of C_{DES} is in line with expectation, as this exhibits the strongest limitation in LES mode (the substitution is active in all model terms).

[9] Perhaps an un-inclined flat plate of finite streamwise length, where the turbulent boundary layers coalesce to a separated wake at the trailing edge?

8.4.1 Massively-separated external flow: NACA0021 at $\alpha = 60^\circ$

This test case has been employed in the descriptions of the RANS and LES zone distribution and hybrid convection scheme functionality in Sections 8.1.2 and 7.2, respectively. Instantaneous snapshots of the flow field were shown, from which the highly-unsteady massively separated wake flow could be observed. Due to the relative sharpness of the leading and trailing edges, the separation can be considered geometry-induced and, as a result, relatively insensitive to model-specific differences in the prediction of the upstream boundary layers. The level of similarity of the solutions will be investigated by a detailed comparison of time-averaged and unsteady flow characteristics. The test case, grid and numerical setup are described in Section 6.4. All results in this section were computed with the NTS-1c grid, and the SALSA-DES97, LLR-DES97 and CEASM-DES97 variants have been employed.

Statistical convergence of the mean integral force coefficients

For such highly unsteady flows, the validity of the time-averaged quantities depends on the size of the time sample computed for averaging. To ascertain the level of statistical convergence of these simulations, running averages of the integral lift and drag coefficient have been computed and are plotted in Fig. 8.9. These curves begin at the first time step employed in the statistical analysis (i.e. following the elimination of initial transient behaviour) and show how the mean forces develop as the averaging sample increases. It is seen that substantial shifts in the mean value can occur even after a very long simulation time. This is due to the random low frequency modulation of the force signals, a feature discussed in Sect. 8.5.2 for the cylinder flow case.

Despite the very long simulation times (a minimum of over 40000 time steps has been computed in all cases, corresponding to roughly $1000\,t^*$, where $t^* = c/|U_\infty|$, or 200 vortex shedding cycles), an appreciable statistical convergence error is still apparent. The magnitude of this is furthermore hard to specify, due to the random drift of the mean values (e.g. for the CEASM-DES at $t^* \approx 1400$). A statistical convergence error of around ± 0.03 units (for both C_L and C_D) could be considered a conservative estimate.

Time-averaged flow

The time-averaged integral force components are summarised in Tab. 8.6, together with the total number of time steps over which the averaging has been conducted, $N_{\Delta t}$. Considering the residual statistical averaging error estimated in the preceding section, the small differences in the values may not be interpreted as arising from model dependency. The predicted forces are considered identical to within the estimated statistical convergence error.

In addition to the lift and drag coefficients, the force coefficient components normal and tangential to the airfoil chord have been computed using a coordinate rotation and tabulated in Tab. 8.6. Again, these values are very similar between the variants,

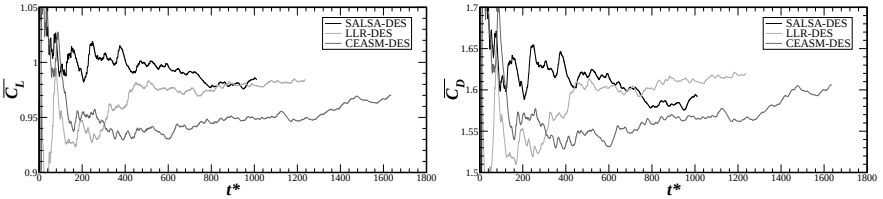

Figure 8.9: Running averages of the lift and drag coefficients (integrated over the entire span) over the time range used for statistical analysis.

	$\overline{C_L}$	$\overline{C_D}$	$\overline{C_N}$	$\overline{C_T}$	St	Wake length	$N_{\Delta t}$
SALSA-DES	0.9842	1.5916	1.8705	-0.0565	0.1855	1.725	40443
LLR-DES	0.9846	1.6204	1.8956	-0.0425	0.1878	1.697	49424
CEASM-DES	0.9701	1.6059	1.8758	-0.0372	0.1868	1.729	65457

Table 8.6: Time-averaged integral lift, drag, chord-normal and chord-tangential force coefficients, Strouhal number, wake length (defined as the saddle point position relative to the leading edge, $x = y = 0$) and the number of time steps used for statistical analysis.

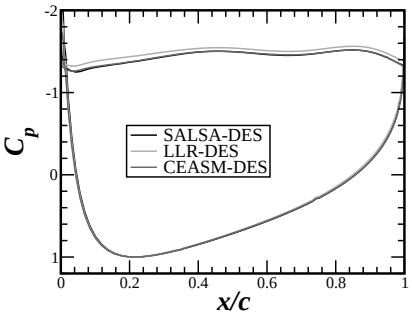

Figure 8.10: Profiles of time and spanwise-averaged pressure coefficient.

although the somewhat higher C_N value for the LLR-DES deserves some further investigation. Examination of the time and spanwise-averaged pressure coefficient profiles in Fig. 8.10 reveals a stronger suction along the downstream airfoil surface for the LLR-DES, corresponding to the higher C_N. This suggests a difference in the mean wake flow field, which will be described in the following.

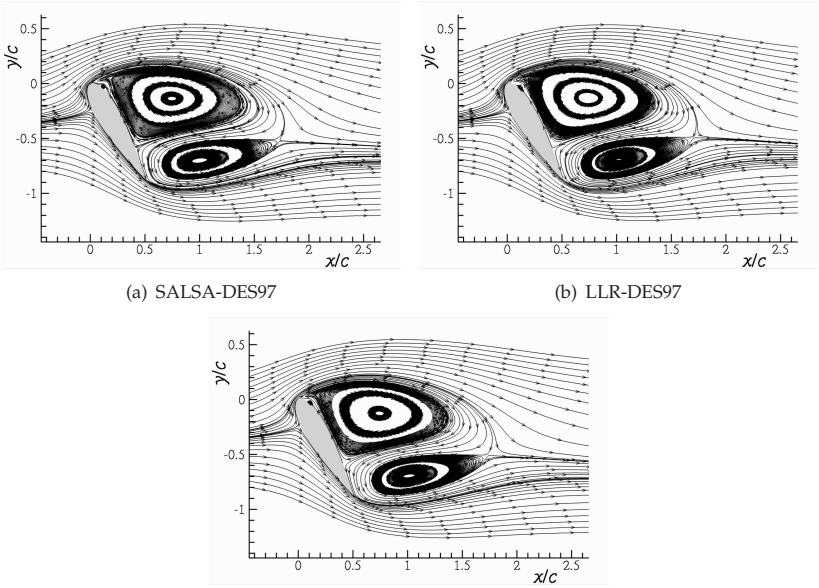

(a) SALSA-DES97

(b) LLR-DES97

(c) CEASM-DES97

Figure 8.11: Streamlines of the time and spanwise-averaged flow field.

Streamlines for the time and spanwise-averaged flow field have been plotted in Fig. 8.11. All models deliver the same fundamental features: the stagnation point in a similar location on the upstream airfoil surface, separation at the leading and trailing edges, the formation of two large counter-rotating mean vortices (the uppermost of which is larger), a secondary separation of the re-attached flow towards the leading edge on the rear airfoil surface and the closure of the wake at a saddle point. The plots appear identical visually, however a quantitative comparison reveals some minor differences. Interpreting the saddle point as the closure of the time-averaged wake, a measure of the wake length can be obtained. This is defined as the streamwise distance between the saddle point and the coordinate origin at the profile leading edge, and the values are listed in Tab. 8.6. Whereas the values for the SALSA and CEASM variants are very similar, the LLR-DES exhibits a shorter wake. This physical link between the wake length, rear surface pressure level and force coefficient is in line with the findings of Roshko [129] (summarised in Section 2.5).

To examine the time-averaged resolved and modelled turbulence quantities returned by each simulation, contours of the resolved and modelled turbulent kinetic energy are shown in Fig. 8.12. These quantities are obtained using the methods described in

Appendix E[10]. The resolved fluctuations predicted by each model are highly similar both in level and distribution. It can be seen that $\overline{k_{res}}$ develops within the separated shear layers and reaches its highest levels in the regions of the time-averaged vortex cores and saddle point. The impinging flow on the downstream airfoil surface causes a further amplification of the resolved fluctuations in the near wall region.

Contrastingly, a marked model dependency is observed in the time-averaged modelled turbulent kinetic energy: The SALSA implementation exhibits much higher levels of $\overline{k_{mod}}$ throughout the wake, most markedly within the shear layers, whereas the LLR and CEASM are similar. It could be supposed that this is an artefact of the estimation of k from ν_t for the one-equation SALSA model, employing the Bradshaw hypothesis [15] as described in Appendix E (k is not available directly as for the other models). To examine this possibility the time-averaged eddy viscosity is plotted in the leading edge region in Fig. 8.13 and shows considerably higher levels for the SALSA computation. The approximation in the post processing is therefore not responsible for this difference. Two hypotheses are proposed:

- The equivalent Smagorinsky constant value for SALSA-DES is higher than that of CEASM-DES (see Tab. 8.1 in Section 8.2). The equivalent C_S for LLR-DES cannot be determined analytically, however this could be expected to be similar the value for WCX-DES upon which the LLR model is based.

- The SALSA model may inherit the behaviour identified by Breuer et al. [18] and Riou et al. [125] for SA-DES, discussed in Section 3.7.6: The damping terms f_{v1}, f_{v2} and f_w were observed to give rise to excessive eddy viscosity in the early shear layer.

It is of course possible that both hypotheses are true: The first would be responsible for the general level of ν_t throughout the wake and the second for a localised increase at the shear layer. The $\overline{k_{mod}}$ levels in the wake show a similar distribution for each model, with the increase at $x/c \approx 1.3$ arising due to the increase in Δ there (see Fig. 6.6).

Whatever the cause of this model dependent behaviour, the global solution appears to be insensitive to different levels of eddy viscosity in the LES-mode region, with a negligible difference observed. This is probably because the natural instability of the shear layer is so strong for this massively-separated flow that the development of resolved turbulent structures is not damped by the higher levels of eddy viscosity produced by SALSA-DES. Indeed, the levels of k_{res} in the early shear layers are very similar for all models (Fig. 8.12). The apparent insensitivity of such natural DES solutions to the general eddy viscosity level in the wake region fortifies some elements of the discussion on dynamic DES made in Sect. 8.2.

[10] It should be pointed out that much of the resolved kinetic energy is due to the coherent von-Kármán vortex shedding and is hence not entirely turbulent in origin. Separating the coherent and incoherent, turbulent motions would require phase averaging (Appendix F).

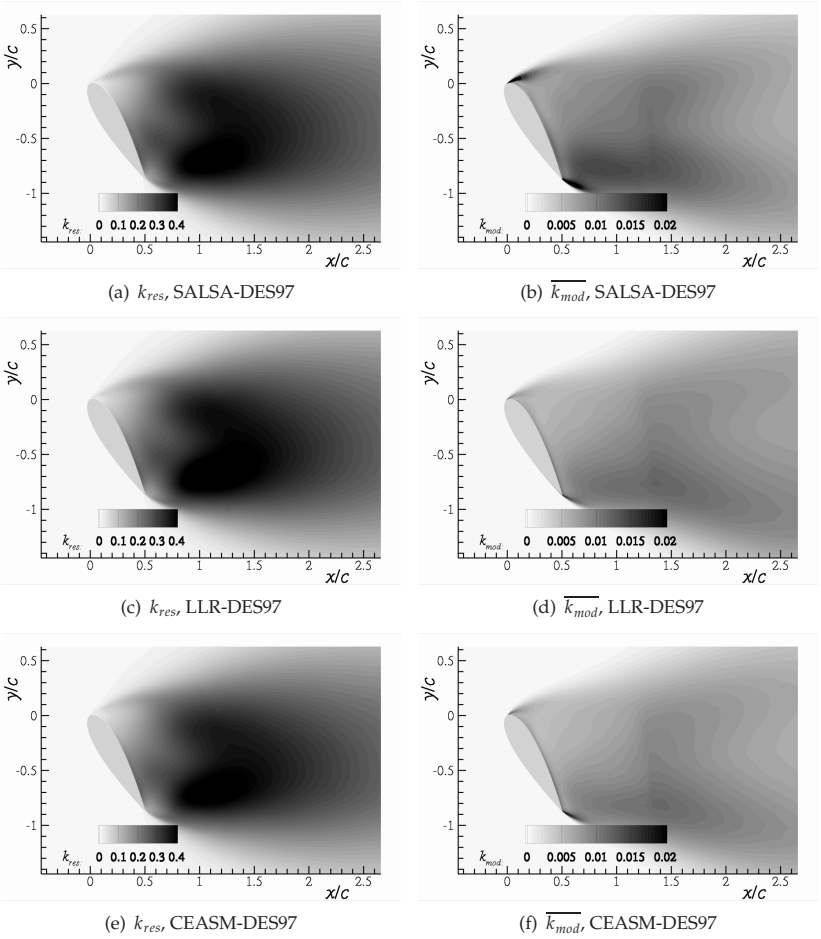

(a) k_{res}, SALSA-DES97

(b) $\overline{k_{mod}}$, SALSA-DES97

(c) k_{res}, LLR-DES97

(d) $\overline{k_{mod}}$, LLR-DES97

(e) k_{res}, CEASM-DES97

(f) $\overline{k_{mod}}$, CEASM-DES97

Figure 8.12: Resolved kinetic energy (left) and time-averaged modelled kinetic energy (right) (time and spanwise-averaged data).

Spectral content

Having established the negligible model dependency in the time-averaged forces and wake field, the unsteady content of the solutions should be compared. The power spectral densities of the four integral force components have been evaluated and are compared in Fig. 8.14. The spectra are obtained from the force time traces obtained at each spanwise slice, which are then averaged to provide smoothing. Each

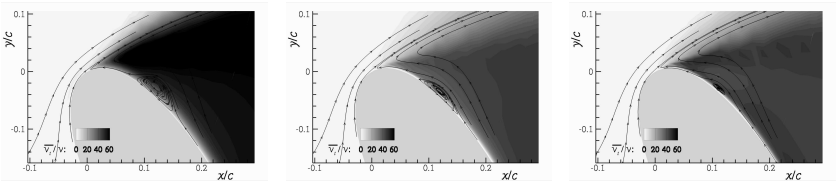

(a) SALSA-DES97 (b) LLR-DES97 (c) CEASM-DES97

Figure 8.13: Time-averaged eddy viscosity ratio, $\overline{\nu_t}/\nu$, and streamlines compared in the leading edge region (time and spanwise-averaged data).

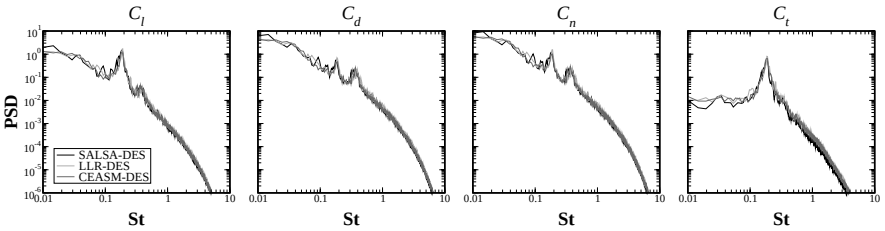

Figure 8.14: Power spectral density of sectional force signals (lift, drag, chord-normal and chord-tangential components).

PSD computation is conducted over a multiple of windows using the Hanning window function and then averaged[11].

The spectra are essentially identical, showing that the negligible model dependency for this case extends to the unsteady flow prediction as well as time-averaged quantities. The spectra for the different components show interesting differences, with the tangential component exhibits a very strong peak corresponding to the coherent vortex shedding. The corresponding Strouhal numbers (calculated as $\mathrm{St} = fc/|U_\infty|$) for the vortex shedding frequency are listed in Tab. 8.6 and are very similar. The fact that the greatest remaining differences between the spectra occur in the low frequency range lends weight to the assumption that the small deviations between the simulations are due to imperfect statistical convergence, as the low-frequency portion of the spectra is the most sensitive to statistical convergence errors.

[11] The spectral processing employing averaging of overlapping windows was carried out using the in-house tool *dftavg* written by D. Eschricht.

8.4.2 Separating-reattaching internal flow: Bump in a rectangular duct

Having established a near independence of the results on the DES background model for the NACA0021 flow in the preceding section, the level of model dependency will be investigated for a strongly contrasting flow case: A separating-reattaching flow with a very sensitive pressure-induced separation from a smoothly-curved surface and complex three-dimensional phenomena. The flow and the expected challenges it presents are outlined in Sect. 6.6 together with the test case setup. The CEASM-DES with model-specific GIS shield (Sect. 5.5.4) and the SAE-DDES implementations will be compared, which represent RANS background models occupying different levels in the modelling hierarchy (Fig. 3.5, Sect. 3.4.3). Unfortunately, different time step sizes were computed in each case, which strictly limits the comparability of the computations. The time step sizes together with the number of time steps computed are summarised in Tab. G.1. The statistical sample lengths, although less than those employed in the NACA0021 case, are considered adequate as no low-frequency modulation occurs in this flow (e.g. shear layer flapping) [4].

The qualitative nature of the flow topology along the symmetry plane is the same for both models (Figs. G.1): An initial separation occurs near the bump crest, followed shortly by an early flow reattachment. The flow separates again near the bump foot before reattaching somewhat further downstream. The location of these phenomena is however predicted very differently by each model, with the CEASM predicting a longer and larger recirculation region. These features are also clearly visible in the centreline pressure coefficient plot of Fig. G.2(a): The earlier reattachment of the SAE-DDES gives rise to an upstream shift of the pressure recovery region. It is furthermore notable that the differences due to the background model are much more significant than those between the DDES and IDDES formulations.

The positions of the separation and reattachment points are also listed in Tab. G.1, from which it can be seen that the CEASM model predicts a slightly earlier initial separation point than the SAE model. In fact, the difference in separation point prediction amounts to only one streamwise grid cell. It is commonly observed however that small differences in the prediction of the separation point can lead to strong differences in the extent of the recirculation region (see e.g. the periodic hills and Obi diffuser test cases studied in the FLOMANIA project [55]). A quantitative comparison of the velocity field profiles is given in Fig. G.3, from which the greater strength and size of the recirculation region predicted by the CEASM-DES is again observed.

The modelled, resolved and total Reynolds shear stresses are compared in Fig. G.4. Generally, the maximum levels are predicted very similarly by both models, with a displacement of the peak locations caused by the variation in the shear layer location. Some notable exceptions however occur, firstly in the early shear layer region (at $x = -0.079$) where greater levels of modelled stress are predicted by the SAE-DDES. This is most likely the same phenomenon observed for the NACA0021 case in Sect. 8.4.1 (see Figs. 8.12 & 8.13), albeit for the SALSA model, which was suspected

to arise from an analogous effect to that reported by Breuer et al. [18] and Riou et al. [125] (described in Sect. 3.7.6). Secondly, the CEASM-DES profiles show greater levels of modelled turbulence in both the upper and lower wall boundary layers downstream of the reattachment location (around $x > 0.6$). The upper wall boundary layer turbulence is furthermore purely modelled by the CEASM-DES, whereas the growth of some resolved content is apparent for the SAE-DDES at the $x = 0.925$ station. The infiltration of resolved turbulence into the upper wall boundary layer in the case of SAE-DDES is visible in the instantaneous vortex core plot of Fig. G.5 and the fact that this is sustained implies that the DDES shield has receded inside the boundary layer. The GIS shield functions are plotted in Fig. G.9, which indeed reveals a somewhat thicker layer of shield function activity in the case of the CEASM-DES. This is assumed to cause the absence of resolved turbulence along the upper wall boundary layer and the greater level of modelled turbulence at the lower wall.

The issue of the model-dependency of the initial separation position will be returned to. The analysis has so far been confined to data at the symmetry plane, however three-dimensional effects are of great importance in this low-aspect ratio geometry. In Fig. G.6 the three-dimensional topology of the mean flow is shown, which is qualitatively identical for all computations: Large reverse flow regions are predicted in the corners downstream of the bump, which coincide with a pair of counter-rotating streamwise vortices. These vortices induce a strong downwards motion of the core flow near the symmetry plane (visible also in Fig. G.7), which is responsible for the rapid reattachment observed down the bump slope. The streamwise vortices predicted by the SAE-DDES are stronger than those of the CEASM-DES, which is seen in Fig. G.7 to give rise to a stronger W-shaped distortion of the shear layer. The shear layer predicted by the CEASM-DES is in contrast relatively flat in the channel centre, up to about one bump height away from each side wall. The higher degree of three-dimensionality of the flow for the SAE-DDES is furthermore reflected in the pressure distributions at various z positions depicted in Fig. G.2(c). The pressure profiles differ very strongly between the spanwise stations, whereas those for CEASM-DES are highly similar (Fig. G.2(b)).

A further difference between the solutions that can be directly linked to the modelling hierarchy (Sect. 3.4.3) concerns the corner vortices observed at the prescribed inlet[12], which are depicted in Fig. 6.11. Whereas the anisotropy-resolving CEASM model is capable of propagating these vortices downstream into the solution domain, these are rapidly damped by the linear SAE model: This is shown in Fig. G.8, where instantaneous contours of the streamwise vorticity at the slice $x = -0.2$ are compared. This leads to a notable difference in the corner flow topology at the separation region predicted by each model. The extent to which this influences the downstream corner vortex strength or indeed the separation point prediction is however uncertain.

[12] Recall from Sect. 6.6 that the inflow data was provided by a DRSM computation by Ansys Inc.

In summary therefore, a stark contrast is seen with the results for the NACA0021 case, which were shown to be essentially model-independent. Because of the high importance of the separation point prediction and the strong reliance of this upon the upstream RANS modelling, a very strong level of DES model dependency is witnessed for this flow.

8.5 Comparison of DES with experiment for the flow around a circular cylinder

The test case of a circular cylinder in a square channel at Re $= 140000$, described in detail in Sect. 6.5, is employed as a validation case for DES working in its intended application environment of massively-separated flow. The subject of the investigation is the CEASM-DES variant with the model-specific GIS-shield function described in Sect. 5.5.4 and by Bunge et al. [21]. The laminar cylinder boundary layers existing at this precritical Reynolds number (Sect. 2.5.2) in fact limit the validation to the LES-mode operation of the DES[13]. The highly detailed experimental data allows many levels of comparison, and the result will be presented according to the type of post-processing carried out. The comparison represents a validation of DES to an unprecedented level of detail.

8.5.1 Transition behaviour

In a similar manner to Shur et al. [147] and Travin et al. [171], it was decided to manually adjust the transition behaviour of the RANS model to enforce the laminar cylinder boundary layers known to exist in the experiment. This is justifiable, as it is widely acknowledged that the prediction of laminar to turbulent transition falls outside the scope of RANS models. Without user intervention or the use of an external transition prediction method, RANS models tend to predict boundary layer turbulence too early on in their development.

The authors cited above developed and applied a technique they named the "tripless" approach, whereby a laminar boundary layer is ensured up to the separation point by exploiting the sensitivity of certain model terms to very low levels of freestream eddy viscosity. If applied using a uniform inflow profile however, the tripless approach would also laminarise the side wall boundary layers. Although the tripless approach would be applicable with a non-uniform inflow profile of the turbulence quantities, it was decided to adopt an alternative approach. Instead, a minor adjustment to the CEASM model formulation was undertaken to delay its inherent boundary layer transition behaviour to a sufficient extent to ensure laminar separation on the cylinder whilst maintaining the turbulent side walls. The laminar separation from the cylinder is verified in the eddy viscosity ratio plot of Fig. 8.15.

[13] Although the RANS mode operation is active on the channel side walls, this is not expected to play an important role in the flow.

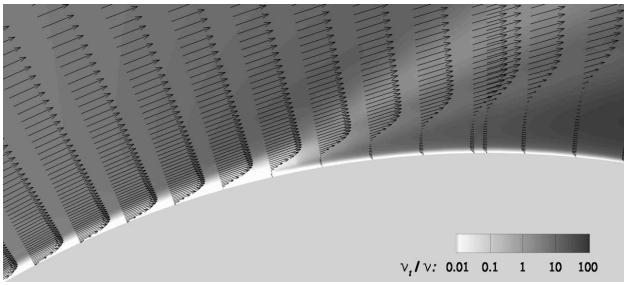

Figure 8.15: Instantaneous velocity vectors (at every second circumferential grid line) tangential to the spanwise median plane and contours of eddy viscosity ratio.

8.5.2 Instantaneous flow

Instantaneous snapshots of the flow field have already been portrayed in Figs. 8.1 & 8.2, and a description of the resolved vortex structures was given in Sect. 8.1.1. That discussion will now be extended to cover the temporal behaviour of the flow, based on the time traces of the pressure lift and drag integrated over the entire cylinder shown in Fig. 8.16. The lift component exhibits strong oscillations around zero with a very regular frequency and irregular amplitude. The drag component by contrast contains higher-frequency fluctuations of a generally weaker amplitude. The irregularity of the time traces, with a strong degree of low-frequency modulation, is considered analogous to the weak shedding cycle behaviour already noted for the NACA0021 profile in Sect. 8.4.1. The strong tonal nature of the lift coefficient and more broadband nature of the drag coefficient furthermore compares well with the behaviour seen for the tangential and normal force components of the NACA0021, respectively. Strong, medium and weak shedding cycles can clearly be discerned from the lift trace, which correspond respectively to higher, intermediate and lower levels of the drag coefficient. Because the experimental surface pressure readings were obtained from a single tapping, no time traces of the force coefficients are available from the experiment so a direct comparison of this character is not possible. However, the nature of the low-frequency modulation compares very well with the time traces published by Szepessy & Bearman [168] at a similar Reynolds number and aspect ratio, although at a much lower blockage coefficient.

Comparison of the velocity fields in the wake can however be made between the DES and the experiment. Fig. 8.17 is adapted from the joint numerical and experimental investigation of the flow physics published by Perrin et al. [112]. Velocity field snapshots from instants identified as strong and weak shedding cycles are compared, these being identified using surface pressure time traces in the case of the

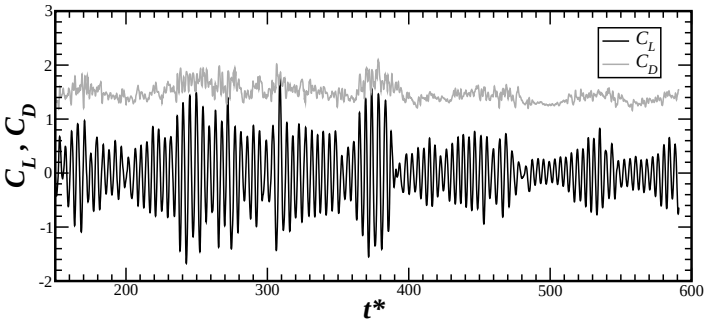

Figure 8.16: Time traces of lift and drag coefficient over the time range used for statistical analysis (pressure components only, integrated over the entire cylinder).

experiment and point velocity signals in the DES[14]. From the snapshots, a strong flow asymmetry and large-scale, coherent vortex shedding can be seen during the strong shedding. By contrast, the near wake flow is symmetric and populated with chaotic small-scale structures during weak shedding. The formation region of the large scale vortices is furthermore displaced downstream. The comparability of the DES and experiment in this respect is excellent. In addition to validating the ability of the DES to predict such unsteady flow phenomena, this investigation has therefore also provided evidence to support the hypothesis of Szepessy & Bearman [168] (mentioned in Section 2.5.2) that the weak shedding cycles are associated with increased three-dimensionality of the wake flow. A similar observation was made for the NACA0012 test case by Mockett et al. [94].

8.5.3 Time-averaged flow

Some time-averaged quantities are portrayed at a spanwise slice at $y = 0$ in Fig. 8.18. It is seen that the mean flow is almost two-dimensional over a large portion of the span in the central region, up to about $1D$ from each side wall. The regions of appreciable near-wall effect then extend slowly with increasing downstream distance. It is also apparent that the averaged quantities exhibit some statistical scatter, in particular the spanwise component of the resolved Reynolds stress. In order to enhance the statistical convergence, additional averaging has been performed over the observed homogeneous central region, as described in Sect. 6.5.

Running averages of the pressure lift and drag integrated over the cylinder are shown in Fig. 8.19, using the technique discussed in Section 8.4.1. These plots show

[14]The comparability of these quantities was demonstrated in the publication [112].

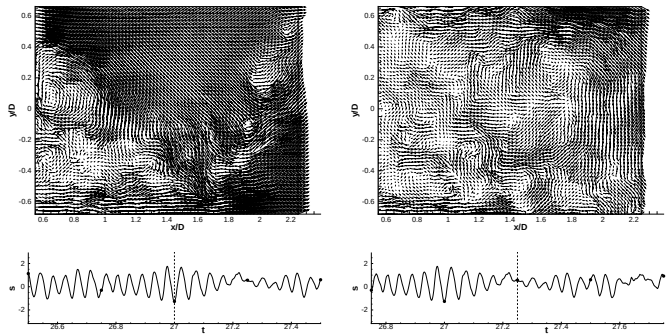

(a) PIV

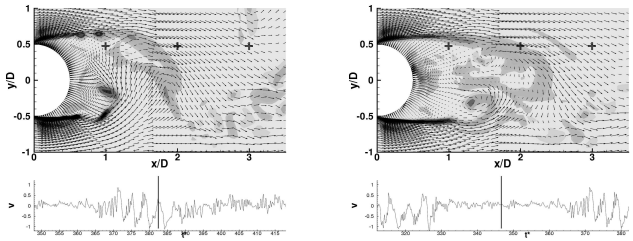

(b) DES

Figure 8.17: Near wake behaviour at instants where the vortex shedding is strong (*left*) and weak (*right*). The time trace depicted from the experiment (*upper*) is of surface pressure, whereas the velocity at $y/D = 0.5$ and $x/D = 1$ is shown for the DES (*lower*).

how the time-averaged force values develop as an increasing number of time steps are computed for averaging, and cover the time range used for Reynolds averaging (i.e. after the removal of initial transient character). The lift component converges very quickly as the mean value is not changed by switches from strong to weak shedding patterns. The fact that the lift inexplicably converges to a slightly non-zero value is cause for some concern for this symmetric geometry. The drag force drifts considerably however, the value still showing a fairly strong downwards trend near the end of the statistical range (because of a protracted absence of strong shedding behaviour). A considerable statistical convergence error must therefore be assumed despite the respectable time sample employed for averaging (14000 time steps, corresponding to a physical time of $420D/U_\infty$ or roughly 85 vortex shedding periods).

Figure 8.20 presents a comparison of the time-averaged streamlines between the

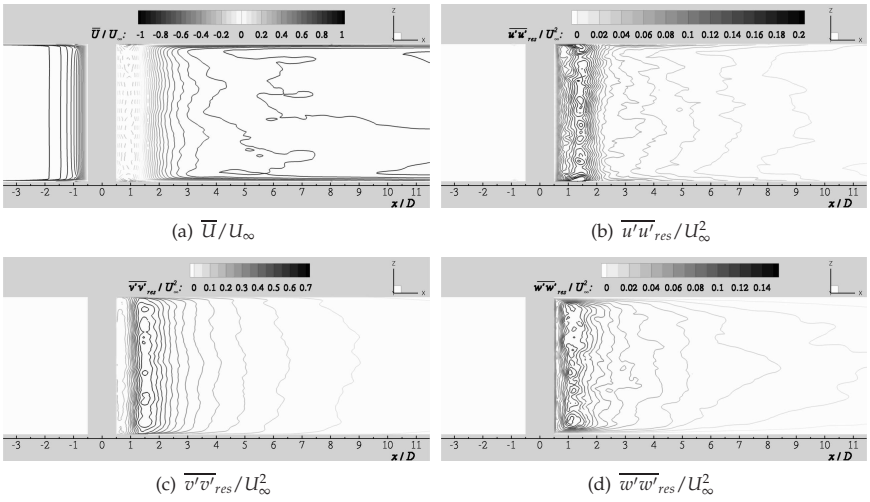

(a) $\overline{U}/U_\infty$ (b) $\overline{u'u'}_{res}/U_\infty^2$

(c) $\overline{v'v'}_{res}/U_\infty^2$ (d) $\overline{w'w'}_{res}/U_\infty^2$

Figure 8.18: Spanwise homogeneity of the flow: various statistical quantities on the slice $y/D = 0$.

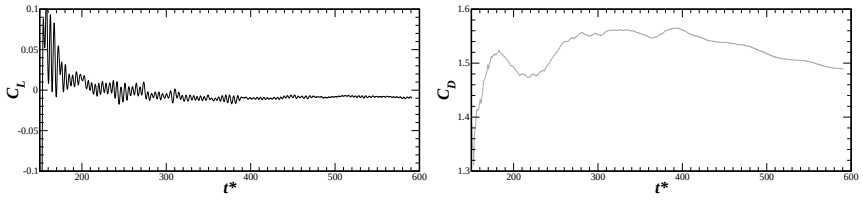

Figure 8.19: Running averages of the pressure lift and drag coefficients (integrated over the entire cylinder) over the time range used for statistical analysis.

DES and the experiment, showing excellent qualitative agreement. The quantitative agreement of the mean recirculation length (measured from the rear surface of the cylinder at $x/D = 0.5$) is also very good, as summarised in Tab. 8.7. Correspondingly, the mean pressure drag obtained at the spanwise median plane ($z = 0$) and likewise listed in Tab. 8.7 also shows very good agreement with the experiment. The fact that the total drag coefficient (i.e. including the effects of skin friction) integrated over the entire span is so similar reflects the fact that pressure drag is dominant for such bluff-body flows. This can also be interpreted as a further indicator of the high degree of spanwise homogeneity observed above.

A more detailed quantitative comparison of the mean velocity in the wake is offered

	$C_{d,p}$	$C_{D,p}$	C_D	Recirc. length
Experiment	1.45	—	—	0.78
CEASM-DES	1.48	1.48	1.49	0.85

Table 8.7: Time-averaged drag coefficient (pressure drag on spanwise median plane, $C_{d,p}$, pressure drag over whole cylinder, $C_{D,p}$ and total drag over whole cylinder, C_D) and recirculation length (relative to the cylinder rear surface) for DES and experiment.

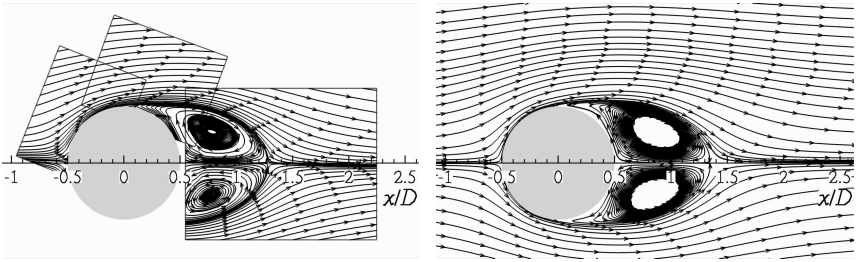

(a) PIV (b) DES

Figure 8.20: Comparison of the time-averaged streamlines between DES and experiment.

by Fig. 8.22 at vertical lines traversing the wake at a range of x/D positions. The agreement is generally excellent, although the profiles of the vertical velocity component show a stronger inflective nature. The small deviations could to some extent be a result of the remaining statistical convergence error noted above.

Contour plots of the Reynolds-averaged turbulent stresses are depicted in Fig. 8.21 in comparison with 2C and 3C PIV. The qualitative and quantitative agreement of the $\overline{u'u'}$ stress is excellent, whereas the effect of the mildly excessive recirculation length can be seen for the $\overline{v'v'}$ and $\overline{w'w'}$ components. Furthermore, the peak levels of $\overline{v'v'}$ are slightly over-predicted, whereas those of $\overline{w'w'}$ are slightly under-predicted.

A more detailed comparison can again be made with reference to the profiles of Fig. 8.22. The level of $\overline{u'u'}$ at the symmetry line ($y/D = 0$) agrees almost perfectly with the experiment. As the profiles move towards the shear layer however, a consistent over-prediction is apparent. The vertical component, $\overline{v'v'}$ in contrast reproduces the shape of the experimental plots very well, although the magnitude is under-predicted at the more upstream stations and over-predicted further downstream. The profiles coincide very well at $x/D = 1.3$. Finally, the shear stress component $\overline{u'v'}$ is in excellent agreement with the experimental data, except perhaps at $x/D = 1.0$, where the DES curve is excessively inflective.

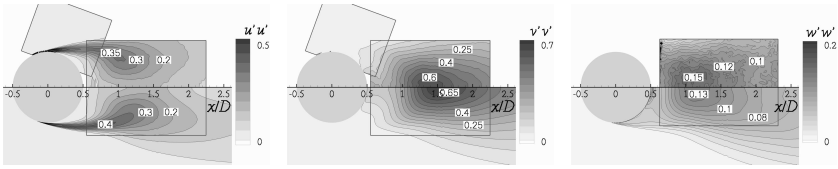

(a) $\overline{u'u'}_{res}$ (b) $\overline{v'v'}_{res}$ (c) $\overline{w'w'}_{res}$

Figure 8.21: Comparison of the resolved turbulent stress components from the DES *below* with PIV data *above*.

The Reynolds stress profiles in Fig. 8.22 also compare the resolved-only and total (i.e. resolved plus modelled) contributions (computed as described in Appendix E). The modelled contribution is clearly negligible in comparison to the resolved component, which could be interpreted as a sign of sufficient grid resolution (discussed in Sect. 3.5.2). However, the resolved part includes both the coherent and incoherent contributions to the motion, and is not purely made up of turbulent motion. To make a statement concerning the sufficiency of the grid resolution therefore, the coherent contribution should be subtracted using phase averaging (Appendix F).

8.5.4 Spectral content

Velocity time traces have been extracted from the TRPIV measurements for a range of positions in the near wake shown in the lower right-hand corner of Fig. 8.23. Spectra obtained for the U and V velocity components at each location are compared between DES and the TRPIV measurements in Fig. 8.23. The agreement seen is generally excellent, with reproduction of the variations in the spectra from point to point (e.g. the elimination of the peak due to symmetry for the U component at point 9, located near the centre line). Some significant deviations do however occur: The peak in the spectra represents the quasi-periodic vortex shedding, and occurs at a Strouhal number of $\mathrm{St} = 0.21$ in the experiment whereas the DES slightly over-predicts this at $\mathrm{St} = 0.23$. A fairly sharp drop off is furthermore seen at the higher frequencies, after around $St \approx 2$ (the precise value appearing to vary from point to point), which is due to either the spatial or temporal filtering of the simulation. The simulation time step corresponds to $\mathrm{St} \approx 30$, which when combined with the Nyquist criterion [104] results in a temporal cut-off at $\mathrm{St} \approx 15$. It is therefore apparent that the spatial resolution, rather than the time step is responsible for this behaviour.

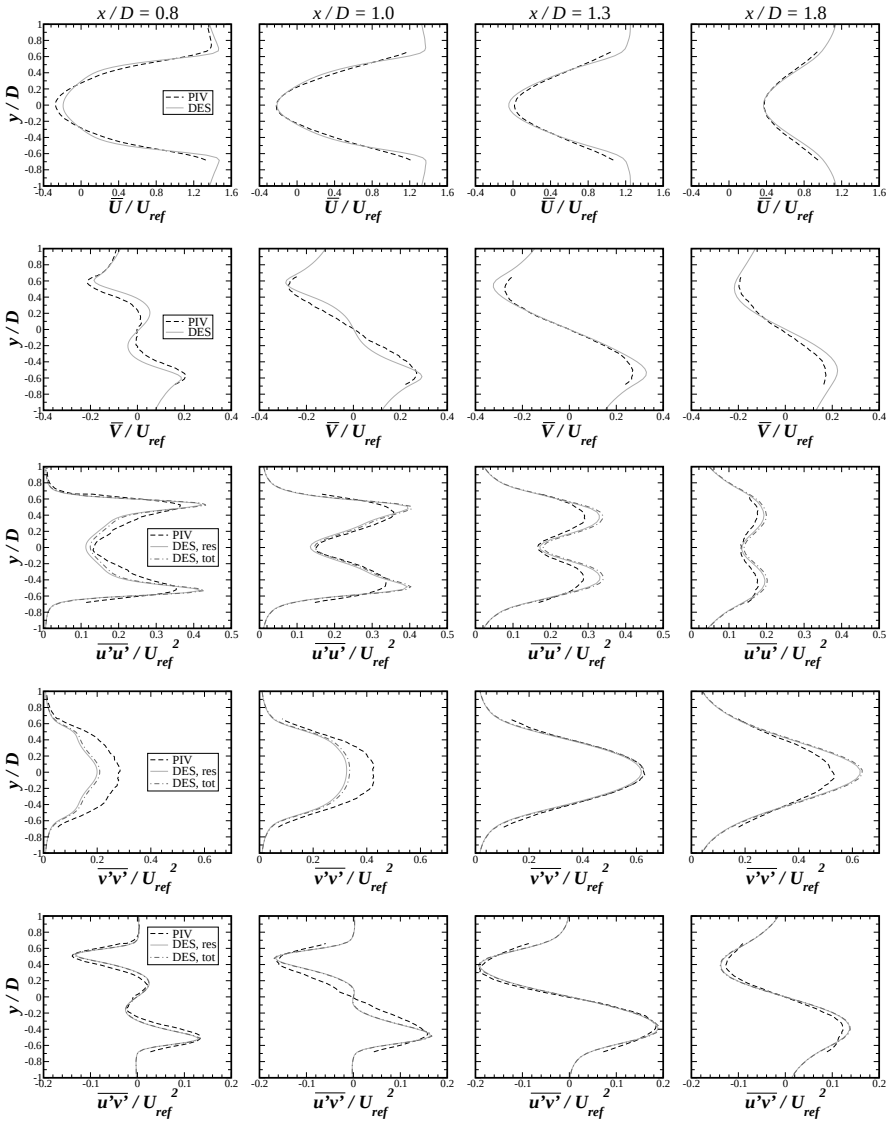

Figure 8.22: Comparison of time-averaged profiles at various x/D slices between 2C-PIV and DES (time and spanwise-averaged data).

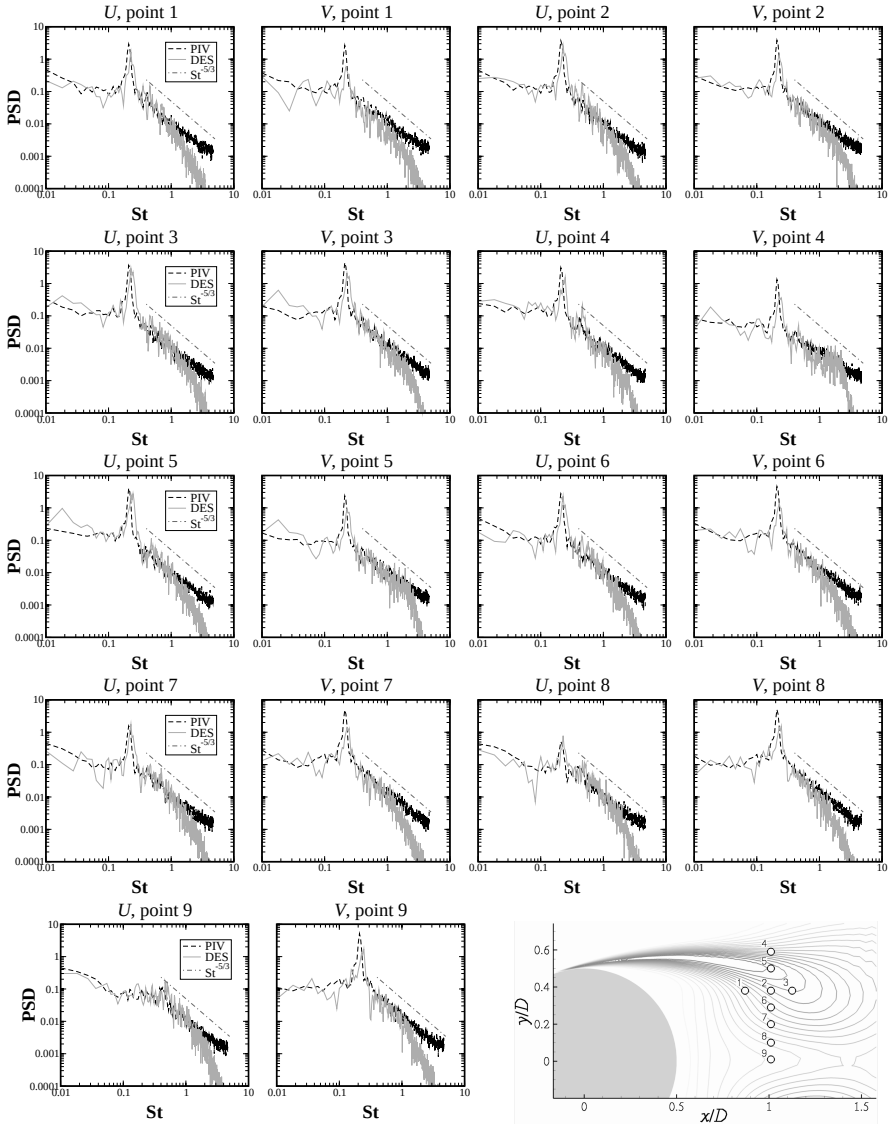

Figure 8.23: Comparison of U and V velocity spectra between DES and experiment (TRPIV) at nine probes in the near wake region.

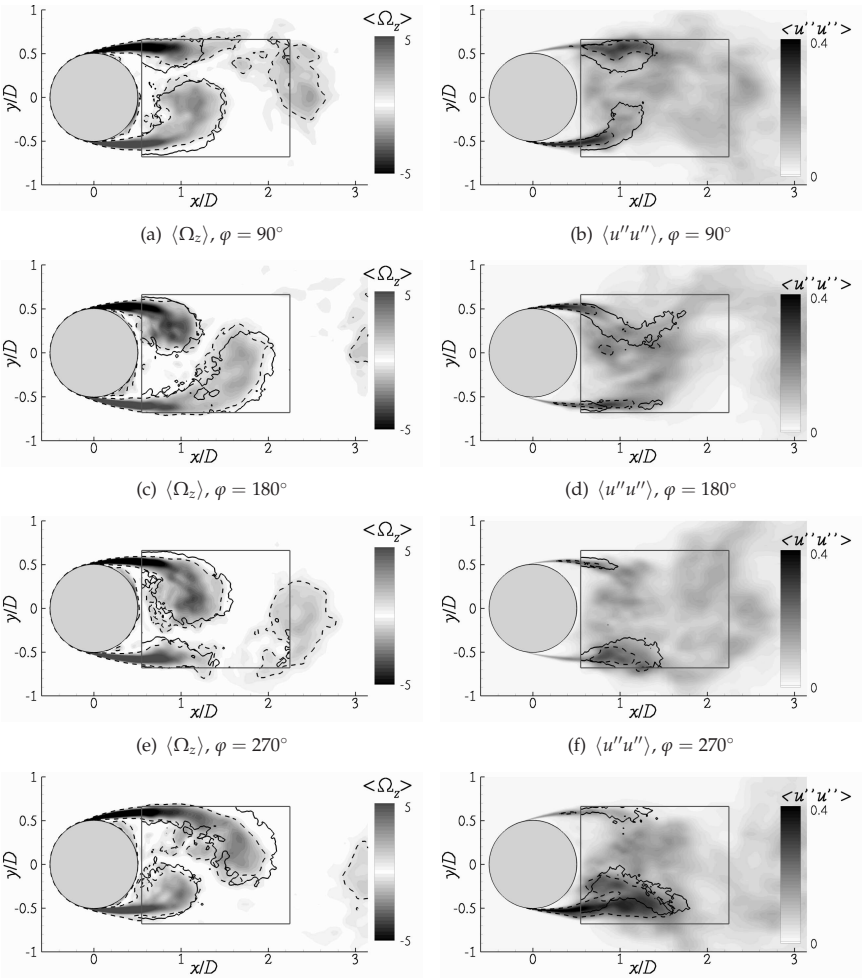

(a) $\langle \Omega_z \rangle$, $\varphi = 90°$ (b) $\langle u''u'' \rangle$, $\varphi = 90°$

(c) $\langle \Omega_z \rangle$, $\varphi = 180°$ (d) $\langle u''u'' \rangle$, $\varphi = 180°$

(e) $\langle \Omega_z \rangle$, $\varphi = 270°$ (f) $\langle u''u'' \rangle$, $\varphi = 270°$

(g) $\langle \Omega_z \rangle$, $\varphi = 360°$ (h) $\langle u''u'' \rangle$, $\varphi = 360°$

Figure 8.24: Phase-averaged spanwise vorticity $\langle \Omega_z \rangle$ (left) and streamwise turbulent stress $\langle u''u'' \rangle$ (right) for phase angles $\varphi = 90°$, 180°, 270° and 360°. Contour shading from DES. Contour lines depict values of $\langle \Omega_z \rangle = \pm 1$ and $\langle u''u'' \rangle = 0.2$ for the PIV (——) and DES (– – –).

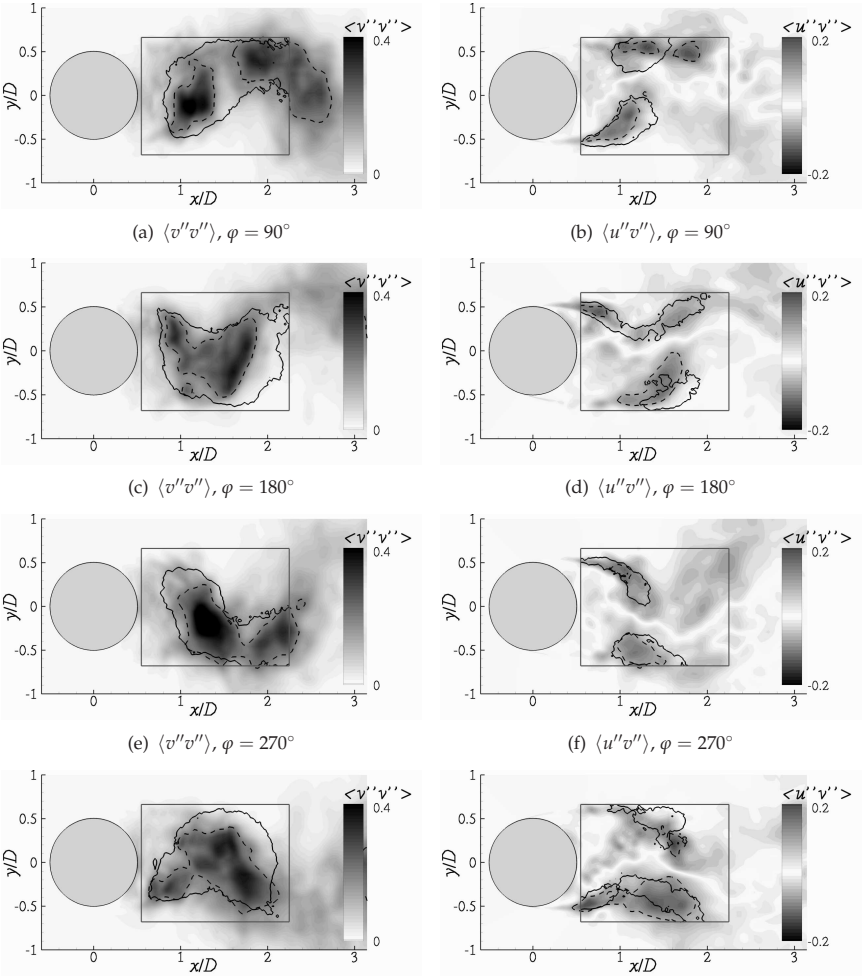

(a) $\langle v''v'' \rangle$, $\varphi = 90°$ (b) $\langle u''v'' \rangle$, $\varphi = 90°$

(c) $\langle v''v'' \rangle$, $\varphi = 180°$ (d) $\langle u''v'' \rangle$, $\varphi = 180°$

(e) $\langle v''v'' \rangle$, $\varphi = 270°$ (f) $\langle u''v'' \rangle$, $\varphi = 270°$

(g) $\langle v''v'' \rangle$, $\varphi = 360°$ (h) $\langle u''v'' \rangle$, $\varphi = 360°$

Figure 8.25: Phase-averaged vertical turbulent stress $\langle v''v'' \rangle$ (left) and turbulent shear stress $\langle u''v'' \rangle$ (right) for phase angles $\varphi = 90°$, $180°$, $270°$ and $360°$. Contour shading from DES. Contour lines depict values of $\langle v''v'' \rangle = 0.2$ and $\langle u''v'' \rangle = \pm 0.1$ for the PIV (——) and DES (– – –).

8.5.5 Phase-averaged flow field

The quasi-periodic nature of the vortex shedding enables an analysis using phase-averaging to separate the coherent vortex shedding from the incoherent turbulent motions. Reference is made to Appendix F, where this process and the notation of the different components are described. Phase averaging has been performed for both the PIV and simulation data, using the surface pressure on the cylinder as a trigger signal [108, 112], facilitating a deeper comparison of the unsteady flow prediction. The left hand column of Fig. 8.24 shows the phase-averaged spanwise vorticity, $\langle \Omega_z \rangle$, for the phase angles $\varphi = 90°$, $180°$, $270°$ and $360°$. The contour shading and dashed contour lines are taken from the DES, whereas the solid contour lines are from the PIV. In both cases, the contour lines represent the values $\langle \Omega_z \rangle = \pm 1$. The positions of the shed vortices are predicted very well by the DES, although a slight and consistent upstream shift is observed. Considering that a *downstream* shift in the wake length was seen in the time-averaged data (Fig. 8.20), this is at first sight paradoxical. A viable mechanism to explain this can however be outlined: The snapshots falling within the weak shedding cycles cannot easily be allocated a phase angle, due to the breakdown of the regular shedding motion. For this reason, the weak shedding events are detected using a procedure described in [110] and neglected from the phase averaging. The discussion surrounding Fig. 8.17 indicated that the weak shedding cycles are associated with a lengthening of the wake. The weak and strong shedding behaviour emerges sporadically. If the DES time series employed for statistical analysis happens to involve a greater proportion of weak shedding behaviour than the experimental sample, this would explain the phenomenon. To prove or disprove this, a selective Reynolds averaging could be carried out employing the same criteria as employed in the phase averaging to neglect the weak shedding events.

Nonetheless, the discrepancy between the phase-averaged vortex locations of the DES and experiment is minor. The process by which the shear layers roll up into the coherent vortex street is hence predicted very well by the DES, both qualitatively and quantitatively.

The phase-averaged incoherent contributions to the turbulent stresses, $\langle u_i'' u_j'' \rangle$ are similarly plotted for the same phase angles in the right hand side of Fig. 8.24 and in Fig. 8.25. The line contours continue to represent the same values for both the DES and the experiment, with the thresholds $\langle u''u'' \rangle = \langle v''v'' \rangle = 0.2$ and $\langle u''v'' \rangle = \pm 0.1$ chosen. The topology of the incoherent stresses agrees very well with the experiment over all phase angles: The shear layers exhibit maxima of $\langle u''u'' \rangle$ and $\langle u''v'' \rangle$, the vortex centres maxima of $\langle u''u'' \rangle$ and $\langle v''v'' \rangle$ and the saddle points maxima of $\langle u''v'' \rangle$. However, the magnitude appears in all cases to be under-predicted by the DES. Possible explanations for this are suggested:

- The modelled turbulence quantities were not included in the phase averaging procedure so the $\langle u_i'' u_j'' \rangle$ data hence represents the resolved portion only. Including the modelled contribution would thus improve the agreement.

- A related point concerns the grid resolution: The spectra of Fig. 8.23 demonstrate a sharp cut-off in the resolved energy at high frequencies due to the grid filtering. Ideally, this energy would be represented by the subgrid-scale model. That the cut-off concerns amplitudes at least a decade lower than the strongest resolved incoherent scales implies however that the unresolved quantities are minimal.

- Statistical convergence: this was shown to be imperfect for the time-averaged drag, and the situation can be expected to be much worse for the quantities considered here – the number of samples is considerably less (around 85 per phase angle compared to 14000 for the Reynolds-averaging) and second-order statistics are furthermore considered. The poor statistical convergence is reflected in the fairly noisy appearance of the data.

- An under-prediction of the incoherent contributions to the Reynolds stresses together with the slight over-prediction of the total Reynolds stresses (e.g. Fig. 8.21) could arise from a prediction of excessive coherent motion strength in the simulation.

It could indeed be the case that a combination of these possibilities is in effect. It is in any case clear that the balance of coherent and incoherent motion is strongly dependent on the statistical sample: Predominantly coherent motion has been associated with the strong shedding regime and an incoherent character with the weak shedding (Fig. 8.17). The transition between these regimes is apparently random and with a very long time scale (around an order of magnitude larger than the shedding period). All of this serves to underline the fact that the collection of phase-averaged data from such simulations requires extremely long time samples that well exceed those obtainable using currently acceptable computing capacity. As described in Section 6.5, an alternative phase averaging technique can be applied whereby POD coefficients from each velocity field snapshot are used to determine the phase angle. This has since been applied to this data by Perrin et al. [110], and an improvement in the quality of the data (in particular a cleaner separation of the coherent and incoherent contributions to the motion) was reported.

Despite these limitations, it can nonetheless be said that the prediction of the phase-averaged motion by the DES agrees well with the experiment to within the level of accuracy that can be obtained statistically. The validation of the DES with experimental data for the cylinder case can hence be considered extremely successful, with impressive levels of agreement achieved in the integral drag coefficient, the mean velocity field and Reynolds stresses, the vortex shedding frequency, the velocity spectra and the phase-averaged data.

One caveat must however be acknowledged. In Sect. 6.5, a serious limitation in the comparability between experiment and simulations was identified for this test case, namely the neglection of the appreciable levels of free stream turbulence (the effect

of which was described in Sect. 2.5.2). In the following Sect. 8.6, an extreme sensitivity of the flow prediction to the numerical time step size will be presented and discussed for the cylinder case. Because only two values of time step have been computed, there is no reason to suppose that the finer time step applied here corresponds to time step convergence. It is highly possible therefore, that a further refinement of the time step would in fact give rise to a degradation of the agreement with the experiment. It is thought that a cancellation of errors is in effect here, i.e. the neglected FST effects are compensated for by a residual level of time filtering. Dissatisfying though this is to the purist, the value of these results is not diminished entirely: They show that provided the correct separation point and shear layer transition behaviour occurs, excellent wake flow prediction can be achieved by the adopted simulation methodology.

8.6 Time step sensitivity

Besides the detailed validation of DES presented in the preceding section, the cylinder test case was also employed to determine the sensitivity of the solution to the numerical time step size. As has been established in Sect. 3.5.2, a time step size corresponding to a CFL number [31] of unity is a common guideline for LES. This therefore applies in the LES mode region of DES, and indeed this guideline is invoked for DES by Spalart [154]. From the point of view of industrial practice however, such limitation of the time step gives rise to a considerable increase in the computational cost of DES. Particularly in comparison to URANS, for which significantly coarser time steps can be applied, the LES time step criterion often results in surprisingly high computational costs for DES (as the focus when estimating computational cost often appears to be on the grid cell count). It is of great practical interest therefore to quantify the influence of a coarser time step in DES. Can an approximately valid solution be obtained at a fraction of the computational cost in this manner?

In addition to the time step $\Delta t = 0.03D/|U|_\infty$ applied in Sect. 8.5, a slightly coarser time step of $\Delta t = 0.05D/|U|_\infty$ has been used. In all other respects, the simulation setup is identical. As mentioned in Sect. 6.5, the same physical time sample length has been computed for statistical evaluation.

An idea of the impact of the time step size can be obtained from the instantaneous field. Figure 8.26 shows the resolution of vortical structures and the model eddy viscosity in the early shear layer for an individual snapshot for each time step size. Whereas the shear layer for the finer time step shows the development of instabilities, the shear layer for the coarser time step remains smooth and stable. Moreover, although the resolved turbulence is significantly reduced by the coarser time step, the level of modelled turbulence (represented by the eddy viscosity ratio in Figs. 8.26(c) & 8.26(d)) remains very similar.

It appears then as if the coarser temporal resolution does not allow the formation of

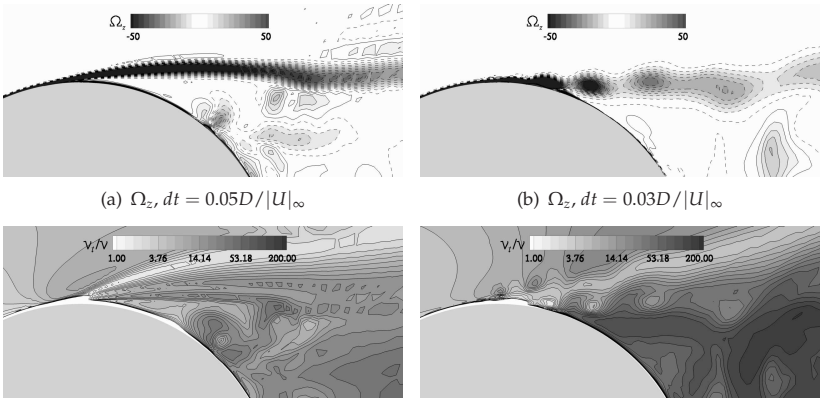

(a) Ω_z, $dt = 0.05D/|U|_\infty$ (b) Ω_z, $dt = 0.03D/|U|_\infty$

(c) ν_t/ν, $dt = 0.05D/|U|_\infty$ (d) ν_t/ν, $dt = 0.03D/|U|_\infty$

Figure 8.26: Effect of time filtering on resolved shear layer structures and modelled turbulence for coarse and fine time steps (contours of spanwise vorticity Ω_z and eddy viscosity ratio ν_t/ν on a slice at the spanwise mid-section).

these structures in the shear layer, and that a time filtering effect occurs. To investigate the potential of the CFL number as a rule of thumb, a temporal filter width is constructed as $\Delta_t = |U|\,\Delta t$. When the ratio of this to the local spatial filter width is considered, a kind of CFL number emerges:

$$\mathrm{CFL} = \frac{\Delta_t}{\Delta_x} = \frac{\Delta t\,|U|}{\Delta_x}\,, \tag{8.13}$$

where $|U|$ is the local velocity magnitude and Δ_x is the DES grid length scale. The precise definition of the quantities making up the CFL number is in some respects open to interpretation. The choice of quantities here is motivated by the interest in balancing the spatial and temporal capability to resolve turbulence, hence the use of the largest grid dimension for Δ_x. The expectation is therefore that a criterion of $\mathrm{CFL} \leq 1$ is necessary in all regions of resolved turbulent flow.

Figure 8.27 shows the distribution of the CFL number for the coarse and fine time steps. It is seen that the criterion is met throughout the domain for the finer time step, whereas values greater than unity emerge, notably at the edge of the early shear layer, for the coarser time step. From these observations, it seems as if this kind of CFL criterion could indeed offer a sound basis for the judgement of the sufficiency of the time step size for DES.

To provide a quantitative assessment of the time step influence, the time-averaged and phase-averaged flow field is considered. The time-averaged streamlines are

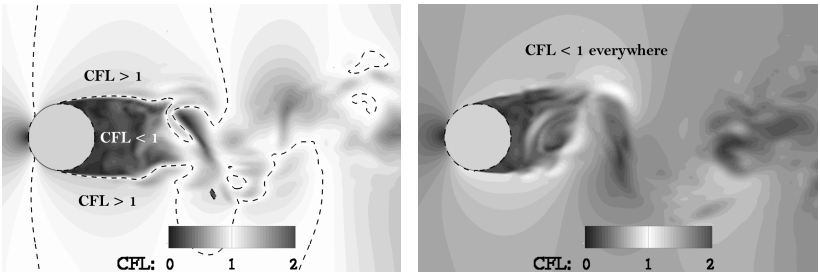

(a) CFL, $dt = 0.05D/|U|_\infty$ (b) CFL, $dt = 0.03D/|U|_\infty$

Figure 8.27: Extent of time filtering of resolved scales depicted using a CFL number for the coarse and fine time steps (slice at the spanwise mid-section).

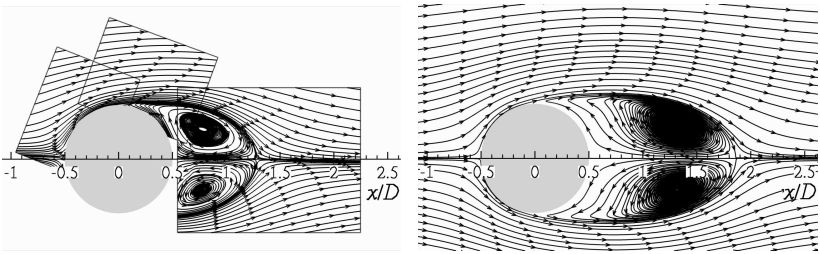

(a) PIV (b) DES, $dt = 0.05D/U_\infty$

Figure 8.28: Comparison of the time-averaged streamlines for the DES with the coarse time step and experiment.

compared with the PIV data in Fig. 8.28. Recall that an excellent agreement was observed between the experiment and the fine time step in Fig. 8.20, whereas the coarse time step exhibits an excessive recirculation length. The recirculation length (measured from the rear surface of the cylinder at $x/D = 0.5$) is 1.36, in comparison to 0.78 for the experiment and 0.85 for the fine time step. This is accompanied by a strong under-prediction of the pressure drag coefficient at the centre plane at $C_{d,p} = 1.12$ in comparison to 1.45 and 1.48 for the experiment and fine time step, respectively. It is interesting to note that all of the cases presented by Travin et al. [171] in their cylinder flow DES study suffered from an excessive recirculation length. As these employed the same time step size as the coarse time step computed here, this suggests (at least for higher Re values) that insufficient time resolution may have been a contributory factor.

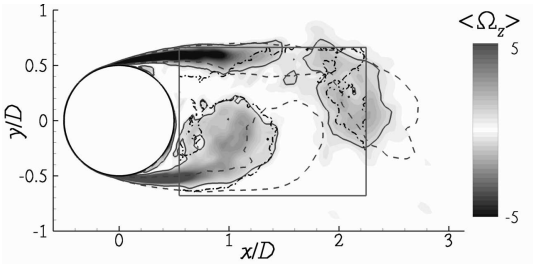

Figure 8.29: Phase-averaged spanwise vorticity $\langle\Omega_z\rangle$ for a single phase angle $\varphi = 45°$. Contour shading from DES with finer time step. Lines depict values of $\langle\Omega_z\rangle = \pm 1$ for the PIV (– · –·), DES with finer time step (—) and coarser time step (– – –).

Turning to the phase-averaged flow, contours of the phase-averaged spanwise vorticity $\langle\Omega_z\rangle$ are compared in Fig. 8.29 for the single phase angle $\varphi = 45°$ between both time step sizes and the PIV data. As established in greater detail in Sect. 8.5, the position of the shed vortices is predicted very well by the finer time step. The roll-up of the shear layer can however be seen to be significantly delayed for the coarser time step, resulting in a downstream displacement of the vortex locations.

In summary then, these results indicate that the coarse time step hinders the development of turbulent structures in the early shear layer, and that this deficit in resolved turbulence is not compensated for by an increase in modelled turbulence. Even this relatively mild coarsening of Δt causes a drastic degradation in the prediction of the wake flow, which serves to underscore the importance of sufficient time resolution. As a result, any application of DES with a coarser time step for pragmatic reasons should not be recommended .

The fact that the deficit in LES turbulence caused by the time filtering is not compensated by RANS turbulence is caused by the dependency of the LES/RANS switching on the spatial resolution alone. As such, some inclusion of the temporal filter width in the DES length scale definition, such as that proposed by Bush & Mani (Sect. 3.7.6) may hold some promise to reduce the time step dependency. The goal of such a modification would be to provide a more gradual and predictable decay of solution quality with increasing Δt. In the limit case of a very coarse time step, such a modified DES formulation should tend to a URANS solution. This would significantly enhance the robustness of the method in an industrial context, perhaps making the coarsening of the time step a justifiable means to sacrifice a limited degree of solution quality in the interests of a reduced computational burden.

It could be argued that this case is unusually sensitive to time step effects, and that the strong warning issued regarding practical applications could be exaggerated: Es-

pecially at this precritical Reynolds number (Sect. 2.5.2), even small changes in the shear layer turbulence level would have a very strong impact on the global flow. However, it is believed that this case is highly representative of natural DES applications to bluff bodies in general. The highest CFL numbers in the flow can be expected to occur at the region of highest velocity, which would likely coincide with the separation point. For natural DES the upstream turbulent boundary layer structures are modelled entirely by RANS, meaning that the LES resolved structures in the shear layer must develop via a quasi-transition mechanism (as noted in the description of the grey area problem, Sect. 3.7.3). A high sensitivity to the time step size can hence be anticipated for all such flows, even at turbulent separation Reynolds numbers. Only low Reynolds number flows where the early shear layer is laminar should be expected to be more tolerant of coarser time steps.

8.7 Comparison of DES with experiment for the bump test case

Excellent agreement with reliable and comprehensive experimental data has been reported in Sect. 8.5 for the type of flow for which DES was intended, namely massively separated bluff body flow. In this section, a comparison with experimental data will be carried out for a contrasting flow for which it can be expected that DES will encounter many problems. The flow phenomena occurring in the bump test case and the challenges that these present to DES are described in detail in Sect. 6.6. Much discussion of the results for this test case has already been offered in Sect. 8.4.2, which will be referred to whenever the differences occurring between the SAE and CEASM background models become relevant. Only the results from the shielded DES variants (the CEASM-DES with model-specific GIS shield, Sect. 5.5.4, and the SAE-DDES formulation) will be discussed here: The effect of the IDDES modifications are to be treated in Sect. 8.9.

Beginning with the pressure coefficient plots of Fig. G.2, it can indeed be seen that the agreement with experiment is very poor: A significantly under-proportioned separation region is predicted by both models, although the CEASM-DES results are better than those of the SAE-based DES. The CEASM-DES outperforms the SAE-DDES in a further respect, namely the level of spanwise homogeneity. Both the experiment and the CEASM-DES return nearly identical pressure profiles at $z = 0$, $z = 0.085$ and $z = 0.17$, whereas those of the SAE-DDES differ fairly strongly. In Sect. 8.4.2 this higher three-dimensionality was explained with reference to Fig. G.7 in terms of the stronger separated streamwise vortices predicted by the SAE-DDES. Although no transverse measurements are available from the experiment downstream of the bump, it can be supposed that the strength of the side vortices is over-predicted by both simulations. This would agree with a common observation that RANS models predict excessively strong corner separations[15]. Further evidence for this is offered

[15] Examples include the computation of the A-airfoil including spanwise end plates and the excessive streamwise vortices suppressing flow separation in the symmetry plane for the idealised Ahmed car body case, both of which are reported in the FLOMANIA project [55].

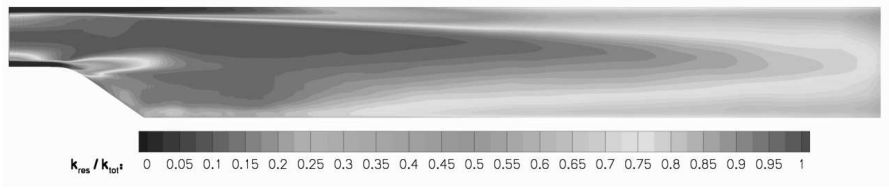

Figure 8.30: Ratio of resolved to total kinetic energy at the symmetry plane for CEASM-DES.

by the computations of Davidson for this test case [33]: In order to reduce the grid size, a thinner spanwise domain extent was computed and the side walls were neglected. These results achieved, in some respects, the best agreement with the experimental data of all the DESider computations [56].

The mean velocity profiles at the symmetry plane are compared between the experimental LDV and the computations in Fig. G.3. Again, strong discrepancies are observed with the experimental data together with a clear trend in favour of the CEASM-DES over the SAE-DDES. The comparison of the Reynolds shear stress in Fig. G.4 suggests that both models predict the correct maximum level throughout the duct, once the distortion of the profiles by the mean flow discrepancy is taken into account. The stations further downstream exhibit larger discrepancies in the shear stress, and the higher values for the experiment are believed to reflect the flow reattachment much further downstream than the computations.

The high level of accuracy in the prediction of the peak Reynolds shear stresses in the shear layer (e.g. at $x = 0$), together with the rapid development of the resolved component and its dominance over the modelled component, suggest that the grey area problem (Sect. 3.7.3) is not an important issue for this flow. Further evidence for this is obtained from Fig. G.5, where a very rapid development of resolved turbulence is seen (this plot is shown only for the SAE-DDES as there is no notable difference between the models). This is perhaps contrary to expectation: The thin, shielded, high-Reynolds-number oncoming boundary layer contains entirely modelled turbulence and the level of recirculation of resolved turbulence was expected to be weak. However, the strong recirculation regions seen in the corners downstream of the bump (Fig. G.6) buffet the shear layer with resolved structures, which likely drives the development of resolved turbulence following separation. To give an estimate of the extent of the grey area region, the ratio of resolved to total turbulent kinetic energy (computed as described in Appendix E) is plotted in Fig. 8.30. Indeed, assuming the region $k_{res}/k_{tot} \geq 0.8$ to correspond to a sufficient level of resolved LES content (refer to the 80% estimate of Pope [116], discussed in Sect. 3.5.2), a grey area length of around 30% of the bump height can be estimated. Whether this can be considered long or short would require a broader comparison with other test cases.

DES therefore can be said to encounter significant problems with this test case, for both of the the background models chosen. Of the two supposed failure mechanisms, namely inaccuracy of the RANS solution region and a protracted grey area problem, the former is believed to be principally responsible. The strong degree of model dependency established in Sect. 8.4.2 adds weight to this conclusion, underlining both the weaknesses of RANS models in such complex flows and the sensitivity of the global flow to the upstream boundary layer prediction.

8.8 Investigation of wall-modelled LES of channel flow

A thorough investigation of the IDDES method (published by Travin et al. [170] and Shur et al. [149]) on the basis of the canonical turbulent channel flow test case will be presented. The method has been introduced in Section 3.7.5 and implemented as described in Section 5.5.5, and the numerical setup and description of the channel flow can be found in Section 6.2. Background information concerning the flow physics is presented in Section 2.4. An impression of the improvement offered by IDDES over a DES97 simulation is given in Section 8.8.1 followed by a more detailed examination of the IDDES blending function behaviour in Section 8.8.2. The grid requirements and numerical cost scaling of WMLES are then discussed in Section 8.8.3. Finally, the scope for easing the wall-normal grid resolution requirements by employing the hybrid-adaptive wall boundary condition of Rung et al. [135] (presented in Appendix C) is investigated in Section 8.8.4 for the extreme case of cubic grid cells.

To reduce repetition of figures and to enhance comparability between different cases, visualisations of the same quantity have been grouped into single combined figures. As a result, some figures referred to in the earlier sections also contain results pertaining to later discussions.

8.8.1 Comparison of DES97 and IDDES

To provide an initial impression of the IDDES implementation before a more detailed analysis of the blending functions in Section 8.8.2, a comparison is made with a computation employing DES97. Both simulations were carried out on a wall-refined grid at $\mathrm{Re}_\tau = 4000$ (i.e. case WR-4000 from Tab. 6.1) and employed the CEASM-based DES implementations. One modification was however made for the CEASM-DES97 computation compared to the standard formulation, namely the filter was defined as $\Delta = \sqrt[3]{\Delta x\, \Delta y\, \Delta z}$ instead of the standard maximum edge length expression. This was motivated by the consideration that the cube-root definition is widely accepted as common practice for fully-resolved LES of wall-bounded flows. This means that the comparison is not ideal for the purposes of this discussion: The improvement achieved by IDDES is of course best demonstrated relative to a DDES computation. The reader is referred to the papers of the method authors [149, 170] for this. The influence of this modification can be assessed by comparison with the results published by Nikitin et al. [101] and Piomelli et al. [114], who employed the DES-standard max-

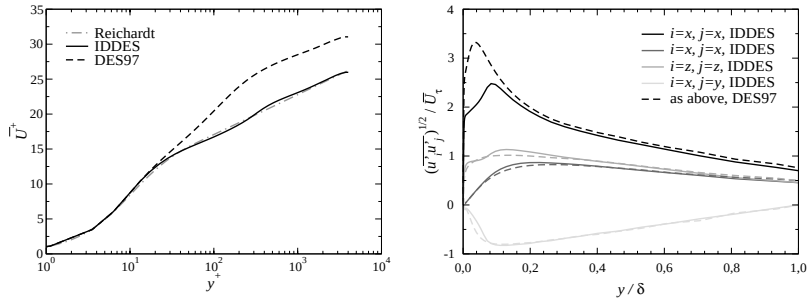

(a) Mean velocity profiles

(b) Resolved Reynolds stresses

Figure 8.31: Comparison of IDDES with DES97 for fully-developed channel flow at $\mathrm{Re}_\tau = 4000$, CEASM model.

imum expression for Δ in their studies of DES97 for channel flow.

The mean velocity profiles and resolved Reynolds stresses are compared in Fig. 8.31. A strong displacement of the log-law region at y^+ values greater than around 400 is seen for the DES97 computation, which is connected relatively smoothly to the viscous sublayer region by what appears to be an extended buffer layer. The impact of this log law displacement can be seen in Tab. 8.8 and Fig. 8.33 where the skin friction coefficient is compared with the value from Dean's correlation. A significant deviation of -28.59% is seen for the DES97.

The displacement of the log law region agrees well with the results obtained by Nikitin et al. [101] at similar Reynolds numbers, however the transition region is more compact in their simulations. Indeed, two distinct log law regions can be discerned in the Nikitin et al. profiles, one provided by the RANS model that reaches up to $y^+ \approx 100$, and one from the LES resolution of the core flow. These are separated by what is termed a "super buffer layer". The reason for this discrepancy is clearly the Δ formulation, as the cube-root variant pushes the LES-RANS interface much closer to the wall for the high aspect-ratio cells there.

By comparison, the IDDES velocity profile shows much improvement with very good agreement relative to the Reichardt correlation and Dean's skin friction correlation (Tab. 8.8) achieved. Only a minimum of log layer mismatch (LLM) remains, visible in the form of a small kink in the profile at $y^+ \approx 300$. Considering that the method was adopted directly from the published SST-variant without any additional tuning of the model-specific C_l and C_t parameters, this is highly satisfactory. When the resolved Reynolds stresses are examined, it can be seen that the principal discrepancy occurs in the near wall region at $y/\delta < 0.1$ (corresponding to $y^+ < 400$).

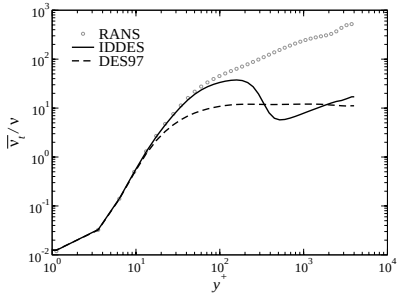

Figure 8.32: Profiles of time-averaged eddy viscosity ratio for RANS, IDDES and DES97 for fully-developed channel flow at $\mathrm{Re}_\tau = 4000$, CEASM model.

Here, the streamwise Reynolds stresses continue to be resolved closer to the wall by the DES97, whereas these are fairly strongly damped by the IDDES. This trend can also be observed, albeit less markedly, for the resolved shear stress profiles. The good agreement between the methods for the Reynolds stresses and log law slope in the channel core lends weight to the interpretation that the DES97 operates correctly in LES-mode when sufficient grid resolution is available and that the problem arises from the "boundary condition" provided to the LES core by the near wall region.

Some insight into the model activity can be obtained from Fig. 8.32, in which profiles of the time-averaged eddy viscosity ratio are compared between RANS, DES97 and IDDES. The near-wall eddy viscosity of the IDDES follows the RANS values very closely before switching fairly sharply to values approximately one order of magnitude lower at $y^+ \approx 300$. Although the eddy viscosity levels for the DES97 are approximately similar in the LES region, a strong depletion of the model activity (relative to the RANS and IDDES curves) is observed right down to the viscous sublayer. The nature of the IDDES profile provides evidence of the "sharpening" of the RANS-LES interface achieved by the IDDES blending functions mentioned in Section 3.7.5.

The behaviour of this DES97 simulation contrasts strongly to the DDES simulations for channel flow presented for comparison in the publications of the IDDES method by Travin et al. [170] and Shur et al. [149]. The action of the DDES shield function in fact generates higher eddy viscosity levels near the wall, which are damped less sharply in the transition to the LES region.

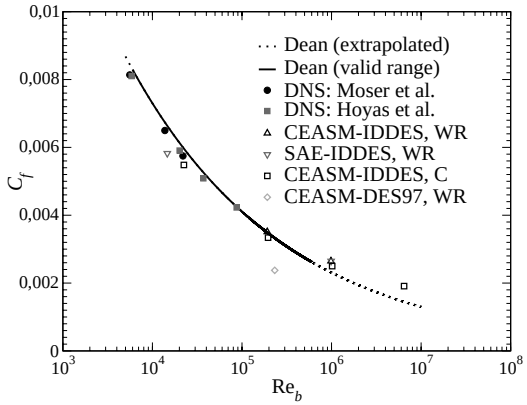

Figure 8.33: C_f dependency on Re_b compiled for all simulation data, compared with the DNS data of Moser et al. [100] and Hoyas et al. [63] and with the empirical correlation of Dean [34].

Model	Case	$\overline{U}_\tau$	$\overline{U}_b^+$	$\overline{U}_\delta^+$	C_f deviation (%)
CEASM-DES97	WR-4000	0.9992	29.02	31.05	−28.59
CEASM-IDDES	WR-4000	1.0036	23.86	25.97	0.66
CEASM-IDDES	WR-18000	0.9964	27.48	29.62	14.34
SAE-IDDES	WR-395	1.0010	18.53	20.90	−12.23
SAE-IDDES	WR-18000	0.9993	27.49	29.55	14.36
CEASM-IDDES	C-590	0.9959	19.10	21.34	−8.08
CEASM-IDDES	C-4000	0.9988	24.48	26.59	−3.83
CEASM-IDDES	C-18000	0.9980	28.28	30.71	8.74
CEASM-IDDES	C-100000	0.9979	32.36	34.75	31.90

Table 8.8: Global characteristics of the channel flow simulations and percent deviation in skin friction coefficient relative to the empirical correlation of Dean [34] (given by $[(C_f - C_{f,Dean})/C_{f,Dean}] \times 100$).

The comparison of DES97 with IDDES can be rounded up by inspection of instantaneous flow field snapshots. The x-vorticity contours at slices normal to the streamwise direction (Fig. 8.34) show the higher damping of resolved structures in the very near wall region by IDDES, which is caused by the higher eddy viscosity levels there (Fig. 8.35). The y-vorticity contours at a near-wall tangential slice (Fig. 8.36) show the occurrence of excessively long "super streaks" in the DES97 resolved field, which are also stronger compared to the IDDES streaks. The occurrence of such structures and the phenomenon of LLM in general are acknowledged by Baggett [5] and Piomelli et al. [114] to be a common feature to many hybrid RANS-LES methods for WMLES.

8.8.2 Examination of IDDES functionality

Having gained an initial impression of the IDDES performance for WMLES of channel flow, a more detailed examination of the blending functions will be carried out. The response of CEASM-IDDES to a variation of the Reynolds number will first be considered, before the level of dependency on the background RANS model is assessed by comparison between the SAE-IDDES and CEASM-IDDES variants.

IDDES blending functions with varying Re_τ

Figure 8.37 presents a comparison of the mean velocity and resolved Reynolds stress profiles for the WR-4000 and WR-18000 cases with CEASM-IDDES. The grids are detailed in Tab. 6.1, however it is reminded that only the wall-normal grid spacing is adjusted between the Reynolds numbers. The velocity profile at $\mathrm{Re}_\tau = 18000$ shows a similar behaviour to that of $\mathrm{Re}_\tau = 4000$, although the residual LLM is perhaps slightly weaker for the higher Reynolds number case. The transition region between RANS and LES remains at a similar y/δ position (as can be determined from the inflection of the streamwise resolved Reynolds stress component), which corresponds to a higher $y^+ \approx 2000$ for the $\mathrm{Re}_\tau = 18000$ case. The skin friction coefficient shows a much increased deviation relative to Dean's correlation (Tab. 8.8 and Fig. 8.33) at the higher Reynolds number. However, the corresponding bulk Reynolds number lies outside the quoted validity range of Dean's correlation, so the extent to which this represents a genuine inaccuracy is unclear.

The instantaneous vorticity snapshots of Fig. 8.34 show the resolution of finer structures further into the channel core for the higher Reynolds number. The instantaneous eddy viscosity ratio plots of Fig. 8.35 indicate a similar distribution with elevated levels in the near-wall RANS region and at the coarser grid in the channel core. The general level of ν_t/ν is furthermore higher for $\mathrm{Re}_\tau = 18000$. The instantaneous vorticity parallel to the wall indicates similar streaky structures in both cases, which are perhaps more densely distributed at $\mathrm{Re}_\tau = 18000$. A direct comparison is potentially misleading however, as the slices are at different y^+ values in each case.

The mean eddy viscosity ratio variation with Reynolds number, plotted in Fig. 8.38, demonstrates the scaling of the interface region to higher y^+ with increasing Re_τ. In

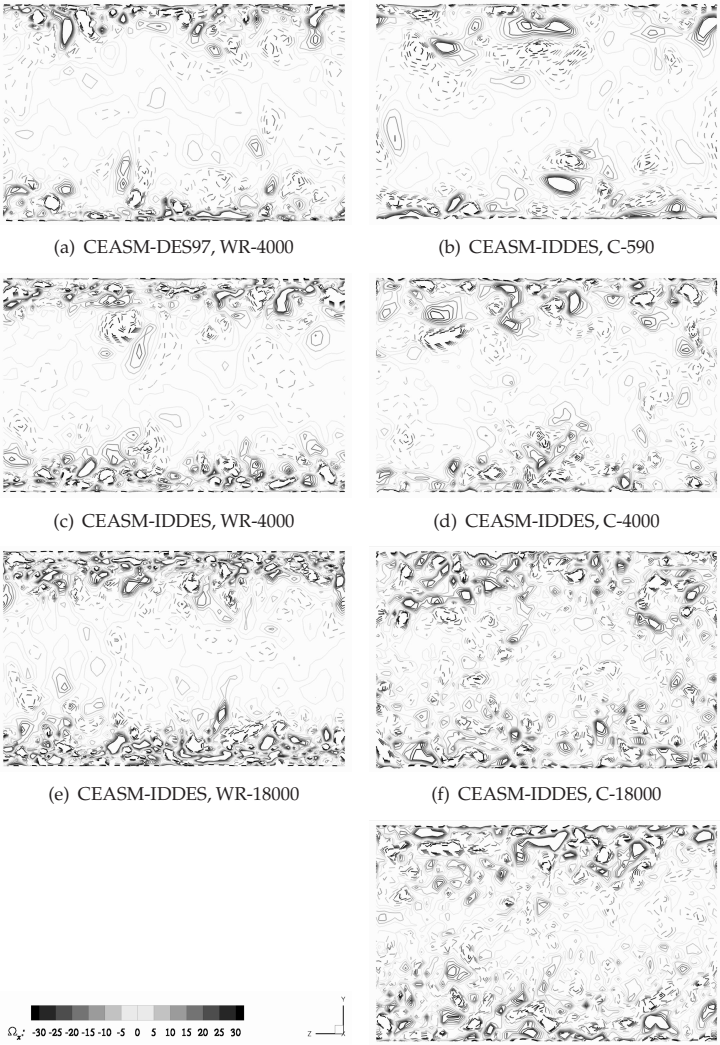

(a) CEASM-DES97, WR-4000

(b) CEASM-IDDES, C-590

(c) CEASM-IDDES, WR-4000

(d) CEASM-IDDES, C-4000

(e) CEASM-IDDES, WR-18000

(f) CEASM-IDDES, C-18000

(h) CEASM-IDDES, C-100000

Figure 8.34: Comparison of instantaneous x-vorticity at a constant x-slice between various simulations for fully-developed channel flow. Solid and dashed lines denote positive and negative values, respectively.

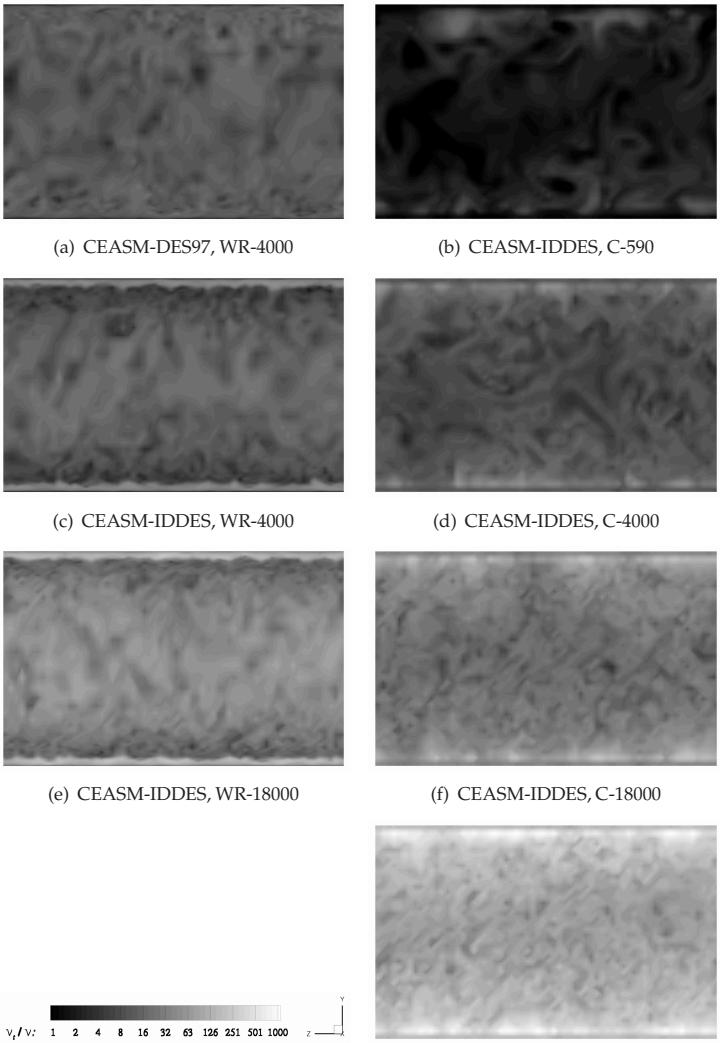

(a) CEASM-DES97, WR-4000

(b) CEASM-IDDES, C-590

(c) CEASM-IDDES, WR-4000

(d) CEASM-IDDES, C-4000

(e) CEASM-IDDES, WR-18000

(f) CEASM-IDDES, C-18000

(h) CEASM-IDDES, C-100000

Figure 8.35: Comparison of instantaneous eddy viscosity ratio at a constant x-slice between various simulations for fully-developed channel flow.

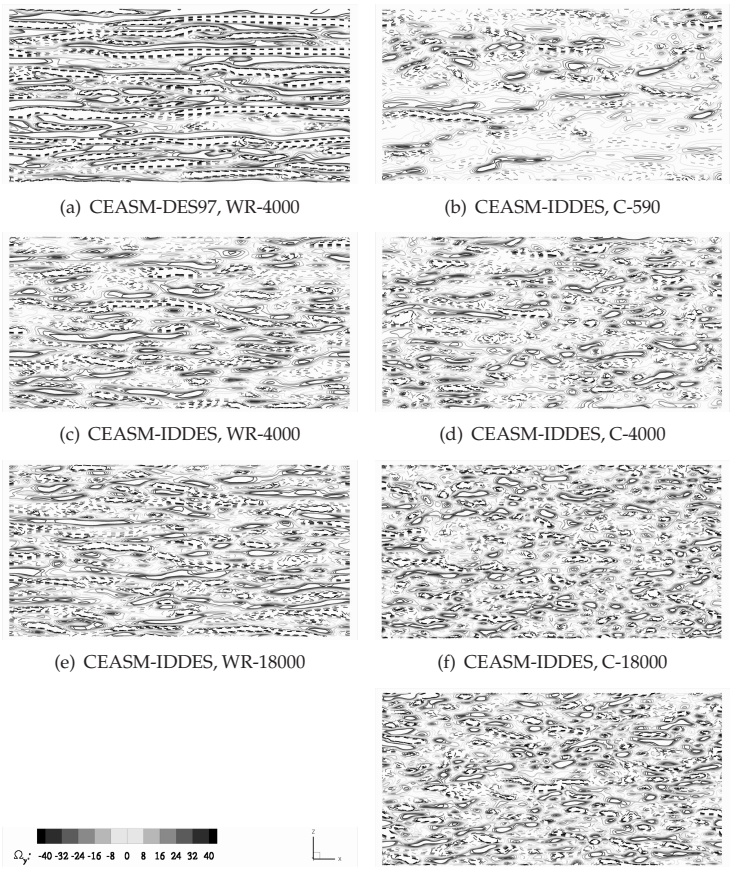

(a) CEASM-DES97, WR-4000

(b) CEASM-IDDES, C-590

(c) CEASM-IDDES, WR-4000

(d) CEASM-IDDES, C-4000

(e) CEASM-IDDES, WR-18000

(f) CEASM-IDDES, C-18000

(h) CEASM-IDDES, C-100000

Figure 8.36: Comparison of instantaneous y-vorticity at a slice $y/\delta = 0.05$ between various simulations for fully-developed channel flow. Solid and dashed lines denote positive and negative values, respectively.

both cases, the IDDES eddy viscosity follows that of the pure RANS simulation fairly closely up to the interface region, however some deficit is apparent just inside of the interface, on the RANS side. It is supposed that this could contribute to the residual LLM observed in the velocity profiles, a theme to be returned to in the following.

Some important IDDES blending functions are plotted for the CEASM-IDDES computations at $\mathrm{Re}_\tau = 4000$ and $\mathrm{Re}_\tau = 18000$ in Fig. 8.39. It must be noted that these

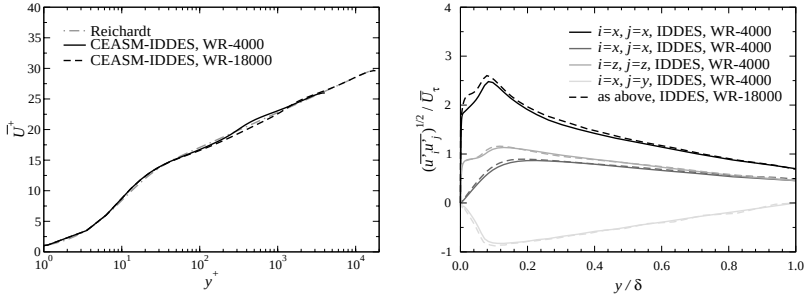

(a) Mean velocity profiles

(b) Resolved Reynolds stresses

Figure 8.37: Variation of Reynolds number for CEASM-IDDES for fully-developed channel flow at $\mathrm{Re}_\tau = 4000$ and $\mathrm{Re}_\tau = 18000$.

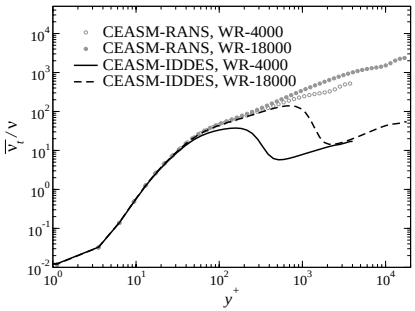

Figure 8.38: Profiles of time-averaged eddy viscosity ratio for RANS and IDDES of fully-developed channel flow at $\mathrm{Re}_\tau = 4000$ and $\mathrm{Re}_\tau = 18000$, CEASM model.

plots are extracted from a single wall-normal grid line and time step, so some fluctuation of the solution-dependent quantities must be borne in mind. The near wall reduction of the grid filter definition Δ, Eq. (3.23), is portrayed by its ratio to the maximum cell length h_{max}. This purely grid-dependent quantity is essentially identical for both simulations, as both exhibit similar wall-normal stretching ratios in the region of $k \leq 1 + C_w$ and the same tangential grid resolution. The filter width is therefore reduced compared to the standard DES Δ (which is equal to h_{max}) below around $y/\delta = 0.7$, and reaches a minimum near-wall value of $C_w h_{max}$.

The quantity $1 - f_{dt}$ shows the activity of the modelled log layer sensor, which as-

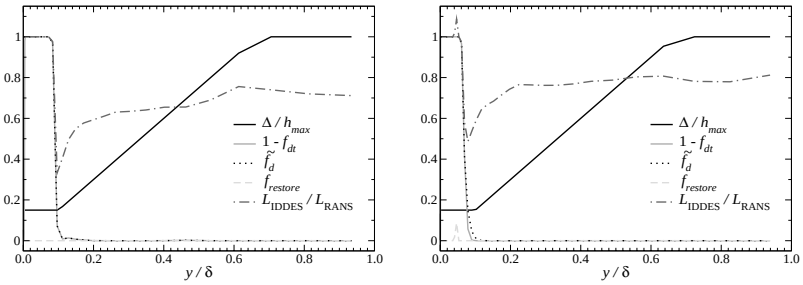

(a) WR-4000 (b) WR-18000

Figure 8.39: Instantaneous profiles of selected IDDES blending functions for CEASM-IDDES at $\mathrm{Re}_\tau = 4000$ and $\mathrm{Re}_\tau = 18000$.

sumes a value of unity within the RANS log layer region. This, together with the grid dependent f_{step} function (portrayed in Fig. 3.9), makes up the IDDES RANS-to-LES switching control $\tilde{f}_d$, which selects the maximum of each quantity, Eq. (3.35). $\tilde{f}_d$ is seen to follow the $1 - f_{dt}$ branch at $\mathrm{Re}_\tau = 4000$, which occurs at greater y/δ than the f_{step} transition (not shown). In the $\mathrm{Re}_\tau = 18000$ snapshot, $\tilde{f}_d$ follows $1 - f_{dt}$ initially, switching to f_{step} near to the end of the transition region.

The final component contributing to the IDDES length scale is the boosting function $f_{restore}$, Eq. (3.26). This is inactive in the $\mathrm{Re}_\tau = 4000$ snapshot and weakly active at $\mathrm{Re}_\tau = 18000$, giving rise to an amplification of L_{IDDES} just on the RANS side of the transition region. In comparison to the plots of these quantities published by Shur et al. [149], $f_{restore}$ appears to be insufficiently active in the CEASM-IDDES. This function is designed to counteract the damping of eddy viscosity on the RANS side of the interface by diffusive effects of the lower values on the LES side. As a result, it is supposed that this under-activity of $f_{restore}$ is the cause of the reduced eddy viscosity relative to the RANS value observed in Fig. 8.38, which was in turn identified as a possible reason for the residual LLM observed. A calibration of the model-specific C_l and C_t parameters is therefore seen as a promising route to improving the performance of the IDDES implementation.

The effect of the constituent blending functions on the IDDES length scale can hence be traced from the plots of Fig. 8.39, where the ratio $L_{\mathrm{IDDES}}/L_{\mathrm{RANS}}$ is shown[16]. The switching behaviour is determined by $\tilde{f}_d$ and $f_{restore}$, whereas the profile in the LES-mode region is determined by the Δ function. The reduced near-wall value of Δ gives

[16]The quantity L_{RANS} could possibly be misinterpreted – this is value of the RANS model length scale arising from the quantities k and ε present locally in the IDDES simulation. This is not the value of L_{RANS} that would be obtained from a RANS simulation.

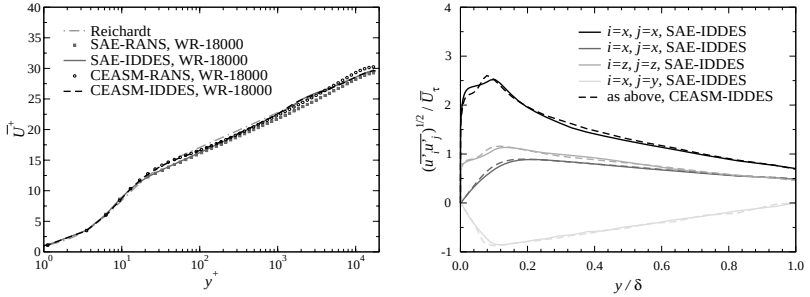

(a) Mean velocity profiles

(b) Resolved Reynolds stresses

Figure 8.40: Comparison of SAE-IDDES and CEASM-IDDES for fully-developed channel flow at $\mathrm{Re}_\tau = 18000$.

rise to the trough in the $L_{\mathrm{IDDES}}/L_{\mathrm{RANS}}$ distribution just on the LES-side of the interface. The peak-and-trough nature of the IDDES length scale around the interface is characteristic of the sharpened RANS-LES blending of IDDES compared to previous versions. The general level of $L_{\mathrm{IDDES}}/L_{\mathrm{RANS}}$ is seen to rise as the Reynolds number increases. The $L_{\mathrm{IDDES}}/L_{\mathrm{RANS}}$ profiles are qualitatively very similar to those of ν_t/ν (Figs. 8.35 and 8.38), indicating the strong linkage of these quantities.

Comparison of the SAE and CEASM IDDES variants

The mean velocity and resolved Reynolds stress profiles from SAE-IDDES and CEASM-IDDES simulations at $\mathrm{Re}_\tau = 18000$ are compared in Fig. 8.40. The velocity profiles are highly similar above $y^+ \approx 600$ indicating that the RANS-LES blending and LES mode functionality of the implementations is equivalent. A similar level of residual LLM is also seen for the SAE-IDDES and the skin friction coefficient values give a very similar discrepancy relative to Dean's correlation (Tab. 8.8 and Fig. 8.33). The inclusion of the RANS velocity profiles for each model in Fig. 8.40 elucidates the deviation around the early log law region. In line with expectation therefore, the RANS-mode region of IDDES is dominated by the particular RANS formulation employed. The C_f similarity however indicates that the near-wall differences exert a minimal influence on the global characteristics.

The resolved Reynolds stress profiles also reveal very similar behaviour in the LES-mode region. Minor differences are seen in the near wall region $y/\delta < 0.1$, where the damping behaviour of the resolved turbulence appears to differ slightly between the models. The eddy viscosity distributions in Fig. 8.41 show a high degree of comparability, although the blending occurs at slightly higher y^+ for the SAE-IDDES and slightly higher values are seen in the LES-mode region. A possible explanation for

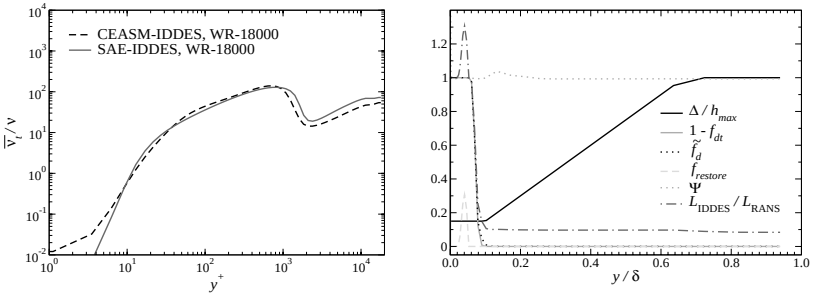

(a) $\overline{\nu}_t/\nu$, SAE-IDDES and CEASM-IDDES

(b) SAE-IDDES blending functions

Figure 8.41: IDDES functionality for the SAE implementation at $\mathrm{Re}_\tau = 18000$. Profiles of time-averaged eddy viscosity ratio in comparison to CEASM-IDDES and selected IDDES blending functions.

the higher LES-mode eddy viscosity is offered by the higher equivalent Smagorinsky constant for SAE-based DES compared to CEASM-based DES, derived in Section 8.2. The fact that the velocity profiles are nonetheless so similar echoes the observation by Nikitin et al. [101] of a low sensitivity to C_{DES}[17].

The SAE-IDDES blending function behaviour is also depicted in Fig. 8.41, from which a number of differences to the CEASM-IDDES (Fig. 8.39) are noteworthy. Firstly, a Ψ function is implemented in this model, as described in Section 5.5.2 and Appendix D. As could be expected at such a high Reynolds number (with $\overline{\nu}_t/\nu > 25$ in the LES mode region), the snapshot profile indicates that this is hardly active. A second difference concerns the $f_{restore}$ behaviour, which, if this snapshot can be considered representative, exhibits somewhat stronger activity than for CEASM-IDDES. Indeed, a different set of C_l and C_t parameters is used, those for SAE-IDDES adopting the published values for SA-IDDES [170, 149]. Finally, strongly reduced values of $L_{\mathrm{IDDES}}/L_{\mathrm{RANS}}$ are seen compared to CEASM-IDDES. This is however predominantly a cosmetic difference arising from the fact that $L_{\mathrm{RANS}} = d_w$ for the SAE-model[18].

The issue of the residual LLM apparent in the velocity profiles will be returned to. One possible route to improving this behaviour has already been identified, namely a tuning of the model-specific C_l and C_t parameters, which has as yet not been carried out. Another hypothetical explanation for the residual LLM exists however, which

[17] This furthermore fuels the discussion in Sect. 8.2 concerning the expected value of a dynamic DES formulation.

[18] This is loosely related to the discussion of the DES-interface behaviour in Section 8.1.2. The RANS model length scales are summarised in Tab. 5.2.

offers a further line of investigation and will be briefly described. The discussion of the LLM phenomenon in hybrid RANS-LES methods by Baggett [5] (mentioned in Sect. 3.7.3) noted that the super-streak structures associated with LLM scale with the grid resolution, i.e. that these correspond to the smallest structures resolvable by the grid and numerical scheme applied. Part of the task allocated to the IDDES blending functions is therefore to assess the grid resolution and to displace the RANS/LES interface further from the wall until this is deemed sufficient. The development of the IDDES functions was strongly driven by empirical calibration, which was carried out using the flow solver of NTS and its fourth order central difference convection scheme. Such a scheme can of course accurately represent smaller vortices on a given grid than the second order CDS applied here. This difference in the numerical order of accuracy between the NTS solver and the ELAN solver therefore provides a likely explanation for the residual LLM observed in the ELAN implementation. Two avenues could therefore be pursued to resolve the remaining LLM problem: The implementation of 4th order numerics in ELAN and the modification of the relevant IDDES blending functions to push the RANS/LES interface further from the wall for 2nd order CDS. Should the latter route prove successful, this would reveal an important numerics dependency of the method. In this case, clear guidelines for code-specific tuning would be required.

8.8.3 Numerical cost of WMLES and grid considerations

Some comments can be made at this juncture concerning the numerical cost of WMLES and the reduction relative to fully-resolved LES achieved by the tangential coarsening it allows. To illustrate the saving achieved, the number of grid points and time steps that would be required by pure LES will be estimated for the highest Reynolds number IDDES computation presented above, i.e. $\mathrm{Re}_\tau = 18000$.

The estimate must assume a maximum permissible tangential grid spacing for pure LES, and as commented in Section 3.5 the literature exhibits some variability in the guidelines. The values $\Delta x^+_{max} = 40$ and $\Delta z^+_{max} = 20$ will be assumed here, together with the same domain extent of $L_x = 6.4\delta$ and $L_z = 3.2\delta$ from the WMLES. This gives rise to 2880 grid points in each tangential direction, and assuming the same wall-normal point distribution as the WMLES over a billion (1×10^9) cells in total. Concerning the time step, this scales with Δx in order to maintain CFL ≤ 1, resulting in a factor of 45 increase in the number of time steps. Combining the spatial and temporal cost factors and assuming a constant numerical expense per grid cell and time step, the cost saving of WMLES compared to LES is around a factor 90000 at this Reynolds number.

This illustrative cost factor calculation must be accompanied with the acknowledgement that the potential cost reduction of WMLES increases with Reynolds number. Furthermore, a variation in the tangential refinement has not been carried out, and it is possible that a further cost reduction could be achievable. In tests maintaining

$\Delta z = 0.05\delta$, Shur et al. [149] demonstrate that IDDES maintains a reasonable solution quality when $\Delta x/\Delta z$ is increased up to 4.

Although the tangential resolution of WMLES is unlimited in terms of wall units [149], this implies that there is no upper limit on the Reynolds number that can be computed and should not be interpreted to mean that an arbitrarily coarse grid can be used. Whereas fully-resolved LES is dictated by criteria for resolving the near-wall structures, WMLES resolution criteria are based on resolution of the outer boundary layer turbulence. This indicates a fixed number of points per boundary layer thickness, and indeed Piomelli et al. [114] cite the criterion of 15 to 20 points per δ derived theoretically by Chapman [26] and observed numerically by Nikitin et al. [101].

Finally, it should be remarked upon that the estimate of the numerical expense of a fully-resolved LES assumes structured grids. As a consequence of keeping the wall-normal distribution from WMLES but refining tangentially, highly-stretched columnar cells would result in the channel core. Obtaining optimal cubic cells with a structured solver would require a limitation of $\Delta y = \max(\Delta x\ ;\ \Delta z)$ and a significant further increase in the grid density. Alternatively, the adoption of an unstructured grid methodology would potentially allow a coarsening of the tangential grid further from the wall and a corresponding reduction of the numerical expense.

The fixation of the grid resolution relative to δ for WMLES results in an identical tangential grid for any Reynolds number in the case of fully-developed internal flows. For external flows however, the boundary layer thickness decreases as Re increases. For this reason, Piomelli et al. [114] quote a scaling of the necessary number of grid points proportional to $\mathrm{Re}^{0.4}$.

8.8.4 Combination with the hybrid-adaptive boundary condition

The WMLES concept embodied in the IDDES method has been demonstrated to relieve the tangential resolution requirements of wall-bounded LES. The wall-normal grid spacing must however still be adapted to the Reynolds number to provide $y^+ \approx 1$ in the first cell, as required by the background RANS model treated with standard low-Re boundary conditions. The hybrid-adaptive boundary condition of Rung et al. [135] was formulated to relieve this problem for RANS simulations, providing a seamless blend of high-Re and low-Re boundary conditions. This boundary condition therefore allows any value of y^+ at the wall, and its formulation is described in Appendix C.

The attractiveness of combining the hybrid-adaptive boundary condition with IDDES is not so much oriented towards a further reduction of computational expense for WMLES, as might at first be expected. Indeed, Nikitin et al. [101] point out that "*the economic incentive to use 'wall functions' to relax the* $\Delta y^+ \approx 1$ *requirement is weak*", as "*a factor of* 10 *increase in* Re_τ *adds only* 17 *grid layers for each wall: the evolution is logarithmic*". Nonetheless, such functionality is attractive from the perspective of complex

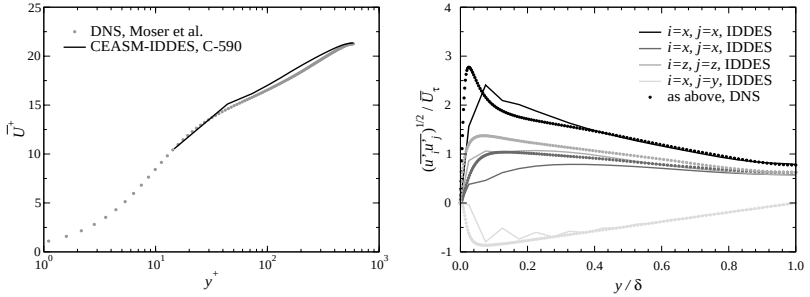

(a) Mean velocity profiles

(b) Resolved Reynolds stresses

Figure 8.42: Comparison of CEASM-IDDES employing the hybrid-adaptive wall function with the DNS of Moser et al. [100] for fully-developed channel flow at $\mathrm{Re}_\tau = 590$, cubic grid.

applications: in particular, the need to know the τ_w distribution in advance in order to safeguard the correct specification of y^+ often leads to iterative grid generation. The practical advantages of the hybrid-adaptive boundary condition for RANS are described in Section 3.4.4 and Appendix C and demonstrated by Schmidt et al. [145] and Mockett et al. [95]. It is expected that many of these benefits would carry over to WMLES.

In principle, the law of the wall is only valid in a time-averaged sense, so it is unclear whether its application in a simulation of resolved, unsteady turbulence is valid. This has also been remarked upon by Deardorff in his pioneering LES study of channel flow [35], which employed essentially an equivalent of a high-Re boundary condition to parameterise the near wall profile. In a similar vein to Deardorff's investigation, an equidistant grid spacing is applied as a challenging test for the hybrid-adaptive boundary condition with IDDES – the cubic grid is not however suggested for practical application[19]. A secondary point of interest is the behaviour of the grid-dependent blending functions in the IDDES formulation, in particular the Δ definition that anticipates a stretched wall-normal grid: Does the IDDES method respond in a robust manner when the equivalent grid essentially deactivates these functions?

As described in Section 6.2, the cubic grid resolution is $\Delta x = \Delta y = \Delta z = 0.05\delta$ (i.e. 20 points per boundary layer thickness) and this has been computed with the CEASM-IDDES formulation at various Reynolds numbers. An impression of the performance will first be obtained for the $\mathrm{Re}_\tau = 590$ computation in comparison with the DNS of Moser et al. [100], before the behaviour with increasing Reynolds number is exam-

[19] (although it would be highly relevant if used in conjunction with the immersed boundary method, whereby complex geometries are "immersed" in a Cartesian grid instead of using body-fitted meshing)

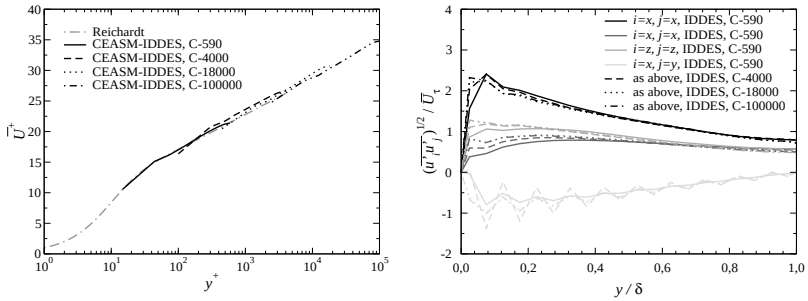

(a) Mean velocity profiles

(b) Resolved Reynolds stresses

Figure 8.43: Reynolds number sweep of cubic grid calculations with CEASM-IDDES employing the hybrid-adaptive wall function (n.b. the Reynolds stress profiles for $\mathrm{Re}_\tau = 18000$ and $\mathrm{Re}_\tau = 100000$ are almost identical).

ined.

The profiles of mean velocity and resolved Reynolds stress components at $\mathrm{Re}_\tau = 590$ are plotted in Fig. 8.42. The mean velocity at the first cell centre ($y^+ \approx 15$) agrees perfectly with the DNS data, illustrating the correct functionality of the hybrid-adaptive boundary condition even within the buffer layer, where standard high-Reynolds formulations would be invalid. The velocity profile then continues to follow the DNS log law profile fairly closely, although with a slightly excessive intercept and varying gradient. Considering the extremely coarse wall-normal resolution of the near wall region however, the agreement is highly satisfactory. The skin friction coefficient deviates by -8.08% from Dean's correlation (Tab. 8.8), however the Dean correlation itself deviates from the DNS data by 4.21% in the same sense (as indicated by the comparison of collated DNS data with Dean's correlation in Fig. 2.8).

The resolved Reynolds stress profiles show very good agreement with the DNS in the channel core, however this deteriorates nearer to the wall, below around $y/\delta \approx 0.4$. This is interpreted as a consequence of under-resolution in this region (the over-prediction of the streamwise and under-prediction of the wall-normal and spanwise components is a typical indication of this [17]). An alarming oscillation of the shear stress profile is also observed, for which two hypothetical explanations are offered. One possibility is the instability of the 2nd order CDS convection scheme with excessively coarse grids (Sect. 4.2.2, [106]). The second possible cause is related to the Rhie & Chow interpolation used to damp the pressure-velocity decoupling of the SIMPLE method for collocated numerics (Section 4.3). As shown by Choi [28], the Rhie & Chow damping can become inactive for the combination of a coarse grid and a fine time step. Apart from the resolved shear stress however, this instability does not

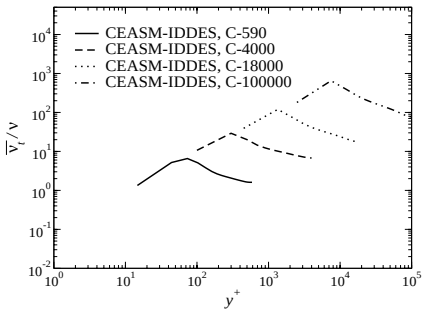

Figure 8.44: Profiles of time-averaged eddy viscosity ratio for CEASM-IDDES of fully-developed channel flow for a range of Re_τ. Cubic grid calculations employing the hybrid-adaptive wall function.

appear to impact the statistical quantities, and furthermore a systematic oscillation cannot be detected in the instantaneous flow snapshots of Figs. 8.34 and 8.36.

Turning to the cubic grid computations at higher Reynolds numbers, the mean velocity and resolved Reynolds stresses are plotted in Fig. 8.43. The satisfactory agreement with the Reichardt correlation is also exhibited at higher Reynolds numbers, even improving at the very highest values. The poorest agreement is in fact given by the intermediate $\mathrm{Re}_\tau = 4000$ calculation, with a slight over-prediction of the log-law intercept. The skin friction coefficient values (Tab. 8.8, Fig. 8.33) deviate increasingly from Dean's correlation as Re_τ increases above 18000. However, the corresponding bulk Reynolds numbers lie outside the range of validity specified for the empirical correlation (Sect. 2.4.2), so the comparison is perhaps invalid. The resolved Reynolds stresses exhibit a similar behaviour at the higher Reynolds numbers, although the symptoms of under-resolution (excessive streamwise stresses, insufficient spanwise and normal stresses) appear to diminish as Re_τ is increased, reaching however an apparent convergence at $\mathrm{Re}_\tau = 18000$. The oscillation of the shear stress profile is also apparent for all Reynolds numbers, but is significantly stronger at the intermediate $\mathrm{Re}_\tau = 4000$.

Attention will now be turned to the instantaneous snapshots of Figs. 8.34, 8.35 and 8.36. With increasing Re_τ, the streamwise vorticity reveals an increase in the number of fine vortical structures and in their strength. The wall-normal snapshots similarly depict a decrease in the size of the streaks with increasing Re_τ. The near wall streaks are also strongly represented, despite the fact that this slice is located at the first near wall cell vertex. For both the wall-normal and streamwise structures, a saturation of the grid resolution appears to occur at around $\mathrm{Re}_\tau = 18000$ (i.e., no appreciable

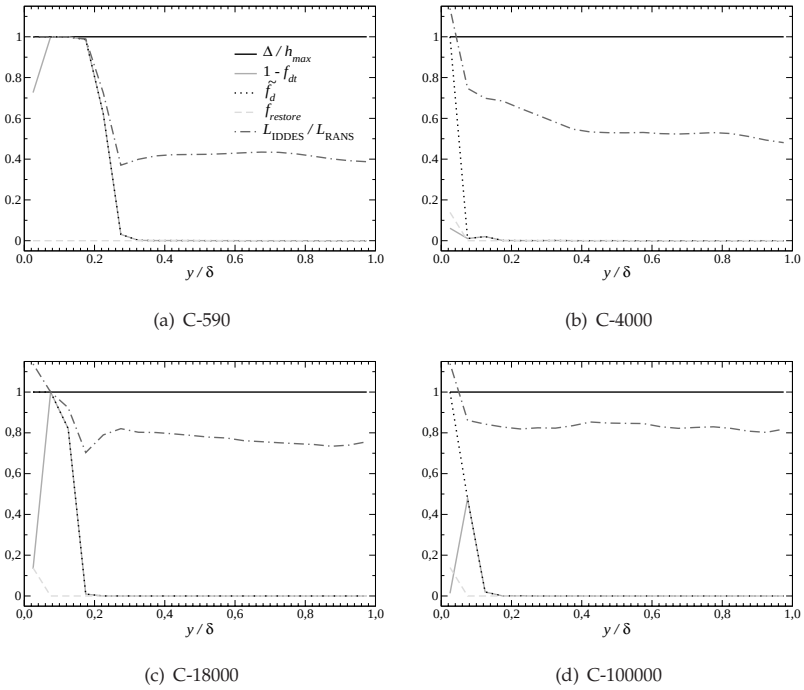

(a) C-590

(b) C-4000

(c) C-18000

(d) C-100000

Figure 8.45: Instantaneous profiles of selected IDDES blending functions for cubic grid calculations with CEASM-IDDES employing the hybrid-adaptive wall function at various Reynolds numbers.

increase in the resolution of fine structures is observed at $\mathrm{Re}_\tau = 100000$). This is most probably the reason for the similarity of the resolved Reynolds stress profiles at $\mathrm{Re}_\tau = 18000$ and 100000 commented on previously.

The instantaneous eddy viscosity ratio plots of Fig. 8.35 show a similar near-wall peak as for the wall-refined grids at $\mathrm{Re}_\tau \geq 4000$, due to the RANS activity there. The coarse grid resolution however appears to shift this peak slightly further from the wall. The eddy viscosity distributions in the channel core exhibit an inverse behaviour to the wall-refined cases, due to the uniform grid spacing. The general level of the eddy viscosity ratio increases considerably with Re_τ, reflecting a higher proportion of subgrid turbulent activity modelled.

This latter observation is more objectively portrayed by the mean eddy viscosity ratio profiles, plotted in Fig. 8.44. An identical distribution is seen in this dual-logarithmic

representation, only shifted to higher y^+ and $\overline{\nu}_t/\nu$ values at higher Re_τ. A comparison with the corresponding plot from the wall-refined grids (Fig. 8.38) reveals a stark contrast in the character of the profiles. The RANS-LES transition region is very poorly resolved by the cubic grid and the profiles show an opposite gradient in the LES-mode region.

Some explanation of this behaviour is given by the instantaneous snapshots of the IDDES blending functions, plotted in Fig. 8.45. When comparing with their counterpart for the wall-refined grids (Fig. 8.39), the most notable difference can be seen in the quantity Δ/h_{max}. This remains equal to 1 across the channel due to the absence of grid stretching, as a consequence of which the trough in $L_{\mathrm{IDDES}}/L_{\mathrm{RANS}}$ is absent, and a relatively flat profile in the LES region is retained. The general value of $L_{\mathrm{IDDES}}/L_{\mathrm{RANS}}$ increases with Re_τ, reflecting the increased subgrid-scale activity commented upon above. An interesting question is therefore the behaviour at still higher Reynolds numbers: would $L_{\mathrm{IDDES}}/L_{\mathrm{RANS}}$ exceed unity, giving rise to RANS across the channel?

Finally, an important observation should be reported concerning the computational expense of these simulations. Although identical in terms of grid resolution and time step size, a computational cost increase nonetheless occurs with increasing Reynolds number. Although employing the same initialisation method reported in Sect. 6.2 (with a separate RANS profile computed for each Reynolds number), the higher Reynolds number calculations required significantly more time steps before u_τ had settled to oscillation around unity and a stable value of $\overline{U}_b$ had been obtained. The reason for this is not entirely clear, however this could be because the same fluctuation strength was applied at all Reynolds numbers. Perhaps if the superimposed fluctuations were amplified at higher Reynolds numbers, this effect could be diminished.

8.9 IDDES application to complex flow

Having examined the performance and functionality of the IDDES method for the canonical and geometrically simple channel flow case, a more complex flow will be studied. For this purpose, the separating–reattaching bump test case will be employed, which is described in Sect. 6.6. Because of the steady-state inlet, RANS attached turbulent boundary layers, LES separated flow region and the impingement of the resolved turbulence onto the wall at reattachment, this case represents an ideal and challenging test of the IDDES method operating in a "mixed mode" simulation. This functionality was similarly demonstrated by the method's authors for a backward-facing step flow [170, 149]. Results from this test case have already been presented in the assessment of the model-dependency of DES in Sect. 8.4.2 and in the comparison of shielded DES with experiment in Sect. 8.7, and reference will be made to these sections where appropriate. As no good agreement with the experi-

mental data can be expected (due to the limitations of the upstream RANS portion, as established in Sect. 8.7), the aim is primarily to test the performance of the sensors and blending functions of IDDES rather than to assess the predictive accuracy: Does the model automatically and appropriately switch between its DDES and WMLES branches?

A collection of instantaneous visualisations of flow quantities and various blending functions are given in Fig. 8.47 for a lateral plane at $z = 0$ and a longitudinal plane at $x = 0$ (located at the bump foot). The vorticity magnitude and eddy viscosity ratio plots serve to illustrate the flow and simulation characteristics at the slices chosen. The oncoming boundary layers and the earlier upper wall boundary layer exhibit a RANS nature, with smooth profiles and high values of eddy viscosity. Downstream of the bump however, LES and WMLES character is evident through finely-resolved turbulent structures and low values of eddy viscosity, except very near the wall.

The ratio Δ/h_{max} is again employed to portray the filter width damping according to Eq. (3.23). Up to $x \approx 0.3$, the damping is not active and the filter width is equal to h_{max}. This is because the tangential grid spacing is fine (see the grid depiction in Fig. 6.10), so $h_{max} < \max\left(C_w d_w \; ; \; C_w h_{max} \; ; \; h_{wn}\right)$. This reflects the almost cubic grid cells in this region and mimics the behaviour for the cubic channel grids in Sect. 8.8.4. Examination of the longitudinal cross-section however reveals Δ damping in the corners caused by the compression of the grid cells in two directions simultaneously (whilst the streamwise spacing stays constant). Returning to the lateral cross-section, only when the streamwise grid spacing begins to coarsen after $x \approx 0.3$ does a damping of the filter width relative to h_{max} start to occur. The strength and extent of this increases downstream, accompanying the increase in streamwise grid spacing and anisotropy.

The log-layer sensor visualised by $(1 - f_{dt})$ together with the hybrid blending function $\tilde{f}_d$ can be used to determine the active branch of the IDDES. In the inflow and early separated regions, $\tilde{f}_d = (1 - f_{dt})$, meaning that the DDES functionality is in effect. Further downstream, at around $x > 0.8$, $\tilde{f}_d = f_{step}$ is seen to dominate, and the WMLES branch is active. The IDDES model therefore appropriately selects the correct DDES and WMLES functionality locally, allowing such mixed-mode computations. Figure 8.46 compares the eddy viscosity ratios between the DDES and IDDES computations. This confirms that an identical behaviour is apparent up to $x \approx 0.45$, whereas strong differences in the level of model activity occurs downstream of this. The activation of the WMLES mode leads to much reduced eddy viscosity levels here.

The influence of the IDDES on the results in comparison to DDES can be evaluated from the cross-plots in Appendix G. In line with expectation, the effect on the flow in the early separated region is minor as both models act in DDES mode there. As the flow has been demonstrated to depend strongly on the upstream separation predic-

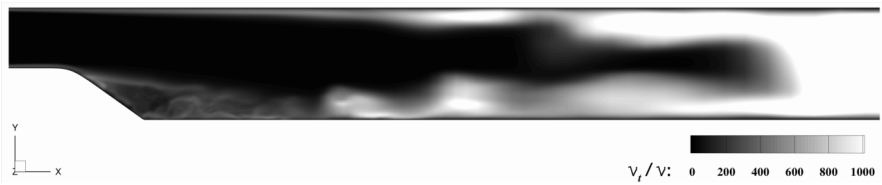

(a) SAE-DDES

(b) SAE-IDDES

Figure 8.46: Instantaneous contours of profiles of eddy viscosity ratio compared between DDES and IDDES at a lateral cross-section $z = 0$ throughout the entire computational domain.

tion, this gives rise to a negligible difference between SAE-IDDES and SAE-DDES for global flow characteristics such as time-averaged streamlines (Fig. G.1), pressure coefficient profiles (Fig. G.2(a)), separation and reattachment locations (Tab. G.1) and time-averaged flow topology (Fig. G.6). The discrepancies between IDDES and DDES grow further downstream, in the region where the WMLES branch of the IDDES is active. In particular, the streamwise velocity profile exhibits greater values near to the wall (Fig. G.3) and a reduced level of modelled and resolved shear stress is apparent in the downstream boundary layers (Fig. G.4).

These results fall short of demonstrating any improvement in predictive accuracy for the IDDES compared to the DDES, due to the problem of comparing with experimental data when the flow topology disagrees so strongly (Sect. 8.7). For this purpose, the backward facing step flow (with a geometry-induced separation point) reported by Travin et al. [170] and Shur et al. [149] was much more successful. However, these results demonstrate important and encouraging features of the mixed-mode operation of IDDES as well as its general applicability to complex flows. At the same time however, some concerning new issues arise regarding the transition between different turbulence treatment paradigms. Two examples occur in this flow: Firstly, a transition between WMLES and RANS occurs in the lower wall boundary layer due to gradual streamwise coarsening. Secondly, the inverse transition of a RANS to a WMLES boundary layer is brought about by the transmission of flow field fluc-

tuations from the opposite WMLES boundary layer[20]. It is clear that each of the limit cases (i.e. RANS and WMLES) are treated appropriately by IDDES. It is the protracted transition between these states where the uncertainty arises. This issue can hence be interpreted as another form of grey area (Sect. 3.7.3). These issues are indeed unimportant for the flow in question and for many other flows, however applications are conceivable for which such issues may represent serious problems. In any case, some targeted investigations should be carried out. Canonical flow cases such as developing channel flows and fully-developed channel flow with gradual streamwise coarsening come to mind.

[20]These issues were brought to light by M. Leschziner in private communication.

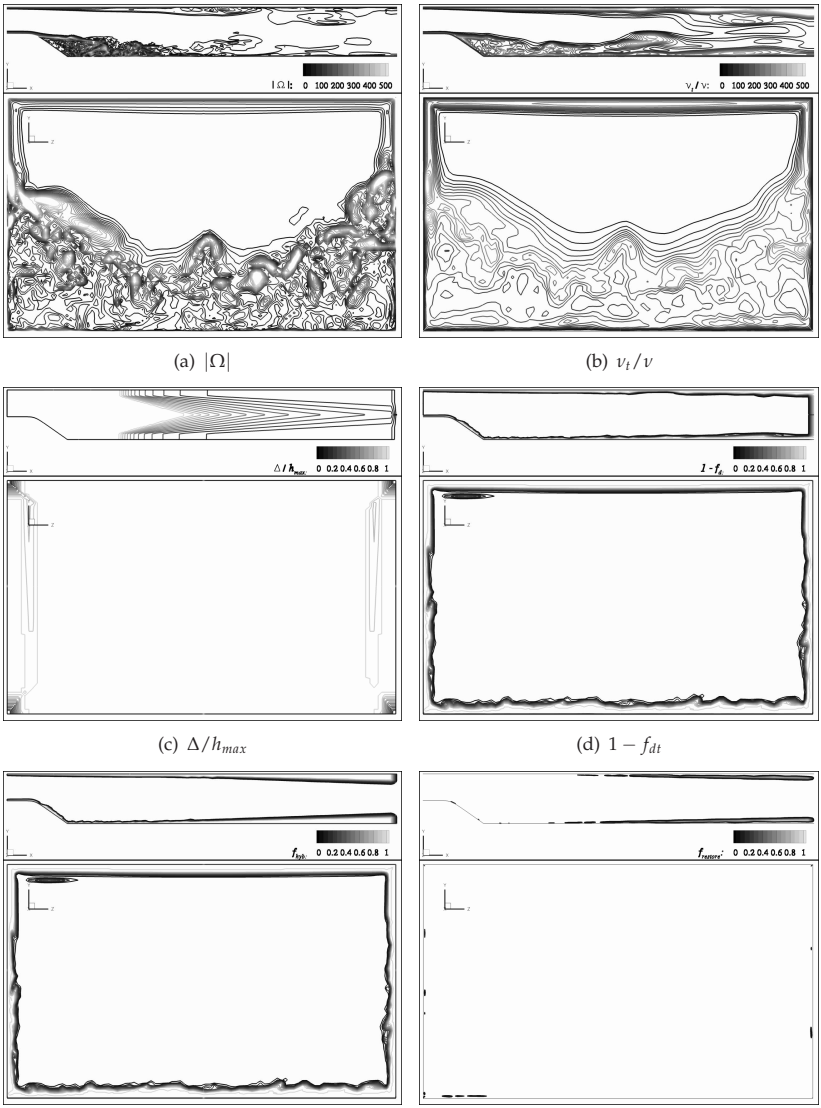

(a) $|\Omega|$ (b) ν_t/ν

(c) Δ/h_{max} (d) $1 - f_{dt}$

(e) $\tilde{f}_d$ (f) $f_{restore}$

Figure 8.47: Instantaneous contours of selected IDDES blending functions for the bump test case calculated with SAE-IDDES. The slices $z = 0$ (symmetry plane) and $x = 0$ (bump foot) are portrayed.

9 Conclusion

A diverse and comprehensive set of investigations into the performance of DES for a wide range of flow cases has been documented. It is hoped that these further the understanding of the approach, both in terms of its capabilities as well as its limitations. Much effort has been invested in presenting a complete monograph, with all physical and numerical background information upon which the arguments are based summarised in the literature review chapters of Part I. A concise description of the numerical solver and implementation details has been given in Part II, together with collated descriptions of the numerous test cases employed. A thorough demonstration, validation and calibration of key features of the implementation has been presented in Chap. 7, which provides a foundation for the investigations reported in Chap. 8. These partly provide an initial overall impression of typical DES solutions and partly target a deeper insight into more advanced topics and several avenues for further exploration are outlined. The findings will be summarised and some closing comments will be given in the following two sections.

9.1 Summary of findings

A bullet point list of the principal findings will be given, which are formulated in a deliberately concise manner. References to the relevant sections direct the reader to more detailed descriptions.

- An original approach to taxonomy of hybrid RANS-LES methods has been proposed based on four identified ambitions and ignoring formulation issues. This provides clarity and overview particularly to the industrial end user concerning an expansive field of research. It furthermore elaborates the definition of DES and elucidates its differentiation from other approaches. This could form a useful basis for the formulation of industrial recommendations as well as providing a link between different hybrid method formulations and a range of target applications.

  $\Rightarrow$ Section 3.6

- Tests employing inviscid isotropic turbulence demonstrate that the CDS convection scheme conserves kinetic energy, at least on the equidistant Cartesian grids considered. The ELAN numerical setup is hence deemed suitable for LES. The UDS and TVD schemes cannot be applied, even when combined with reduced C_{DES} values.

  $\Rightarrow$ Section 7.1

- The Ψ functions derived for the SAE and SALSA models function correctly. No such correction is required for the WCX model and none could be derived for the LLR and CEASM models due to their inherent complexity. DIT tests expose this as a problem for LLR-DES, whereas CEASM-DES functions satisfactorily. Use of LLR-based DES is therefore advised against.

  $\Rightarrow$ Section 7.4 & Appendix D

- An analytical framework for deriving C_{DES} as a function of the Smagorinsky parameter is demonstrated to hold for SA-family models, but over-predicts C_{DES} for the two-equation models tested. This emphasises the importance of empirical calibration.

  $\Rightarrow$ Section 8.2

- Arguments for and against the usefulness of a dynamic DES enhancement are presented, together with a suggested formulation approach based on Davidson's dynamic one-equation SGS model. Comparison of the Smagorinsky and Germano/Lilly dynamic SGS models for DIT indicate that dynamic DES could reduce the dependency exhibited by C_{DES} on the grid resolution.

  $\Rightarrow$ Sections 3.5.1 & 8.2

- DES formulations involving alternative substitutions of the length scale produce equivalent results for a natural DES application once the dissipativity is balanced via calibration of C_{DES}.

  $\Rightarrow$ Section 8.3

- Results for jet flow are cited indicating that a dual substitution of the DES length scale reduces the grey area problem and an explanatory mechanism has been proposed in terms of the behaviour of the substituted model terms.

  $\Rightarrow$ Section 8.3

- The sensitivity of DES to the underlying RANS model is negligible for massively-separated flow with geometry-induced separation. For flows with sensitive turbulent separation from smooth surfaces however the model sensitivity is high. This elucidates the importance of RANS modelling in a DES context.

  $\Rightarrow$ Section 8.4

- Excellent agreement with experiment is demonstrated in an in-depth comparison for cylinder flow. The predictive capability of the LES-mode of DES for massively-separated wakes is thereby validated. The suspected cancellation of errors does not diminish this.

  $\Rightarrow$ Section 8.5

- Natural DES is shown to exhibit a strong sensitivity to the time step size, with a relatively minor coarsening leading to a dramatic degeneration of the solution quality. It is argued that this effect can be expected for all DES of bluff bodies with turbulent separation or laminar separation near the critical Reynolds number.

  ⇒ Section 8.6

- The implementation of IDDES is thoroughly validated and examined for channel flow. The results are generally very promising, however a small degree of log-layer mismatch occurs and hypothetical explanations for this are proposed.

  ⇒ Section 8.8

- The WMLES modelling paradigm enabled by IDDES is demonstrated to eliminate the grid spacing requirements in terms of wall friction units that limit LES to very low Reynolds numbers. An estimated factor 90000 reduction in computational cost is achieved.

  ⇒ Sections 3.5.2 & 8.8.3

- The model sensitivity of WMLES is limited to the near wall RANS region and negligible in terms of skin friction.

  ⇒ Section 8.8.2

- The combination of IDDES with hybrid-adaptive RANS wall functions successfully removes the dependency of the wall-normal grid resolution on the Reynolds number and increases the robustness of the method.

  ⇒ Section 8.8.4

- The combined IDDES and wall function methodology produces acceptable results on cubic grids, thereby demonstrating the robustness of IDDES to unconventional mesh construction.

  ⇒ Section 8.8.4

- IDDES successfully enables mixed DDES and WMLES operation within a single solution domain and automatically selects the appropriate modelling framework locally. The IDDES method hence extends DES to include WMLES as an additional hybrid RANS-LES capability.

  ⇒ Section 8.9

- Some topics of concern have been documented regarding regions of transition in IDDES between WMLES and RANS boundary layers and vice-versa.

  ⇒ Section 8.9

9.2 Closing comments

In general, the relatively new family of hybrid RANS-LES methods presents the engineer with a significantly enhanced set of tools for the simulation of turbulent flows. Although generally too computationally expensive to be considered for everyday application, the expected increases in computational capability will inevitably lead to increasing reliance on hybrid RANS-LES in the near future. The additional cost must of course be justified by corresponding benefits for the application in question. Hence, two key scenarios are anticipated for the industrial application of hybrid RANS-LES approaches: Situations in which (U)RANS methods provide poor results (in particular strongly-separated flows) and applications for which the resolution of unsteady turbulent motion is essential (a notable example being the field of computational aeroacoustics).

Among the hybrid RANS-LES approaches, DES has in particular achieved widespread popularity, accounting for the majority of industrial hybrid RANS-LES to date. It is by now clearly established that excellent results can be achieved for suitable applications, which is further supported by the findings of this work. Although a recent proposition, the IDDES enhancement appears to successfully extend the range of suitable applications of DES through the inclusion of WMLES capability. This work corroborates the findings of the method authors in this respect, although more experience and confidence must be gained from further application to a wider range of test cases.

Despite these considerably positive perspectives and the significant achievements in the method development since 1997, a number of fundamental issues remain to be resolved. It is perhaps important to note that these are inherent to hybrid RANS-LES methods in general: The grey area problem arises in any formulation interfacing RANS with LES and the requirement of a sufficiently fine temporal resolution is a property inherited from LES. An amelioration or resolution of these issues is a clear direction for future research.

From an industrial perspective, just as important as continuing method development is accessibility of the technology, for which many factors play a role. In particular, user education and the availability of concise and comprehensive guidelines are essential if a long term move away from RANS is targeted. Examples of the kind of practical questions that these must address include the choice of an appropriate hybrid RANS-LES strategy for the problem in question, the generation of suitable grids, the choice of time step and the length of simulation time required for statistics at the desired level of accuracy. A further key technlology to be pursued in the industrialisation of hybrid RANS-LES is a dedicated strategy for automated grid generation and adaptation.

Part IV

Appendices

A The governing equations of fluid motion

A brief description of the origin and properties of the governing equations of fluid flow will first of all be given, which is a summary of the introductions given by Pope [116]. The first necessary physical assumption is the *continuum hypothesis*, i.e. that the fluid is a continuum of differential variables, and that the discrete nature of the fluid at molecular scales can be ignored. Considering a fixed inertial, *Eulerian* reference frame x_i, the variation of a physical quantity ϕ for a moving fluid particle is given by the substantial derivative

$$\frac{D\phi}{Dt} = \frac{\partial \phi}{\partial t} + u_i \frac{\partial \phi}{\partial x_i} \,, \tag{A.1}$$

where u_i is the velocity vector.

A.1 Conservation of mass

The conservation of mass, or continuity equation is given by

$$\frac{\partial \rho}{\partial t} + \frac{\partial \rho u_i}{\partial x_i} = 0 \,. \tag{A.2}$$

For all the flows considered in this work, the density ρ is assumed to be constant. This incompressible flow assumption is approximately valid for aerodynamic flows at Mach numbers of $M \leq 0.3$, and results in considerable simplification of the governing equations and the numerical implementation. For incompressible flows, the continuity equation can be rewritten as

$$\frac{\partial u_i}{\partial x_i} = 0 \,. \tag{A.3}$$

The velocity field is therefore seen to be *divergence free* or *solenoidal*, and this assumption will be implicit in the remaining presentation of the fluid flow equations and the work as a whole.

A.2 Conservation of momentum

The momentum equation is derived from Newton's second law, relating the acceleration of a fluid particle Du_i/Dt to the surface and body forces it experiences. The surface forces are molecular in origin and represented by the *stress tensor* τ_{ij}, whereas the body forces $\boldsymbol{\Psi}$ represent external forces with only gravity considered here.

$$\rho \frac{Du_j}{Dt} = \frac{\partial \tau_{ij}}{\partial x_i} - \rho \frac{\partial \Psi}{\partial x_j} \tag{A.4}$$

To obtain the expression for the surface forces, the further assumption of a Newtonian, constant property fluid is made, giving

$$\tau_{ij} = -\tilde{p}\delta_{ij} + \mu \left(\frac{\partial u_i}{\partial x_j} + \frac{\partial u_j}{\partial x_i} \right), \tag{A.5}$$

where $\tilde{p}$ is the pressure, acting as an isotropic normal force, and μ is the dynamic viscosity coefficient relating the shear force to the velocity gradients. The velocity gradient tensor can be decomposed into isotropic, symmetric-deviatoric and antisymmetric-deviatoric parts as

$$\frac{\partial u_i}{\partial x_j} = \frac{1}{3}\frac{\partial u_i}{\partial u_i} + S_{ij} + \Omega_{ij} \,. \tag{A.6}$$

The isotropic part is zero for incompressible flows according to Eq. (A.3). The symmetric-deviatoric rate of strain tensor and antisymmetric-deviatoric rate of rotation tensor are given by

$$S_{ij} = \frac{1}{2}\left(\frac{\partial u_i}{\partial x_j} + \frac{\partial u_j}{\partial x_i} \right) \quad \text{and} \quad \Omega_{ij} = \frac{1}{2}\left(\frac{\partial u_i}{\partial x_j} - \frac{\partial u_j}{\partial x_i} \right) \tag{A.7}$$

respectively. The stress tensor can therefore be reformulated as

$$\tau_{ij} = -\tilde{p}\delta_{ij} + 2\mu S_{ij} \,. \tag{A.8}$$

Some degree of simplification is obtained when the "modified pressure" p is considered to include the isotropic body forces, i.e. $p = \tilde{p} + \rho\Psi$. Substituting the stress tensor expression (A.8) into the momentum equation (A.4) with uniform ρ and μ and the modified pressure, the incompressible Navier–Stokes equations are obtained:

$$\frac{Du_i}{Dt} = -\frac{1}{\rho}\frac{\partial p}{\partial x_i} + \frac{\partial}{\partial x_j}(2\nu S_{ij}) \,, \tag{A.9}$$

where ν is the kinematic viscosity given by $\nu = \mu/\rho$.

B RANS models

The purpose of this appendix is to list the formulations of the RANS models applied in the study, with discussions of the model properties and derivations kept to a minimum. In cases where variations of the formulations exist, the version as it is implemented in the flow solver will be quoted and the existence of variations noted. The following definitions for the scalar norms of the deformation tensor will be used throughout:

$$S^* = \sqrt{2S_{ij}S_{ij}}\,, \qquad \Omega^* = \sqrt{2\Omega_{ij}\Omega_{ij}}\,, \tag{B.1}$$

where S_{ij} and Ω_{ij} are defined in Eq. (A.7).

B.1 One-equation models

B.1.1 Spalart–Allmaras

The Spalart-Allmaras (SA) one-equation model [157] takes the form of a transport equation for a modified eddy viscosity, $\tilde{\nu}$ as follows:

$$\frac{D\tilde{\nu}}{Dt} = P_{\tilde{\nu}} + D_{\tilde{\nu}} - \epsilon_{\tilde{\nu}}\,,$$

where the production, diffusion and dissipation terms are

$$P_{\tilde{\nu}} = C_{b1}[1 - f_{t2}]\tilde{S}\tilde{\nu}\,, \qquad D_{\tilde{\nu}} = \frac{1}{\sigma}\left[\frac{\partial}{\partial x_k}\left((\nu + \tilde{\nu})\frac{\partial \tilde{\nu}}{\partial x_k}\right) + C_{b2}\frac{\partial \tilde{\nu}}{\partial x_k}\frac{\partial \tilde{\nu}}{\partial x_k}\right]\,,$$

$$\epsilon_{\tilde{\nu}} = \left(C_{w1}f_w - \frac{C_{b1}}{\kappa^2}f_{t2}\right)\left(\frac{\tilde{\nu}}{d_w}\right)^2\,, \tag{B.2}$$

respectively. $\tilde{\nu}$ is related to the eddy viscosity, ν_t by

$$\nu_t = \tilde{\nu}f_{v1}\,, \qquad f_{v1} = \frac{\chi^3}{\chi^3 + C_{v1}^3}\,, \qquad \chi = \frac{\tilde{\nu}}{\nu}\,. \tag{B.3}$$

The modified scalar norm of the deformation tensor is given by

$$\tilde{S} = \Omega^* + \frac{\tilde{\nu}}{\kappa^2 d_w^2}f_{v2}\,, \qquad f_{v2} = 1 - \frac{\chi}{1 + \chi f_{v1}}\,. \tag{B.4}$$

The wall-damping function in the destruction term is defined by

$$f_w = g\left(\frac{1+C_{w3}^6}{g^6+C_{w3}^6}\right)^{1/6}, \qquad g = r + C_{w2}(r^6 - r), \qquad r = \frac{\tilde{\nu}}{\tilde{S}\kappa^2 d_w^2}. \tag{B.5}$$

The remaining terms with subscript t are intended to enable a smooth transition between a user-defined laminar region and the modelled turbulent region. As this functionality is not employed, these terms are ignored, i.e. $f_{t1} = f_{t2} = 0$. The values of the model constants are

$$C_{b1} = 0.1355, \qquad C_{b2} = 0.622, \qquad \sigma = 2/3, \qquad C_{w1} = \frac{C_{b1}}{\kappa^2} + \frac{1+C_{b2}}{\sigma},$$
$$C_{w2} = 0.3, \qquad C_{w3} = 2, \qquad \kappa = 0.41, \qquad C_{v1} = 7.1. \tag{B.6}$$

B.1.2 Edwards modification

The Edwards modification [39] to the original SA model, referred to as SAE, was proposed to address stability problems in the semi-viscous region. This involves a modified formulation of $\tilde{S}$, which guarantees a positive production term and furthermore employs the usual S^* rather than Ω^*:

$$\tilde{S} = S^*\left[\left(\frac{1}{\chi}\right) + f_{v1}\right]. \tag{B.7}$$

A modified definition of r is also proposed:

$$r = 1.313\tanh\left(\frac{\tilde{\nu}}{\tilde{S}\kappa^2 d_w^2}\right). \tag{B.8}$$

B.1.3 SALSA

The strain-adaptive linear variant of the Spalart–Allmaras (SALSA) model of Rung et al. [134] is based on the SAE formulation, and involves a modification of the production and dissipation terms to sensitise these to non-equilibrium flows. The modification is effected by a replacement of the constant C_{b1} with a function $f_{C_{b1}}$ and by a slightly modified r, as follows:

$$f_{C_{b1}} = C_{b1}\sqrt{\Gamma}, \qquad \Gamma = \min\left[1.25; \max\left(\gamma; 0.75\right)\right], \qquad \gamma = \max\left(\alpha_1; \alpha_2\right),$$
$$\alpha_1 = \left(1.01\frac{\tilde{\nu}}{S^*\kappa^2 d_w^2}\right)^{0.65}, \qquad \alpha_2 = \max\left[0; 1 - \tanh\left(\frac{\chi}{68}\right)\right]^{0.65}, \tag{B.9}$$

$$r = 1.6 \tanh\left(0.7\frac{\tilde{\nu}}{\tilde{S}\kappa^2 d_w^2}\right) . \tag{B.10}$$

B.2 Two-equation models

B.2.1 Wilcox $k-\omega$

The Wilcox $k-\omega$ model [181] comprises two transport equations for k and ω, where the turbulent frequency is defined as

$$\omega = \frac{\varepsilon}{C_\mu k} . \tag{B.11}$$

The k and ω transport equations are given in Eqs. B.12 and B.13 respectively.

$$\frac{Dk}{Dt} = P_k + D_k - \epsilon_k ,$$

$$P_k = \nu_t S^{*2} , \qquad D_k = \frac{\partial}{\partial x_j}\left[\left(\nu + \frac{\nu_t}{\sigma_k}\right)\frac{\partial k}{\partial x_j}\right] , \qquad \epsilon_k = C_\mu k\omega . \tag{B.12}$$

$$\frac{D\omega}{Dt} = P_\omega + D_\omega - \epsilon_\omega ,$$

$$P_\omega = C_{\omega 1}\frac{\omega}{k}P_k , \qquad D_\omega = \frac{\partial}{\partial x_j}\left[\left(\nu + \frac{\nu_t}{\sigma_\omega}\right)\frac{\partial \omega}{\partial x_j}\right] , \qquad \epsilon_\omega = C_{\omega 2}\omega^2 . \tag{B.13}$$

The parameters k and ω give an eddy viscosity defined by

$$\nu_t = \frac{k}{\omega} \tag{B.14}$$

and the model constants are

$$C_\mu = 0.09 , \qquad C_{\omega 1} = 5/9 , \qquad C_{\omega 2} = 3/40 , \qquad \sigma_k = \sigma_\omega = 2 . \tag{B.15}$$

This is the original version of the model, published in 1988. Wilcox continued to develop the model to include re-calibrated constants and additional terms to address laminar to turbulent transition [182]. These modifications have not been incorporated in the implemented version.

B.2.2 LLR $k-\omega$

The local linear realisable (LLR) model of Rung et al. [136] has been derived from non-linear models in order to sensitise the $k-\omega$ model to strain and rotation effects and improve behaviour in the wall region. The eddy viscosity level depends on the strain and rotation rates while the model coefficients depend on the turbulent Reynolds number. Note in particular that, in contrast to the Wilcox $k-\omega$ model, the

turbulent frequency is defined without C_μ (or its LLR variable counterpart, f_{C_μ}):

$$\omega = \frac{\varepsilon}{k} \,. \tag{B.16}$$

The remaining changes compared to the Wilcox $k-\omega$ model are as follows:

$$\epsilon_k = f_{\beta_k}\, k\omega \tag{B.17}$$

$$P_\omega = S^{*2}\sqrt{f_{C_\mu}}\, f_1 \left(f_{C_1} - \frac{f_{C_\mu}\, S^*}{\omega} \right) \,, \qquad \epsilon_\omega = f_{\beta_\omega}\, \omega^2 \tag{B.18}$$

$$\nu_t = f_{C_\mu} \frac{k}{\omega} \tag{B.19}$$

$$f_{C_\mu} = f_\mu \max\left[0.04;\ \min\left(0.1; \frac{1}{4 + A_S \tilde{U}} \right) \right] \,, \qquad A_S = 2.12 \,,$$

$$\tilde{U} = \frac{\sqrt{0.5\,(S^{*2} + \Omega^{*2})}}{\omega} \,, \qquad f_\mu = \frac{\frac{1}{80} + \mathrm{Re}_\mu}{1 + \mathrm{Re}_\mu} \,, \qquad \mathrm{Re}_\mu = \left(\frac{\mathrm{Re}_t}{70} \right)^\alpha \,,$$

$$\mathrm{Re}_t = \frac{k}{\nu\omega} \,, \qquad \alpha = 1 + 0.9\ \mathrm{sign}\left(1; \frac{\mathrm{Re}_t}{70} - 0.9 \right) \,,$$

$$f_{C_1} = \max\left(0.43; \frac{S^*/\omega}{S^*/\omega + 4.265} \right) \,, \qquad f_1 = \frac{\frac{1}{90} + \left(\frac{\mathrm{Re}_t}{70}\right)^2}{1 + \left(\frac{\mathrm{Re}_t}{70}\right)^2} \,, \qquad f_{\beta_k} = \frac{\frac{0.83}{3} + \mathrm{Re}_k}{1 + \mathrm{Re}_k} \,,$$

$$\mathrm{Re}_k = A^* \left(\frac{\mathrm{Re}_t}{100} \right)^{2.5} + \ (1 - A^*) \left(\frac{\mathrm{Re}_t}{100} \right)^{0.5} \,, \qquad A^* = \tanh\left(0.5 \sqrt{\frac{\mathrm{Re}_t}{100}} \right) \,,$$

$$f_{\beta_\omega} = \max\left[1.83 \left(1 + \sqrt{\frac{f_{C_\mu}}{1 + \frac{\nu_t}{\nu}}} \right)^{-1} - 1 \ ;\ 0 \right] \,. \tag{B.20}$$

This is the version of the LLR model as it is implemented in ELAN, although some modifications exist as reported by Xue [184], Schatz [141], Franke [46] and Rung et al. [136]. In particular, it should be noted that according to Schatz, the constant

value of $A_S = 2.12$ is an approximation of a more complex function valid for two-dimensional flows only. The full variant is in fact

$$A_S = 3\cos\left[0.5\cos^{-1}\left(\frac{\sqrt{6}S_{ij}S_{jk}S_{ki}}{\left(S_{ij}S_{ij}\right)^{3/2}}\right)\right] . \tag{B.21}$$

The effect of this modification has not been studied in the current work.

B.2.3 LL $k-\varepsilon$

The Lien–Leschziner (LL) $k-\varepsilon$ model [81] is used as the background model for the CEASM (Section B.3), and consists of two transport equations for k and ε combined with damping terms to allow resolution directly to the wall. The transport equations are given in Eqs. B.22 and B.23.

$$\begin{gathered}\frac{Dk}{Dt} = P_k + D_k - \epsilon_k ,\\ P_k = \nu_t S^{*2} , \qquad D_k = \frac{\partial}{\partial x_i}\left[\left(\nu + \frac{\nu_t}{\sigma_k}\right)\frac{\partial k}{\partial x_i}\right] , \qquad \epsilon_k = \varepsilon .\end{gathered} \tag{B.22}$$

$$\begin{gathered}\frac{D\varepsilon}{Dt} = P_\varepsilon + D_\varepsilon - \epsilon_\varepsilon ,\\ P_\varepsilon = \frac{\varepsilon}{k}\tilde{C}_{\varepsilon 1}P_k , \qquad D_\varepsilon = \frac{\partial}{\partial x_i}\left[\left(\nu + \frac{\nu_t}{\sigma_\varepsilon}\right)\frac{\partial \varepsilon}{\partial x_i}\right] , \qquad \epsilon_\varepsilon = \frac{\varepsilon}{k}\tilde{C}_{\varepsilon 2}\varepsilon .\end{gathered} \tag{B.23}$$

The eddy viscosity is given by

$$\nu_t = f_\mu C_\mu \frac{k^2}{\varepsilon} \tag{B.24}$$

and the coefficients and constants of the model are

$$\begin{gathered}\tilde{C}_{\varepsilon 1} = C_{\varepsilon 1}\left(1 + \frac{P'}{P_k}\right) , \qquad \tilde{C}_{\varepsilon 2} = C_{\varepsilon 2}\left(1 - 0.3e^{-\mathrm{Re}_t^2}\right) , \qquad P' = \frac{\tilde{C}_{\varepsilon 2}k^{3/2}}{C_{\varepsilon 1}L_\varepsilon}e^{-\alpha_d \mathrm{Re}_k^2} ,\\ \mathrm{Re}_t = \frac{k^2}{\nu\varepsilon} , \qquad \mathrm{Re}_k = \frac{\sqrt{k}d_w}{\nu} , \qquad L_\varepsilon = \kappa C_\mu^{3/4} d_w\left(1 - e^{-\alpha_\varepsilon \mathrm{Re}_k}\right) ,\\ f_\mu = \frac{1 - e^{-\alpha_\mu \mathrm{Re}_k}}{1 - e^{-\alpha_\varepsilon \mathrm{Re}_k}} ,\end{gathered} \tag{B.25}$$

$$\sigma_k = 1\,, \qquad \sigma_\omega = 1.3\,, \qquad C_{\varepsilon 1} = 1.44\,, \qquad C_{\varepsilon 2} = 1.92\,, \qquad C_\mu = 0.09\,,$$
$$\alpha_d = 0.00222\,, \qquad \alpha_\varepsilon = 0.263\,, \qquad \alpha_\mu = 0.016\,. \tag{B.26}$$

B.3 CEASM model

The compact explicit algebraic stress model (CEASM) of Lübcke [84] was developed for application to strongly three-dimensional flows and derived by simplification of the Reynolds stress transport equations under equilibrium assumptions. The model uses a restricted set of tensors in the representation of Pope [115] (which is not repeated here), for which the coefficients are

$$\beta_1 = -2 f_{C_\mu}\,, \qquad \beta_2 = -\frac{4 A_3 f_{C_\mu}}{g}\,, \qquad \beta_4 = \frac{A_2 f_{C_\mu}}{g} - \frac{II_S}{2}\beta_8\,,$$
$$\beta_5 = \frac{12 A_2 f_{C_\mu}\left(A_3 - A_2\sqrt{-\frac{II_\Omega}{II_S}}\right)}{-2g^2 + A_3^2 II_S + A_2^2 II_\Omega}\,, \qquad \beta_8 = -\frac{12 A_2 f_{C_\mu}}{II_S g}\,,$$
$$A_1 = -0.472\,, \qquad A_2 = -0.775\,, \qquad A_3 = -0.375\,,$$
$$f_{C_\mu} = \frac{-A_1 g}{g^2 - \frac{2}{3}A_3^2 II_S - 2A_2^2 II_\Omega}\,, \tag{B.27}$$

with g given by

$$g = C_1 - 1 + \frac{II_S}{4 + 1.83\sqrt{0.4 II_S - 1.6 II_\Omega}}\,\frac{2k^2}{\varepsilon^2}\,. \tag{B.28}$$

These coefficients provide a description of the anisotropy tensor based on the mean flow gradients. Alongside these, a description of the turbulent length and time scales must be provided – this is the role of the background model in explicit algebraic stress models. Although the CEASM framework could be applied to any two-equation model, the LL $k-\varepsilon$ model was chosen by Lübcke for its robustness and ability to resolve the viscous sublayer.

C Hybrid-adaptive wall boundary condition

The existence of two distinct wall boundary conditions has its origins in the physical nature of turbulent boundary layer flow: as detailed in Section 2.4, distinct zones are seen to exist at various distances to the wall. One class of boundary conditions (widely known as "low-Reynolds number" boundary conditions) targets the full resolution of the boundary layer profile to the wall, including the viscous sublayer. Best practice guidelines for RANS grid design [23] hence stipulate that low-Re boundary conditions require the placement of the first point at a distance of $y^+ \approx 1$ in order to sufficiently resolve the strong flow field gradients here. The alternative boundary condition type, referred to as "high-Reynolds number" or "wall functions", exploit the self-similarity of turbulent boundary layers to bridge the viscous sublayer and buffer layer. The first grid cell is therefore placed within the log-law region and the corresponding best practice recommendation is that the first point be located at $y^+ > 20$. Although this allows the use of much coarser wall-normal grid resolution, the self-similar boundary layer profiles are only valid for flows with weak tangential pressure gradients and low surface curvature where approximate local turbulent equilibrium can be assumed. When the simulated flow departs significantly from these assumptions, such as in the vicinity of shocks or flow separation and reattachment, a considerable loss of solution quality can be expected.

Different families of RANS models exhibit different "inherent" wall boundary conditions - whereas the $k-\varepsilon$ models are of the high-Re type, unmodified $k-\omega$ model solutions must be resolved entirely using a low-Re formulation. The Spalart–Allmaras and related models are similarly designed for integration directly to the wall, although reliable solutions are reported with y^+ values as large as five [157]. Nonetheless, damping terms can be incorporated into $k-\varepsilon$ formulations in order to incorporate the viscous sublayer into the solution (e.g. the Lien–Leschziner $k-\varepsilon$ model [81]) and high-Re boundary conditions can be added to $k-\omega$ models [145].

Inspection of the y^+ criteria for low-Re and high-Re boundary conditions reveals a further important problem with this state of affairs: a gap is present in the region $1 < y^+ < 20$ for which neither formulation is valid. A simple switch between the alternative formulations depending on the local y^+ value is therefore not possible. In order to address these problems, a more general unified boundary condition that can deliver robust and reliable solutions on arbitrary grids is highly desirable. Such a generic boundary condition has been proposed by Rung et al. [135], the formulation of which shall be presented.

The hybrid adaptive boundary condition represents an extension of the high-Re formulation such that it blends seamlessly into a low-Re formulation inside the viscous

sublayer. The dimensionless wall-normal distance in the log-law region is given by the following rearrangement of Eq. (2.20):

$$y^+ = \frac{e^{(\kappa \overline{U}^+)}}{E} \,, \tag{C.1}$$

where $E = e^{\kappa B}$. A Taylor series expansion of the numerator of Eq. (C.1) for small values of $\kappa \overline{U}^+$ about the origin combined with the low-Re value of y^+ (i.e. $y^+ = \overline{U}^+$) delivers the hybrid expression for the dimensionless wall distance

$$y^+_{hyb} = \overline{U}^+ + \frac{1}{E}\left[e^{(\kappa \overline{U}^+)} - \left(1 + \kappa \overline{U}^+ + \frac{(\kappa \overline{U}^+)^2}{2!} + \frac{(\kappa \overline{U}^+)^3}{3!} + ...\right)\right] \,. \tag{C.2}$$

This incidentally corresponds to the law of the wall formula published by Spalding [161]. Armed with this relatively simple expression for y^+_{hyb}, the hybrid adaptive boundary condition can be formulated. This is activated in place of the high-Re boundary condition when the criterion $y^+ \leq 15$ is met. The mechanism of the boundary condition is as follows:

$$y^+_{hyb} = \overline{U}^+ + \frac{1}{E}\left(e^{\kappa \overline{U}^+} - 1 - \kappa \overline{U}^+ - ... - \frac{(\kappa \overline{U}^+)^9}{9!}\right)$$

$$\overline{U}^+ = \left(1 - e^{-0.14 y^+_{hyb}}\right) \frac{\ln(E y^+_{hyb})}{\kappa}$$

$$\varphi = \left(1 - e^{-0.09 y^+_{hyb}}\right)^2 \,, \qquad \theta = (1-\varphi)\,\frac{\mu}{d_w} + \varphi \frac{\rho \kappa \overline{U}_\tau}{\ln(E y^+_{hyb})} \,, \qquad \tau_w = \theta(\Delta \overline{U}_w) \tag{C.3}$$

The blending function φ varies smoothly between near-zero in the viscous sublayer to unity deep inside the log law region, at approximately $y^+ > 100$. This serves to define the blending between laminar and turbulent viscosity in the low-Re and high-Re regions respectively, which is effective in the parameter θ. This in turn gives the effective viscosity divided by the wall normal distance for determination of the shear stress τ_w in conjunction with the velocity magnitude relative to the wall at the first point, $\Delta \overline{U}_w$. The velocity profile resulting from Eqs. (C.3) is plotted in Fig. C.1 and shows good agreement with the analytical linear and logarithmic distributions.

A demonstration of the effectiveness of the hybrid-adaptive boundary condition formulation of Rung et al. [135] for a range of aerodynamic validation cases and industrial aerodynamic applications is given by Schmidt et al. [145] and Mockett et al. [95].

Knopp [74] has recently proposed a similar but more elaborate boundary condition, which also allows placement of the first grid point at any value of y^+. It also utilises Spalding's formula, Eq. (C.2), but combines this with elements of Reichardt's correla-

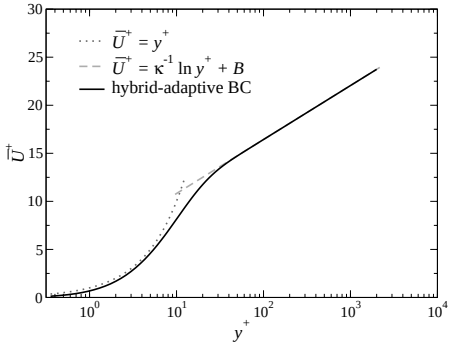

Figure C.1: Mean velocity profile given by the hybrid-adaptive boundary condition of Eqs. (C.3) compared to the linear and log-law profiles of Eq. 2.19 and Eq. 2.20 respectively.

tion, Eq. (2.21), and terms derived specifically for different families of RANS models. Knopp's method is hence model-specific and gives grid-independent solutions up to the limitations of numerical errors. The effects of streamwise pressure gradients are furthermore incorporated to give a more generalised formulation, which is particular important for flows with boundary layer separation and attachment.

D Derivation of model-specific Ψ functions

The derivation of the Ψ functions for each DES model follows the procedure outlined by Spalart et al. [158] and presented in more detail by Garbaruk et al. in an internal DESider project report [50].

D.1 Spalart–Allmaras model without "trip terms"

Although this model has not been applied in the presented investigations, the derivation of the low-Reynolds correction function is presented as an initial step, based upon which the derivation of Ψ_{SAE} is presented in the next section. The low-Reynolds term correction function derived by Spalart et al. [157] and discussed in Section 3.7.3 was obtained by consideration of the original SA model, including the terms allowing a user-specified laminar region. As these terms are not implemented, an alternative version of the low-Reynolds term correction function, Ψ_{SA} needs to be derived. A Smagorinsky-like form for the SA model without trip terms can be derived by employing the local equilibrium assumption (i.e. a balance of production and destruction terms in the transport equation). Adopting the LES length scale including the correction term (3.18) in the derivation gives rise to the following Smagorinsky form:

$$\nu_t = A_{\mathrm{SA}}(\Psi_{\mathrm{SA}} C_{\mathrm{DES}}\, \Delta)^2 S^* \,, \tag{D.1}$$

with

$$A_{\mathrm{SA}} = \frac{C_{b1}\, f_{v1}}{C_{w1}\, f_w}\, \frac{\tilde{S}}{S^*} \,. \tag{D.2}$$

As observed in Section 3.7.3, this coefficient term is not a constant. In order to return to the desired Smagorinsky behaviour, the correction function must cancel this tendency, i.e. $A_{\mathrm{SA}}\Psi_{\mathrm{SA}}^2 = \mathrm{const}$. Examining the variation of A_{SA} with eddy viscosity shows that the function has an asymptotic value A_{SA}^* for $\nu_t \to \infty$. Correspondingly, we seek a function such that the asymptotic correction function $\Psi_{\mathrm{SA}}^* = 1$, which gives the following expression for the correction function:

$$\Psi_{\mathrm{SA}}^2 = \frac{A_{\mathrm{SA}}^*}{A_{\mathrm{SA}}} \,. \tag{D.3}$$

Rearranging the expression for $\tilde{\nu}$ obtained using local turbulent equilibrium gives

$$\frac{\tilde{\nu}}{\tilde{S}(\Psi_{\mathrm{SA}} C_{\mathrm{DES}}\, \Delta)^2} = \frac{C_{b1}}{C_{w1}\, f_w} \,, \tag{D.4}$$

which together with the definition of r (B.5) in LES-mode (i.e. $d_w = \Psi_{\mathrm{SA}} C_{\mathrm{DES}}\, \Delta$) gives

$$r = \frac{C_{b1}}{C_{w1}\, f_w\, \kappa^2} \,. \tag{D.5}$$

Substituting (D.5) in the definition of $\tilde{S}$ in LES-mode, one obtains

$$\frac{S^*}{\tilde{S}} = 1 - \frac{f_{v2}\, C_{b1}}{\kappa^2\, C_{w1}\, f_w} \,. \tag{D.6}$$

The asymptotic value A^*_{SA} shall now be derived by considering the dependencies of the constituent functions on the eddy viscosity ratio, χ. Clearly, as $\nu_t \gg \nu$ and $\chi \to \infty$, $\tilde{S} \to S^*$ and $f_{v1} \to 1$. The resulting function is:

$$A^*_{\mathrm{SA}} = \frac{C_{b1}}{C_{w1}\, f^*_w} \,, \tag{D.7}$$

where f^*_w denotes the asymptotic value of f_w, for which an iterative solution delivers $f^*_w = 0.4241$. Unlike the full SA model, however, this is not a function of χ, so $f^*_w = f_w$.

The correction function can now be derived from (D.3) and (D.6), and is presented in (D.8). As also reported by Spalart and coworkers [158], the value of Ψ_{SA} is limited to 10. Furthermore, in line with expectation, the expression is equal to the function derived for DDES [158] with the trip terms deactivated (i.e. $f_{t1} = f_{t2} = 0$).

$$\Psi^2_{\mathrm{SA}} = \min\left[10^2; \frac{1}{f_{v1}} - \frac{f_{v2}\, C_{b1}}{f^*_w\, f_{v1}\, \kappa^2\, C_{w1}}\right] \tag{D.8}$$

D.2 Spalart–Allmaras model with Edwards modification

For the SAE model [39], the derivation of the DES correction function follows the same method as for the SA model without trip terms, described above. The same Smagorinsky form is obtained, with an identical expression for the coefficient term, i.e. $A_{\mathrm{SAE}} = A_{\mathrm{SA}}$. However, due to the different definition of $\tilde{S}$, the resulting correction function differs; this definition gives

$$\frac{S^*}{\tilde{S}} = \left(\frac{1}{\chi} + f_{v1}\right)^{-1} \,, \tag{D.9}$$

which together with the definition of the correction function (D.3) and the expression for the Smagorinsky coefficient (D.2) and its asymptotic limit (D.7) results in:

$$\Psi^2_{\mathrm{SAE}} = \frac{f_w}{f^*_w\, f_{v1}} \left(\frac{1}{\chi} + f_{v1}\right)^{-1} \,. \tag{D.10}$$

Due to the modified definition of r, a slightly different value of $f^* = 0.4685$ is obtained for SAE. As for the SA model without trip terms, $f^*_w = f_w$, which together with an analogous limitation of the function and the denominator used by Spalart et al. [158], gives:

$$\Psi^2_{\mathrm{SAE}} = \min\left\{10^2; \left[\frac{\max(f_{v1}, 10^{-10})}{\max(\chi\,, 10^{-10})} + f^2_{v1}\right]^{-1}\right\}\,. \tag{D.11}$$

The behaviour of Ψ_{SAE} with eddy viscosity ratio is plotted in Fig. D.1.

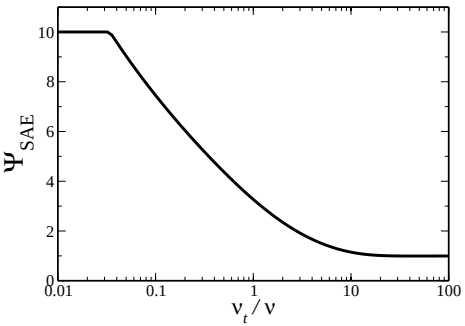

Figure D.1: Profile of Ψ_{SAE} with ν_t/ν.

D.3 SALSA model

As mentioned in Appendix B, the SALSA model is implemented including the Edwards correction. There are two relevant changes to the formulation compared to the SAE model, namely the SA and SAE constant C_{b1} is replaced by a function denoted $f_{C_{b1}}$ and a change is introduced to the expression for r. $f_{C_{b1}}$ is present in the destruction term directly as well as in C_{w1}, which no longer being a constant is termed

$$f_{C_{w1}} = \frac{f_{C_{b1}}}{\kappa^2} + \frac{1 + C_{b2}}{\sigma}\,. \tag{D.12}$$

Correspondingly the coefficient term becomes

$$A_{\mathrm{SALSA}} = \frac{f_{C_{b1}}\, f_{v1}}{f_{C_{w1}}\, f_w}\,\frac{\tilde{S}}{S^*}\,. \tag{D.13}$$

Examination of the asymptotic value of the coefficient term for high values of eddy viscosity is made slightly more complex by the additional functions, however the asymptotic values can be obtained when assumed values are chosen for S^* and d_w, which appear in the α_2 component of $f_{C_{b1}}$ (n.b. d_w is not substituted by the DES length scale in this expression). Furthermore, the development of $f_{C_{b1}}$, $f_{C_{w1}}$ and f_w as a function of χ can be examined, and it emerges that all of these functions remain bounded within specific values for all χ and for any values of d_w and S^*. The

minimum, maximum and asymptotic values of each function are summarised in Table D.1.

	Minimum:	Maximum:	$\chi \to 0$:	$\chi \to \infty$:
$f_{C_{b1}}$	0.1174	0.1515	0.1355 ($= C_{b1}$)	0.1515
$f_{C_{w1}}$	3.1311	3.3342	3.2391 ($= C_{w1}$)	3.3342
f_w	0.7032	0.7055	0.7042	0.7055

Table D.1: Bounding and asymptotic values of the variable terms appearing in A_{SALSA}.

The correction function for the low-Reynolds terms is therefore derived to be

$$\Psi^2_{\mathrm{SALSA}} = \frac{f^*_{C_{b1}}}{f_{C_{b1}}} \frac{f_{C_{w1}}}{f^*_{C_{w1}}} \frac{f_w}{f^*_w} \frac{1}{f_{v1}} \left[\frac{1}{\chi} + f_{v1} \right]^{-1} . \tag{D.14}$$

As the functions shown in Table D.1 are seen to vary only weakly with χ, the following simplification is justifiable:

$$\frac{f^*_{C_{b1}}}{f_{C_{b1}}} = \frac{f_{C_{w1}}}{f^*_{C_{w1}}} = \frac{f_w}{f^*_w} = 1 . \tag{D.15}$$

Together with the implemented limits used for the SAE model, this gives

$$\Psi^2_{\mathrm{SALSA}} = \min \left\{ 10^2; \left[\frac{\max(f_{v1}, 10^{-10})}{\max(\chi, 10^{-10})} + f^2_{v1} \right]^{-1} \right\} = \Psi^2_{\mathrm{SAE}} . \tag{D.16}$$

D.4 Wilcox $k - \omega$ model

The Smagorinsky form can be simply derived from the original (1988) Wilcox $k - \omega$ model [181] by the assumption of local equilibrium in the k equation (in LES-mode) and ω equation respectively:

$$\nu_t S^{*2} = \frac{k^{3/2}}{\Psi_{\mathrm{WCX}}\, C_{\mathrm{DES}}\, \Delta} \tag{D.17}$$

$$\nu_t S^{*2} = \frac{C_{\omega 2}}{C_{\omega_1}} k\omega . \tag{D.18}$$

Substituting $\omega = k/\nu_t$ in (D.18) gives the following expression for k:

$$k = \sqrt{\frac{C_{\omega 1}}{C_{\omega 2}}}\, \nu_t\, S^* , \tag{D.19}$$

which together with (D.17) gives the Smagorinsky form of the Wilcox subgrid scale model

$$\nu_t = A_{\mathrm{WCX}}(\Psi_{\mathrm{WCX}}\, C_{\mathrm{DES}}\, \Delta)^2 S^* \,, \tag{D.20}$$

where

$$A_{\mathrm{WCX}} = \left(\frac{C_{\omega 2}}{C_{\omega 1}}\right)^{3/2} \,. \tag{D.21}$$

As this is a constant, no low-Reynolds number correction term need be implemented:

$$\Psi_{\mathrm{WCX}} = 1 \,. \tag{D.22}$$

D.5 LLR $k-\omega$ model

Due to the complex terms constituting the LLR $k-\omega$ model formulation, the derivation of Ψ_{LLR} is not as straightforward as for other models. Indeed, it is difficult to reach a conclusion concerning the necessity of this by analytical means alone, as will become apparent. The local equilibrium assumption delivers

$$\nu_t S^{*2} = \frac{k^{3/2}}{\Psi_{\mathrm{LLR}}\, C_{\mathrm{DES}}\, \Delta} \tag{D.23}$$

for the k-equation in LES mode, and

$$S^{*2}\sqrt{f_{C_\mu}}\, f_1 \left(f_{C_1} - \frac{f_{C_\mu}\, S^*}{\omega}\right) = f_{\beta_\omega}\, \omega^2 \tag{D.24}$$

for the ω equation. Substituting $\omega = f_{C_\mu} k/\nu_t$ in (D.24) gives the following expression for k

$$k = \sqrt{\frac{f_1}{f_{C_\mu}^{3/2} f_{\beta_\omega}} \left(f_{C_1} - \frac{f_{C_\mu} S^*}{\omega}\right)}\;\; \nu_t S^* \,, \tag{D.25}$$

which when substituted in (D.23) gives the Smagorinsky form of the LLR $k-\omega$ model in LES-mode

$$\nu_t = A_{\mathrm{LLR}}(\Psi_{\mathrm{LLR}}\, C_{\mathrm{DES}}\, \Delta)^2 S^* \tag{D.26}$$

with

$$A_{\mathrm{LLR}} = \left[\frac{f_1}{f_{C_\mu}^{3/2}\, f_{\beta_\omega}} \left(f_{C_1} - \frac{f_{C_\mu}\, S^*}{\omega}\right)\right]^{2/3} \,. \tag{D.27}$$

It can be seen that A_{LLR} is a function of ν_t, k and ω as well as the deformation tensor in the form of S^* and the argument of the variable $\tilde{U}$ (a function of S^* and Ω^*). This lack of a simple dependency on ν_t complicates the situation considerably, and

a function Ψ_{LLR} cannot be derived[1]. A parameter variation study reveals that A_{LLR} can even have an amplifying effect as well as damping. Furthermore, the damping effect is weak in comparison to the SA model family, with the coefficient minimum value roughly 0.5. This, together with the difficulty of derivation mean that

$$\Psi_{\mathrm{LLR}} = 1 \tag{D.28}$$

is implemented. Unfortunately, it is demonstrated empirically in Sect. 7.4 that the subgrid viscosity is indeed damped to an unacceptable extent for fine grids in the simulation of DIT. An effective Ψ_{LLR} function would hence be required in order for LLR-based DES to be considered valid and its use is not advised.

D.6 LL $k-\varepsilon$ model

The properties of the LL $k-\varepsilon$ model will be investigated due to the role this plays as background model for the CEASM-based DES. For the k and ε equations in LES-mode, the local equilibrium assumption delivers

$$\nu_t S^{*2} = \frac{k^{3/2}}{\Psi_{\mathrm{LL}}\, C_{\mathrm{DES}}\, \Delta} \tag{D.29}$$

and

$$\tilde{C}_{\varepsilon 1}\, \nu_t\, S^{*2} = \tilde{C}_{\varepsilon 2}\, \varepsilon\,, \tag{D.30}$$

respectively. A rearrangement of the eddy viscosity expression gives

$$\varepsilon = \frac{f_\mu\, C_\mu\, k^2}{\nu_t}\,, \tag{D.31}$$

which when substituted in (D.30) gives

$$k = \sqrt{\frac{\tilde{C}_{\varepsilon 1}}{\tilde{C}_{\varepsilon 2}\, f_\mu\, C_\mu}}\, \nu_t S^*\,. \tag{D.32}$$

Substituting (D.32) in (D.29) delivers the Smagorinsky form

$$\nu_t = A_{\mathrm{LL}} (\Psi_{\mathrm{LL}}\, C_{\mathrm{DES}}\, \Delta)^2\, S^*\,, \tag{D.33}$$

with

$$A_{\mathrm{LL}} = \left(\frac{\tilde{C}_{\varepsilon 2}\, f_\mu\, C_\mu}{\tilde{C}_{\varepsilon 1}} \right)^{3/2}\,. \tag{D.34}$$

Inspection reveals that A_{LL} is not a constant, rather a function of k, ε, d_w and S^*. The strongest damping behaviour is however a function principally of k, with the other

[1] It cannot of course be ruled out that a researcher with greater algebraic ability may be able to derive an effective Ψ_{LLR}.

variables adjusting only the profile of the curve. Asymptotic behaviour is observed for $k \to \infty$ independent of the other variables: $\tilde{C}_{\varepsilon 1} \to C_{\varepsilon 1}$, $\tilde{C}_{\varepsilon 2} \to C_{\varepsilon 2}$ and $f_\mu \to 1$. The asymptotic limit $A_{\mathrm{LL}} \to A^*_{\mathrm{LL}}$ is therefore

$$A^*_{\mathrm{LL}} = \left(\frac{C_{\varepsilon 2}\, C_\mu}{C_{\varepsilon 1}} \right)^{3/2} . \tag{D.35}$$

Applying the usual definition $\Psi^2_{\mathrm{LL}} = A^*_{\mathrm{LL}} / A_{\mathrm{LL}}$, the correction function including numerical limitations is obtained:

$$\Psi^2_{\mathrm{LL}} = \min \left\{ 10^2 \; ; \; \left[\frac{C_{\varepsilon 2}\, \tilde{C}_{\varepsilon 1}}{\max(f_\mu \; ; \; 10^{-10})\, \tilde{C}_{\varepsilon 2}\, C_{\varepsilon 1}} \right]^{3/2} \right\} . \tag{D.36}$$

D.7 CEASM model

Although a low-Reynolds term correction function could be derived above for the LL $k - \varepsilon$ model, the background model for the CEASM, analysis of the CEASM is made difficult by the complex dependencies on the velocity field gradients. These are partly manifest in an adjustment of the C_μ parameter which is a constituent of A_{LL} (and hence A_{CEASM}), as well as determining an anisotropic Reynolds stress tensor. A straightforward derivation of a correction function analogous to the LL model is therefore considered impossible, partly due to the algebraic complexity of the modified C_μ, and partly because the Reynolds stress anisotropy will also be active in LES mode although not "captured" by the local equilibrium based analysis. Empirical testing of the LES mode performance of CEASM-based DES is hence considered essential.

The results of such a test employing decaying isotropic turbulence are shown in Section 7.4. It is seen that despite the indications from the LL $k - \varepsilon$ analysis, which suggest the necessity of a Ψ_{LL}, and despite the complex dependencies outlined in the above paragraph, CEASM-based DES delivers reliable results without a Ψ function.

E Obtaining resolved and modelled turbulent statistics

A short description of the method used to collect resolved and modelled Reynolds stress data from DES simulations is given. This involves a combination of the methods used for RANS and LES, which will therefore be described first.

E.1 Method for RANS

If a non-linear RANS model (such as the CEASM) is used, the Reynolds stress components are a direct output of the model. For linear eddy viscosity models however, the Boussinesq hypothesis ([13], Section 3.4.2) must be invoked to provide values of the approximated Reynolds stress components:

$$\overline{u_i' u_j'} = \frac{2}{3}\delta_{ij}k - \nu_t \left(\frac{\partial U_i}{\partial x_j} + \frac{\partial U_j}{\partial x_i} \right) . \tag{E.1}$$

This is written out in full for the $\overline{u'u'}$ and $\overline{v'v'}$ normal stress components and the $\overline{u'v'}$ component of the shear stress:

$$\overline{u'u'} = \frac{2}{3}k - \nu_t \left(\frac{\partial U}{\partial x} + \frac{\partial U}{\partial x} \right) \tag{E.2}$$

$$\overline{v'v'} = \frac{2}{3}k - \nu_t \left(\frac{\partial V}{\partial y} + \frac{\partial V}{\partial y} \right) \tag{E.3}$$

$$\overline{u'v'} = -\nu_t \left(\frac{\partial U}{\partial y} + \frac{\partial V}{\partial x} \right) . \tag{E.4}$$

If a model is used that does not directly include the parameter k (for example the SA and derivative models), this can be approximated from the eddy viscosity employing Bradshaw's hypothesis ([15], Section 3.4.3):

$$k \approx \frac{\nu_t \, S^*}{\sqrt{C_\mu}} . \tag{E.5}$$

E.2 Method for LES

Whereas the RANS Reynolds stresses are purely modelled quantities emerging from a steady-state solution, the majority of the turbulent stresses in LES are resolved directly in the flow field. These must therefore be obtained statistically over a large number of time steps N as follows:

$$\overline{U} = \frac{1}{N}\left\{\sum_{t=1}^{N} U\right\} \tag{E.6}$$

$$\overline{u_i' u_j'} = \frac{1}{N}\left\{\sum_{t=1}^{N} U_i U_j\right\} - \overline{U_i}\,\overline{U_j} \tag{E.7}$$

It is assumed that the time averaging is begun at a time step $t = 1$ where the flow field is fully-developed and free of initial transient character. Note that the summation part of the computation (inside the curly brackets) can be done cumulatively during the simulation, and the division by N and subtraction of mean values at the final output stage. This makes it unnecessary to store the entire flow domain at every time step. From the resolved Reynolds stresses, the resolved turbulent kinetic energy can be computed as:

$$k_{res} = \frac{1}{2}\overline{u_i' u_i'}\,. \tag{E.8}$$

The resolved Reynolds stresses obtained above are however only part of the total Reynolds stresses in LES. Because the modelled subgrid-scale stresses should be much smaller than the resolved stresses in LES (Section 3.5.2), these are often neglected. It is however simple to calculate the modelled component: Assuming that a subgrid-scale model is used that produces an eddy viscosity (e.g. the Smagorinsky model), the modelled part of the Reynolds stress can be obtained using the same method as for the RANS. Unlike the RANS however, these quantities must also be time averaged. Comparing the relative levels of resolved and modelled Reynolds stress is a useful means of determining the sufficiency of the grid resolution: the resolved stresses should be much larger than the modelled stresses.

E.3 Method for DES

In DES, pure RANS and pure LES coexist in different regions of the flow. It is therefore imperative that both the modelled and resolved turbulent quantities are computed, requiring a combination of the methods for RANS and LES. As mentioned for the modelled Reynolds stresses in the LES case, the same method as for RANS can be used although the quantities must be time averaged.

F Phase averaging of quasi-periodic turbulent flows

For many types of flow, for example bluff body wakes, oscillating airfoils or pulsating jets employed in active flow control, the fluctuations consist of a coherent, quasi-periodic part and an incoherent, turbulent part. In many cases, the coherent fluctuations exist at much larger scales than the turbulent eddies with which they are overlaid, and it can be argued that these are non-turbulent in nature. For example, as described in Section 2.5, a laminar vortex street behind a circular cylinder exists at Reynolds numbers much lower than those where turbulent flow first emerges [189] and the oscillation of a shock over a transonic airfoil is an acoustically-driven phenomenon that occurs for both laminar and turbulent boundary layers [36].

In such cases, pure Reynolds averaging of the velocity signals would deliver an overestimation of the turbulent stresses, as the contribution of the non-turbulent coherent fluctuations to the unsteadiness would be included in the budget. A more appropriate method of analysis is therefore the triple decomposition, proposed by Reynolds & Hussain [122], into a mean component, a quasi-periodic coherent fluctuation and a random fluctuation:

$$u_i(x_i,t) = \overline{U}_i(x_i) + \tilde{u}_i(x_i,t) + u_i''(x_i,t)\ . \tag{F.1}$$

A pictorial representation of this process is given in Fig. F.1 for the simple example of a sinusoidal signal $\tilde{u}$.

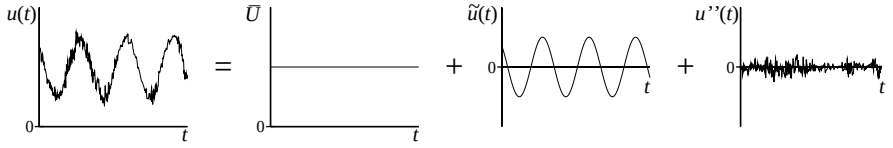

Figure F.1: Triple decomposition of an unsteady velocity signal u into a constant mean component $\overline{U}$, a periodic fluctuation $\tilde{u}$ and an incoherent turbulent fluctuation u'' [122].

The notation u_i'' is adopted for the incoherent fluctuation in order to differentiate it from the fluctuation u_i' obtained by Reynolds averaging (described in Section 3.4.1). The fluctuating velocity in the sense of Reynolds averaging can hence be expressed as

$$u_i' = \tilde{u}_i + u_i'' \tag{F.2}$$

and the Reynolds stress tensor as the sum of the coherent and incoherent contributions

$$\overline{u_i' u_j'} = \overline{\tilde{u}_i \tilde{u}_j} + \overline{u_i'' u_j''} \,. \tag{F.3}$$

To realise the triple decomposition practically, the conditional averaging technique of phase averaging is applied. The phase-averaged velocity is defined as

$$\langle U_i \rangle = \overline{U}_i + \tilde{u}_i \,. \tag{F.4}$$

The coherent fluctuation $\tilde{u}_i(x_i, t)$ is by definition periodic, repeating with a period τ that can be divided into discrete phase angles $0 < \varphi < 2\pi$. Once a method has been established to determine the corresponding phase angle for each instant t (such as the methods discussed in Section 6.5), conditional averaging of the signals with respect to φ can be conducted. The quantities $\langle U_i \rangle(x_i, \varphi)$ and $\langle u_i'' u_j'' \rangle(x_i, \varphi)$ can hence be obtained, where $\langle u_i'' u_j'' \rangle$ represents the phase-averaged incoherent turbulent stresses. From these phase-averaged quantities the time-independent quantities

$$\overline{U}(x_i) = \overline{\langle U_i \rangle} \,, \tag{F.5}$$

$$\overline{\tilde{u}_i \tilde{u}_j}(x_i) = \overline{\left(\langle U_i \rangle - \overline{U}_i\right) \left(\langle U_j \rangle - \overline{U}_j\right)} \text{ and} \tag{F.6}$$

$$\overline{u_i'' u_j''}(x_i) = \overline{\langle u_i'' u_j'' \rangle} \tag{F.7}$$

can be obtained by ensemble averaging over all φ.

G Figures for the bump test case

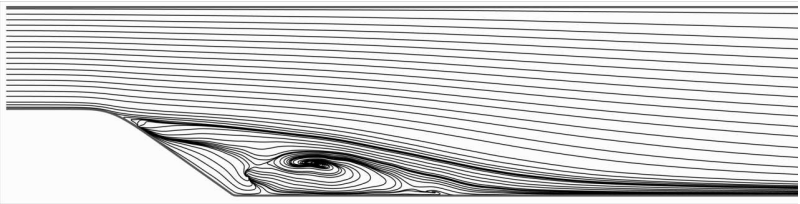

(a) CEASM-DES

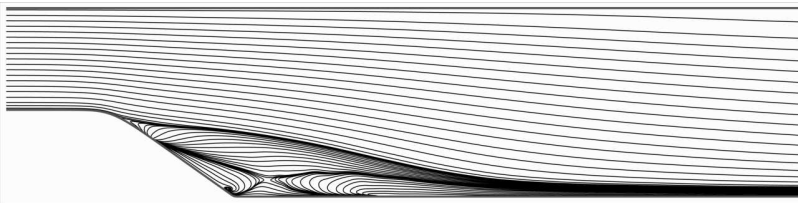

(b) SAE-DDES

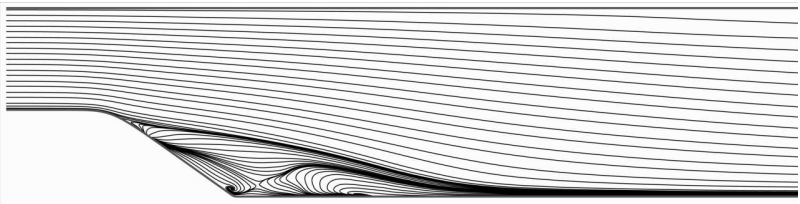

(c) SAE-IDDES

Figure G.1: Comparison of time-averaged streamlines between computations.

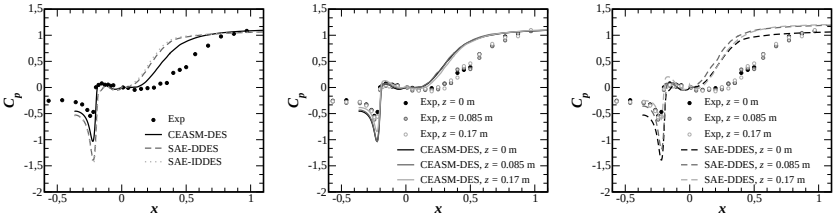

(a) $z = 0$, all models (b) various z, CEASM-DES (c) various z, SAE-DDES

Figure G.2: Comparison of time-averaged pressure coefficient along the bump floor at $z = 0$, $z = 0.085$ and $z = 0.17$. The reference pressure is taken at $x = 0.01$.

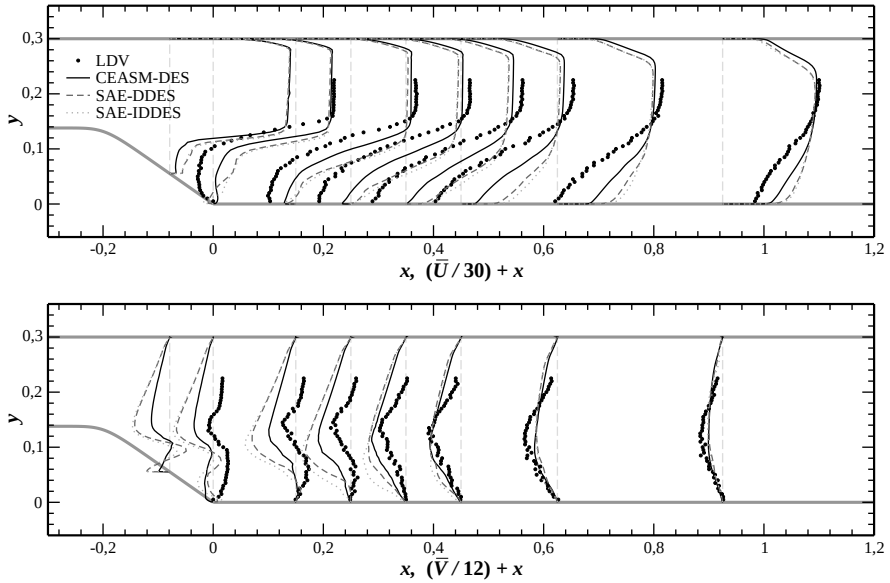

Figure G.3: Comparison of time-averaged velocity profiles at $z = 0$.

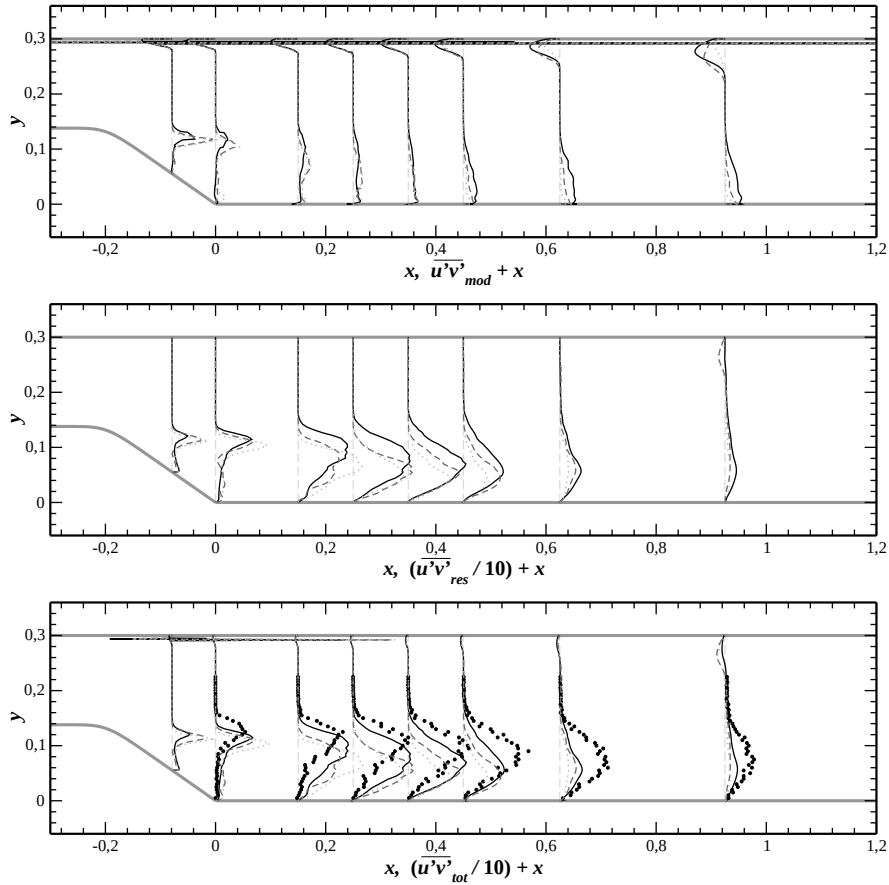

Figure G.4: Comparison of Reynolds shear stress profiles at $z = 0$.

	Δt	$N_{\Delta t}$	t_{avg}	$x_{s1}\|_{z=0}$	$x_{r1}\|_{z=0}$	$x_{s2}\|_{z=0}$	$x_{r2}\|_{z=0}$
CEASM-DES	8×10^{-4} s	9000	7.2s	-0.188	-0.156	0.043	0.347
SAE-DDES	5×10^{-4} s	21000	10.5s	-0.187	-0.128	-0.023	0.256
SAE-IDDES	5×10^{-4} s	23300	11.65s	-0.186	-0.131	-0.026	0.233
Experiment	—	—	—	—	—	—	0.630

Table G.1: Summary of time step size, number of time steps collected for averaging and the equivalent physical time. The right hand four columns give the x positions of the first and second separation and reattachment points in the centre plane.

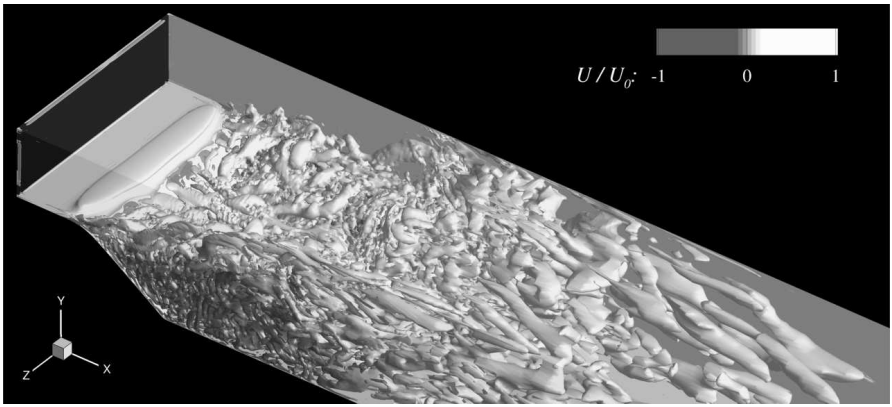

Figure G.5: Instantaneous vortex core structures visualised as isosurfaces of the λ_2 criterion shaded with streamwise velocity (SAE-DDES).

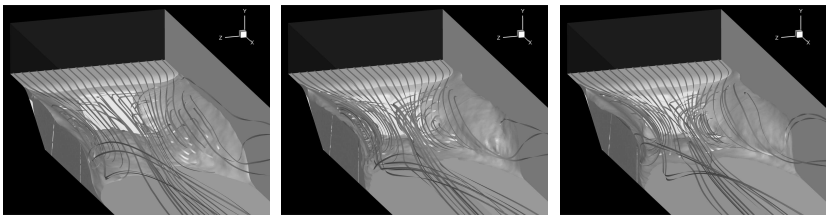

(a) CEASM-DES (b) SAE-DDES (c) SAE-IDDES

Figure G.6: Comparison of the mean flow topology using an isosurface of $\overline{U} = -0.0001$ to depict reverse flow regions and stream ribbons seeded in the lower incoming boundary layer.

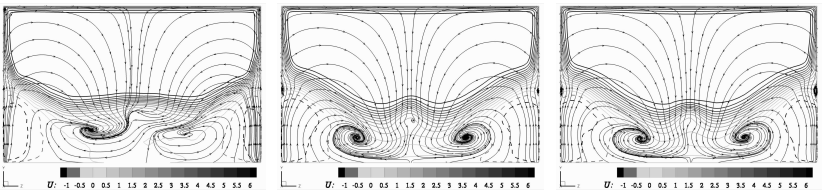

(a) CEASM-DES (b) SAE-DDES (c) SAE-IDDES

Figure G.7: Contours of streamwise velocity (thicker lines, dashed lines denote negative values) and cross-flow streamlines (thinner lines, obtained from the tangential $\overline{V}$ and $\overline{W}$ components only) at the plane $x = 0$ located at the bump foot.

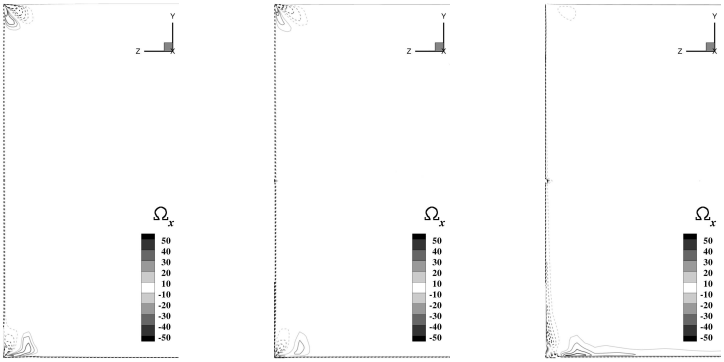

(a) Inflow, $x = -0.367$ (b) CEASM-DES, $x = -0.2$ (c) SAE-DDES, $x = -0.2$

Figure G.8: Downstream development of the inflow plane corner vortices for CEASM-DES and SAE-DDES at $x = -0.2$. Contours of instantaneous x-vorticity (dashed lines indicate negative values).

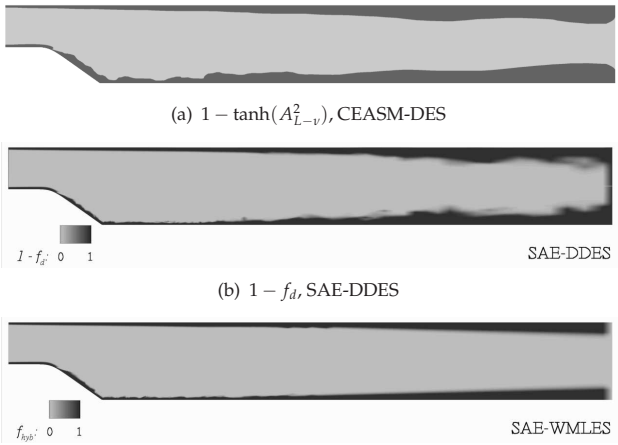

(a) $1 - \tanh(A_{L-v}^2)$, CEASM-DES

(b) $1 - f_d$, SAE-DDES

(c) $\tilde{f}_d$, SAE-IDDES

Figure G.9: Instantaneous contours of the GIS-shield functions for CEASM-DES and SAE-DDES and the hybrid blending function for SAE-IDDES along the centre plane $z = 0$.

Bibliography

[1] F. Abernathy. Flow over an inclined plate. *Transactions of the ASME. Series D, Journal of Basic Engineering*, 61:380–388, 1962.

[2] Y. Addad, U. Gaitonde, D. Laurence, and S. Rolfo. Optimal unstructured meshing for large eddy simulations. In Meyers, Guerts, and Sagaut, editors, *Quality and Reliability of Large-Eddy Simulations*, volume 12 of *ERCOFTAC Series*, pages 93–103. Springer, 2008.

[3] B. Aupoix. *Application of two-point closures to subgrid scale modelling for homogeneous, 3D turbulence*. Lecture Series 1989-03, Turbulent Shear Flows. von Karman Institute for Fluid Dynamics, 1989.

[4] B. Aupoix, P. Barricau, Y. Egorov, C. Geiler, A. Gilliot, F. Menter, J. Monnier, G. Pailhas, L. Perret, M. Stanislas, and Y. Touvet. The DESider bump experiment. In *Proceedings of the 7th International Symposium on Engineering Turbulence Modelling and Measurements (ETMM7)*, pages 249–254, Limassol, Cyprus, 2008.

[5] J. Baggett. On the feasibility of merging LES with RANS for the near-wall region of attached turbulent flows. Annual Research Briefs, Center for Turbulence Research, Stanford University, 1998.

[6] B. Baldwin and H. Lomax. Thin-layer approximation and algebraic model for separated turbulent flows. In *16th Aerospace Sciences Meeting*, Huntsville, Alabama, USA. AIAA Paper 78-257.

[7] P. Bearman. On vortex shedding from a circular cylinder in the critical Reynolds number régime. *Journal of Fluid Mechanics*, 37(3):577–585, 1969.

[8] P. Bearman and T. Morel. Effect of free stream turbulence on the flow around bluff bodies. *Progress in Aerospace Sciences*, 20:97–123, 1983.

[9] S. Benhamadouche. *Large eddy simulation with the unstructured collocated arrangement*. PhD thesis, School of Mechanical, Aerospace and Civil Engineering, University of Manchester, 2006.

[10] S. Benhamadouche and D. Laurence. Global kinetic energy conservation with unstructured meshes. *International Journal for Numerical Methods in Fluids*, 40:561–571, 2002.

[11] M.S. Bloor. The transition to turbulence in the wake of a circular cylinder. *Journal of Fluid Mechanics*, 19:290–304, 1964.

[12] J Boris and D Book. Flux-corrected transport I. SHASTA, a fluid transport algorithm that works. *Journal of Computational Physics*, 11:38–69, 1973.

[13] J. Boussinesq. *Theorie de l'écoulement tourbillonnant et tumultueux des liquides dans les lits rectilignes a grande section*. Gauthier-Villars et fils, Paris, France, 1897.

[14] P. Bradshaw. *An introduction to turbulence and its measurement*. Pergamon Press, 1971.

[15] P. Bradshaw, D. Ferriss, and N. Atwell. Calculation of boundary-layer development using the turbulent energy equation. *Journal of Fluid Mechanics*, 28:593–616, 1967.

[16] P. Bradshaw and G. Huang. The law of the wall in turbulent flow. *Proceedings of the Royal Society of London A*, 451:165–188, 1995.

[17] M. Breuer. *Direkte Numerische Simulation und Large-Eddy Simulation turbulenter Strömungen auf Hochleistungsrechnern*. Shaker Verlag, 2002.

[18] M. Breuer, N. Jovičić, and K. Mazaev. Comparison of DES, RANS and LES for the separated flow around a flat plate at high incidence. *International Journal for Numerical Methods in Fluids*, 41:357–388, 2003.

[19] U. Bunge. *Numerische Simulation turbulenter Strömungen im Kontext der Wechselwirkung zwischen Fluid und Struktur*. PhD thesis, Technische Universität Berlin, Universitätsbibliothek (Diss.-Stelle), 2004.

[20] U. Bunge, C. Mockett, and F. Thiele. Calibration of different models in the context of detached-eddy simulation. In *AG STAB Mitteilungen*, Göttingen, 2003. DGLR.

[21] U. Bunge, C. Mockett, and F. Thiele. Guidelines for implementing detached-eddy simulation using different models. *Aerospace Science and Technology*, 11:376–385, 2007.

[22] R. Bush and M. Mani. A two-equation large eddy stress model for high sub-grid shear. In *Proceedings of the 15th AIAA Computational Fluid Dynamics Conference*, Anaheim, California, USA, June 11–14 2001.

[23] M. Casey and T. Wintergerste. *Best Practice Guidelines*. ERCOFTAC Special Interest Group on Quality and Trust in Industrial CFD, 2000.

[24] I. Çelik, Z. Cehreli, and I. Yavuz. Index of resolution quality for large eddy simulations. *Journal of Fluids Engineering*, 127(5):949–958, 2005.

[25] T. Cebeci and A. Smith. Analysis of turbulent boundary layers. *Series in Applied Mathematics and Mechanics, No. 15), 1974. 418 p*, 1974.

[26] D. Chapman. Computational aerodynamics development and outlook. *AIAA Journal*, 17(12):1293–1313, 1979.

[27] H. Choi and P. Moin. Effects of the computational time step on numerical solutions of turbulent flow. *Journal of Computational Physics*, 113:1–4, 1994.

[28] S. Choi. Note on the use of momentum interpolation method for unsteady flows. *Numerical Heat Transfer, Part A*, 36:545–550, 1999.

[29] C. Cichowlas, P. Bonaïti, F. Debbasch, and M. Brachet. Effective dissipation and turbulence in spectrally truncated euler flows. *Physical Review Letters*, 95(264502), 2005.

[30] G. Comte-Bellot and S. Corrsin. Simple Eulerian time correlation of full- and narrow-band velocity signals in grid generated, "isotropic" turbulence. *Journal of Fluid Mechanics*, 48:273–337, 1971.

[31] R. Courant, K. Friedrichs, and H. Lewy. Über die partiellen Differenzengleichungen der mathematischen Physik. *Mathematische Annalen*, 100(1):32–74, 1928.

[32] L. Davidson. Large eddy simulation: a dynamic one-equation subgrid model for three-dimensional recirculating flow. In *Proceedings of the 11th International Symposium on Turbulent Shear Flow*, volume 3, pages 26.1–26.6, Grenoble, 1997.

[33] L. Davidson. Hybrid LES-RANS: Inlet boundary conditions for flows with recirculation. In S.-H. Peng and W. Haase, editors, *Advances in hybrid RANS-LES modelling, Papers contributed to the 2007 Symposium of Hybrid RANS-LES Methods, Corfu, Greece*, volume 97 of *Notes on Numerical Fluid Mechanics and Multidisciplinary Design*, pages 55–66. Springer Verlag, 2008.

[34] R. Dean. Reynolds number dependence of skin friction and other bulk flow variables in two-dimensional rectangular duct flow. *Journal of Fluids Engineering*, 100:215–223, 1978.

[35] J. Deardorff. A numerical study of three-dimensional turbulent channel flow at large Reynolds numbers. *Journal of Fluid Mechanics*, 41:453–480, 1970.

[36] S. Deck. Numerical simulation of transonic buffet over a supercritical airfoil. *AIAA Journal*, 43(7):1556–1566, 2005.

[37] H. Djeridi, M. Braza, R. Perrin, G. Harran, E. Cid, and S. Cazin. Near-wake turbulence properties around a circular cylinder at high Reynolds number. *Flow, Turbulence and Combustion*, 71(1):19–34, 2003.

[38] P. Durbin. Separated flow computations with the $k - \varepsilon - v^2$ model. *AIAA Journal*, 33(4):659–664, 1995.

[39] J. Edwards and S. Chandra. Comparison of eddy viscosity-transport turbulence models for three-dimensional, shock-separated flowfields. *AIAA Journal*, 34(4):756–763, 1996.

[40] T. Esch, F. Menter, and W. Vieser. Heat transfer predictions based on two-equation turbulence models. In *Proceedings of the 6th ASME-JSME Thermal Engineering Joint Conference*, number TED-AJ03-542, 2003.

[41] A. Fage and F. Johansen. The structure of vortex streets. *Philosophical Magazine, Series 7*, 5(28):417–441, 1928.

[42] E. Fares and W. Schröder. A general one-equation turbulence model for free shear and wall-bounded flows. *Flow, Turbulence and Combustion*, 73(3):187–215, 2005.

[43] F. Felten and T. Lund. Kinetic energy conservation issues associated with the collocated mesh scheme for incompressible flow. *Journal of Computational Physics*, 215:465–484, 2006.

[44] J. Ferziger and M. Perić. *Computational methods for fluid dynamics*. Springer Verlag, 2002.

[45] O. Flachsbart. Messungen an ebenen und gewölbten Platten. *Ergebnisse der Aerodynamischen Versuchsanstalt zu Göttingen*, 4:96–100, 1932.

[46] M. Franke. *Untersuchung zum Potential höherwertiger Turbulenzmodelle für den aerodynamischen Entwurf*. PhD thesis, Technische Universität Berlin, 2003.

[47] J. Fröhlich and D. von Terzi. hybrid LES/RANS methods for the simulation of turbulent flows. *Progress in Aerospace Sciences*, 44:349–377, 2008.

[48] C. Fureby. Large eddy simulation of rearward-facing step flow. *AIAA Journal*, 37(11):1401–1410, 1999.

[49] B. Ganapathisubramani, E. Longmire, and I. Marusic. Characteristics of vortex packets in turbulent boundary layers. *Journal of Fluid Mechanics*, 478:35–46, 2003.

[50] A. Garbaruk, M. Shur, M. Strelets, and A. Travin. D3.2-12, Preliminary report on DES method investigation. Technical report, New Technologies and Services, 2004. Unpublished DESider project deliverable.

[51] M. Germano, U. Piomelli, P. Moin, and W. Cabot. A dynamic subgrid-scale eddy viscosity model. *Physics of Fluids A*, 3(7):1760–1765, 1991.

[52] S. Ghosal, T. Lund, P. Moin, and K. Akselvoll. A dynamic localization model for large-eddy simulation of turbulent flows. *Journal of Fluid Mechanics*, 286:229–255, 1995.

[53] F. Grinstein, L. Margolin, and W. Rider, editors. *Implicit large eddy simulation: computing turbulent fluid dynamics*. Cambridge University Press, 2007.

[54] D. Guenot. *Simulation des effets instationnaires à grande échelle dans les écoulements décollés*. PhD thesis, SUPAERO, Toulouse, 2004.

[55] W. Haase, B. Aupoix, U. Bunge, and D. Schwamborn, editors. *FLOMANIA - A European initiative on flow physics modelling*, volume 94 of *Notes on Numerical Fluid Mechanics and Multidisciplinary Design*. Springer Verlag, 2006.

[56] W. Haase, M. Braza, and A. Revell, editors. *DESider – A European effort on hybrid RANS-LES modelling*, volume 103 of *Notes on Numerical Fluid Mechanics and Multidisciplinary Design*. Springer Verlag, 2009.

[57] F. Hamba. An approach to hybrid rans/les calculation of channel flows. In W. Rodi and N. Fueyo, editors, *Engineering Turbulence Modelling and Experiments - 5*, pages 297–305. Elsevier, 2002.

[58] K. Hanjalić, M. Hadžiabdić, L. Temmerman, and M. Leschziner. Merging LES and RANS strategies: Zonal or seamless coupling? In R. Friedrich, B. Guerts, and O. Métais, editors, *Direct and Large-Eddy Simulation V*, pages 451–464. Springer, 2004.

[59] A. Harten. High resolution schemes for hyperbolic conservation laws. *Journal of Computational Physics*, 49:357–393, 1983.

[60] S. Hickel and N. Adams. On implicit subgrid-scale modeling in wall-bounded flows. *Physics of Fluids*, 19(105106), 2007.

[61] J. Hinze. *Turbulence*. McGraw-Hill Book Company, 1975.

[62] S. Hoerner. *Fluid-dynamic drag*. Hoerner Fluid Dynamics, 1965.

[63] S. Hoyas and J. Jiménez. Scaling of the velocity fluctuations in turbulent channels up to $\mathrm{Re}_\tau = 2003$. *Physics of Fluids*, 18(011702), 2006.

[64] J. Humphreys. On a circular cylinder in a steady wind at transition Reynolds numbers. *Journal of Fluid Mechanics*, 9:603–612, 1960.

[65] H. Jasak. *Error analysis and estimation for the finite volume method with applications to fluid flows*. PhD thesis, Imperial College of Science, Technology and Medicine, London, 1996.

[66] J. Jeong and F. Hussain. On the identification of a vortex. *Journal of Fluid Mechanics*, 285:69–94, 1995.

[67] J. Jiménez and S. Hoyas. Turbulent fluctuations above the buffer layer of wall-bounded flows. *Journal of Fluid Mechanics*, 2007. Submitted for publication.

[68] J. Jiménez and P. Moin. The minimal flow unit in near-wall turbulence. *Journal of Fluid Mechanics*, 225:213–240, 1991.

[69] J. Jiménez, A. Wray, P. Saffman, and R. Rogallo. The structure of intense vorticity in isotropic turbulence. *Journal of Fluid Mechanics*, 255:65–90, 1993.

[70] D. Johnson and L. King. A mathematically simple turbulence closure model for attached and separated turbulent boundary layers. *AIAA Journal*, 23(11):1684–1692, 1985.

[71] W. Jones and B. Launder. The prediction of laminarization with a two-equation model of turbulence. *International Journal of Heat and Mass Transfer*, 15(2):301–314, 1972.

[72] K. Karki and S. Patankar. Pressure based calculation procedure for viscous flows at all speeds. *AIAA Journal*, 27:1167–1174, 1989.

[73] P. Klebanoff. Characteristics of turbulence in a boundary layer with zero pressure gradient. Report 1247, NACA, 1955.

[74] T. Knopp. On grid-independence of RANS predictions for aerodynamic flows using model-consistent universal wall-functions. In P. Wesseling, E. Oñate, and J. Périaux, editors, *Proceedings of the European Conference on Computational Fluid Dynamics ECCOMAS CFD 2006*, Egmond aan Zee, The Netherlands, 2006.

[75] J. Kok. Resolving the dependence on freestream values for the $k-\omega$ turbulence model. *AIAA Journal*, 38(7):1292–1295, 2000.

[76] J. Kok, H. Dol, B. Oskam, and H. van der Ven. Extra-large eddy simulation of massively separated flows. In *Proceedings of the 42nd AIAA Aerospace Sciences Meeting and Exhibit*, Reno, Nevada, USA, 5–8 January 2004.

[77] A. Kolmogorov. The local strcuture of turbulence in incompressible viscous fluid for very large reynolds numbers. *Dokl. Akad. Nauk SSSR*, 30:299–303, 1941.

[78] R. Kraichnan. Inertial ranges in two-dimensional turbulence. *Physics of Fluids*, 10(7):1417–1423, 1967.

[79] H. Lamb. In an address to the British Association for the Advancement of Science, 1932.

[80] M. Leschziner and D. Drikakis. Turbulence modelling and turbulent-flow computation in aeronautics. *Aeronautical Journal*, 106(1061):349–383, 2002.

[81] F. Lien and M. Leschziner. Computational modelling of 3D turbulent flow in S-diffuser and transition ducts. In W. Rodi and F. Martelli, editors, *Engineering Turbulence Modelling and Experiments 2*, pages 217–228. Elsevier, 1993.

[82] D. Lilly. On the application of the eddy viscosity concept in the inertial sub-range of turbulence. NCAR Manuscript 123, National Center for Atmospheric Research, Boulder, Colorado, USA, 1966.

[83] D. Lilly. A proposed modification of the germano subgrid-scale closure method. *Physics of Fluids A*, 4(3):633–635, 1992.

[84] H. Lübcke. *Entwicklung expliziter Darstellungen zweiter statistischer Momente zur numerischen Simulation turbulenter Strömungen*. PhD thesis, Technische Universität Berlin, 2001.

[85] H. Lübcke, T. Rung, and F. Thiele. Prediction of the spreading mechanisms of 3D turbulent wall jets with explicit Reynolds-stress closures. In W. Rodi and N. Fueyo, editors, *Engineering Turbulence Modelling and Experiments 5*, pages 127–145. Elsevier, 2002.

[86] K. Mahesh, G. Constantinescu, and P. Moin. A numerical method for large-eddy simulation in complex geometries. *Journal of Computational Physics*, 197:215–240, 2004.

[87] B. Massey and J. Ward-Smith. *Mechanics of Fluids*. Stanley Thornes (Publishers) Ltd, 7th edition, 1998.

[88] F. Menter. Performance of popular turbulence models for attached and separated adverse pressure gradient flows. *AIAA Journal*, 30(8):2066–2072, 1992.

[89] F. Menter. Eddy viscosity transport equations and their relation to the $k-\varepsilon$ model. Technical Memorandum 108854, NASA Ames Research Center, 1994.

[90] F. Menter. Two-equation eddy-viscosity turbulence models for engineering applications. *AIAA Journal*, 32(8):1598–1605, 1994.

[91] F. Menter, Y. Egorov, and D. Rusch. Steady and unsteady flow modelling using the $k-\sqrt{k}l$ model. In K. Hanjalić, Y. Nagano, and S. Jakirlic, editors, *5th International Symposium on Turbulence, Heat and Mass Transfer*, pages 403–406, Dubrovnik, Croatia, 2006.

[92] F. Menter and M. Kuntz. *The Aerodynamics of Heavy Vehicles: Trucks, Buses, and Trains*, volume 19 of *Lecture notes in applied and computational mechanics*, chapter Adaption of eddy-viscosity turbulence models to unsteady separated flow behind vehicles. Springer Verlag, 2004.

[93] U. Michel, D. Eschricht, B. Greschner, T. Knacke, C. Mockett, Ĺ. Panek, F. Thiele, and J. Yan. Simulation of the sound radiation of turbulent flows with des. In *Proceedings of the West-East High Speed Flow Field Conference*, Moscow, Russia, 2007.

[94] C. Mockett, U. Bunge, and F. Thiele. Turbulence modelling in application to the vortex shedding of stalled airfoils. In W. Rodi and M. Mulas, editors, *Engineering Turbulence Modelling and Experiments 6*, pages 617–626. Elsevier, 2005.

[95] C. Mockett, O. Frederich, T. Schmidt, and F. Thiele. Numerical prediction of the aerodynamic interference of twin-sting model supports on empennage measurements. In *Proceedings of the 7th International Symposium on Engineering Turbulence Modelling and Measurements (ETMM7)*, pages 811–816, Limassol, Cyprus, 2008.

[96] C. Mockett, B. Greschner, T. Knacke, R. Perrin, J. Yan, and F. Thiele. Demonstration of improved DES methods for generic and industrial applications. In S.-H. Peng and W. Haase, editors, *Advances in hybrid RANS-LES modelling, Papers contributed to the 2007 Symposium of Hybrid RANS-LES Methods, Corfu, Greece*, volume 97 of *Notes on Numerical Fluid Mechanics and Multidisciplinary Design*, pages 222–231. Springer Verlag, 2008.

[97] C. Mockett, R. Perrin, T. Reimann, M. Braza, and F. Thiele. Analysis of detached-eddy simulation for the flow around a circular cylinder with reference to PIV data. In *Proceedings of the IUTAM Symposium on Unsteady Separated Flows and their Control*, Corfu, Greece, June 18–22 2007.

[98] C. Mockett, R. Perrin, T. Reimann, M. Braza, and F. Thiele. Analysis of detached-eddy simulation for the flow around a circular cylinder with reference to PIV data. *Flow, Turbulence and Combustion*, 2009. To be published.

[99] C. Mockett and F. Thiele. Overview of detached-eddy simulation for external and internal turbulent flow applications. In F. G. Zhuang and J. C. Li, editors, *New Trends in Fluid Mechanics Research, Proceedings of the 5th International Conference on Fluid Mechanics*, pages 79–82, Shanghai, China, 2007. Tsinghua University Press & Springer.

[100] R. Moser, J. Kim, and N. Mansour. Direct numerical simulation of turbulent channel flow up to $\mathrm{Re}_\tau = 590$. *Physics of Fluids*, 11(4):943–945, April 1999.

[101] N. Nikitin, F. Nicoud, B. Wasistho, K. Squires, and P. Spalart. An approach to wall modeling in large-eddy simulations. *Physics of Fluids*, 12(7):1629–1632, 2000.

[102] C. Norberg. Effects of Reynolds number and a low-intensity freestream turbulence on the flow around a circular cylinder. Technical Report Publikation Nr 87/2, Department of Applied Thermodynamics and Fluid Mechanics, Chalmers University of Technology, Göteborg, Sweden, 1987.

[103] C. Norberg. Fluctuating lift on a circular cylinder: review and new measurements. *Journal of Fluids and Structures*, 17:57–96, 2003.

[104] H. Nyquist. Certain topics in telegraph transmission theory. *Transactions of the American Institute of Electrical Engineers*, 47:617–644, April 1928.

[105] S. Obi, M. Perić, and G. Scheuerer. Second-moment calculation procedure for turbulent flows with collocated variable arrangement. *AIAA Journal*, 29(4):585–590, 1991.

[106] S. Patankar. *Numerical heat transfer and fluid flow*. McGraw-Hill, New York, 1980.

[107] M. Perić. *A finite volume method for the prediction of three-dimensional fluid flow in complex ducts*. PhD thesis, Imperial College of Science, Technology and Medicine, London, 1985.

[108] R. Perrin. *Analyse physique et modélisation d'ecoulements incompressibles instationnaire turbulents autor d'un cylindre circulaire à grand nombre de Reynolds*. PhD thesis, Institut National Polytechnique de Toulouse, 5th July 2005.

[109] R. Perrin, M. Braza, E. Cid, S. Cazin, A. Barthet, A. Sevrain, C. Mockett, and F. Thiele. Phase averaged turbulence properties in the near wake of a circular cylinder at high Reynolds number using POD. In *Proceedings of the 13th International Symposium on Applications of Laser Techniques to Fluid Mechanics*, Lisbon, Portugal, 2006.

[110] R. Perrin, M. Braza, E. Cid, S. Cazin, A. Barthet, A. Sevrain, C. Mockett, and F. Thiele. Obtaining phase averaged turbulence properties in the near wake of a circular cylinder at high Reynolds number using POD. *Experiments in Fluids; Springer Verlag*, 43(2-3):341–355, 2007.

[111] R. Perrin, M. Braza, E. Cid, S. Cazin, P. Chassaing, C. Mockett, T. Reimann, and F. Thiele. Coherent and turbulent process analysis in the flow past a circular cylinder at high Reynolds number. In *Proceedings of the IUTAM Symposium on Unsteady Separated Flows and their Control*, Corfu, Greece, June 18–22 2007.

[112] R. Perrin, C. Mockett, M. Braza, E. Cid, S. Cazin, A. Sevrain, P. Chassaing, and F. Thiele. Joint numerical and experimental investigation of the flow around a circular cylinder at high Reynolds number. In A. Schröder and C. E. Willert, editors, *Particle Image Velocimetry – New Developments and Recent Applications*, volume 112 of *Topics in Applied Physics*. Springer Verlag, 2008.

[113] A. Perry and T. Lim. Coherent structures in coflowing jets and wakes. *Journal of Fluid Mechanics*, 88:451–463, 1978.

[114] U. Piomelli, E. Balaras, H. Pasinato, K. Squires, and P. Spalart. The inner–outer layer interface in large-eddy simulations with wall-layer models. *International Journal of Heat and Fluid Flow*, 24:538–550, 2003.

[115] S. Pope. A more general effective-viscosity hypothesis. *Journal of Fluid Mechanics*, 72:331–340, 1975.

[116] S. Pope. *Turbulent Flows*. Cambridge University Press, 2000.

[117] L. Prandtl. Bericht über Untersuchungen zur ausgebildeten Turbulenz. *Zeitschrift für angewandte Mathematik und Mechanik*, 5:136–139, 1925.

[118] H. Reichardt. Vollständige Darstellung der turbulenten Geschwindigkeitsverteilung in glatten Leitungen. *Zeitschrift für angewandte Mathematik und Mechanik*, 31:208–219, 1951.

[119] O. Reynolds. An experimental investigation of the circumstances which determine whether the motion of water shall be direct or sinuous, and of the law of resistance in parallel channels. *Philosophical Transactions of the Royal Society of London*, 174:935–982, 1883.

[120] O. Reynolds. On the dynamical theory of incompressible viscous flows and the determination of the criterion. *Philosophical Tranactions of the Royal Society of London A*, 186:123–161, 1894.

[121] W. Reynolds. The potential and limitations of direct and large eddy simulations. In J. Lumley, editor, *Whither Turbulence? Turbulence at the Crossroads: Proceedings of a Workshop Held at Cornell University*, volume 357 of *Lecture Notes in Physics*, pages 313–343, Ithaca, NY, USA, 1990. Springer.

[122] W. Reynolds and A. Hussain. The mechanics of an organized wave in turbulent shear flow. Part 3: Theoretical models and comparisons with experiments. *Journal of Fluid Mechanics*, 54:263–288, 1972.

[123] L. Richardson. *Weather Prediction by Numerical Process*. Cambridge University Press, 1922.

[124] A. Richter and E. Naudascher. Fluctuating forces on a rigid circular cylinder in confined flow. *Journal of Fluid Mechanics*, 78(3):561–576, 1976.

[125] J. Riou, E. Garnier, S. Deck, and C. Basdevant. An extension of DDES applied to the computation of a generic missile fin in transonic regime. In *Proceedings of the 7th International Symposium on Engineering Turbulence Modelling and Measurements (ETMM7)*, pages 732–737, Limassol, Cyprus, 2008.

[126] J. Riou, E. Garnier, S. Deck, and C. Basdevant. Improvement of delayed-detached eddy simulation applied to separated flow over missile fin. *AIAA Journal*, 47(2):345–360, 2009.

[127] W. Rodi. Experience with two-layer models combining the $k - \varepsilon$ model with a one-equation model near the wall. In *29th Aerospace Sciences Meeting*, Reno, Nevada, USA, Jan 7th-10th 1991. AIAA Paper 1991-216.

[128] R. Rogallo and P. Moin. Numerical simulation of turbulent flows. *Annual Review of Fluid Mechanics*, 16:99–137, 1984.

[129] A. Roshko. On the wake and drag of bluff bodies. *Journal of the Aeronautical Sciences*, 22:124–132, 1955.

[130] J. Rotta. Über eine Methode zur Berechnung turbulenter Strömung. *Mitteilungen der Aerodynamischen Versuchsanstalt Göttingen*, Rep 69 A 14, 1968.

[131] T. Rung. Erweiterung von Eingleichungs-Turbulenzmodellen für lokales Nichtgleichgewicht. Internal report 3-98, Technische Universität Berlin, 1998.

[132] T. Rung. *Entwicklung anisotroper Wirbelzähigkeitsbeziehungen mit Hilfe von Projektionstechniken*. PhD thesis, Technische Universität Berlin, 2000.

[133] T. Rung. Statistische Turbulenzmodellierung. Notes accompanying the lecture course "statistische Turbulenzmodellierung" at the Institute of Fluid Mechanics and Engineering Acoustics, Technische Universität Berlin, http://www.cfd.tu-berlin.de, 2004.

[134] T. Rung, U. Bunge, M. Schatz, and F. Thiele. Restatement of the Spalart–Allmaras eddy-viscosity model in strain-adaptive formulation. *AIAA Journal*, 41(7):1396–1399, 2003.

[135] T. Rung, H. Lübcke, and F. Thiele. Universal wall-boundary conditions for turbulence-transport models. *Zeitschrift für angewandte Mathematik und Mechanik*, 81(1):1756–1758, 2000.

[136] T. Rung and F. Thiele. Computational modelling of complex boundary-layer flows. In *Proceedings of the 9th International Symposium on Transport Phenomena in Thermal-Fluid Engineering*, Singapore, 1996.

[137] T. Rung, L. Xue, J. Yan, M. Schatz, and F. Thiele. Numerische Methoden der Thermo- und Fluiddynamik. Notes accompanying the lecture course "CFD1" at the Institute of Fluid Mechanics and Engineering Acoustics, Technische Universität Berlin, http://www.cfd.tu-berlin.de.

[138] P. Sagaut. *Large eddy simulation for incompressible flows, an introduction*. Springer, 2nd edition, 2004.

[139] P. Sagaut, S. Deck, and M. Terracol. *Multiscale and multiresolution approaches in turbulence*. Imperial College Press, London, 2006.

[140] M. Schatz. Konvektionschemata in FAN/ELAN2/ELAN3. Internal report, Technische Universität Berlin, 2003.

[141] M. Schatz. *Numerische Simulation der Beeinflussung instationärer Strömungsablösung durch frei bewegliche Rückstromklappen auf Tragflügeln*. PhD thesis, Technische Universität Berlin, 2003.

[142] G. Schewe. On the force fluctuations acting on a circular cylinder in crossflow from subcritical up to transcritical Reynolds numbers. *Journal of Fluid Mechanics*, 133:265–285, 1983.

[143] H. Schlichting. *Boundary-Layer Theory*. McGraw-Hill, 7th edition, 1979.

[144] S. Schmidt. *Grobstruktursimulation turbulenter Strömungen in komplexen Geometrien und bei hohen Reynoldszahlen*. PhD thesis, Technische Universität Berlin, 2000.

[145] T. Schmidt, C. Mockett, and F. Thiele. Adaptive wall function for the prediction of turbulent flows. In N. Kroll, D. Schwamborn, K. Becker, H. Rieger, and F. Thiele, editors, *MEGADESIGN and MegaOpt - Aerodynamic Simulation and Optimization in Aircraft Design*, Notes on Numerical Fluid Mechanics and Multidisciplinary Design. Springer Verlag, 2008. To be published.

[146] M. Shur, P. Spalart, K. Squires, M. Strelets, and A. Travin. Three dimensionality in Reynolds-averaged Navier–Stokes solutions around two-dimensional geometries. *AIAA Journal*, 43(6):1230–1242, 2005.

[147] M. Shur, P. Spalart, M. Strelets, and A. Travin. Navier–Stokes simulation of shedding turbulent flow past a circular cylinder and a cylinder with a backward splitter plate. In G. Desideri, C. Hirsch, P. Le Tallec, M. Pandolfi, and J. Périaux, editors, *Proceedings of the Third European Conference on Computational Fluid Dynamics ECCOMAS CFD 1996*, pages 676–682, Paris, France, 1996. John Wiley & Sons, Chichester.

[148] M. Shur, P. Spalart, M. Strelets, and A. Travin. Detached-eddy simulation of an airfoil at high angle of attack. In W. Rodi and D. Laurence, editors, *Engineering Turbulence Modelling and Experiments 4*, pages 669–678. Elsevier, 1999.

[149] M. Shur, P. Spalart, M. Strelets, and A. Travin. A hybrid RANS-LES approach with delayed DES and wall-modeled LES capabilities. *International Journal of Heat and Fluid Flow*, 29:1638–1649, 2008.

[150] J. Smagorinsky. General circulation experiments with the primitive equations: I. the basic experiment. *Monthly Weather Review*, 91:99–164, 1963.

[151] A. Sohankar, L. Davidson, and C. Norberg. Large eddy simulation of flow past a square cylinder: comparison of different subgrid scale models. *Journal of Fluids Engineering*, 122:39–47, 2000.

[152] A. Sohankar, C. Norberg, and L. Davidson. Low–Reynolds–number flow around a square cylinder at incidence: Study of blockage, onset of vortex shedding and outlet boundary condition. *International Journal for Numerical Methods in Fluids*, 26, 1998.

[153] P. Spalart. Strategies for turbulence modelling and simulations. *International Journal of Heat and Fluid Flow*, 21(3):252–263, 2000.

[154] P. Spalart. Young person's guide to detached-eddy simulation grids. NASA contractor report NASA/CR-2001-211032, 2001.

[155] P. Spalart. The uses of DES: natural, extended, and improper. Invited presentation at the DESider Hybrid RANS-LES Symposium, Stockholm, Sweden, 14th-15th July 2005. http://cfd.mace.manchester.ac.uk/desider/index2.html.

[156] P. Spalart. Detached-eddy simulation. *Annual Review of Fluid Mechanics*, 41:181–202, 2009.

[157] P. Spalart and S. Allmaras. A one-equation turbulence model for aerodynamic flows. In *Proceedings of the 30th AIAA Aerospace Sciences Meeting and Exhibit*, Reno, Nevada, USA, 1992.

[158] P. Spalart, S. Deck, M. Shur, K. Squires, M. Strelets, and A. Travin. A new version of detached-eddy simulation, resistant to ambiguous grid densities. *Theoretical and Computational Fluid Dynamics*, 20:181–195, 2006.

[159] P. Spalart, W. Jou, M. Strelets, and S. Allmaras. Comments on the feasibility of LES for wings, and on a hybrid RANS/LES approach. *Advances in DNS/LES*, 1, 1997.

[160] P. Spalart and C. Rumsey. Effective inflow conditions for turbulence models in aerodynamic calculations. *AIAA Journal*, 45(10):2544–2553, 2007.

[161] D. Spalding. A single formula for the law of the wall. *Journal of Applied Mechanics*, 28(3):444–458, 1961.

[162] H. Stone. Iterative solution of implicit approximations of multidimensional partial differential equations. *SIAM Journal on Numerical Analysis*, 5:530–558, 1968.

[163] M. Strelets. Detached eddy simulation of massively separated flows. In *Proceedings of the 39th AIAA Aerospace Sciences Meeting and Exhibit*, Reno, Nevada, USA, 2001.

[164] M. Strelets and M. Shur. Private communication.

[165] V. Strouhal. Über eine besondere Art der Tonerregung. *Annalen der Physik und Chemie, Neue Folge*, 5(10):216–251, 1878.

[166] K. Swalwell. *The effect of turbulence on stall of horizontal axis wind turbines*. PhD thesis, Dept. of Mechanical Engineering, Monash University, 2005.

[167] K. Swalwell, J. Sheridan, and W. Melbourne. Frequency analysis of surface pressure on an airfoil after stall. In *Proceedings of the 21st AIAA Applied Aerodynamics Conference*, 2004.

[168] S. Szepessy and P Bearman. Aspect ratio and end plate effects on vortex shedding from a circular cylinder. *Journal of Fluid Mechanics*, 234:191–217, 1992.

[169] H. Tennekes and J.L. Lumley. *A First Course in Turbulence*. MIT Press, 1972.

[170] A. Travin, M. Shur, P. Spalart, and M. Strelets. Improvement of delayed detached-eddy simulation for LES with wall modelling. In P. Wesseling, E. Oñate, and J. Périaux, editors, *Proceedings of the European Conference on Computational Fluid Dynamics ECCOMAS CFD 2006*, Egmond aan Zee, The Netherlands, 2006.

[171] A. Travin, M. Shur, M. Strelets, and P. Spalart. Detached-eddy simulations past a circular cylinder. *Flow, Turbulence and Combustion*, 63(1):293–313, 2000.

[172] A. Travin, M. Shur, M. Strelets, and P. Spalart. Physical and numerical upgrades in the detached-eddy simulation of complex turbulent flows. In *Proceedings of the 412th Euromech Colloquium on LES and Complex Transitional and Turbulent Flows*, Munich, Germany, 2000.

[173] E. van Driest. On turbulent flow near a wall. *Journal of the Aeronautical Sciences*, 23(11):1007–1011, 1956.

[174] M. Vanella, U. Piomelli, and E. Balaras. Effect of local grid refinement on large-eddy simulation statistics and flow-fields. In *Proceedings of the 7th International Symposium on Engineering Turbulence Modelling and Measurements (ETMM7)*, pages 287–296, Limassol, Cyprus, 2008.

[175] T. von Kármán. Mechanische Ähnlichkeit und Turbulenz. In *Proceedings of the Third International Congress on Applied Mechanics*, pages 85–105, Stockholm, Sweden, 1930.

[176] T. von Kármán and H. Rubach. über den Mechanismus des flüssigkeits- und luftwiderstandes. *Physikalische Zeitschrift*, 13(2):49–59, 1912.

[177] S. Šarić, S. Jakirlić, A. Djugum, and C. Tropea. Computational analysis of locally forced flow over a wall-mounted hump at high-re number. *International Journal of Heat and Fluid Flow*, 27(4):707–720, 2006.

[178] S. Wallin and A. Johansson. An explicit algebraic Reynolds stress model for incompressible and compressible turbulent flows. *Journal of Fluid Mechanics*, 2000.

[179] K. Weinman, H. van der Ven, C. Mockett, T. Knopp, J. Kok, R. Perrin, and F. Thiele. A study of grid convergence issues for the simulation of the massively separated flow around a stalled airfoil using DES and related methods. In P. Wesseling, E. Oñate, and J. Périaux, editors, *Proceedings of the European Conference on Computational Fluid Dynamics ECCOMAS CFD 2006*, Egmond aan Zee, The Netherlands, 2006.

[180] P. Welch. The use of fast Fourier transform for the estimation of power spectra: a method based on time averaging over short, modified periodograms. *IEEE Transactions on Audio and Electroacoustics*, 15(2):70–73, June 1976.

[181] D. Wilcox. Reassessment of the scale-determining equation for advanced turbulence models. *AIAA Journal*, 26:1299–1310, 1988.

[182] D. Wilcox. *Turbulence modeling for CFD*. DCW Industries Inc, 1993.

[183] A. Wray. Unpublished DNS data. Available on AGARD database "*Test Cases for the Validation of Large-Eddy Simulations of Turbulent Flows*", ftp://torroja.dmt.upm.es, 1997.

[184] L. Xue. *Entwicklung eines effizienten parallelen Lösungsalgorithmus zur dreidimensionalen Simulation komplexer turbulenter Strömungen*. PhD thesis, Technische Universität Berlin, Universitätsbibliothek (Diss.-Stelle), 1998.

[185] J. Yan. *Effiziente Simulation komplexer Strömungen auf semi-strukturierten Gittern*. PhD thesis, Technische Universität Berlin, 2003.

[186] J. Yan, C. Mockett, and F. Thiele. Investigation of alternative length scale substitutions in detached-eddy simulation. *Flow, Turbulence and Combustion*, 74(1):85–102, 2005.

[187] J. Yan, K. Tawackolian, U. Michel, and F. Thiele. Computation of jet noise using a hybrid approach. In *Proceedings of the 13th AIAA/CEAS Aeroacoustics Conference (28th AIAA Aeroacoustics Conference)*, Rome, Italy, 2007. AIAA Paper 2007-3621.

[188] A. Yoshizawa and K. Horiuti. A statistically-derived subgrid-scale kinetic energy model for the large-eddy simulation of turbulent flows. *Journal of the Physical Society of Japan*, 54(8):2834–2839, 1985.

[189] M. Zdravkovich. *Flow around circular cylinders*, volume 1: Fundamentals. Oxford University Press, 1997.